

Spark Plasma Sintern von Nanomaterialien und Biomaterialien

Habilitationschrift

zur

Erlangung des akademischen Grades

Dr.-Ing. Habil.

Fakultät für Maschinenbau und Schiffstechnik

und

Mathematisch-Naturwissenschaftliche Fakultät

der Universität Rostock

Vorgelegt von

Faming Zhang, geb.am 01.12.1978 in Hebei

aus Rostock

Rostock, den 02.04.2013

Aus

der Physik für neue Materialien (Leiter: Prof. Dr. Eberhard Burkel)

der Mathematisch-Naturwissenschaftliche Fakultät

und

dem Lehrstuhl für Werkstofftechnik (Leiter: Prof. Dr. Olaf Kessler)

der Fakultät für Maschinenbau und Schiffstechnik

der Universität Rostock

**SPARK PLASMA SINTERING OF NANOMATERIALS AND
BIOMATERIALS**

FAMING ZHANG

PHD (HARBIN INSTITUTE OF TECHNOLOGY)

A THESIS SUBMITTED

FOR

HABILITATION

FACULTY OF MECHANICAL ENGINEERING AND MARINE

TECHNOLOGY, AND FACULTY OF MATHEMATICS AND

NATURAL SCIENCES, UNIVERSITY OF ROSTOCK

2013

Gutachter:

1. Prof. Dr.ner Eberhard Burkel

Chair of physics of new materials, Institute of Physics, University of Rostock,

August Bebel Str. 55, D-18055 Rostock, Germany

2. Prof. Dr.-Ing Olaf Keßler

Chair of Materials Science, Faculty of Mechanical Engineering and Marine

Technology, Albert- Einstein- Str. 2, D-18059 Rostock, Germany

3. Prof. Dr. James Zhijian Shen

Department of Inorganic Chemistry, Arrhenius Laboratory, Stockholm University,

SE-10691 Stockholm, Sweden

Datum der Abgabe: 02.04.2013

Datum der Verteidigung: 24.09.2013

CONTENTS

Abstract.....	i
List of publications included as part of the thesis.....	vi
Chapter 1 Introduction.....	1
1.1 Spark plasma sintering (SPS).....	1
1.2 Nanomaterials: nanocarbons and diamonds.....	6
1.3 Metallic biomaterials: Ti alloys and foams.....	12
1.4 Objectives of the thesis.....	16
Chapter 2 Indirect evidences for the presence of plasmas in SPS.....	24
2.1 Stability and phase transformation of nanocarbon materials under SPS (based on Publication A).....	24
2.2 Effect of atmosphere on the generation of plasmas in SPS (based on Publication B).....	37
Chapter 3 Synthesis of diamond from nanocarbon and graphite by SPS.....	47
3.1 Synthesis of diamond from carbon nanotubes with solvent catalysts by SPS (based on Publication C).....	47
3.2 Synthesis of diamond from fullerene C ₆₀ by SPS (based on Publication D).....	60
3.3 Synthesis of diamond from graphite with catalysts by SPS.....	68
Chapter 4 SPS of titanium alloys for biomedical applications.....	73
4.1 Preparation and properties of TiMn Alloys for biomedical applications (based on Publication E).....	73
4.2 Modification of Ti6Al4V alloys by rapid cooling SPS (based on publication F).....	86
Chapter 5 SPS of titanium foams for biomedical applications.....	105
5.1 SPS of macroporous pure titanium foams (based on Publication G).....	105
5.2 Ti6Al4V foams prepared by SPS with post heat treatment (based on Publication H).....	118
5.3 Other methods for preparation of titanium foams by SPS and surface modification.....	131
Chapter 6 Conclusions and outlook.....	138

Acknowledgements.....	144
Declaration.....	146
Appendix.....	147
Curriculum vitae	147
Original publications included as part of the thesis.....	158

Abstract

Spark plasma sintering (SPS) is a novel technique to fabricate advanced materials. The chapter 1 describes the origin, mechanism and development of the SPS as well as its applications in nanomaterials synthesis, diamond synthesis and biomaterials synthesis especially titanium based biomaterials. There are many mechanisms suggested to account for the enhanced sintering abilities of the SPS process. The one that draws the most controversy of these mechanisms involves the presence of momentary plasma. Additionally, the SPS has a potential to be used as an alternative method for diamond generation from nanocarbon and graphite, and is also a high efficient method to produce titanium alloys and foams for biomedical applications.

Chapter 2 concerns the study on the indirect evidences for the presence of plasmas in SPS. The thermal stabilities of carbon nanotubes, fullerene, graphene and graphite were investigated under SPS. Results were compared with data from synchrotron radiation in-situ high temperature X-ray diffraction of these materials. Part of the nanotubes, fullerene and graphene was transformed into diamond under SPS, but graphite kept stable. There was no diamond conversion in the in-situ X-ray diffraction experiments under the same condition. Their phase transition mechanism indicated the presence of plasmas during the SPS operation. In addition, the SPS experiments were conducted in vacuum and argon atmosphere with carbon nanotubes based materials. The phases and microstructures of the prepared samples were analyzed by Raman spectroscopy, Synchrotron X-ray and scanning electron microscopy. Results showed that diamond phase can be transformed from carbon nanotubes/FeNi mixtures at the minimum uniaxial pressure of 9.55 MPa in both vacuum and argon atmospheres of the SPS. At this pressure, high quality diamond crystals with hexahedron structures are obtained at 1200 °C in the argon atmosphere. Such a low pressure diamond formation provides an important indirect evidence for the existence of plasma during the SPS. The argon atmosphere can enhance the plasma generation and promote the diamond transition.

Chapter 3 reports the synthesis of diamond from nanocarbon and graphite by SPS.

Multiwalled carbon nanotubes (MWCNTs) with Fe₃₅Ni powders as solvent catalysts were used to synthesize diamond by SPS. The MWCNTs/Fe₃₅Ni mixtures were spark plasma sintered at various conditions. The microstructures and diamond phase were analyzed by using X-ray diffraction, Raman spectroscopy, scanning electron microscopy and transmission electron microscopy techniques. Experimental results show that the diamond crystals can be synthesized from MWCNTs/Fe₃₅Ni by using the SPS at lower temperature of 1200 °C under pressure of 70 MPa. Well-crystallized cubic diamonds consisted of mono-crystals and poly-crystals exhibiting particle sizes ranged (10-40) μm. The Fe₃₅Ni catalysts achieved an effective enhancement for diamond conversion from MWCNTs during the SPS. A model was also proposed to describe the diamond growth as a layer-by-layer growth mechanism. In addition, fullerene C₆₀ is unstable and can be transformed into crystalline diamond by SPS under a pressure of 50 MPa above temperatures of 1150 °C without any catalysts being involved. Well-defined diamonds with particle sizes up to 250 μm and transition rate about 30 vol.% are obtained at 1300 °C and no further growth in particle size is seen beyond this temperature. It is a direct transition process from C₆₀ to diamond with a structural reconstruction of carbon atoms without intermediate phases being involved. Additionally, the Ni, MnNi, MnNiFe and AlCuFe quasicrystal powder were used as the solvent catalysts for the diamond synthesis from graphite by the SPS. Diamond crystals have been converted from the graphite at the SPS condition of 1300 °C, 50 MPa for 20 min. Diamond nano- and micro-rods (80 nm-2 μm) have been obtained with the Ni catalysts from the graphite by the SPS. Diamond crystals with good diamond shapes in the range of (1-3) μm have been converted from the graphite with the AlCuFe catalyst. The diamond/copper composites are prepared by SPS. This composite shows the hard diamond phase with hardness of (15.1 ± 1.6) GPa embedded in the soft copper matrix with hardness of (1.45 ± 0.2) GPa with a uniform distribution.

Chapter 4 studies the SPS of titanium alloys for biomedical applications. The titanium-manganese (TiMn) alloys have been extensively used in aerospace and hydrogen storage. In this part, the TiMn alloys with various manganese contents ranging (2-12) wt.% were prepared by using mechanical alloying and SPS techniques.

The microstructures, mechanical properties including hardness, elastic modulus and ductility, cytotoxicity and cell proliferation properties of the TiMn alloys were investigated to explore their biomedical applications. The addition of manganese to the titanium reduced the α to β transformation temperature and was confirmed as a β stabilizer element. The manganese increased the relative density of the alloy and thus high density TiMn alloys with $\alpha+\beta$ structure were prepared by using SPS at 700 °C. The hardness increased significantly ranging from (2.4±0.24) GPa of Ti2Mn to (5.28±0.36) GPa of Ti12Mn and the elastic modulus as well ranging from (83.3±3.0) GPa of Ti2Mn to (122±6.0) GPa of Ti12Mn, the ductility decreased ranging from (21.3±2.4)% of Ti2Mn to (11.7±2.0)% of Ti12Mn with increasing manganese content in the Ti. Concentrations of Mn below 8 wt.% in titanium reveal negligible effects on the metabolic activity and the cell proliferation of human osteoblasts. The Mn could be used in lower concentrations as an alloying element for biomedical titanium. The Ti2Mn, Ti5Mn and Ti8Mn alloys with good mechanical properties and acceptable cytocompatibility have a potential for use as bone substitutes and dental implants. Additionally, the Ti6Al4V alloys are prepared by SPS with a novel integrated nitrogen gas quenching system. Finite element simulations of heat transfer coefficient and temperature distribution during cooling process of the Ti6Al4V alloy in the SPS were performed. The mechanical properties and microstructures of the Ti6Al4V alloy using various cooling rates were investigated. Simulation results reveal that the gas quenching can increase the heat transfer coefficient up to (5-7) times higher and magnify the temperature gradient of the Ti6Al4V alloys. Experimental results show that sinter-hardening of the Ti6Al4V alloy has been achieved, where the hardness rises from 327 HV1 to 353 HV1 with the cooling rate ranging from 1.6 °C/s to 6.9 °C/s. The ultimate compressive strength and the ductility have increased up to 1832 MPa and 34%, respectively. The gas quenching leads to much more pronounced dimples in fracture surfaces, the precipitation of intermetallic phases and a morphological change to lamellar α -Ti phase in metallography. The mechanical properties and microstructures of the Ti6Al4V alloys have been tailored by the rapid cooling-SPS combining sintering and

gas quenching.

Chapter 5 investigates the SPS of titanium foams for biomedical applications. Macroporous pure titanium (Ti) foams with porosity of (30-70) % and pore size of (125-800) μm were fabricated by SPS. A mixture of Ti and sodium chloride (NaCl) powders were spark plasma sintered at 700 °C under pressure of 50 MPa and the NaCl phase was then dissolved in water. The resulting Ti foams consist of pure α -Ti phase with interconnected macropores in quadratic cross sections. The plateau stress and Young's modulus agree with the Gibson-Ashby models, and coarsely follow a linear decline with the increase of the pore sizes, and exponential decay with the increase of the porosity. The macroporous Ti foams with plateau stress (27.2-94.2) MPa and Young's modulus (6.2-36.1) GPa have a potential to be used as bone implants. Additionally, Ti6Al4V foams were fabricated by SPS with post heat treatment using a blend of Ti6Al4V and NaCl powders. The Ti6Al4V foams fabricated at 700 °C and 50 MPa in SPS cannot get high relative densities. These sintered foams were post heat treated in a pressureless mode of the SPS at 1100 °C for 5 min. This heat treatment is very effective to reduce the microporosity and to fully densify the foam walls. Young's modulus of the foams was in the range of 33.0 GPa to 9.5 GPa and yield strength ranged from 110.2 MPa to 43.0 MPa with porosity values from 44.7% to 70.0% obeying the Gibson-Ashby models. The human osteoblast cell line MG-63 validated the cellular acceptance of the foam surfaces. The pressureless SPS provides a new method for the heat treatment of metallic foams. The Ti6Al4V foams with Cu spacer were prepared by the SPS. The Cu spacer was removed by HNO₃ acid washing afterwards. The in-situ pore forming method by soaking of the spark plasma sintered TiMg solids in simulated body fluid was also introduced. In the end, TiO₂ nanostructures in anatase/rutile phases were modified on the pore walls of the Ti8Mn foam uniformly by NaOH solution soaking and heat treatment. This surface modified TiMn foam exhibited high *in vitro* bioactivity with a fast apatite-forming ability in the simulated body fluid. The Ti, Ti6Al4V and TiMn foams processed by SPS have a potential to be used as ideal bone implants.

In the Chapter 6, conclusions drawn from the entire body of the work and outlook for the future are given. The thesis was then followed by selected original publications which contain the experimental data, the substantial results as well as the detailed discussion of the respective results.

List of publications included as part of the thesis

- [A] **F. Zhang**, C. Mihoc, F. Ahmed, C. Latte, E. Burkel. Thermal stability of carbon nanotubes, fullerene and graphite under spark plasma sintering. **Chemical Physics Letters** 2011,510 (1-3):109-114.
- [B] **F. Zhang**, F. Ahmed, J. Bednarcik, and E. Burkel. Diamond synthesis through the generation of plasma during spark plasma sintering. **Phys. Status Solidi A**. 2012, 209(11): 2241-2246.
- [C] **F. Zhang**, M. Adam, E. Otterstein, E. Burkel. Pulsed electric field induced diamond synthesis from carbon nanotubes with solvent catalysts. **Diamond and related Materials**. 2011, 20(5-6): 853-858.
- [D] **F. Zhang**, F. Ahmed, G. Hölzhuter, E. Burkel . Growth of diamond from fullerene C60 by spark plasma sintering. **Journal of Crystal Growth**. 2012, 340(1):1-5.
- [E] **F. Zhang**, A. Weidmann, J. B. Nebe, U. Beck, E. Burkel. Preparation, microstructures, mechanical properties and cytocompatibility of TiMn Alloys for biomedical applications. **Journal of Biomedical Materials Research B** 2010, 94B: 406-413.
- [F] **F. Zhang**, M. Reich, O. Kessler, E. Burkel. Potential of rapid cooling spark plasma sintering for metallic materials. **Materials Today**. 2013,16(5): 192-197.
- [G] **F. Zhang**, E. Otterstein, E. Burkel. Spark plasma sintering, microstructures and mechanical properties of macroporous titanium foams. **Advanced Engineering Materials** 2010, 12 (9): 863-872.
- [H] Y. Quan, **F. Zhang**, H. Rebl, B. Nebe, O. Kessler, E. Burkel. Ti6Al4V foams fabricated by spark plasma sintering with post heat treatment. **Materials Science and Engineering A**. 2013, 565:118-125.

Chapter 1 Introduction

Sintering is a process to consolidate powders into solids. It has been practiced for thousands of years in the making of bricks and pottery and in the consolidation of precious metal jewelries [1]. During the period 1920-1950, sintering began as a solid-state science came out of the empirical work [2]. Contributions to the understanding of the basic phenomena of consolidation by mass transport mechanisms were subsequently made by Frenkel, Kuczynski, Lenel, Coble, Kingery and Berg, German and Munir, as well as Idem during the period from 1948 to 1976 [3-8]. From the view point of thermal dynamics, the ability to achieve consolidation without melting is realized by the thermal activation of mass transport processes driven by reduction of surface and grain boundary energies. In order to activate the sintering and attain high density and strength, many sintering methods have been studied and used, e.g. high temperature sintering, gas-pressure sintering [9], mechanical pressure sintering (hot pressing) [10], addition of sintering aids [11], minimization Ostwald Ripening [12] and so on. Significant efforts have been made and continue to be directed towards other means of activation to achieve high density at lower temperatures and/or in shorter times [13]. These efforts have strong practical and economic reasons to increase the sintering efficiency and save energy. Among these is the recent use of a pulsed DC current to activate sintering. It is referred to spark plasma sintering.

1.1 Spark plasma sintering (SPS)

Spark plasma sintering (SPS), commonly also defined as pulsed electric current sintering (PECS), field assisted sintering (FAST) is a novel pressure assisted pulsed electric current sintering process utilizing ON-OFF DC pulse energizing. Due to the repeated application of the ON-OFF DC pulsed voltage and current in powder materials, the spark discharge point and the Joule heating point (local high temperature-state) are transferred and dispersed to the overall specimen [14]. The SPS process is based on the electrical spark discharge phenomenon: a high energetic, low voltage spark pulse current momentarily generating high localized temperatures, from

several to ten thousand degrees between the particles resulting in high thermal and electrolytic diffusion [14, 15].

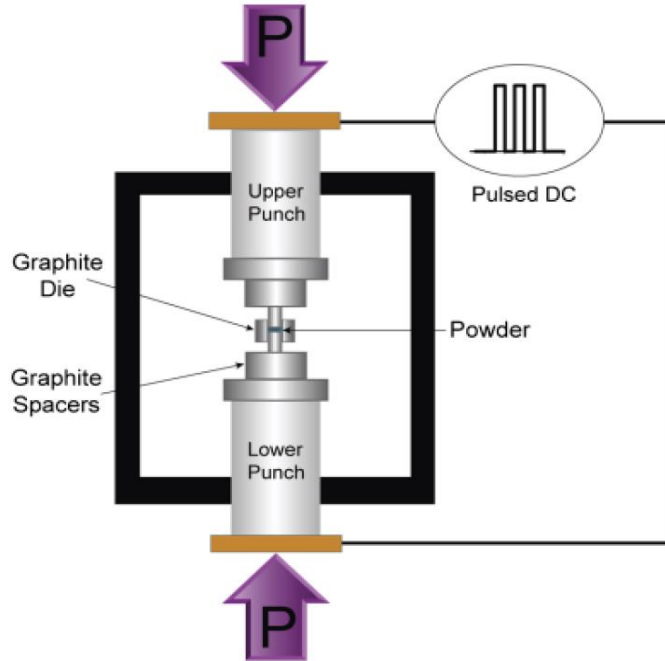
1.1.1 The history of the SPS

The history of the technology related to the process in question started in the late 1930s when a sintering process using electrical energizing was introduced in the United States [16]. The term of ‘spark sintering’ first appeared in a publication by Lenel in the 1950s [17]. In Japan, a process based on the pulse current applied sintering method was researched and patented in the 1960s and is known as spark sintering [18, 19]. But it was not put to wide use due to the lack of application at that time, and unsolved problems associated with industrial production, equipment cost and sintering efficiency. The first commercialized SPS (DR. SINTER) was born in Japan on 1990 from Sumitomo Coal Mining Co. Ltd [20]. Then, FCT (Fine Ceramics Technologies) GmbH & Co in Germany produced the first SPS unit in Europe in the year of 2003 [21]. More recently, SPS equipment has been manufactured in the U.S.A. [22] and China [23].

1.1.2 The SPS process

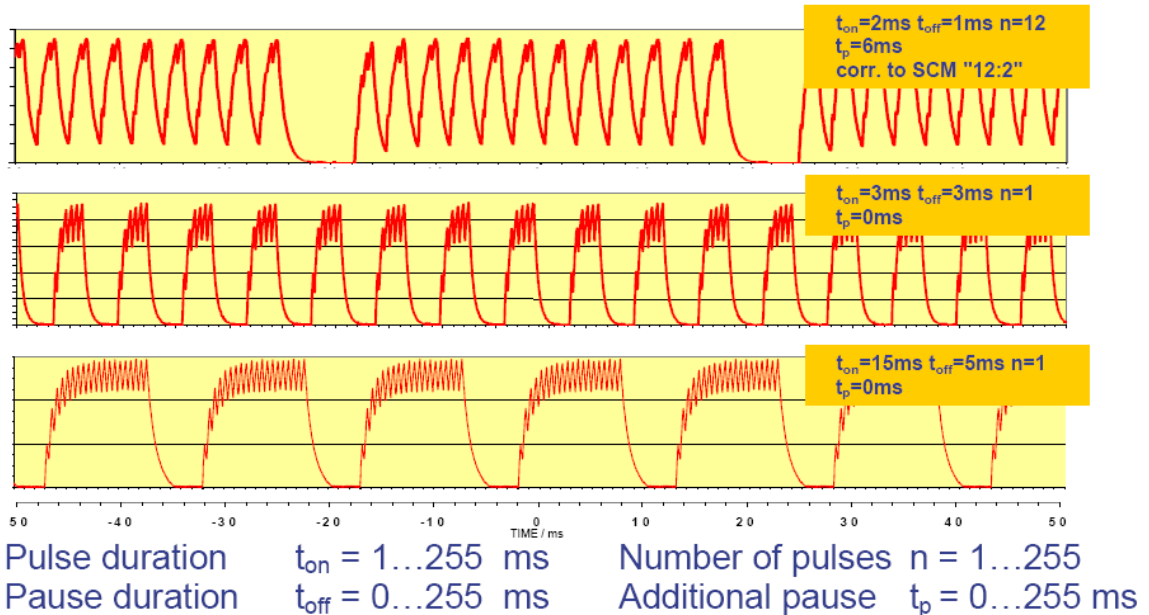
Figure 1-1(a) shows a schematic diagram of the SPS apparatus [13]. The SPS process is similar to hot pressing, in that the powders are loaded into a die (typically graphite) and a uniaxial pressure is applied during the sintering [24]. However, instead of using external heating source through the normal AC current, a pulsed DC current passed through the sample and the electrically conducting pressure die. Therefore, the die acts as a heating source and the sample can be heated from both outside and inside. Due to the efficient thermal transfer, the mechanical stress applied, and most possibly the enhanced diffusion rates due to the presence of an DC electric field, the diffusion-oriented processes progress very rapidly once activated in this process [12]. Typically, a pulsed DC current is applied with a relatively low voltage (below 10 V) and a high current (1-20 kA). The current pulse density can be in the order of (1-10) kA cm⁻². Figure 1-1(b) shows the DC pulse forms used in the SPS [25]. The pulsing pattern is made up of a sequence of pulses with the current, followed by a duration pause of a current. Pulse spans in a typical SPS apparatus are

3.3 ms (DR. SINTER) or 3 ms (FCT) in duration. In the FCT system, the pulsed form ($t_{on}=15$ ms, $t_{off}=5$ ms, $n=1$, $t_p=0$) in the bottom of the Figure 1-1(b) and a similar form ($t_{on}=12$ ms, $t_{off}=2$ ms, $n=1$, $t_p=0$) are usually used during the sintering.



(a)

High flexibility from pure DC current to variable pulse forms



(b)

Figure 1-1 Schematic diagram of the SPS apparatus [13] (a) and the DC pulse forms used in the SPS [25] (b).

1.1.3 Mechanisms of the SPS

There are many mechanisms proposed to account for the enhanced sintering abilities of the SPS process; for example:

- (a) Joule's heating [26, 27],
- (b) Local melting and evaporation especially in metallic systems [28],
- (c) Surface activation on particles [29],
- (d) Mechanical activation and plastic deformation,
- (e) Field assisted diffusion [30,31],
- (f) Spark impact pressure [26, 28],
- (g) Plasma cleaning of particle surfaces [27,31],
- (h) Plasma sintering
- (i) Electron wind force [32].

The mechanisms from (a) to (e) have been relatively well accepted. As mentioned above, during the SPS processing, the die acts as a heating source and the sample can be heated from both outside and inside by the DC currents. The joule heating effects from both external and internal can be greatly enhanced during the SPS. The Joule's heating mechanism (a) has been well established. The application of low pressure and high frequency impulsive current was particularly effective in the first stage of sintering. It promoted sparks and rapid local heating at particle contact interfaces due to the high initial contact resistance. It can lead to the local melting and evaporation especially in metallic systems, as well as the surface activation on particles. The mechanisms (b) and (c) have been accepted. Under the uniaxial force, the heated material becomes softer and it exerts plastic deformation during the SPS. The surface, grain boundary and volume diffusion among particles can be enhanced by the electric field assisted sintering. Plastic deformation combined with enhanced diffusion result in the densification of the powder compact to over 99% of its theoretical density. The mechanism of mechanical activation and plastic deformation (d) and field assisted diffusion (e) are acceptable. During the experiments, spark plasma sintered bodies were fully densified usually using a two stage pressure cycle [33]: low pressure to promote interparticle heating (<10MPa) and relatively high pressure to enhance

powder densification. The mechanism (i) is much more hypothetical in nature. The one that draws the most controversy of these mechanisms involves the presence of momentary plasma. Early on, it was suggested that plasma developed in the interparticle regions, as raised in the mechanisms of (f) to (h). Some researcher [32] presented experimental investigations and claimed that plasma is absent in SPS processing. This problem on the presence or absence of plasmas during SPS needs further investigations.

1.1.4 Application and research tendency of the SPS

The SPS is a remarkable technique for synthesizing and consolidating a large variety of both new and traditional materials. The main advantage of the SPS over more conventional sintering techniques, such as hot pressing or pressureless sintering, lies in its ability to rapidly sinter traditionally difficult-to-sinter materials to full density. This time saving translates directly into a cost savings both in terms of potential product output and in energy saving (power consumption is reduced to 20 to 30% of the hot-press method). The materials those have been prepared by the SPS are nanophase materials [34], electronic materials (thermoelectric semiconductors, target, magnetic and dielectric materials, etc.) [35, 36], fine ceramic materials (oxides, carbides, nitrides, etc.) [37], functionally graded materials (FGM's) (ceramic-metal, polymer-metal and other materials) [38], biomaterials (titanate or apatite implants, artificial bones and joints, etc.) [39, 40], hard alloy tool materials (WC/Co, ceramic or cermet cutting tools) [41,42], mold and die materials (press, plastic and wire drawing dies, etc.), diamond tool materials (bonded cobalt and bronze segmented and straight stone grinding and cup wheels, cutting blades, etc.) [43], porous materials (ceramic and metallic bioreactors, filters, battery cell materials, etc.) [44, 45] and other sintering applications.

Grasso et al [33] reviewed the number of published patents from 1900 to 2008 applied to functional and structural materials by the SPS. The large number of industrial applications underlines the wide flexibility of the SPS. There are still relative few researches in SPS of optical materials, FGM, carbon nanotubes and

porous materials. Munir et al [46] have consolidated nanometric functional oxides by SPS using a super high pressure (up to 1.0 GPa). They achieved densities of upward of 95% and with a grain size as low as 13 nm. With this grain size, the normally ionically conducting YSZ (for example) become photonically conducting at room temperature [47]. Morsi et al [48, 49] have modified the SPS to a spark plasma extrusion process, whereby aluminum samples with extruded geometries have been prepared. Based on the above analysis, we propose the future tendency of the SPS: optical material, FGM, porous materials, super-high pressure SPS, complex shape components with net-shaping, new modification of the SPS process, e.g. spark plasma extrusion, pressureless sintering SPS, especially our researches in this thesis on rapid cooling SPS combining sintering and gas quenching, and finally the spark plasma system (sintering, joining, surface treatment and synthesis).

1.2 Nanomaterials: nanocarbons and diamonds

Nanomaterials have been the subject of enormous interests over the past two decades. Their defining characteristic is that at least one dimension of the material's microstructure is in the range of 1-100 nanometers (nm). These materials have the potential for wide-ranging industrial, biomedical, energy, environment and electronic applications. Nanomaterials can be metals, ceramics, polymeric materials, or composite material. The SPS is a suitable technique to prepare bulk nanomaterial from powders of almost all of the materials. It belongs to a bottom-up method for preparation of bulk nanomaterials. The fast heating rate and short soaking time can inhibit the grain growth of the nanocrystalline particles to some extent. There are many nanostructured ceramics [50, 51], metals [52, 53] and their composites [54, 55] have been prepared by the SPS successfully. The nanocarbon materials are a group of very popular nanomaterials with superior physical and chemical properties.

1.2.1 The nanocarbon materials

Diamond and graphite are the traditional forms of crystalline carbon familiar to us. The nanocarbon materials include fullerene C₆₀, carbon nanotubes (CNTs), graphene and nano-diamonds. C₆₀ is a carbon allotrope that consists of 60 carbon atoms,

arranged as 12 pentagons and 20 hexagons [56]. The shape is the same as that of a soccer ball. The discovery of C₆₀ has stimulated a large activity in chemistry. It opened up the new branch of Fullerene-Chemistry which studies the new families of molecules that are based on Fullerenes. The 1996 Nobel Prize for Chemistry has been won by Harold W. Kroto, Robert F. Curl and Richard E. Smalley for their discovery of C₆₀ in 1985 of a new allotrope of carbon [57].

Carbon nanotubes have attracted the fancy of many scientists worldwide. The small dimensions, strength and the remarkable physical properties of these structures make them a very unique material with a whole range of promising applications. Carbon nanotubes were discovered accidentally by Sumio Iijima in 1991 [58], while studying the surfaces of graphite electrodes used in an electric arc discharge. Carbon nanotubes with incredible strength and fascinating electronic properties appear to be ready to overtake fullerenes in the race to the technological marketplace.

Graphene is the name given to a monolayer of carbon atoms tightly packed into a two-dimensional (2D) honeycomb lattice, and is a basic building block for graphitic materials of all other dimensionalities [59]. It can be wrapped up into 0D fullerenes, rolled into 1D nanotubes or stacked into 3D graphite. Recent years have witnessed many breakthroughs in research on graphene as well as a significant advance in the mass production of this material. This one-atom-thick fabric of carbon uniquely combines extreme mechanical strength, exceptionally high electronic and thermal conductivities, impermeability to gases, as well as many other supreme properties, all of which make it highly attractive for numerous applications.

Nanoscale diamond particles were first produced by detonation in the USSR in the 1960 s, but they remained essentially unknown to the rest of the world until the end of the 1980s. Then, beginning in the late 1990s, a number of important breakthroughs led to wider interest in these particles, which are now known as nanodiamonds [60]. Nanodiamonds have excellent mechanical and optical properties, high surface areas and tunable surface structures. The nanodiamonds have very broad applications as well as they are non-toxic, which makes them also well suited to biomedical applications.

1.2.2 Diamonds

Diamond is a typical covalent crystal in which carbon atoms are bonded together very strongly. This structural feature leads to the highest hardness among all materials and superior thermal conductivity, as well as excellent chemical stability and transparency. Owing to these outstanding properties, diamond has been employed in a wide range of uses. Small diamond crystals in micrometers can be used for polish, wear resistance parts and additives for composites. Large diamond crystals of several millimeters in size are used for high precision cutting tools, wire-drawing dies, heat sinks, optical windows, surgical blades, jewelries and so on. In many fields of scientific research such as space, high pressure and radiation, large diamond crystals are the essential components of research equipment, and will become more essential to a wider variety of commercial and scientific purposes in future.

Commercial methods of manufacturing synthetic diamond evolved out of a number of technical developments of the 1950s. From a scientific perspective, it is interesting to note that both principal processes by which synthetic diamond is currently manufactured come from that decade. Diamond particles and diamond films have now been successfully obtained by many methods including high-pressure and high-temperature (HPHT) [61], detonation [62], combustion flames [63] and chemical vapour deposition (CVD) [64], RF plasma [65] and microwave plasma [66] etc., where the HPHT method is still the most popular commercial method for the diamond synthesis.

1.2.2.1 HPHT Method

Since it was first developed by Bundy et al. at GE in 1955 [67], high pressure–high temperature (HPHT) technology via a temperature gradient process has been widely used to produce diamond single crystals. Today, the high-pressure-high temperature (HPHT) diamond synthesis process remains the dominant manufacturing process for industrial diamond. The pressure and temperature required for the process, generally around (5-6.5) GPa and (1300-1700) °C, depend on the chemistry of the solvent used and the desired crystal geometry [68]. The HPHT, a process which mimics the way in which natural diamonds are formed by geophysical processes deep in the earth, has

allowed synthetic diamond to become a key material in the cutting and abrasive business, being widely used in the machine tool industry, oil and gas drilling, mining, quarrying and construction. The most commonly used machines for producing diamond have been Belt, cubic, tetrahedral, toroidal or split sphere type machines [68, 69]. The apparatus, as schematically shown in Fig.1-2a, consists of two spherical halves held together with steel clamps [69]. Pressurized oil is pumped into the cavity between the inner surface of the spherical chamber and a rubber membrane, which surrounds eight truncated octet shaped anvils. The latter anvils in turn transfer the pressure into the tetragonal growth cell via six pyramid shaped WC-Co anvils. As pictured in Fig. 1-2b, the split sphere apparatus is rather compact and is capable of maintaining pressure for matter of days by using a small mechanical pump.



Figure. 1-2 Schematic diagram of split sphere apparatus (a):1-split sphere pressure chamber, 2-safety clamps, 3-large dies, 4-small dies, 5-core, 6-power inlet, 7-rubber membrane, 8-oil inlet, 9-cooling water; and photograph of the split sphere apparatus (b) [69].

1.2.2.2 CVD Method

In contrast, synthesis of diamond by Chemical Vapor Deposition (CVD) uses a low pressure process. The process relies on decomposing carbon-containing gas molecules, such as methane, acetylene or carbon dioxide at sub-atmospheric pressure and depositing diamond as a film on a substrate. The first attempts to grow diamond from the gas phase were made in Europe as early as 1911 [70]. The starting material was acetylene in the presence of mercury vapor at 1000 °C. The real advancement of CVD

diamond has evolved from work carried out from the 1950s onwards by researchers in the USA, Russia and Japan. The first successful documented attempt to grow diamond at low pressures was by William G. Eversole of the Union Carbide Corporation (USA) in 1952, making Eversole the first person to make diamond of any kind [71]. Today there are three main CVD methods used to create diamond films involving thermal (for example, hot filament) or plasma (DC, RF or microwave) activation, or use of a combustion flame (oxyacetylene or plasma torches) [72]. The substrate temperature, the concentration of plasma species, and the substrate materials determine the crystallinity of the growing material. The importance of CVD methods is that they do not require the huge pressures required for HPHT synthesis and can create diamond that can be tailored for a wide range advanced engineering applications. This technology opens the possibility of making new shapes, coatings, films and qualities that can exploit diamond's unique properties in a breath-taking array of industries.

1.2.2.3 Detonation method

Another dynamic method to produce diamond is the detonation of pure and composite CHNO explosives with a negative oxygen balance. The study of detonation-synthesized diamond first appeared in 1988 and has drawn tremendous attention in recent years [73]. Explosives with a negative oxygen balance (for example a mix of 60 wt% TNT ($C_6H_2(NO_2)_3CH_3$) and 40 wt% hexogen ($C_3H_6N_6O_6$) are detonated in a closed metallic chamber in an atmosphere of N_2 , CO_2 and liquid or solid H_2O [60, 74]. After detonation, diamond-containing soot is collected from the bottom and the walls of the chamber. The inherent extremely nonequilibrium process of dynamic loading may induce many defects in the diamonds. It is a good method to prepare nanocrystalline diamond.

1.2.2.4 SPS as new emerging diamond synthesis method

In the year of 2004, during study of the thermal stability of multi-walled carbon nanotubes (MWCNTs) under various SPS conditions, Zhang et al first found that under SPS conditions of 1500 °C at very low pressure (80 MPa) carbon nanotubes were unstable and transformed into diamonds without any catalysts being involved [75]. The transformation mechanism involves the breakage of some C–C bonds, the

formation of carbon nano-onions (multilayer fullerenes), and the nucleation and growth of the diamond phase within the onion cores [76]. The effect of the high temperatures and sparking plasmas is similar to the electron or ion beam irradiations or high pressures. As a result, diamond forms from the intermediate nano-onions when localized high energy conditions are satisfied. Additionally, the low purity MWCNTs (60% purity) with a very cheap price also can be used as starting materials for the direct synthesis of diamond by the SPS technique [77]. It is postulated that the spark plasmas play a key role to provide most of the energy required in these diamond transitions. It is seen as an important evidence for the presence of spark plasmas during the SPS process. These studies indicate that the SPS has a potential to be used as an alternative method for diamond generation. But it needs further and systematically investigation to promote the SPS method to be used as a large-scale synthetic diamond production technique instead of the present hydrostatic HPHT method.

1.2.2.5 Recent research status of SPS nanocarbon materials

In this field, Schmidt et al [78] have used the spark plasma sintering to prepare Diamond/MMCs with Co-free Steel/Cu matrix composition, and the results of that investigation demonstrate that diamond impregnated wire saw beads can be successfully produced by the SPS. The Al/diamond [79] and Ti/Si/TiC/diamond [80] composites by the SPS were also reported. Inam et al. [81] reported that multiwall carbon nanotubes were not preserved for ceramic matrices that require high sintering temperatures (>1600 °C) and longer processing times (>13 min) in the SPS. Huang et al [82] investigated the influence of high current on the structure and integration of carbon nanotubes during the SPS. Observation of the microstructure showed that most carbon nanotubes burn out or diffuse into alumina grains when composite powders directly contact the graphite plungers of the sintering die. Laurent et al [83] prepared bulk samples of double-walled carbon nanotubes. The best SPS conditions are 1100 °C and 100 MPa. Raman spectroscopy and scanning electron microscopy show that the nanotubes are undamaged. The density is equal to 1.29 g/cm³ and the pores are all below 6 nm in diameter. The electrical conductivity is equal to 1650 S/cm. The

transverse fracture strength is equal to 47 MPa. Yang et al [84] found inter-tube bonding, graphene formation and anisotropic transport properties in spark plasma sintered multi-wall carbon nanotube arrays. Li et al [85, 86] investigated the transport properties and super-hydrophobic surface of bulk carbon nanotubes compacted by the SPS. The physical properties of the carbon nanotubes compacts were also studied. The carbon nanotubes bulk samples were fabricated by the SPS. The thermal conductivity of the resulting bulk samples was measured by the conventional laser-flash method, and the corresponding thermal conductivity was found to be as low as 4.2 W/m/K at room temperature [87]. In summary, in this field, some researcher focused on the diamond/metal or diamond/ceramic composites by the SPS, some researchers focused on the stability and degradation of the CNTs during the SPS, and some researches paid attention on the physical properties of the bulk carbon nanotubes compacts by the SPS. In South Africa, one group also started the diamond synthesis by the SPS with the cooperation of Element Six Company that is a subsidiary of De Beers and the world's leading manufacturer and supplier of industrial Diamond supermaterials. Consequently, it is of great importance for a better in-depth understanding of their thermal stability under the pulsed direct current conditions of these nano-carbon materials, especially their possible transition to diamond. The special physical properties of the nanocarbon compacts processed by the SPS are also very interesting.

1.3 Metallic biomaterials: Ti alloys and foams

In contrast to the stainless steel 316L and CoCr based alloys, pure Ti and some Ti-based alloys are nowadays the most attractive metallic biomaterials for orthopedic implants in load bearing sites as dental and orthopedic implants and heart valves, due to their excellent mechanical properties, wonderful biocompatibility and good corrosion resistance. As long-term load-bearing implants in clinic, the incorporation of porous structures into the Ti and its alloys could lead to a reliable anchoring of host tissue into the porous structure, and allow mechanical interlocking between bone and implant

1.3.1 Ti and its alloys for biomedical applications

Pure Ti was once used as biomaterial, but the disadvantage of the pure Ti as implant materials is low strength and insufficient hardness. Therefore, the Ti6Al4V alloy is preferentially in clinical use because of its favourable mechanical properties [88]. However, some studies showed that the vanadium (V) and aluminium (Al) release in Ti6Al4V alloy could induce Alzheimer's disease, allergic reaction and neurological disorders [89]. Therefore, the exploration of high strength new Ti alloys without Al and V for medical implants has gained great attention in the past years and it is still ongoing. Al and V free alloys containing non-toxic elements such as iron (Fe) [90], niobium (Nb) [91], zirconium (Zr) [92], tantalum (Ta) [93], molybdenum (Mo) [94], nickel (Ni) [95], gold (Au) [96], silicon (Si) [97] or hafnium (Hf) [98] etc. were investigated and proposed for biomedical applications. Despite its problems, the Ti6Al4V alloy is currently still the most widely used titanium alloy in clinical applications.

1.3.2 Manufacture techniques of Ti alloys

The traditional manufacture technique of the Ti alloys is casting. For example, Vacuum-die casting [99] and the arc-melting vacuum-pressure-type casting [100] are the commonly used Ti alloy manufacture techniques. Due to high melting point, high reactive activity at high temperature and contamination susceptibility, the Ti alloys are difficult to be produced from the liquid state. The production of Ti alloys via a powder metallurgy (PM) route is attractive due to the ability to produce net-shape components. The titanium PM technologies are including vacuum sintering, hydrogen sintering [101], hot pressing [102], hot-isostatic pressing [103], powder injection molding (PIM) [104]. The additive layer manufacturing techniques include selective laser sintering [105] and electron beam melting [106] are rapid prototyping technologies as emerging technologies for Ti manufacture.

1.3.3 SPS of Ti alloys

Because of their stable surface oxide film (TiO₂), the Ti alloys are difficult to be sintered by traditional PM sintering techniques. Thus the SPS has been used to prepare the Ti alloys. Various TiAl intermetallic [107], nanocrystalline TiAl-X alloys

[108] and TiAl based composites [108] have been prepared by the SPS for aerospace and industry applications. In the group of Prof. Kieback in Dresden, the TiSi alloy was prepared by the SPS where the in-situ formed Ti_5Si_3 phase used as dispersion-strengthening ultrafine particles [97]. As well as the Ti-Hexamethyldisilane (HMDS) mixture aiming to get TiC_x dispersoids was prepared by the SPS at 700 °C for 6 min, and the Ti/1.3HMDS showed the most interesting combination of mechanical properties for application as implant material [109]. The response of human bone marrow stromal cells to the Ti/1.3HMDS revealed a good adhesion of mesenchymal stem cells on Ti/1.3HMDS comparable to that on c.p. Ti or Ti6Al4V, thus the new material Ti/1.3HMDS represents a promising alternative to the comparatively c.p. Ti and Ti6Al4V [110]. Recently, the Ti-Ta-Ag has been prepared by the SPS exhibiting high hardness and proposed as a suitable elastic modulus for implant material for load-bearing applications [111]. In generally, the SPS is a still a relative new and promising technique to prepare the Ti alloys at lower temperatures.

1.3.4 Manufacture techniques of Ti foams

The porous structure is preferable for Ti and its alloys used as bone implants. The various methods can be classified according to the state of the metal is processed in. This defines four kinds of processes summarised at the following [112], each one corresponding to one of the states of matter: A. from liquid metal, B. from solid metal (in powdered form), C. from metal vapour or gaseous metallic compounds, D. from a metal ion solution. Therefore, the production methods of metallic foams can be divided mainly into three: liquid state processing (based on A.), solid state processing (based on B), and coating processing techniques (based on C, D). The liquid state processing techniques have been successful in fabricating aluminium [113] and zinc foam [114], but they are unsuitable for foaming Ti and Ti alloys. Reactivity of liquid Ti with most of the mold materials and requirement of high vacuum during casting are the limitations appeared in liquid foaming techniques. Solid-state PM foaming methods are thus more promising options for the Ti foam production [115].

There are mainly two different PM production methods that yield different types of porosities in Ti. The first one utilizes the inherent pores between powder particles

loosely packed in a suitable crucible under a protective atmosphere without any pressing, i.e. loose powder sintering [116]. The second method of forming porous Ti involves introducing isolated or interconnected bubbles (macro pores), using inert gas [117] or blowing agents [118] or spacers [119]. These methods involves techniques based on expansion of pressurized argon gas [117] or sintering of powders mixed with a gaseous blowing agent (CO₂-based) [118] or foaming agent like TiH₂ [120]. In these processes the size of the macropores produced by gas expansion or fugitive particles cannot be controlled sensitively so that the foams manufactured are generally composed of macropores varying in size. Frequently used spacers are carbamide powders [121], ammonium hydrogen carbonate [122], polymer granules [123] and magnesium powders [124], which can be removed usually at low temperature without excessive contamination of Ti powders. In some cases water soluble spacer particles [125] such as potassium chloride (KCl), potassium sorbate, sodium chloride (NaCl) or sodium fluoride (NaF) are used as spacers to be replicated utilizing a pattern. It is possible to manufacture highly porous titanium foams with homogenous pore size and structure by this method. One possible problem is that the spacer particles have low dissociation or melting point may result in collapse of compact due to insufficient sintering of the powders in the cell walls. Many techniques have been applied to produce Ti foams in recent years. Nevertheless, there are still problems to be solved in the field of Ti foams for biomedical applications [126]: the difficulty to create controlled porosity and pore sizes, the insufficient knowledge of porous structure-property relationships, the requirements of new sintering techniques with rapid energy transfer and less energy consumption and so on.

1.3.5 SPS of foam materials

Most of SPS researches were performed on dense materials; fewer studies were on foam materials. The SPS studies on porous Ti alloys were mainly using low temperature and low pressure to decrease the relative density of samples [127-131]. The samples exhibited pore sizes of some tens of micrometers and a porosity in the range of 20-45%. As bone foams, high porosity (>50%) and macropore size (>200 μm) are essential requirements for the bone growth and the osteoconduction [132].

Macroporous nanostructured tricalcium phosphate scaffolds have been successfully prepared by using SPS with a free pressureless die design [133]. Nevertheless, macroporous Ti foams by SPS were scarcely reported.

The sodium chloride (NaCl) has been used as spacer material for aluminium [134] and titanium alloys [135, 136] due to its relative high melting point (801 °C), its low cost, and the easy dissolution in water, the less corrosive attack of metals and the low toxicity. The combination of the SPS technique with the NaCl dissolution was tried in aluminium metals at SPS temperature of 570 °C [137, 138], and the processed porous aluminium demonstrated high sound absorption property [139]. In fact, Ti has a much higher melting point (1660.0 °C) than aluminium (660.3 °C). Therefore, it is a great challenge to prepare Ti foams by using the SPS and NaCl dissolution methods as well as using other spacers.

1.4 Objectives of the thesis

Due to the still on-going arguments about whether the spark plasmas actually occur during the SPS process, it needs further investigations on this point. In chapter 2, an indirect method to validate the presence of plasmas will be proposed and systematically investigated. The SPS has a potential to be used as an alternative method for diamond generation. But it needs further investigation to promote the SPS method to be used as a large-scale synthetic diamond production technique as an alternative to the present HPHT method. Chapter 3 will focus on the synthesis of diamond using the SPS technique. The SPS is a relative new technique to fabricate Ti alloys and foams for biomedical applications. Chapter 4 will aim at the exploration of new elements within Ti alloys and the modification of traditional Ti6Al4V alloys for biomedical applications. Chapter 5 will be focused on the development of new methods to prepare Ti foams for biomedical applications, the deep understanding of the relationships between the microstructure and properties of the foams. Chapter 6 will give the conclusions.

References

- [1] J. E. Burke. A history of the development of a science of sintering. *Ceram. Civilizat.*, 1985, 1:315–333.
- [2] W. D. Kingery. Chapter in “Sintering’ 91,” edited by A. C. D. Chaklader and J. A. Lund, *Trans Tech*, Brookfield, VT, 1992, p. 1.
- [3] G. C. Kuczynski. *Metallurg. Trans. AIME*.1949, 185:169-171.
- [4] F. V. Lenel. *ibid.* 1948,175: 878-880.
- [5] R. L. Coble. Initial sintering of alumina and hematite. *J. Amer. Ceram. Soc.* 1958, 41: 55-62.
- [6] W. D. Kingery and M. Berg. Study of the Initial Stages of Sintering by Viscous Flow, Evaporation-Condensation and Self-Diffusion. *J. Appl. Phys.* 26 (1955) 1205-1212.
- [7] R. M. German and Z. A. Munir, Morphology relations during bulk-transport sintering, *Met. Trans* 1975, 6A: 2229-2234.
- [8] R. M. German and Z. A. Munir. Surface Area Reduction During Isothermal Sintering, *J. Amer. Ceram. Soc.* 1976, 59: 379-383.
- [9] N. Hirotsuki, A. Okada, Y. Akimune. Gas-pressure sintering of silicon nitride containing small amounts of oxide additives. *Journal of Materials Science Letters*. 1990, 9(11):1322-1323.
- [10] T. Asokan. Grain boundary properties of hot pressed zinc oxide varistors. *Materials Research Bulletin*, 1993, 28(12): 1277-1284.
- [11] U. Neumann, T. Reetz, C. Rüssel. The influence of the anions of calcium-containing sintering aids for aluminium nitride. *Journal of the European Ceramic Society*, 1993, 12(2):117-122.
- [12] M. Nygren and Z. Shen. Spark Plasma Sintering: Possibilities and Limitations. *Key Engineering Materials*. 2004, 264-268: 719-724.
- [13] Z. A. Munir, Dat V. Quach, A. M. Ohyanagi. Electric Current Activation of Sintering: A Review of the Pulsed Electric Current Sintering Process. *J. Am. Ceram. Soc.* 2011, 94 (1) 1-19.
- [14] Z. A. Munir, U. Anselmi-Tamburini, M. Ohyanagi, M. The effect of electric field and pressure on the synthesis and consolidation of materials: A review of the spark plasma sintering method. *Journal of Materials Science*, 2006. 41(3), 763-777.
- [15] J. R. Groza, A. Zavaliangos. Sintering activation by external electrical field. *Materials Science and Engineering A*. 2000, 287: 171-177.
- [16] M. Tokita. Mechanisms of spark plasma sintering. *Sumitomo Coal Mining Company Ltd.* 1995.
- [17] V. F. Lenel. *Trans. AIME*. 1955, 203: 158.
- [18] Inoue, K., (1962) U.S. Patent No. 3241956.
- [19] Inoue, K., (1966) U.S. Patent No. 3250892.
- [20] <http://www.shi.co.jp/sps/eng/index.html>
- [21] <http://www.fct-systeme.de/>
- [22] <http://www.thermaltechnology.com/>
- [23] <http://shexdl.labsdn.com/product-48611.html>
- [24] M. Nygren, Z. Shen. On the preparation of bio-, nano- and structural ceramics and composites by spark plasma sintering. *Solid State Sciences*, 2003, 5(1), 125-131.
- [25] H. U. Kessel, J. Hennicke, J. Schmidt, T. Weißgerber, B.F. Kieback, M. Herrmann, J. Rähel, ‘FAST’ field assisted sintering technology- a new process for the production of metallic and ceramic sintering materials. *Plansee conference*, 2009, 5: 1–37.
- [26] G. D. Zhan, J. Kuntz, J. Wan, J. Garay, and A. K. Mukherjee, A novel processing route to develop a dense nanocrystalline alumina matrix (<100 nm) nanocomposite material. *J. Am. Ceram. Soc.* 2003, 86(1):200-202.

- [27] U. Anselmi-Tamburini, S. Gennari, J.E. Garay, Z. A. Munir. Fundamental investigations on the spark plasma sintering/synthesis process: II. Modeling of current and temperature distributions. *Materials Science and Engineering: A*, 2005. 394(1-2), 139-148.
- [28] M. Omori, Sintering, consolidation, reaction and crystal growth by the spark plasma system (SPS). *Mater. Sci. Eng., A*, 2000, 287, 183-188.
- [29] N. Frage, S. Cohen, S. Meir, S. Kalabukhov, and M. Dariel, Spark plasma sintering (SPS) of transparent magnesium-aluminate spinel. *J. Mater. Sci.* 2007, 42: 3273-3275.
- [30] M. Tokita, Trends in advanced SPS spark plasma sintering system and technology. *Journal of the Society of Powder Technology Japan*. 1993, 30(11):790-804.
- [31] W. Chen, U. Anselmi-Tamburini, J. E. Garay, J. R. Groza, and Z. A. Munir, Fundamental investigations on the spark plasma sintering/synthesis process: I. Effect of dc pulsing on reactivity ss. *Mater. Sci. Eng. A*, 2005, 394, 132-138.
- [32] D. M. Hulbert, A. Anders, D. V. Dudina, J. Andersson, D. Jiang, C. Unuvar, U. Anselmi-tamburini, (2008). The absence of plasma in “spark plasma sintering”, 2008, 104, 033305-7.
- [33] S. Grasso, Y. Sakka and G. Maizza. Electric current activated/assisted sintering (ECAS): a review of patents, *Sci. Technol. Adv. Mater.* 10 (2009) 053001
- [34] F. Bernard, S. Le Gallet, N. Spinassou, S. Paris, E. Gaffet, J. N. Woolman, Z. A. Munir. Dense Nanostructured materials obtained by spark plasma sintering and field activated pressure assisted synthesis starting from mechanically activated powder mixtures, *Science of Sintering*, 2004, 36: 155-164.
- [35] G. D. Zhan, J. D. Kuntz, A. K. Mukherjee, P. Zhu, K. Koumoto, Thermoelectric properties of carbon nanotube/ceramic nanocomposites. *Scripta Materialia*, 2006, 54(1), 77–82.
- [36] N. Millot, S. Le Gallet, D. Aymes, F. Bernard, Y. Grin, Spark plasma sintering of cobalt ferrite nanopowders prepared by coprecipitation and hydrothermal synthesis. *Journal of the European Ceramic Society*, 2007, 27(2-3), 921–926.
- [37] M. Nygren and Z. Shen, Consolidation of Nano-Ceramics by SPS; Kinetic Considerations, in *Pulse Electric Current Synthesis and Processing of Materials* (eds Z. A. Munir, M. Ohyanagi, M. Tokita, M. Khor, T. Hirai and U. Anselmi-Tamburini), John Wiley & Sons, Inc., Hoboken, NJ, USA. (2006) doi: 10.1002/9780470082751.ch20
- [38] F. Watari, A., Yokoyama, M. Omori, T. Hirai, and H. Kondo, Biocompatibility of materials and development to functionally graded implant for bio-medical application. *Composites Science and Technology*, 2004, 64, 893–908.
- [39] Z. J. Shen, E. Adolfsson, M. Nygren, L. Gao, H. Kawaoka, K. Niihara. Dense Hydroxyapatite–Zirconia Ceramic Composites with High Strength for Biological Applications, *Adv. Mater.*, 2001, 13(3): 214–216.
- [40] Y. W. Gu, N. H. Loh, K. Kho, S. B. Tor, and P. Cheang, Spark plasma sintering of hydroxyapatite powders. *Biomaterials*, 2002, 23(1), 37–43.
- [41] F. Zhang, J. Shen, J. Sun. The effect of phosphorus additions on densification, grain growth and properties of nanocrystalline WC/Co composites. *Journal of Alloys and Compounds*. 2004, 385(1-2): 96-103.
- [42] D. Sivaprahasam, S. B. Chandrasekar, R. Sundaresan, Microstructure and mechanical properties of nanocrystalline WC-12Co consolidated by spark plasma sintering, 2007, 25, 144–152.
- [43] W. Tillmann, C. Kronholz, M. Ferreira, A. Knote, W. Theisen, P. Schütte, J. Schmidt. Comparison of Different Metal Matrix Systems for Diamond Tools Fabricated by New Current Induced Short-Time

Sintering Processes. PM2010 World Congress – Diamond Tools..

- [44] M. Kon, L. M. Hirakata, K. Asaoka, Porous Ti-6Al-4V alloy fabricated by spark plasma sintering for biomimetic surface modification. *Journal of Biomedical Materials Research. Part B*, 2004, 68(1), 88–93.
- [45] F. Zhang, K. Lin, J. Chang, J. Lu, C. Ning, Spark plasma sintering of macroporous calcium phosphate scaffolds from nanocrystalline powders. *Journal of the European Ceramic Society*, 2008, 28, 539–545.
- [46] U. Anselmi-tamburini, J. E. Garay, Z. A. Munir, Fast low-temperature consolidation of bulk nanometric ceramic materials. *Scripta Mater*, 2006, 54: 823–828.
- [47] U. Anselmi-Tamburini, F. Maglia, G. Chiodelli, G. Spinolo, P. Riello, S. Bucella, Nanoscale effects on the ionic conductivity of highly doped bulk nanometric cerium oxide. *Advanced Functional Materials*, 2006, 16(18): 2363–2368.
- [48] K. Morsi, E. Desouky, B. Johnson, S. Lanka, Spark plasma extrusion (SPE): Prospects and potential. *Scripta Materialia*, 2009, 61(4), 395–398.
- [49] K. Morsi, A.M.K. Esawi, S. Lanka, A. Sayed, M. Taher, Spark plasma extrusion (SPE) of ball-milled aluminum and carbon nanotube reinforced aluminum composite powders. *Composites Part A*, 2010, 41(2): 322–326.
- [50] Y. Lee, Preparation of nanostructured TiO₂ ceramics by spark plasma sintering. *Materials Research Bulletin*, 2003, 38(6), 925–930.
- [51] X. Guo, P. Xiao, J. Liu, Z. Shen, Z. Fabrication of nanostructured hydroxyapatite via hydrothermal synthesis and spark plasma sintering. *Journal of the American Ceramic Society*, 2005, 88(4): 1026–1029.
- [52] J. Groza, R.J. Dowding, Nanoparticulate materials densification. *Nanostructured Materials*, 1996, 7(7): 749–768.
- [53] Y. Q. Fu, C. Shearwood, B. Xu, L. G. Yu, K. Khor, Characterization of spark plasma sintered Ag nanopowders. *Nanotechnology*, 2010, 21(11): 115707.
- [54] N. Saheb, Z. Iqbal, A. Khalil, A. S. Hakeem, A. Nasser, T. Laoui, A. Al-Qutub and R. Kirchner. Spark plasma sintering of metals and metal matrix nanocomposites: A Review. *Journal of Nanomaterials*. 2012, Article ID 983470, 13 pages.
- [55] V. Viswanathan, T. Laha, K. Balani, A. Agarwal, S. Seal, Challenges and advances in nanocomposite processing techniques, *Materials Science and Engineering R*, 2006, 54: 121–285.
- [56] C. N. R. Rao, R. Seshadri, A. Govindaraj, R. Sen, Fullerenes, nanotubes, onions and related carbon structures. *Materials Science and Engineering, R*, 1995, 15(95): 209-262.
- [57] H. Kroto, *Symmetry, Space, Stars and C60*, Nobel Lecture, December 7, 1996, p. 45;
- [58] S. Iijima, Helical microtubules of graphitic carbon. *Nature*, 1991, 354(56): 56-58.
- [59] K. Geim, K. S. Novoselov, The rise of graphene. *Nature materials*, 2007, 6(3), 183-191.
- [60] V. N. Mochalin, O. Shenderova, D. Ho and Y. Gogotsi, The properties and applications of nanodiamonds. *Nature nanotechnology*, 2012, 7(1):11-23.
- [61] A.A. Giardini, J.E. Tydings, S.B. Levin, Very high pressure-high temperature research apparatus and the synthesis of diamond. *American Mineralogist* 1960, 45 (1–2):217-221.
- [62] A.L. Vereschagin, G.V. Sakovich, V.F. Komarov, E.A. Petrov, Properties of ultrafine diamond clusters from detonation synthesis, *Diamond and Related Materials*, 1994, 3(1–2): 160-162.
- [63] Y. Hirose, S. Amanuma, K. Komaki, The synthesis of high-quality diamond in combustion flames. *Journal of Applied Physics*, 1990, 68 (12): 6401–6405.

- [64] I. Watanabe, T. Matsushita, K. Sasahara, Low-temperature synthesis of diamond films in thermoassisted RF plasma chemical vapour deposition. *Japanese Journal of Applied Physics Part 1*, 1992, 31 (5A): 1428–1431.
- [65] D. E. Meyer, R. O. Dillon and J. A. Woollam. Radio-frequency plasma chemical vapor deposition growth of diamond. *J. Vac. Sci. Technol. A* 1989, 7 (3):2325-2327.
- [66] K. Kobashi, K. Nishimura, Y. Kawate, T. Horiuchi, Synthesis of diamonds by use of microwave plasma chemical-vapor deposition: Morphology and growth of diamond films. *Physical Review B*. 1988, 38(6):4067–4084.
- [67] F.P. Bundy, H.T. Hall, H.M. Strong, R.H. Wentorf Jr., Man-made Diamonds, *Nature* 1955, 176: 51-55.
- [68] F.P. Bundy, Direct Conversion of Graphite to Diamond in Static Pressure Apparatus, *Science*, 1962, 137: 1057-1058.
- [69] R. Abbaschia, H. Zhu, C. Clarke. High pressure–high temperature growth of diamond crystals using split sphere apparatus. *Diamond & Related Materials*, 2005, 14:1916-1919.
- [70] Element Six Company internal document.
- [71] S. Schwarz, C. Rottmair, J. Hirmke, S. Rosiwal, R.F. Singer. CVD-diamond single-crystal growth. *Journal of Crystal Growth*, 2004, 271: 425-434.
- [72] P. W. May. CVD diamond: a new technology for the future? *Endeavour*, 1995,19(3): 101-106.
- [73] N. R. Greiner, D. S. Phillips, J. D. Johnson and F. Volk. Diamonds in detonation soot. *Nature*,1988, 333, 440–442.
- [74] M. Ozawa, Preparation and behavior of brownish, clear nanodiamond colloids. *Adv. Mater.* 2007, 19:1201-1206.
- [75] F. Zhang, J. Shen, J. Sun, Y. Q. Zhu, G. Wang and G. McCartney. Conversion of Carbon Nanotubes to Diamond by a spark plasma sintering, *Carbon*. 2005, 43 (6): 1254-1258
- [76] J. Shen, F. Zhang, J. F. Sun, Y. Q. Zhu and G. McCartney. Spark plasma sintering assisted diamond formation from carbon nanotubes at very low Pressure. *Nanotechnology*. 2006, 17: 2187-2191.
- [77] F. Zhang, J. Shen, J. Sun, D.G. McCartney. Direct synthesis of diamond from low purity carbon nanotubes. *Carbon*. 2006, 44: 3136-3138.
- [78] J. Schmidt, A. Knote, M. Armbrüster, T. Weißgräber, B. Kieback, Spark plasma sintering of diamond impregnated wire saw beads. *PM2010 World Congress – Diamond Tools System*, 3–8.
- [79] K. Chu, C. Jia, X. Liang, and H. Chen. Effect of powder mixing process on the microstructure and thermal conductivity of Al/diamond composites fabricated by spark plasma sintering, *Rare Metals*, 2010, 29(1): 86-89.
- [80] Y. Mu, J. Guo, B. Liang, Q. Wang. Rapid fabrication of the Ti_3SiC_2 bonded diamond composite by spark plasma sintering. *International Journal of Refractory Metals and Hard Materials*. 2011,29(3): 397-400
- [81] F. Inam, H. Yan, M. J. Reece and T. Peijs. Structural and chemical stability of multiwall carbon nanotubes in sintered ceramic nanocomposite. *Advances in Applied Ceramics*, 2010, 109:240-245.
- [82] Q. Huang, D. Jiang, I.A. Ovidko and A. Mukherjee. High-current-induced damage on carbon nanotubes: The case during spark plasma sintering. *Scripta Materialia*, 2010, 63(12): 1181-1184.
- [83] C. Laurent, G. Chevallier, A. Weibel, A. Peigneya and C. Estournès. Spark plasma sintering of double-walled carbon nanotubes. *Carbon*, 2008, 46(13):1812-1816.
- [84] K. Yang, J. He, Z. Su, J. B. Reppert, M. J. Skove, T. M. Tritt and A. M. Rao. Inter-tube bonding, graphene formation and anisotropic transport properties in spark plasma sintered multi-wall carbon

- nanotube arrays, *Carbon*, 2010, 48(3): 756-762.
- [85] J. Li, L. Wang, T. He and W. Jiang. Transport properties of hot-pressed bulk carbon nanotubes compacted by spark plasma sintering. *Carbon*, 2009, 47(4): 1135-1140
- [86] J. Li, L. Wang and W. Jiang. Super-hydrophobic surface of bulk carbon nanotubes compacted by spark plasma sintering followed by modification with polytetrafluorethylene. *Carbon*, 2010, 48(9): 2668-2671.
- [87] H. L. Zhang, J. F. Lia, K. F. Yao, L. D. Chen. Spark plasma sintering and thermal conductivity of carbon nanotube bulk materials, *Journal of Applied Physics*, 2005, 97:114310.
- [88] M. Long, H.J. Rack, Titanium alloys in total joint replacement--a materials science perspective. *Biomaterials*, 1998, 19(18), 1621-1639.
- [89] A. Ito, Y. Okazaki, T. Tateishi, Y. Ito, Corrosion resistance of Ti-Zr-Nb-Ta-Pd and Ti-Sn-Nb-Ta-Pd alloys. *Journal of Biomedical Materials Research*, 1995, 29, 19-21.
- [90] D. Kuroda, H. Kawasaki, S. Hiromoto, T. Hanawa. Development of new Ti-Fe-Ta and Ti-Fe-Ta-Zr system alloys for biomedical applications. *Mater Trans*, 2005;46:1532-1539.
- [91] T. Namura, Y. Fukui, H. Hosoda, K. Wakashima, S. Miyazaki. Mechanical properties of Ti-Nb biomedical shape memory alloys containing Ge or Ga. *Mater Sci Eng C* 2005, 25:426-432.
- [92] W.F. Ho, W.K. Chen, S.C. Wu, H.C. Hsu, Structure, mechanical properties, and grindability of dental Ti-Zr alloys. *J Mater Sci: Mater Med* 2008,19: 3179-3186.
- [93] L.Z. Ying, M. Niinomi, T. Akahori, H. Fukui, H. Toda. Corrosion resistance and biocompatibility of Ti-Ta alloys for biomedical applications. *Mater Sci Eng A* 2005,398:28-36.
- [94] D.J. Lin, C. Chuang, L. J.H. Chern, J.W. Lee, C. P. Ju, H.S.Yin. Bone formation at the surface of low modulus Ti-7.5Mo implants in rabbit femur. *Biomaterials* 2007, 28:2582-2589.
- [95] D. Bogdanski D, M. Koeller, D. Mueller, G. Muhr M. Bram, H.P. Buchkremer, D. Stoever, J. Choi, E. Matthias. Easy assessment of the biocompatibility of Ni-Ti alloys by in vitro cell culture experiments on a functionally graded Ni-Ti material. *Biomaterials* 2002, 23: 4549-4555.
- [96] K. T. Oh, D. K. Kang, G. S. Choi, K. N. Kim. Cytocompatibility and electrochemical properties of Ti-Au alloys for biomedical applications. *J Biomed Mater Res*, 2007, 83:320-326.
- [97] D. Handtrack, F. Despang, C. Sauer, B. Kieback, N. Reinfried, Y. Grin. Fabrication of ultra-fine grained and dispersion-strengthened titanium materials by spark plasma sintering. *Mater Sci Eng A* 2006, 437:423-429.
- [98] B. L. Wang, L. Li, Y. F. Zheng, In vitro cytotoxicity and hemocompatibility studies of Ti-Nb , Ti-Nb-Zr and Ti-Nb-Hf biomedical shape, 2010, 5(4): 044102.
- [99] M. Syverud, T. Okabe, H. Herø Casting of Ti-6Al-4V alloy compared with pure Ti in an Ar-arc casting machine. *European Journal of Oral Sciences*.1995,103(5): 327-330.
- [100] D. Larsen and G. Colvin. Vacuum-die casting titanium for aerospace and commercial components. *JOM*, 1999, 06:26-27.
- [101] Z. Z. Fang, P. Sun, H. Wang. Hydrogen sintering of titanium to produce high density fine grain titanium Alloys. *Adv. Eng. Mater.* 2012, 14: 383-387.
- [102] Z. Gronostajski, P. Bandola, T. Skubiszewski. Argon-shielded hot pressing of titanium alloy (Ti6Al4V) powders. *Acta Bioeng Biomech.* 2010, 12(1):41-46.
- [103] D. Matthew, D. McNeese, C. Dimitris, T. C Pollock. Processing of TiNi from elemental powders by hot isostatic pressing. *Materials Science and Engineering: A* 2000, 280(2): 334-348.
- [104] A. Arockiasamy, R. M. German, D. F. Heaney, P. T. Wang, M. F. Horstemeyer, R. L. King and B. Adcock. Effect of additives on sintering response of titanium by powder injection moulding. *Powder*

Metallurgy 2010.DOI 10.1179/003258910X12740974839468

- [105] S. Das, M. Wohler, J. J. Beaman, and D. L. Bourell. Producing metal parts with selective laser sintering/hot isostatic pressing. *JOM* 1998, 12: 17-20.
- [106] M. Koike, P. Greer, K. Owen, G. Lilly, L. E. Murr, S. M. Gaytan, E. Martinez and T. Okabe. Evaluation of titanium alloys fabricated using rapid prototyping technologies—electron beam melting and laser beam melting. *Materials*, 2011, 4: 1776-1792.
- [107] J. Guyon, A. Hazotte, J.P. Monchoux, E. Bouzy. Effect of powder state on spark plasma sintering of TiAl alloys. *Intermetallics*, 2013, 34: 94-100.
- [108] B. Mei, Y. Miyamoto. Investigation of TiAl/Ti₂AlC composites prepared by spark plasma sintering. *Materials Chemistry and Physics*, 2002, 75: 291-295.
- [109] D. Handtrack, C. Sauer, B. Kieback. Microstructure and properties of ultrafine-grained and dispersion-strengthened titanium materials for implants. *J Mater Sci*, 2008,43:671-679.
- [110] F. Despang, A. Bernhardt, A. Lode, Th. Hanke, D. Handtrack 1, B. Kieback, M. Gelinsky. Response of human bone marrow stromal cells to a novel ultra-fine-grained and dispersion-strengthened titanium-based material. *Acta Biomaterialia*, 2010, 6:1006-1013.
- [111] M. Wen, C. Wen, P. Hodgson, Y. Li, Mechanical property and microstructure of Ti-Ta-Ag alloy for biomedical applications. *Key Engineering Materials* 2012,520:254-259.
- [112] J. Banhart, *Production Methods for Metallic Foams*. MRS Proceedings, 2011, 521: 121. doi:10.1557/PROC-521-121
- [113] I. Duarte, J. Banhart, A study of aluminium foam formation—kinetics and microstructure. *Acta Materialia*, 2000, 48(9): 2349–2362.
- [114] J. Banhart, J. Baumeister. Deformation characteristics of metal foams. *Journal of Materials Science*, 1998, 33:1431-1440.
- [115] D. C. Dunand, *Processing of Titanium Foams*, *Advanced Engineering Materials*, 2004: (6), 369-376.
- [116] I. H. Oh, N. Nomura, N. Masahashi, S. Hanada, Mechanical properties of porous titanium compacts prepared by powder sintering, *Scripta Mater.* 2003,49,1197-1202.
- [117] N. G. Davis, J. Teisen, C. Schuh, D.C. Dunand, Solid-state foaming of titanium by superplastic expansion of argon-filled pores, *Acta Materialia* 2001, 33: 1431-1440.
- [118] C. S. Y. Jee, N. Ozguven, Z. X. Guo, J. R. G. Evans, Preparation of high porosity metal foams, *Metall. Mater. Trans. B* 2000,31,1345-1352.
- [119] M. Bram, C. Stiller, H. P. Buchkremer, D. Stover, H. Baur, High- porosity titanium, stainless steel, and superalloy parts. *Adv. Eng. Mater.* 2000, 2,196-199.
- [120] K. A. Erk, D. C. Dunand, K.R. Shull. Titanium with controllable pore fractions by thermoreversible gelcasting of TiH₂. *Acta Mater* 2008, 56:5147-5157.
- [121] B. Jiang, N.Q. Zhao, C.S. Shi, J. J. Li, Processing of open cell aluminum foams with tailored porous morphology. *Scripta Mater.*, 2005, 53:781-785.
- [122] C. E. Wen, M. Mabuchi, Y. Yamada, K. Shimojima, Y. Chino, T. Asahina, Processing of biocompatible porous Ti and Mg, *Scripta Mater.* 2001,45, 1147-1153.
- [123] G. Rausch, J. Banhart, in *Handbook of Cellular Metals*. Eds H. P. Degischer, B. Kriszt, Wiley,2002 pp 21
- [124] Z. Esen and S. Bor. Processing of titanium foams using magnesium spacer particles. *Scripta Materialia*, 2007, 56: 341-344.
- [125] A. Nouri, P. D. Hodgson and C. Wen. Biomimetic porous titanium scaffolds for orthopedic and

dental applications. Chapter 21 in book of Biomimetics Learning from Nature Edited by Amitava Mukherjee. ISBN 978-953-307-025-4. Publisher InTech. Published online 01, March, 2010

[126] F. Zhang, E. Burkel. Chapter 9: Novel titanium manganese alloys and their macroporous foams for biomedical applications prepared by field assisted sintering. In the book of “Biomedical Engineering, Trends, Researches and Technologies” ISBN 978-953-7619. Edited by Anthony N. Laskovski, Published by InTech 2011.

[127] K. Masayuki, L. M. Hirakata, K. Asaoka. Porous Ti-6Al-4V alloy fabricated by spark plasma sintering for biomimetic surface modification. *Journal of Biomedical Materials Research Part B* 2003; 68(1): 88-93.

[128] Y. Sakamoto, K. Asaoka, M. Kon, T. Matsubara, K. Yoshida. Chemical surface modification of high-strength porous Ti compacts by spark plasma sintering. *Bio-Medical Materials and Engineering* 2006, 16(2): 83-91.

[129] R. Nicula, R. Lüthen, M. Stir, B. Nebe, E. Burkel. Spark plasma sintering synthesis of porous nanocrystalline titanium alloys for biomedical applications. *Biomolecular Engineering* 2007, 24: 564-567.

[130] I. H. Oh, H.T. Son, C.S. Kang, J.S. Lee, J.I. Cho, J.C. Bae, B.T. Lee. Mechanical properties and biocompatibility of porous titanium prepared by powder sintering. *Materials Science Forum*, 2007, 539-543: 635-640.

[131] T. Chandra, J. M. Torralba, T. Sakai. Sintered porous titanium and titanium alloys as advanced biomaterials. *Materials Science Forum*, 2003, 426-4: 3079-3084.

[132] F. Zhang, J. Chang, K. Lin and J. Lu. Preparation, mechanical properties and in vitro degradability of wollastonite/tricalcium phosphate macroporous scaffolds from nanocomposite powders, *Journal of Materials Science: Materials in Medicine* 2008, 19: 167-173.

[133] F. Zhang, K. Lin, J. Chang, J. Lu and C. Ning. Spark plasma sintering of macroporous calcium phosphate scaffolds from nanocrystalline powders. *Journal of the European Ceramic Society* 2008, 28(3): 539-545.

[134] Y. Conde, J.F. Despois, R. Goodall, A. Marmottant, L. Salvo, C.S. Marchi, A. Mortensen. Replication processing of highly porous materials. *Advanced Engineering Materials*, 2006, 8(9): 795-803.

[135] A. Bansiddhi, D.C. Dunand. Shape-memory NiTi foams produced by replication of NaCl space-holders. *Acta Biomaterialia*, 2008, 4: 1996-2007.

[136] X. Zhao, H. Sun, L. Lan, J. Huang, H. Zhang, Y. Wang. Pore structures of high-porosity NiTi alloys made from elemental powders with NaCl temporary space-holders. *Materials Letters*, 2009, 63(28):2402-2404.

[137] C. E. Wen, M. Mabuchi, Y. Yamada, K. Shimojima, Y. Chino, H. Hosokawa and T. Asahina. Processing of fine-grained aluminum foam by spark plasma sintering. *Journal of Materials Science Letters*, 2003, 22(20): 1407-1409.

[138] M. Hakamada, Y. Yamada, T. Nomura, Y. Chen, H. Kusuda, M. Mabuchi. Fabrication of porous aluminum by spacer method consisting of spark plasma sintering and sodium chloride dissolution. *Materials Transaction*, 2005, 46(12):2624-2628.

[139] M. Hakamada, Y. Yamada, T. Nomura, Y. Chen, H. Kusuda, M. Mabuchi. High sound absorption of porous aluminum fabricated by spacer method. *Applied Physics Letters*, 2006, 88: 254106.

Chapter 2 Indirect evidences for the presence of plasmas in SPS

2.1 Stability and phase transformation of nanocarbon materials under SPS

2.1.1 Introduction

The carbon nanotubes, fullerene (C60), graphene and graphite have broad applications as structural and functional materials. Therefore, it is of great importance for a better in-depth understanding of their thermal stability under severe physical conditions [1-2]. The SPS is an electric field assisted sintering process utilizing ON-OFF DC pulse energizing and provides as a severe physical condition. There are still on-going arguments about whether the spark plasmas actually occur during the SPS process. In this study, an indirect way to validate the existence of the plasmas during the SPS is proposed. It is in the light of a thermal dynamic analysis of the phase transformation of nanocarbon materials under the SPS treatments. The thermal stability and phase transitional behavior of carbon nanotubes, C60, graphene and graphite were investigated under the SPS (pulsed DC field). The pure MWCNTs, C60, graphene and graphite powders were processed by using the SPS. Their phase constitutions were investigated by using synchrotron radiation-high energy X-ray diffraction, Raman spectroscopy and Scanning electron microscopy. For a comparison study, these carbon materials were also studied using the in-situ high temperature (AC field) synchrotron radiation X-ray diffraction. Their phase transition mechanisms under such novel sintering technique are discussed.

2.1.2 Experimental

The MWCNTs (10-20 nm) with purity above 95% were obtained from Shenzhen Nanotech Port, Ltd., China. The C60 powders with purity of 99.5% were obtained from SES Research, Huston, USA. The graphene powders used in this study are graphene nanoplatelets (C-750) consisting of short stacks of graphene sheets having a platelet shape. They were gotten from XG Science, Lansing, USA. Grade C-750 particles have an average thickness of 2 nm and a particle diameter of less than 2 μm , and average surface areas of 750 m^2/g . The graphite powders (about 10 μm) with

purity of 99.0% were purchased from Alfa Aesar, Germany.

These carbon powders were pressed into a graphite die for SPS treatment to form disk-shaped samples of 20 mm diameter and 5 mm thickness. The SPS experiments were conducted using a Model HPD-25/1 FCT spark plasma sintering system (FCT Systeme GmbH, Rauenstein, Germany), under an axial pressure of 80 MPa in vacuum (<6 Pa). A heating rate of 100 K/min was adopted, and the sintering process lasted typically 20 min. The applied direct current for SPS was about 1000 A, with a pulse duration of 12 ms and an interval of 2 ms.

The phase identification of the obtained carbon samples was performed using high-energy X-ray diffraction at beamline BW5 (DESY/HASYLAB Hamburger Synchrotron Laboratory) with a wavelength of 0.15339 Å (80.828 keV). The carbon samples were also analyzed by a Renishaw-2000 Laser Raman spectroscopy system with a He-Ne laser excited at 514 nm. The scanning electron microscopy was performed in a Zeiss Supra 25 at 20 keV. The stability of these carbon samples was investigated by the in-situ high temperature X-ray diffraction at the MAX80/F2.1 high-pressure beamline of Helmholtz Centre Potsdam at HASYLAB/DESY. The MAX80 instrument uses a cubic-anvil-type press, which is known to provide better results for isotropic pressure generation compared to other multiple-anvil high-pressure devices [3]. The carbon samples were contained in cube cells made of a mixture of boron and epoxy resin with 4 mm edge length in a non-oxygen atmosphere. The pure MgO powder was used as a reference material in the cube cells. An in-situ measurement comprises the room-temperature compression to the desired pressure, followed by isobaric constant-rate heating. X-ray diffraction patterns were acquired in energy-dispersive mode (EDX) during continuous specimen heating (up to 1500 °C) under an applied pressure of 80 MPa. The EDX method relies on the use of a well-collimated and polychromatic (white) incident synchrotron radiation beam. The XRD patterns were collected each 10 °C during constant heating.

2.1.3 Results

The pure MWCNTs were SPSed at 1500 °C under pressure of 80 MPa for a soaking time of 20 min. Figure 2-1(a) shows the synchrotron radiation-high energy X-ray

diffraction patterns of the raw MWCNTs and the spark plasma sintered (SPSed) MWCNTs. The raw MWCNTs show a main diffraction peak at 3.43 Å corresponding to the CNTs (002) plane spacing, and weak peaks at 2.10 and 1.70 Å corresponding to the CNTs (100) and (004) plane spacing, respectively. After SPS processing, the MWCNTs diffraction peaks are still present in the sintered MWCNTs compacts, but the peaks of the CNTs (002), (100) and (004) are stronger than those in the raw MWCNTs. It indicates that the SPS process improved the crystallinity of the MWCNTs. Additionally, new peaks were detected in the sample centered at 2.05, 1.23, 1.06 and 1.76 Å corresponding to the cubic diamond (ICDD No. 65-537) (111), (220), (311) and n-diamond (ICDD No. 43-1104) (200) plane spacing, respectively. Figure 2-1(b) shows Raman spectra of the raw MWCNTs and the SPSed MWCNTs. The result of the raw MWCNTs show that their D band appeared at 1344 cm^{-1} and G band appeared at 1569 cm^{-1} . After SPS processing, the D peak shifted to 1333 cm^{-1} corresponding to the cubic diamond but there was still a weak peak at 1344 cm^{-1} belonging to the un-reacted MWCNTs, the G band shifted to 1566 cm^{-1} relating to the sp^2 bonded carbon vibrations. The results of the X-ray diffraction and Raman spectroscopy confirmed the diamond formation in the MWCNTs sample after SPS at 1500 °C, 80 MPa for 20 min.

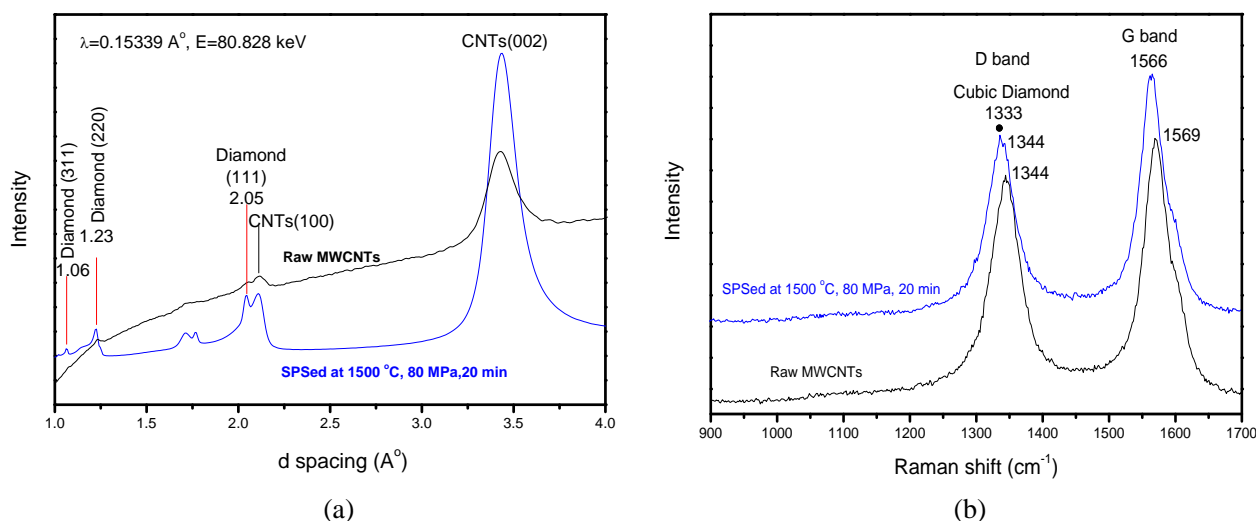


Fig. 2-1. Synchrotron radiation diffraction patterns (a) and Raman spectra (b) of the raw MWCNTs and the spark plasma sintered MWCNTs at 1500 °C, 80 MPa for 20 min.

Figure 2-2 shows the SEM micrographs of the raw MWCNTs and the spark plasma sintered MWCNTs at 1500 °C, 80 MPa for 20 min. The fibrous structures of the raw MWCNTs can be observed in the Figure 2-2(a). But the fibrous structures have disappeared, and some diamond crystals are found in the samples after SPS. Figure 2-2 (b) shows one diamond crystal with particle size of 35 μm around. In the background of this diamond crystal, no MWCNTs are found.

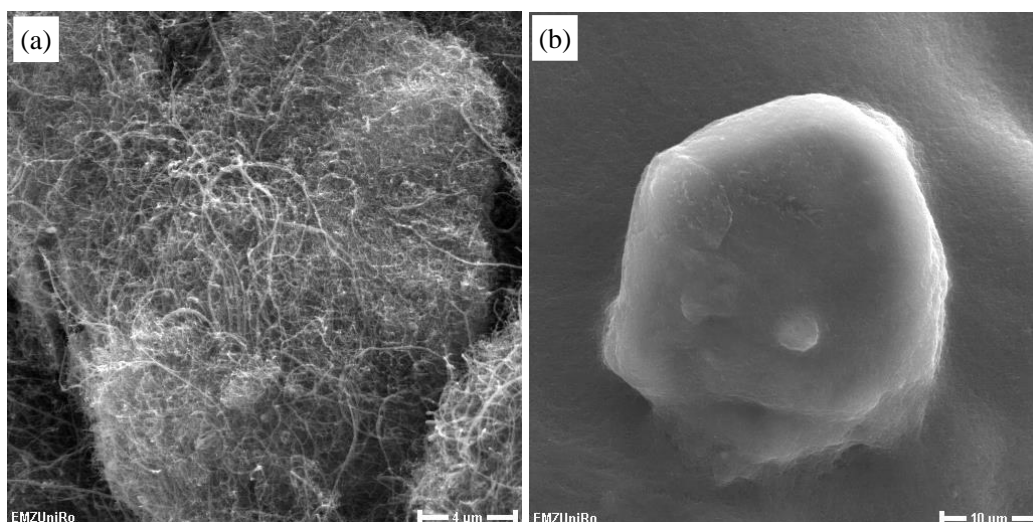


Fig. 2-2 SEM micrographs of the raw MWCNTs (a) and the spark plasma sintered MWCNTs (b) at 1500 °C, 80 MPa for 20 min.

Figure 2-3(a) shows the synchrotron radiation-high energy X-ray diffraction patterns of raw C60 and the SPSed C60 at 1500 °C, 80 MPa for 20 min. The raw C60 exhibits diffraction peaks at d spacing of 5.01, 4.28, 4.11, 3.18, 2.9, 2.74 Å belonging to C60 (110), (112), (004), (114), (300), (006) planes (ICDD No. 47-0787), respectively. The C60 after SPS shows the cubic diamond diffraction peaks at d spacing of 2.06 and 1.23 Å and a broad graphite peak. The C60 diffraction peaks disappeared indicating the C60 has completely transformed into diamond and graphite phases after the SPS processing. Figure 2-3(b) shows the Raman spectra of the raw C60 and the SPSed C60. The raw C60 shows a sharp peak appearing at 1460 cm^{-1} , and two weak, broad peaks centered at 1568 cm^{-1} and 1515 cm^{-1} . After SPS processing, it shows the cubic diamond peak at 1333 cm^{-1} and graphite peak at 1558 cm^{-1} , but the C60 peak at 1460 cm^{-1} disappeared. It is consistent with X-ray

diffraction results that the C60 has completely transformed into diamond and graphite phases after SPS at 1500 °C under 80 MPa for 20 min.

Figure 2-4 shows the SEM micrographs of the raw C60 and the spark plasma sintered C60 at 1500 °C, 80 MPa for 20 min. The raw C60 powders are nano-particle agglomerates and show bundles of C60 in the Figure 2-4(a). Some diamond crystals with sizes from 2 to 8 μm can be observed in the Figure 2-4(b). The structures of C60 are not noticeable in the background of the diamond crystals.

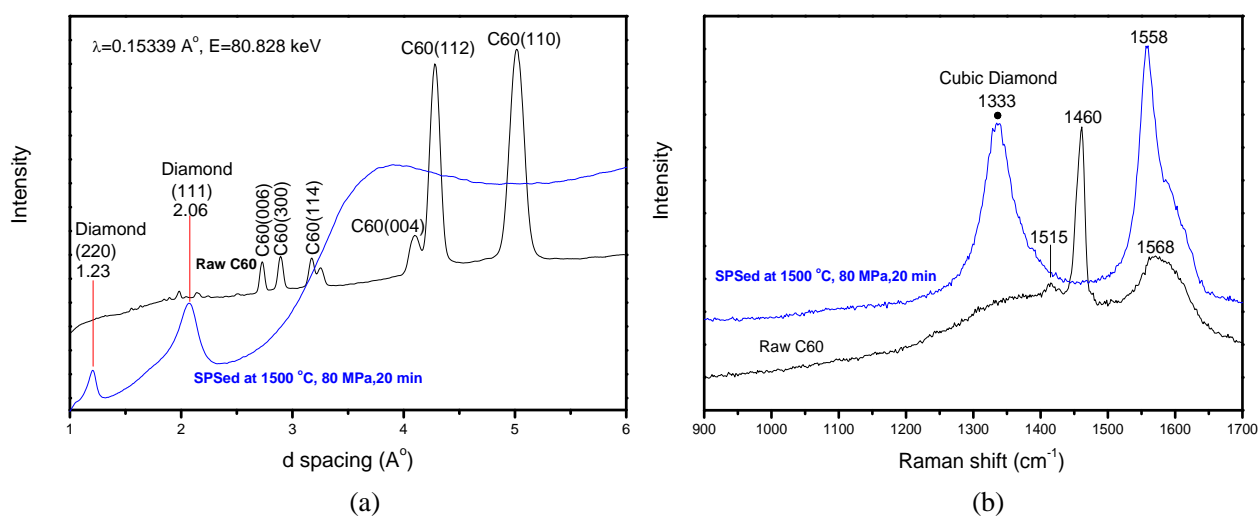


Fig. 2-3 Synchrotron radiation diffraction patterns (a) and Raman spectra (b) of the raw C60 and the spark plasma sintered C60 at 1500 °C, 80 MPa for 20 min.

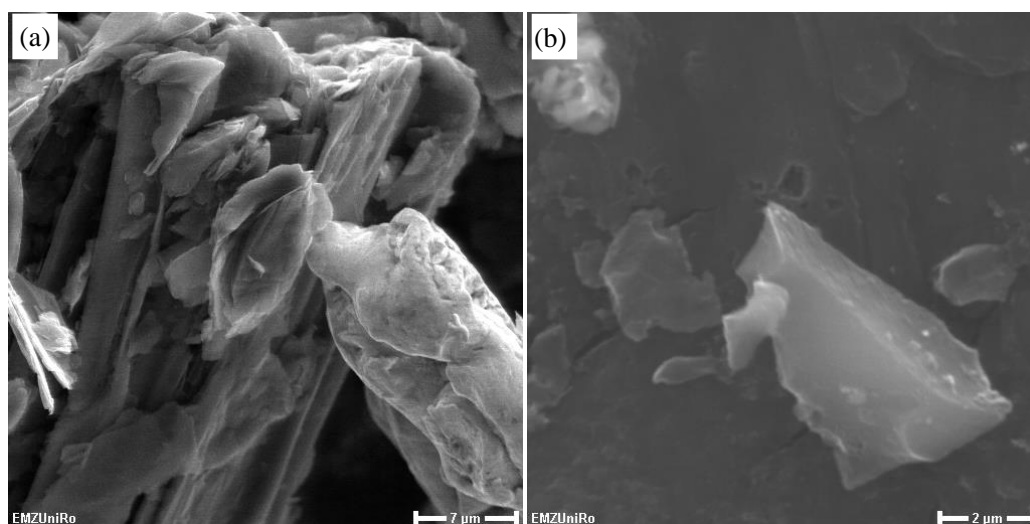


Fig. 2-4 SEM micrographs of the raw C60 (a) and the spark plasma sintered C60 (b) at 1500 °C, 80 MPa for 20 min.

Figure 2-5 shows the synchrotron radiation diffraction patterns of the raw graphene and the SPSed graphene at 1500 °C, 80 MPa for 20 min. The raw graphene shows diffraction peaks of Graphite-2H (002), (004), (110) and Graphite-3R(101), (104). After the SPS at the same condition of other carbon materials, it is found that the intensity of Graphite-2H (002), (004), (110) has been increased and G-3R(113) is visible. Very weak diamond peaks of cubic diamond (311), (400), (311) haven been detected. The Raman spectra results present the cubic diamond sp^3 hybridization bonds with a featured peak at 1332 cm^{-1} Raman shift (D band). The G band shifted from 1592 cm^{-1} to 1563 cm^{-1} indicating the vibration of sp^2 bonds.

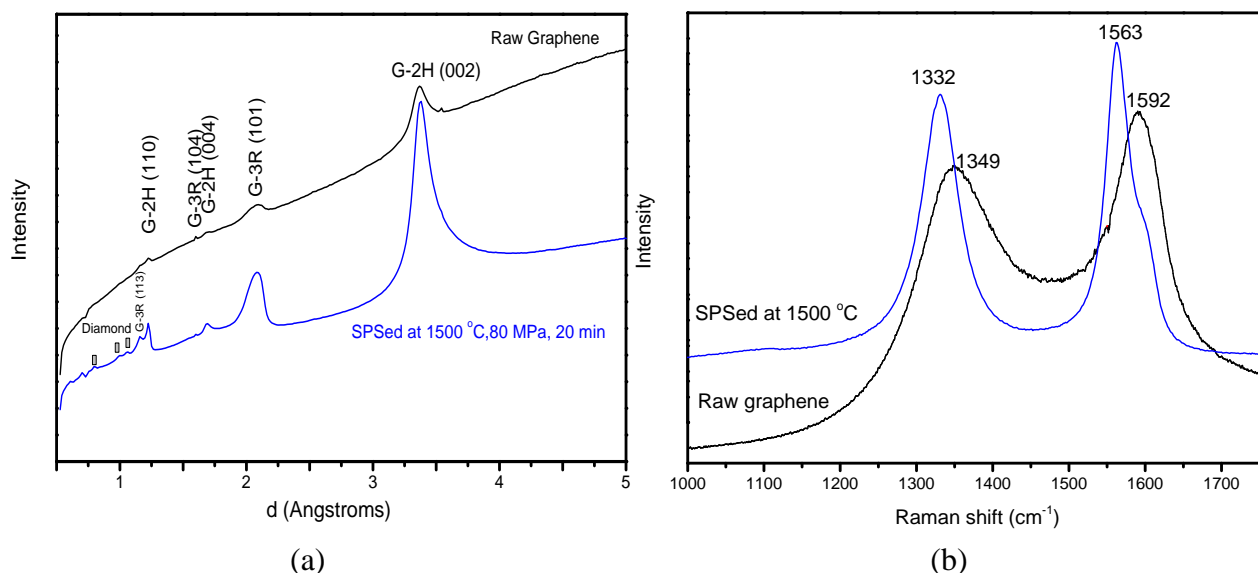


Fig. 2-5 Synchrotron radiation diffraction patterns (a) and Raman spectra of the raw graphene and the spark plasma sintered graphene at 1500 °C, 80 MPa for 20 min (b).

Figure 2-6 shows the SEM images of the raw graphene and SPSed graphene. The raw powders show many agglomerated particles. The SPSed graphene sample exhibit some diamond particles with sizes from 1 μm to 5 μm on the matrix of consolidated graphene. The XRD, Raman and SEM results can confirm that there a small fraction of low crystallinity diamonds converted from the graphene after the SPS at 1500 °C and 80 MPa for 20 min

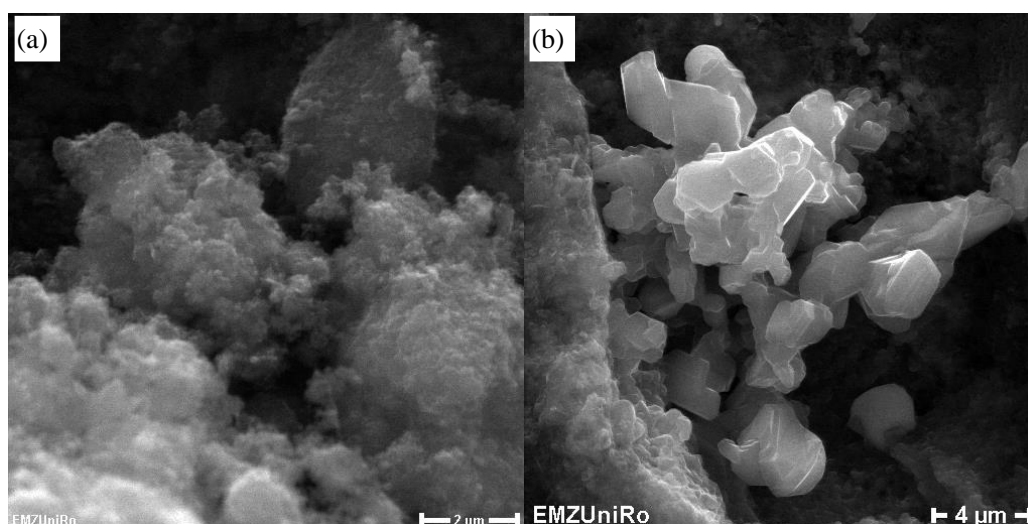


Fig. 2-6 SEM images of the raw grapheme (a) and the spark plasma sintered grapheme (a) at 1500 °C, 80 MPa for 20 min.

Figure 2-7 (a) shows the synchrotron radiation diffraction patterns of the raw graphite and the SPSed graphite at 1500 °C, 80 MPa for 20 min. The raw graphite sample presents Graphite-3R and Graphite-2H diffraction peaks those are centered at 3.348 Å [G-3R(003)], 1.674 Å [G-3R(006)], 1.228 Å [G-3R(110)] (ICDD No. 26-1079), and 2.138 Å [G-2H(100)] , 2.039 Å [G-2H(101)], 1.16 Å [G-2H(112)] (ICDD No. 41-1487). However, the diamond phase is not found in the graphite samples after the SPS processing. Only, an increased intensity in the graphite peaks indicating the improved crystallinity is visible. Figure 2-7(b) shows the Raman spectra of the raw graphite and the SPSed graphite. The raw graphite shows a sharp peak at 1579 cm^{-1} , and a weak peak at 1350 cm^{-1} . After SPS processing, the intensity of the peak at 1350 cm^{-1} has improved, but there is no diamond peak in the Raman spectra. The X-ray diffraction and Raman spectroscopy results confirmed that there is no diamond conversion from pure graphite after SPS at 1500 °C under 80 MPa for 20 min.

Fig. 2-8 shows the SEM micrographs of the raw graphite and the spark plasma sintered graphite at 1500 °C, 80 MPa for 20 min. The raw graphite shows the typical layered structure as shown in Figure 2-8(a). After the SPS at the identical condition of MWCNTs and C60, there is no presence of diamond in the sample (Figure 2-6b). The sample shows the similar structure with the raw graphite. The SEM results agree well

with the XRD and Raman results that there is no diamond conversion from pure graphite after SPS at 1500 °C under 80 MPa for 20 min.

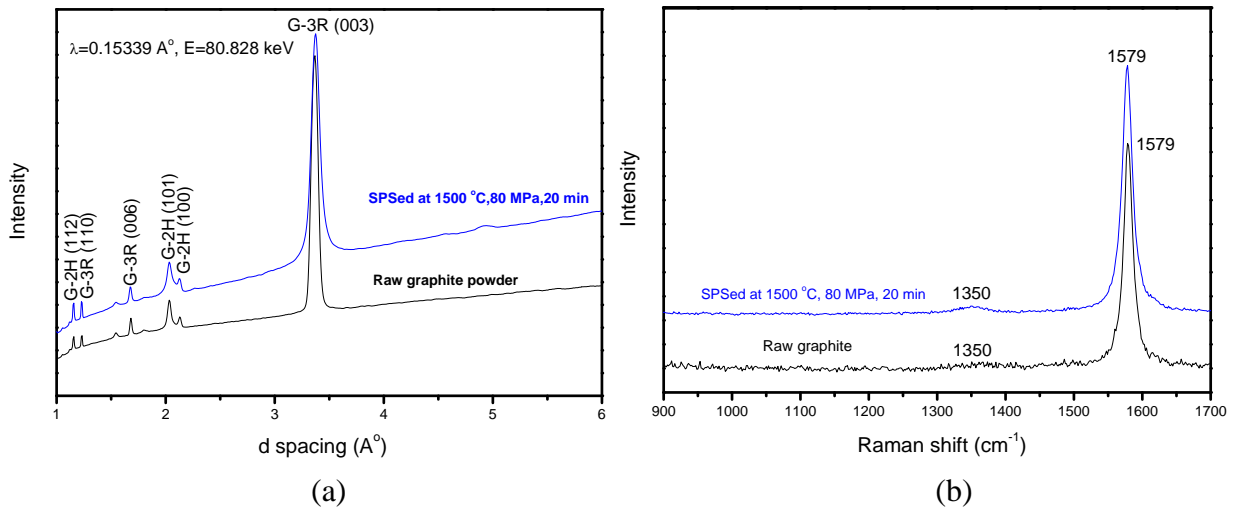


Fig. 2-7 Synchrotron radiation diffraction patterns (a) and Raman spectra (b) results of the raw Graphite and the spark plasma sintered graphite at 1500 °C, 80 MPa for 20 min.

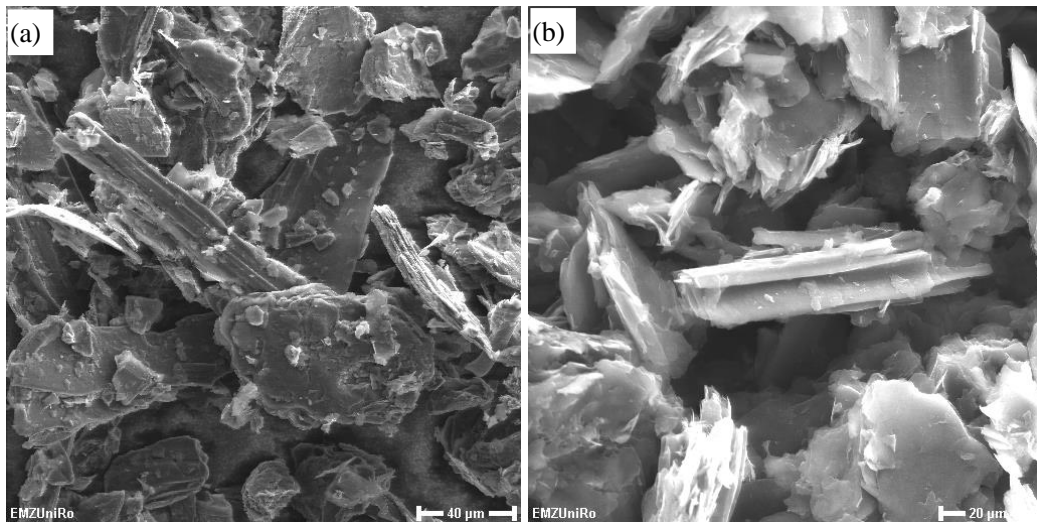
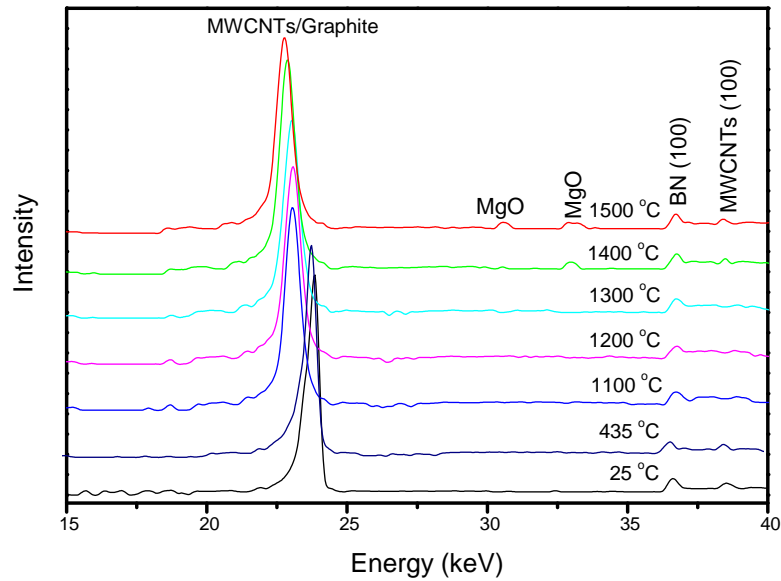


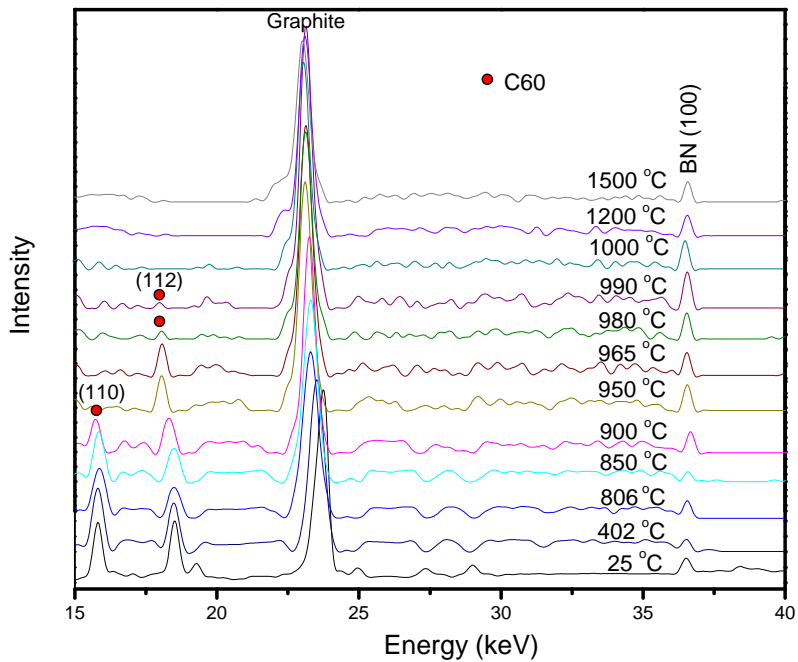
Fig. 2-8 SEM images of the raw graphite (a) and the spark plasma sintered graphite (b) at 1500 °C, 80 MPa for 20 min.

Figure 2-9 (a) shows the synchrotron radiation-in situ X-ray diffraction patterns of the pure MWCNTs at 80 MPa under different temperatures under the in-situ sintering furnace (AC filed) of the MAX80/F2.1 high-pressure beamline. The combination peak of MWCNT and graphite has shifted to lower energy values. It indicates the thermal expansion of the nanotubes and graphite planes with the increase of

temperature. The boron nitride (BN) peaks are from the container of the powder sample during the in-situ high temperature X-ray experiments. However, there is no diamond formation at or below temperature of 1500 °C under 80 MPa. It means that the MWCNTs are dynamically stable at this 1500 °C temperature under 80 MPa in a non-oxygen atmosphere during the AC sintering.



(a)



(b)

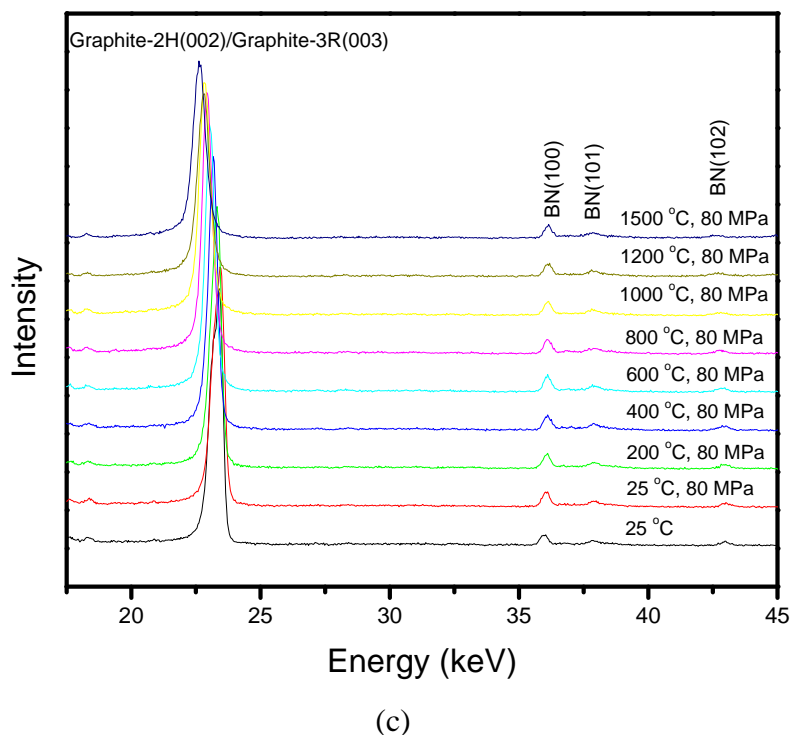


Figure 2-9 Synchrotron radiation-in situ X-ray diffraction patterns of the pure MWCNTs (a), C60 (b) and grapheme (c) at 80 MPa under different temperatures.

Figure 2-9 (b) shows the synchrotron radiation-in situ X-ray diffraction patterns of the pure C60 at 80 MPa under different temperatures. There is no diamond formation in the C60 sample. It shows that the C60 is stable below the temperature of 900 °C. However, the C60 is unstable above that temperature point. The C60 (110) peak disappeared above temperature of 900 °C and C60 (112) peak disappeared above temperature of 990 °C. Figure 2-9(c) shows the synchrotron radiation-in situ X-ray diffraction patterns of the pure graphene at 80 MPa under different temperatures. There are no phase transformations in the graphene samples up to 1500 °C. Additionally, it is found that the graphite is very stable in the in-situ high temperature X-ray experiments at or below 1500 °C under 80 MPa.

2.1.3 Discussions

Synchrotron radiation-high energy X-ray diffraction was used to identify the diamond phase in the carbon samples after SPS. In order to confirm the diamond formation, Raman spectroscopy was also used to identify the formation of sp^3 bonded

diamonds. By using the high energy X-ray diffraction and Raman spectroscopy, the cubic diamond phases were identified and confirmed in the SPSed MWCNTs, C60 and graphene samples. The n-diamond was also found in the SPSed MWCNTs sample. The n-diamond is a new kind of carbon allotrope, which is a metallic form of carbon with face-centred cubic structure [4]. It is a metastable and intermediate phase, can decompose slowly at room temperature, and has been synthesized accidentally by various processes. It is noted that the n-diamond can also be synthesized by the SPS process. The standard d spacing of the cubic diamond (111), (220) and (311) planes are centered at 2.059 Å, 1.261 Å and 1.075 Å (ICDD No. 65-537). The cubic diamond in the SPSed MWCNTs centered at 2.05, 1.23 and 1.06 Å, and in the SPSed C60 appeared at 2.06 and 1.23 Å spacing. The diffraction peaks of the synthesized diamond from MWCNTs and C60 are very close to the standard diamond diffraction data, but there is a little shift. The diamond peak shifts are due to the existence of residual stress in the synthesized diamonds from MWCNTs and C60 by using the SPS. The residual stress of the diamond is because of the stress that remains after the original cause of the stresses (uniaxial forces, heat gradient) has been removed after the SPS processing. In this study, uniaxial force of 80 MPa was applied and there generally existed some temperature gradients during the operation of the SPS. Therefore, the diamond peaks in the SPSed MWCNTs and C60 have shifted a little. Combining the results of the Raman spectroscopy, the formation of diamond phases in these MWCNTs, C60 and graphene samples are confirmed. It is found that there are no C60 peaks in the X-ray diffraction and Raman results of the SPSed C60 sample, but there are strong unreacted MWCNTs peaks in the SPSed MWCNTs sample, and there is strong graphene peaks as well as no diamond phases in the SPSed graphite sample. There exists a high activation barrier from the graphite, graphene, MWCNTs and C60 to diamond, the exact height of which is unknown. The results in this study indicated that the activation barrier between the C60 and diamond is lower than that of the MWCNTs with diamond, and the barrier between MWCNTs and diamond is lower than that of the graphene with diamond. The graphite is the most stable crystalline modification of carbon among the MWCNTs, C60, graphene and graphite

allotropes under the SPS processing.

The SPS is a remarkable technique to synthesize and consolidate a large variety of materials. The process typically uses moderate uniaxial pressures usually below 100 MPa in combination with a pulsing on-off DC current during its operation. There are many mechanisms proposed to account for the enhanced sintering abilities of the SPS process; for example, field assisted diffusion [5], spark impact pressure [5,6], plasma cleaning of particle surfaces [7], Joule's heating [6, 7], local melting and evaporation especially in metallic systems [6], surface activation on particles [8] and electron wind force [9]. The one that draws the most controversy of these mechanisms involves the presence of momentary plasma. In this study, the diamond converted from the MWCNTs, C60 and graphene without any catalysts being involved in the SPS. However, the parallel investigations by using the synchrotron radiation in-situ high temperature X-ray diffraction show that there is no diamond formation in the MWCNTs, C60 and graphene samples in the AC sintering at the same pressure (80 MPa) and temperature (1500 °C). What is the phase transition mechanism from MWCNTs, C60 and graphene to diamond in the SPS? Such a clear, significant difference in the products is due to the special sintering principle of SPS. It is a field activated sintering technique based on an DC electric spark discharge phenomenon, i.e. a high energy and low voltage spark pulse DC momentarily generates sparking plasma between particles, which causes localized high temperatures. It is an electric AC heating in the in-situ high temperature experiments. Without plasma effect, it would need 8000-10000 °C at pressure of 80 MPa to get diamond from the MWCNTs and C60, as we calculated. Therefore, super-high pressures (5-10 GPa) are required for the diamond formation in the hydrostatic HPHT technique. Since the SPS only needs MPa level pressure, it is believed that the plasma plays the key role for the diamond transformation from the MWCNTs, C60 and graphene. The high current, low voltage, momentary pulsed plasma discharge have generated highly localized Joule's heating up to a few thousand degrees Celsius between particles in few minutes. The current density in the SPS is typically on the order of 10^2 A/cm² and is highly concentrated at the inter-granular contact or interface [10]. The momentary pulsed

plasma provided energy equivalent to thousand degrees to help the nano-carbon across their activation barriers to the diamond phase. It leads to the transformation of mainly sp^2 bonded MWCNTs, C60 and graphene to sp^3 bonded diamonds. Despite the on-going argument about whether the spark plasmas actually occur during the SPS process, our present study, regarding on the generating diamond under such a low pressure, suggests that such spark plasmas indeed took place during SPS of these nano-carbon materials. The plasmas generated very high localized temperatures up to about 8000-10000 °C and dramatically reduced the pressures required for diamond formation from the GPa to the MPa level. Eventually, this research provided some new indirect evidences for the presence of plasmas during the SPS operation. So, we take plasma into consideration in the thermodynamic analysis. The total energy for the diamond formation:

$$Q = \Delta H_T + Q_p + \Delta H_M \quad (2-1)$$

where Q is Total Energy, ΔH_T is the Energy due to temperature difference, Q_p is the Energy due to pressure difference, ΔH_M is the Energy due to plasma effect. The enthalpy of plasma:

$$H = H_E + H_K + H_D + H_I \quad (2-2)$$

where H is the Plasma contribution, H_E is the kinetic contribution, H_K is the excitation contribution, H_D is the dissolution contribution, H_I is the electrolytic contribution. Then,

$$dS = \frac{\delta Q}{T} \quad (2-3)$$

$$\Delta Q(T) - \Delta Q(T_0) = \Delta S(T_0 - T) \quad (2-4)$$

Where T is the temperature, T_0 is the starting temperature, ΔQ is the difference of mol free energy, ΔS is the difference of mol entropy. Only when $\Delta Q(T) < 0$, nanocarbons can be transformed into diamond. So, we can get an equation:

$$T > T_0 + \frac{\Delta Q(T_0)}{\Delta S} \quad (2-5)$$

The effect of the plasmas in the SPS has increased the entropy ΔS of the whole SPS

system resulted a lower sintering temperature T for the diamond formation. As a result, diamonds were converted from MWCNTs, C60 and graphene at 1500 °C under very low pressure of 80 MPa. The SPS is a remarkable technique to synthesize and consolidate a large variety of materials. In this study, the diamond conversion in the SPSed MWCNTs and C60 samples without any catalysts being involved has validated the high localized temperatures between particles due to the presence of momentary plasmas during SPS of these electrically conductive and high surface area nano-carbon materials. The plasmas have increased the entropy of the whole SPS system resulted in milder conditions for the diamond formation.

2.1.5 Summary

The thermal stability of MWCNTs, C60, graphene and graphite has been investigated under the pulsed DC field in a SPS furnace. Cubic diamond and n-diamond have been converted from pure MWCNTs; cubic diamond has been converted from pure C60 and graphene without catalysts being involved by the SPS at conditions of 1500 °C, 80 MPa for 20 min. There was no notice of diamond formation in the case of pure graphite sample processed by SPS at this condition. The graphite is the most stable crystalline modification of carbon among the MWCNTs, C60, graphene and graphite allotropes under the SPS. The parallel investigations by using the synchrotron radiation in-situ high temperature (AC field) X-ray diffraction show that there is no diamond formation in the MWCNTs, C60 and graphene samples at the same pressure (80 MPa) and temperature (1500 °C). Their phase transitional mechanism from MWCNTs, C60 and graphene to diamond indicated the high localized temperatures between particles due to the presence of momentary plasmas during the SPS process. The plasmas have increased the entropy of the SPS system resulted in milder conditions for the diamond formation.

2.2 Effect of atmosphere on the generation of plasmas in SPS

2.2.1 Introduction

The SPS process typically uses moderate uniaxial pressures below 100 MPa and commonly in vacuum. As indicated from the plasma spraying technique, gases like H₂,

Ar, O₂ and so on can be used as plasma generating gases which can enhance the plasmas generation [11, 12]. In this study, the diamond synthesis from CNTs through the generation of plasmas during the SPS was investigated by very low pressure and various atmosphere SPS experiments. The pure multiwalled carbon nanotubes (MWCNTs) and MWCNTs/FeNi mixture powders were degassed in the SPS and then sintered in vacuum and Ar gas atmospheres at 3 kN (9.55 MPa) which is the minimum pressure of the Model HP D-5 FCT SPS system. The sintered samples were etched and analyzed by Synchrotron X-ray diffraction, Raman spectroscopy and scanning electron microscopy. The effect of the atmosphere on the diamond synthesis and plasma generation during the SPS is discussed.

2.2.2 Experimental

The MWCNTs (10-20 nm) with purity above 95% were obtained from Shenzhen Nanotech Port, Ltd., China. The Fe₃₅Ni powders with 325 meshes were purchased from Alfa Aesar, Germany, which were prepared by gas atomization method with 99.0% purity. The MWCNTs were mixed uniformly with Fe₃₅Ni powders at a weight ratio of 1:1 by ball milling.

The SPS experiments were conducted using a Model HP D-5 FCT spark plasma sintering system (FCT systeme GmbH, Rauenstein, Germany) installed at the Tycho Sinter Lab in the University of Rostock. The powders were pressed into a ϕ 20 mm graphite die at 3 kN pressure (9.55 MPa). They were degassed at 450 °C for 10 min in vacuum and then sintered in vacuum (1-3 Pa) and argon gas (20 hPa), respectively. A heating rate of 100 K/min was adopted, and the sintering process lasted typically 20 min. The final temperatures were selected to be 1500 °C for pure MWCNTs and 1200 °C for MWCNTs/FeNi mixtures based on our previous researches. The applied direct current for SPS was 1000-1500 A with pulse duration of 12 ms and an interval of 2 ms. The final samples are disk-shaped samples of 20 mm diameter and 5 mm thickness. The sintered MWCNTs and MWCNTs/FeNi samples were etched in a boiling solution of concentrated H₂SO₄ (90 vol.%) and HNO₃ (10 vol.%) for 2 h. The etched samples were washed using deionized water repeatedly and dried in an oven. The phase identification of the etched carbon samples was performed by a high-energy X-ray

diffraction at Beamline BW5 (DESY/HASYLAB Hamburger Synchrotron Laboratory) with a wavelength of 0.123984 Å (100.0 keV) and by a Renishaw-2000 Laser Raman spectroscopy system with a He-Ne laser excited at 514 nm. The samples were also analyzed using scanning electron microscope (SEM, Zeiss Supra 25, Germany) at 20 keV.

2.2.3 Results

Figure 2-10 (a) shows the synchrotron radiation-high energy X-ray diffraction patterns of the MWCNTs powder and the SPSed MWCNTs at 1500 °C under 9.55 MPa in vacuum and Ar gas atmospheres. The MWCNTs powder shows diffraction peaks at 3.43, 2.10, 1.70 and 1.22 (± 0.01) Å corresponding to the CNTs (002), (100), (004) and (110) plane spacing, respectively. After SPS processing, all the diffraction peaks of the CNTs are much sharper than before. However, no diamond peaks were found in the X-ray diffraction patterns.

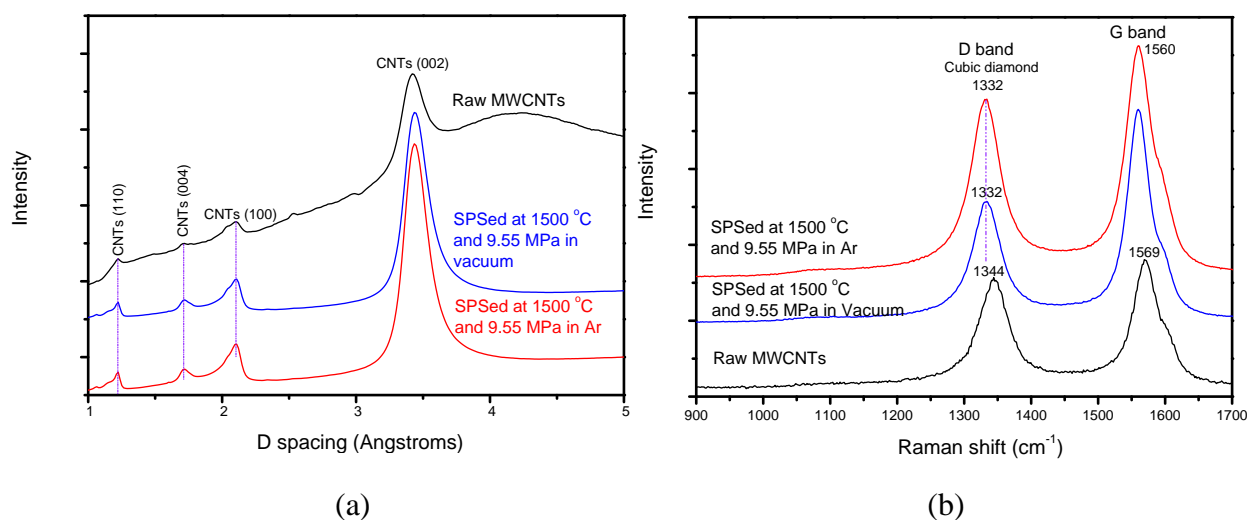


Figure 2-10 Synchrotron radiation-high energy X-ray diffraction patterns (a) and Raman spectra (b) and of the raw MWCNTs and the spark plasma sintered MWCNTs/FeNi at 1200 °C and 9.55 MPa in Vacuum and Ar gas atmospheres.

Figure 2-10 (b) shows the Raman spectra of the MWCNTs powder and SPSed samples. The raw CNTs show D band at 1344 cm⁻¹ and G band at 1569 cm⁻¹ Raman shift. After SPS, the G bands shifted to the same Raman shift of 1560 cm⁻¹ and the D bands shifted to 1332 cm⁻¹ Raman shift indicating the diamond sp³ hybrid. The XRD

results did not show the diamond peak so that only the Raman spectra results cannot confirm the diamond formation. The Raman spectra results only indicate that there are some sp^3 carbon hybrids in the samples after the SPS. The peak area ratio of the D and G bands of the SPSed samples was calculated. The sample sintered in the Ar gas shows higher D/G ratio (0.77) than the vacuum sintered one (0.56). This indicates that there is a higher fraction of sp^3 carbon hybrids in the Ar gas sintered sample.

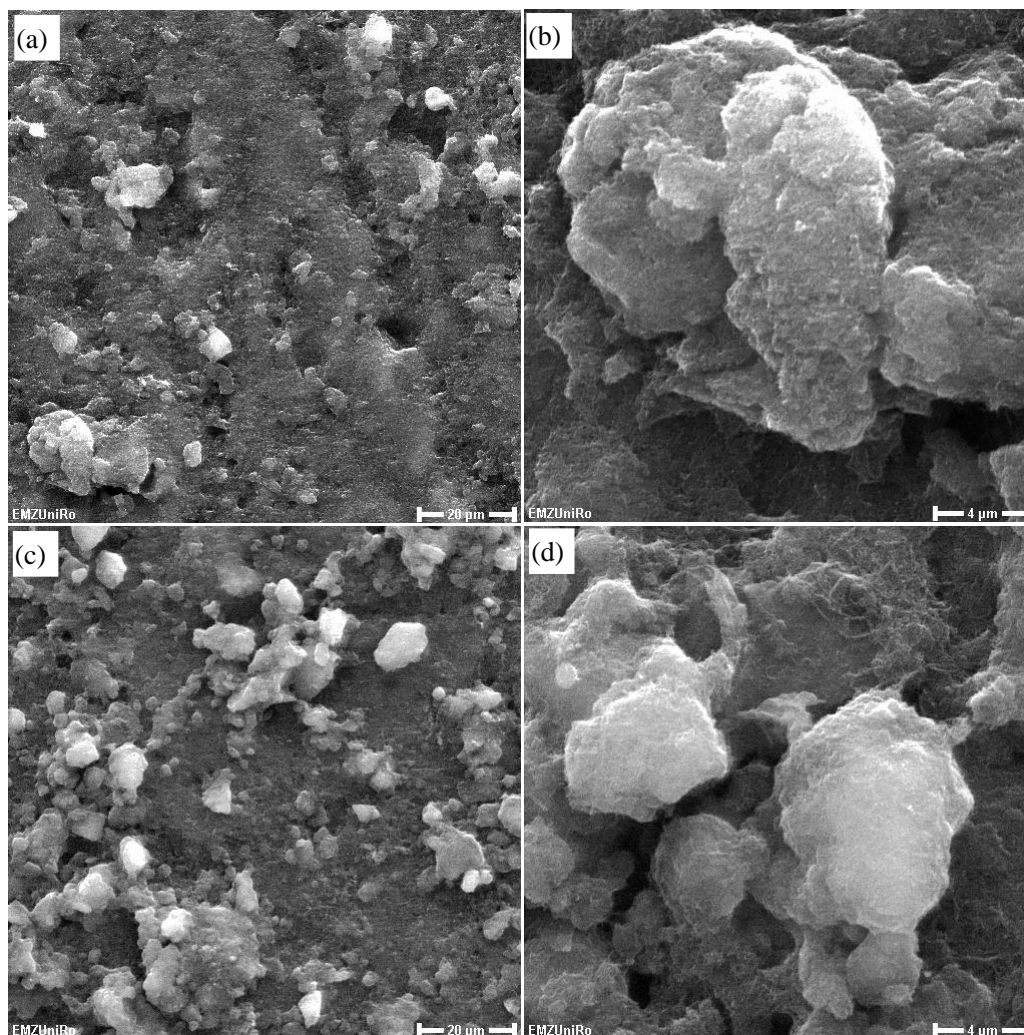


Fig. 2-11 SEM micrographs of the spark plasma sintered MWCNTs at 1500 °C and 9.55 MPa in Vacuum (a, b) and Ar gas atmospheres (c, d) with various magnifications.

Figure 2-11 (a, b) shows the SEM micrographs of the MWCNTs samples SPSed at 1500 °C under 9.55 MPa in vacuum. At lower magnification, some particles can be seen on the surface of the sample (Figure 2-11 a). With a higher magnification, it is found that these particles are in a transition stage to diamond (Figure 2-11b). Figure

2-11(c, d) shows the SEM micrographs of the MWCNTs samples SPSed at 1500 °C under 9.55 MPa in Ar gas. There are much more particles on the surface of the sample. A high magnification micrograph shows that they are in the transition stage too. The SEM results are in accordance with the synchrotron X-ray diffraction and Raman results showing that the SPS processing of pure MWCNTs in Ar gas increased the fraction of sp³ carbon hybrids, without forming crystalline diamonds in the samples.

Figure 2-12 (a) shows the synchrotron radiation-high energy X-ray diffraction patterns of the raw MWCNTs and the SPSed MWCNTs/FeNi at 1200 °C under 9.55 MPa in vacuum and Ar gas. The MWCNTs powder shows a main diffraction peak at 3.43 (± 0.01) Å corresponding to the CNTs (002) plane spacing, and weak peaks at 2.10 and 1.70 (± 0.01) Å corresponding to the CNTs (100) and (004) plane spacing, respectively. After SPS processing of the MWCNTs/NiFe, new peaks were detected in the etched sample and centered at 2.06, 1.25 (± 0.01) Å corresponding to the cubic diamond (ICDD No. 65-537) (111) and (220). The diamond peaks in the Ar gas sintered sample with HWHM (Full Width at Half Maximum) value of 0.046 Å are sharper than that in vacuum with HWHM value of 0.090 Å. Figure 12 (b) shows the Raman spectra of the MWCNTs/FeNi samples SPSed at 1200 °C under 9.55 MPa in vacuum and Ar gas. Both of them show the cubic diamond peak at 1332 cm⁻¹ Raman shift. The vacuum SPSed sample shows very weak diamond peak (D/G=0.12); however, the Ar gas SPSed sample exhibits a strong diamond peak (D/G=0.94). Both of the G bands center at the same Raman shift of 1558 cm⁻¹ after SPS. But these G bands are much sharper in the vacuum SPSed sample with HWHM value of 19.1 cm⁻¹ than that in the Ar gas with HWHM value of 42.0 cm⁻¹ indicating the higher fraction of MWCNTs. The results of the synchrotron X-ray diffraction and Raman spectra confirmed the cubic diamond formation in the MWCNTs/FeNi samples after SPS at 1200 °C and 9.55 MPa for 20 min in both vacuum and Ar atmospheres. The Ar gas enhanced the diamond transition in the SPS.

Figure 2-13 (a, b) shows the SEM micrographs of the MWCNTs/FeNi samples SPSed at 1200 °C and 9.55 MPa in vacuum. There are only a few poor quality diamond crystals created in the vacuum atmosphere of the SPS (Figure 2-13a). A

cubic diamond crystal with an incomplete shape in the reacted MWCNTs matrix is shown in Figure 2-13(b). Figure 13(c-e) shows the SEM micrographs of the MWCNTs/FeNi samples SPSed at 1200 °C and 9.55 MPa in Ar gas. Some flower-like structured carbons are observable in the sample (Figure 2-13c). This indicates that sparking plasmas may have happened and generated such carbon flowers. It is exciting that some high quality diamond crystals with hexahedron structures are found in the sample (Figure 2-13d). A high magnification SEM micrograph of perfect diamond crystals is shown in Figure 2-13(e). The results indicated that the Ar gas atmosphere in the SPS promoted the diamond formation.

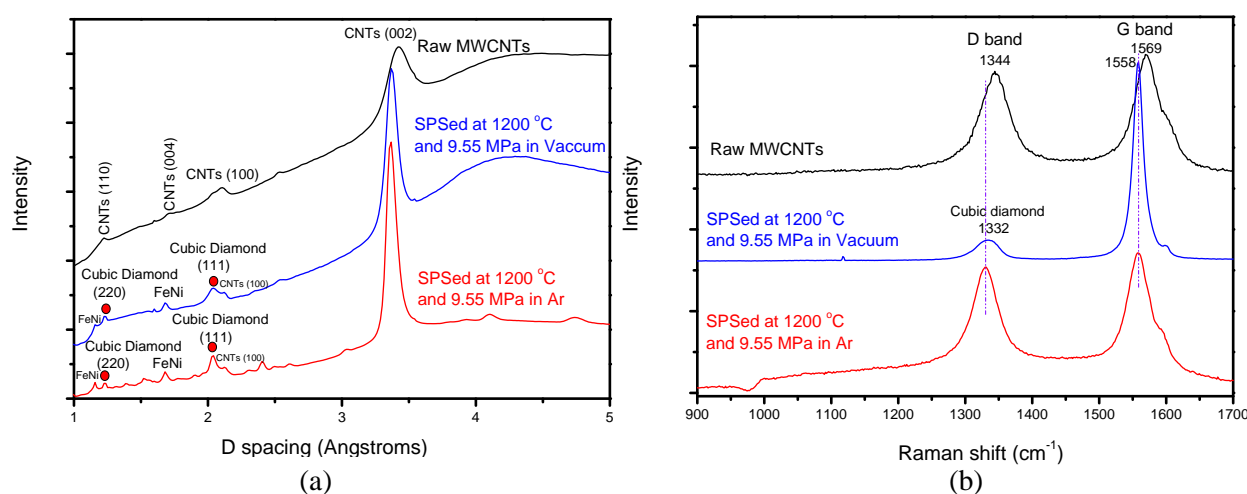


Figure 2-12 Synchrotron radiation-high energy X-ray diffraction patterns (a) and Raman spectra (b) and of the raw MWCNTs and the spark plasma sintered MWCNTs/FeNi at 1200 °C and 9.55 MPa in Vacuum and Ar gas atmospheres.

Figure 2-14 (a, b) shows the current and voltage during SPS of the pure MWCNTs and MWCNTs/FeNi in vacuum and Ar gas atmospheres. It is interesting to find that the current and voltage values in Ar atmosphere are all higher than those in vacuum at the same temperatures using the same raw materials of MWCNTs and MWCNTs/FeNi, respectively. The Ar gas has high electrical resistance as well as it can adsorb some heats during the SPS. The MWCNTs have large surface areas and are sintered at the minimum pressure of the SPS. Some amounts of Ar gas can enter into and be adsorbed by the nanotubes. The resistance of the sample has been increased. Therefore, the SPS in Ar gas need much higher current and voltages.

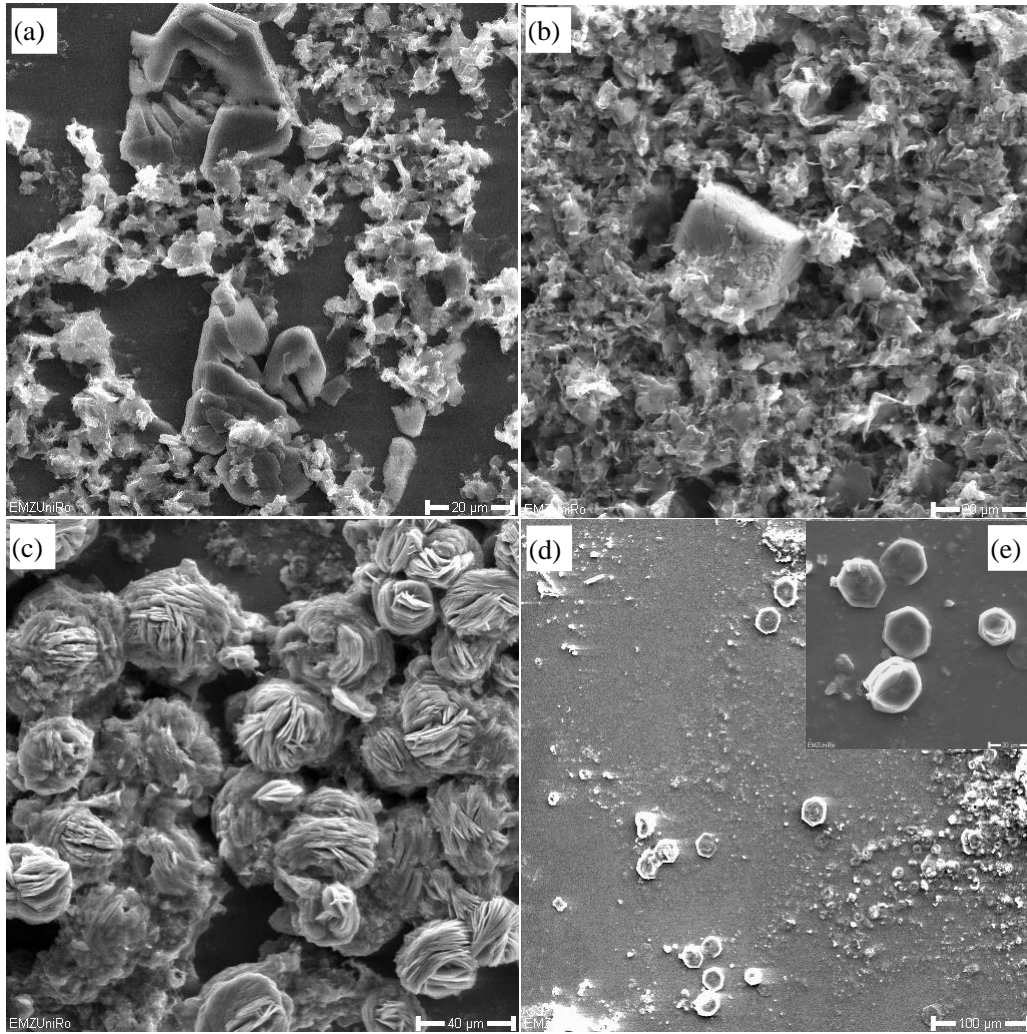


Figure 2-13 SEM micrographs of the spark plasma sintered MWCNTs/FeNi at 1200 °C and 9.55 MPa in Vacuum (a, b) and Ar gas atmospheres (c-e) with various magnifications.

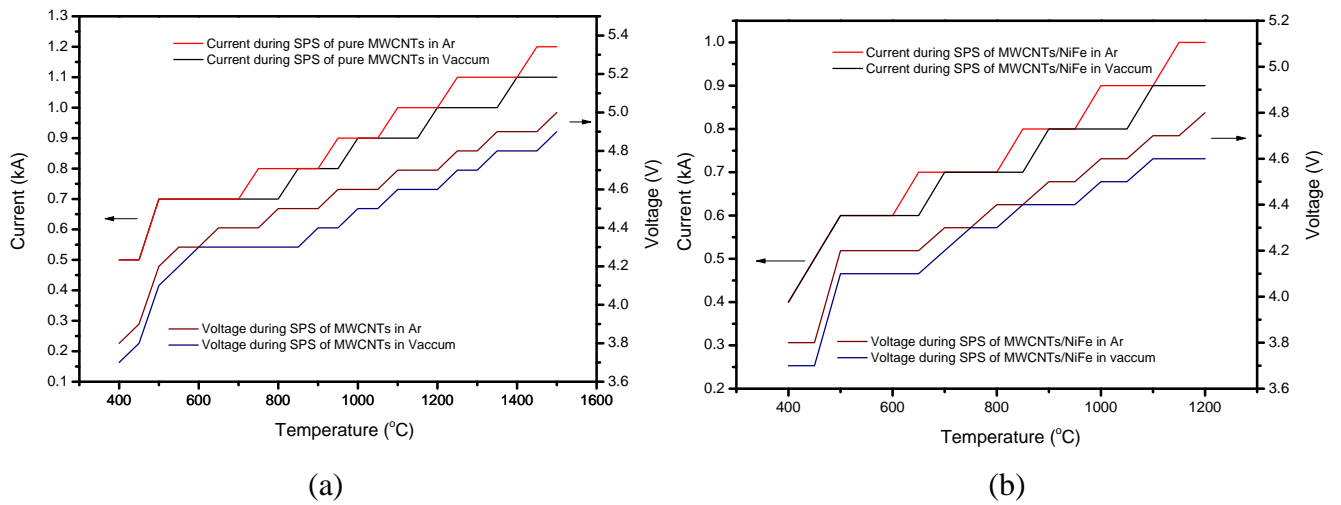


Figure 2-14 Current and voltage values during SPS of the pure MWCNTs (a) and MWCNTs/FeNi (b) in Vacuum and Ar gas atmospheres.

2.2.3 Discussions

In this study, the SPS pressure is very low (9.55 MPa), so that the pressure effect is negligible for the diamond conversion. In both vacuum and Ar gas atmospheres, some fractions of sp^3 carbon hydrides have been obtained from the raw MWCNTs and crystalline cubic diamond crystals have been generated from the MWCNTs/FeNi by the SPS at such a low pressure. Where is the energy coming from for the transition of MWCNTs to diamond? The effect of the plasmas in the SPS has increased the entropy of the whole SPS system resulted a lower sintering temperature for the diamond formation, as raised in the above part. As a result, diamonds were converted from MWCNTs with FeNi catalysts under very low pressure of 9.55 MPa. Based on the above thermal dynamic analysis, it is indicated that the plasma generated during the SPS operation plays the key role and provides most of the energy which is needed for the diamond formation. The momentary pulsed plasma provided energy equivalent to several thousands degree to help the MWCNTs across their activation barriers to form the diamond phase with the assistances from solvent catalyst-FeNi. It leads to the transformation of mainly sp^2 bonded MWCNTs to sp^3 bonded diamonds. Thus, this study provided another important evidence for the existence of plasma during the SPS at such low pressure diamond formation.

The Ar gas-SPS processed MWCNTs samples have higher fractions of sp^3 carbon hydrides than those treated in vacuum. The Ar gas atmosphere-SPS processed MWCNTs/NiFe samples have carbon flowers and perfect, high quality diamond crystals with hexahedron structures; however, only few incomplete shaped diamonds are found in the vacuum processed sample. Such an obvious difference indicates that the Ar gas atmosphere in the SPS operation enhanced the plasma generation and promoted the diamond transition. In present study, the MWCNTs samples were firstly degassed in vacuum at 450 °C for 10 min, and were sintered at the minimum pressure (3 kN) of FCT D-5 SPS system. Because of these special treatments, some amounts of Ar gas will be adsorbed at gas pressure of 20 hPa during the SPS. The values of the voltage and current with function of temperature during SPS are plotted. The results present that the current and voltage are much higher in Ar atmosphere of the SPS

using the same temperature program and starting materials. The higher current and voltage in the Ar atmosphere of the SPS generated larger sparking plasmas, thus created more diamonds. It means that the Ar gas atmosphere should be selected when the enhancement of the plasma effect is needed in the SPS operation.

A plasma is an electrically conductive gas containing charged particles. The plasma generated for plasma spraying technique usually incorporates one or a mixture of the following gases: Ar, He, N₂, H₂ and Air [12, 13, 14]. Ar is probably the most favored primary plasma gas and is usually used with a secondary plasma gas (H₂, He and N₂) to increase its energy [14]. It is the easiest gas to form plasma and tends to be less aggressive towards electrode and nozzle hardware. Most plasmas are started up using pure Ar. The results in this study show that the Ar gas has a similar effect as in the plasma spraying process. The atoms of the Ar gas are excited to high energy levels during the SPS operation, the atoms become ionized producing a plasma containing electrically charged particles-ions and electrons. Monatomic molecule of Ar plus energy gives 1 Ar ion and 1 electron [15]:



The reverse process provides most of the energy for heating without a dramatic drop in temperature. The momentary generated plasmas can produce temperatures around 7,000 to 20,000 K. Therefore, the generated plasma during Ar gas-SPS supplies a high amount of energy, by which promoted the fraction of sp³ hydride carbon in the MWCNTs and the diamond conversion from the MWCNTs/NiFe at a very low pressure of 9.55 MPa.

2.2.5 Summary

Some fractions of sp³ hydride carbon in the transition stage to diamond are obtained from the pure MWCNTs by SPS at 1500 °C and 9.55 MPa in vacuum and Ar atmosphere. Crystalline cubic diamond crystals are generated from the MWCNTs/FeNi by SPS at 1200 °C and 9.55 MPa in vacuum and Ar atmosphere. Carbon flowers and high quality diamond crystals with hexahedron structures are produced only in the Ar atmosphere. Such low pressure diamond formation in both

vacuum and Ar gas atmospheres provides an important indirect evidence for the existence of plasma during the SPS. The Ar atmospheres lead to higher currents and voltages during SPS. It is assumed to promote the plasma generation and sizes. The plasmas momentary generated from ionized gas produced temperatures up to thousands of degree and thus promote the diamond transition.

References

- [1] K. M. Liew, C. H. Wong, X. Q. He, M. J. Tan. Thermal stability of single and multi-walled carbon nanotubes, *Physical Review B*, 2005, 71, 075424:1-6.
- [2] Y.A. Kim, H. Muramatsu, T. Hayashi, M. Endo, M. Terrones, M.S. Dresselhaus. Thermal stability and structural changes of double-walled carbon nanotubes by heat treatment, *Chemical Physics Letters*, 2004, 398 (1-3): 87-92.
- [3] R.J. Hemley, G.L. Chiarotti (eds.), *High pressure phenomena*, IOS Press, Amsterdam, 2002.
- [4] B. Wen, T. Li, C. Dong, X. Zhang, S. Yao, Z. Cao, D. Wang, S. Ji and J. Jin, Study of the stability of n-diamond, *J. Phys.: Condens. Matter*, 2004, 2991, 16.
- [5] G. D. Zhan, J. Kuntz, J. Wan, J. Garay, and A. K. Mukherjee, A novel processing route to develop a dense nanocrystalline alumina matrix (<100 nm) nanocomposite material. *J. Am.Ceram. Soc.* 2003, 86(1):200-202.
- [6] M. Omori, Sintering, consolidation, reaction and crystal growth by the spark plasma system (SPS). *Mater. Sci. Eng., A*, 2000, 287, 183-188.
- [7] W. Chen, U. Anselmi-Tamburini, J. E. Garay, J. R. Groza, and Z. A. Munir, Fundamental investigations on the spark plasma sintering/synthesis process: I. Effect of dc pulsing on reactivity ss. *Mater. Sci. Eng.A*, 2005, 394, 132-138.
- [8] N. Frage, S. Cohen, S. Meir, S. Kalabukhov, and M. Dariel, Spark plasma sintering (SPS) of transparent magnesium-aluminate spinel. *J. Mater. Sci.* 2007, 42: 3273-3275.
- [9] P. Shewmon, *Diffusion in Solids*, 2nd ed. Minerals, Metals & Materials Society, Warrendale, PA, (1989) pp. 246.
- [10] K. Yang, J. He, Z. Su, J. B. Reppert, M. J. Skove, T. M. Tritt and A. M. Rao. Inter-tube bonding, graphene formation and anisotropic transport properties in spark plasma sintered multi-wall carbon nanotube arrays, *Carbon*, 2010, 48(3): 756-762.
- [11] Z. Zheng, L. Liao, B. Yan, J. X. Zhang, H. Gong, Z. X. Shen, T. Yu, Enhanced field emission from argon plasma-treated ultra-sharp α -Fe₂O₃ nanoflakes, *Nanoscale. Res. Lett.* 2009, 4: 1115-1119.
- [12] E. Noguees, M. Vardelle, P. Fauchais, P. Granger, Arc voltage fluctuations: Comparison between two plasma torch types, *Surf. Coat. Tech.* 2008, 202(18):4387-4393.
- [13] A. Rauf, Q. Yu, L. Jin, C. Zhou, Microstructure and thermal properties of nanostructured lanthana-doped yttria-stabilized zirconia thermal barrier coatings by air plasma spraying, *Scripta Mater.* 2002, 66(2):109-112.
- [14] E. Pfender, Fundamental studies associated with the plasma spray process. *Surf. Coat. Tech.* 1988, 34(1):1-14.
- [15] M. I. Boulos, P.Fauchais, A.Vardelle and E. Pfender. Chapter 1 in book: *Plasma spraying:theory and applications*.Editor: R.Suryanarayanan. ISBN 981-02-1363-8. World Scientific. 1993, P17

Chapter 3 Synthesis of diamond from nanocarbon and graphite by SPS

3.1 Synthesis of diamond from carbon nanotubes with solvent catalysts by SPS

3.1.1 Introduction

Diamond particles and diamond films have now been successfully obtained by many methods. The HPHT synthesis of diamond from graphite, fullerenes, and carbon nanotubes (CNTs) has been studied [1-3]; generally, pressures above 5.0 GPa and high temperature above 1300 °C are needed. Additionally, incorporation of solvent catalysts such as Ni, Co, Fe, other transition metals and their alloys is a crucial point for aid of the diamond synthesis in the HPHT method. The results in second chapter indicated that the SPS has a potential to be used as an alternative method for diamond generation. But it needs further investigation to promote the SPS method for using as a large-scale synthetic diamond technique. In the HPHT method, the involved solvent catalysts could decrease the energy barrier and affect the rate of a kinetics reaction for diamond nucleation and contribute to the formation of diamond from graphite [4,5]. Besides being able to reduce the transforming temperature and pressure from graphite to diamond, they can also affect the quality and crystal form of the diamond. It is indicated that the solvent catalysts may have the same effects to promote diamond growth from MWCNTs in the SPS method. Currently preferred metal catalyst materials are Fe-Ni alloys, such as Fe-35Ni, Fe-31Ni-5Co, Fe-30Ni, and other INVAR alloys, where Fe-35Ni being the most preferred and more readily available [6]. In order to increase the diamond transitional rate, the Fe35Ni alloy powders were chosen as catalysts for diamond synthesis from MWCNTs by the SPS method in this study. The MWCNTs/Fe35Ni mixtures were spark plasma sintered at various conditions. The microstructures and phases in the obtained carbon samples were analyzed by using Raman spectroscopy (Raman), X-ray diffraction (XRD), scanning electron microscopy (SEM), and transmission electron microscope (TEM) techniques. The growth model of the diamond crystals from the MWCNTs in the SPS process was proposed.

3.1.2 Experimental

The MWCNTs were obtained from Shenzhen Nanotech Port, Ltd., China, which were produced by catalytic chemical vapour deposition (CCVD) in which CH_4 was converted into CNTs at $1000\text{ }^\circ\text{C}$ in the presence of Ni and La catalysts. The purity of the pristine MWCNTs was claimed above 95% by the producer. It presented less than 5% impurities of amorphous carbon and catalysts. The Fe₃₅Ni powders with 325 meshes were purchased from Alfa Aesar. They were prepared by gas atomization method with 99% purity.

The MWCNTs were mixed with Fe₃₅Ni powders at a weight ratio of 1:1 by ball milling, and pressed into a graphite die for SPS treatment to form disk-shaped samples. The SPS experiments were conducted at temperatures of $1100\text{--}1500\text{ }^\circ\text{C}$ for soaking time of 20 min under an axial pressure of 70 MPa in a vacuum ($<6\text{ Pa}$). A heating rate of 100 K/min was adopted, and the sintering process lasted typically 20 min. The applied direct current for SPS was about 1000 A with a pulse duration of 12 ms and an interval of 2 ms. The resulting disk-shaped samples with diameter of 20 mm and thickness of 6 mm were fabricated. The sintered MWCNTs/Fe₃₅Ni samples were analyzed by a Renishaw-2000 Laser Raman spectroscopy system. A He-Ne laser excited at 512 nm was used with a power density of 4.7 mW and a spot diameter of 5 μm . Additionally, the sintered MWCNTs/Fe₃₅Ni samples were etched in a boiling solution of concentrated H_2SO_4 (90 vol.%) and HNO_3 (10 vol.%) for 2 h. The etched samples were washed using deionized water repeatedly, and dried in an oven. Further identification was performed with an X-ray diffraction (XRD, Bruker D8, Germany) with a $\text{CuK}\alpha$ radiation (0.154178 nm). Scanning electron microscopy (SEM, Zeiss Supra 25, Germany) and transmission electron microscopy (TEM, Zeiss-Libra120, Germany) operating at 120 keV were employed to characterize the starting materials and the products following the SPS treatment.

3.1.3 Effect of catalysts on the diamond formation from CNTs

The typical morphologies of the MWCNTs starting materials are shown in Figure 3-1(a) and (b). They are found to exhibit an external and internal diameter of ca. 40 nm and 20 nm, respectively (Figure 3-1a). No other forms of carbon and metal catalysts were identified during the TEM observations. The SEM micrograph shows

that the MWCNTs appear entangled and agglomerated together (Figure 3-1b). The SEM micrograph of the FeNi catalyst powders is shown in Figure 3-1(c). The gas atomized powders present average particle sizes about 40 μm . After ball milling with the MWCNTs, the FeNi powders are mixed well with the nanotubes as shown in Figure 3-1(d).

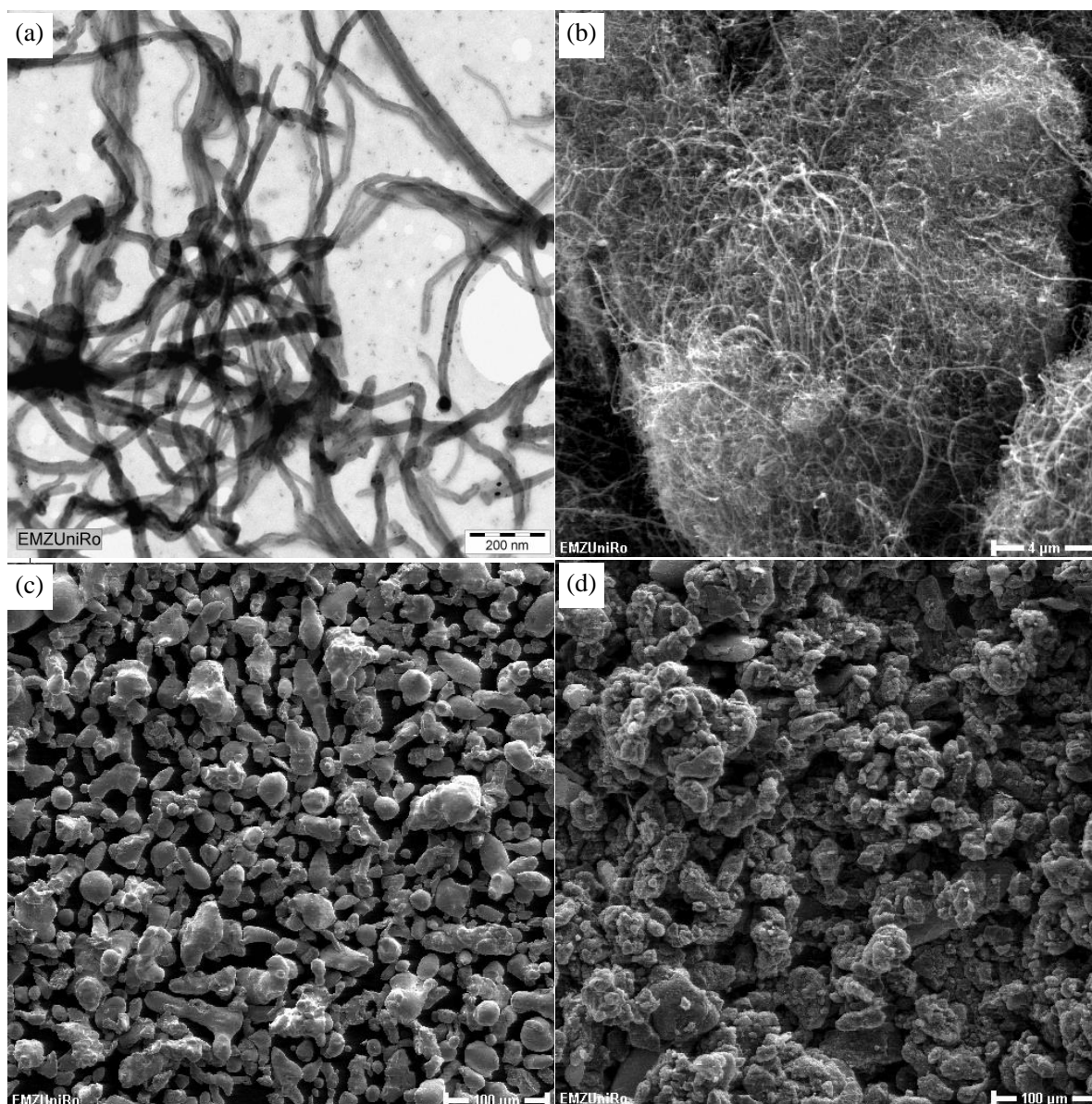


Figure 3-1 TEM (a) and SEM (b) micrographs of the starting MWCNTs, as well as SEM micrographs of the Fe₃₅Ni powder catalysts (c) and MWCNTs/Fe₃₅Ni powder mixtures (d).

The MWCNTs/FeNi samples were sintered in the SPS furnace at various

temperatures under 70 MPa for 20 min. All the obtained samples were etched in boiling acid to remove the FeNi catalysts and the un-reacted MWCNTs. Figure 3-2 shows the X-ray diffraction patterns of the starting MWCNTs, Fe₃₅Ni catalyst, and the spark plasma sintered MWCNTs/Fe₃₅Ni samples at (1100-1500) °C after etching. The starting MWCNTs show the (002) plane at 2θ of 25.86 degree without Ni and La catalysts peaks. The Fe₃₅Ni catalysts show diffraction peaks at 2θ of 43.60 degree and 50.79 degree. After etching of the obtained MWCNTs/Fe₃₅Ni samples, no obvious Fe₃₅Ni diffraction peaks were detected in the (1100-1500) °C sintered samples. It indicated that the FeNi catalysts have been completely removed from the carbon samples by the boiling acid treatment. The peak at 2θ of 42.90 degree in the raw CNTs has shifted to 43.37 degree in the 1100 °C sintered sample. It is noted that this sample is in the transitional stage from CNTs to diamond. It is identified that the cubic diamond peak at 2θ of 43.95 degree with d-spacing of 0.26 nm is present in the samples of (1200-1500) °C. There is still a broad CNTs (002) peak indicating that there are some un-reacted and un-removed CNTs in the samples. Additionally, haxonite (Fe,Ni)₂₃C₆ peaks are found in the XRD results of (1200-1500) °C sintered samples. With temperature increment from 1200 to 1500 °C, the haxonite peaks become stronger and stronger. It is due to the reaction between the FeNi catalysts and the MWCNTs at high temperatures.

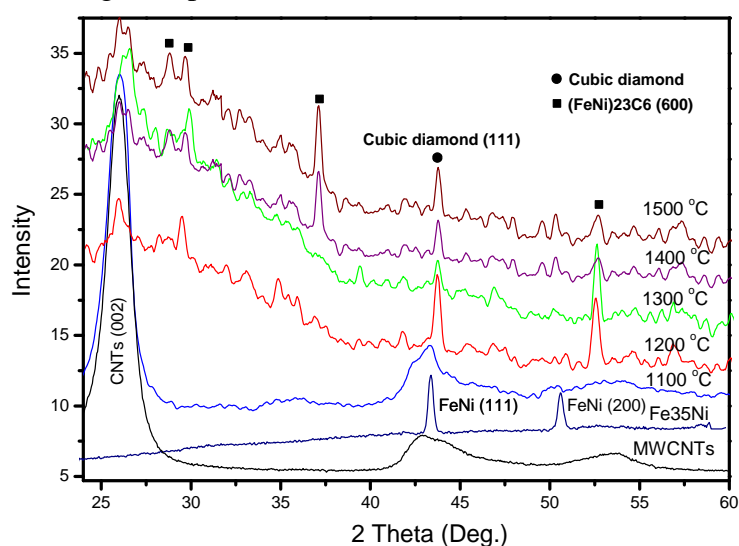


Figure 3-2 X-ray diffraction patterns of the starting MWCNTs, Fe₃₅Ni catalyst, and the spark plasma sintered MWCNTs/Fe₃₅Ni samples at (1100-1500) °C after etching.

Figure 3-3 shows the Raman spectra of the starting MWCNTs and the spark plasma sintered MWCNTs/Fe35Ni samples at (1100-1500) °C after etching. The D band of the starting MWCNTs appeared at 1290 cm^{-1} . After spark plasma sintered at 1100 °C, the MWCNTs peak was still presented in the spectrum, but it appeared as a new small peak centered at 1300 cm^{-1} . In the spectra of the (1200-1500) °C sintered samples, each of them exhibit a sharp and intense line with a frequency shift of 1332 cm^{-1} , which is the characteristic Raman shift of the cubic diamond. However, the MWCNTs peak (1290 cm^{-1}) still existed but became broader in the Raman spectra, which indicated the un-reacted nanotubes haven't been completely removed but their structures have been destroyed by the boiling-acid treatment. The D band shifted from the starting 1290 cm^{-1} to 1332 cm^{-1} indicating the cubic diamond formation above the temperatures of 1200 °C.

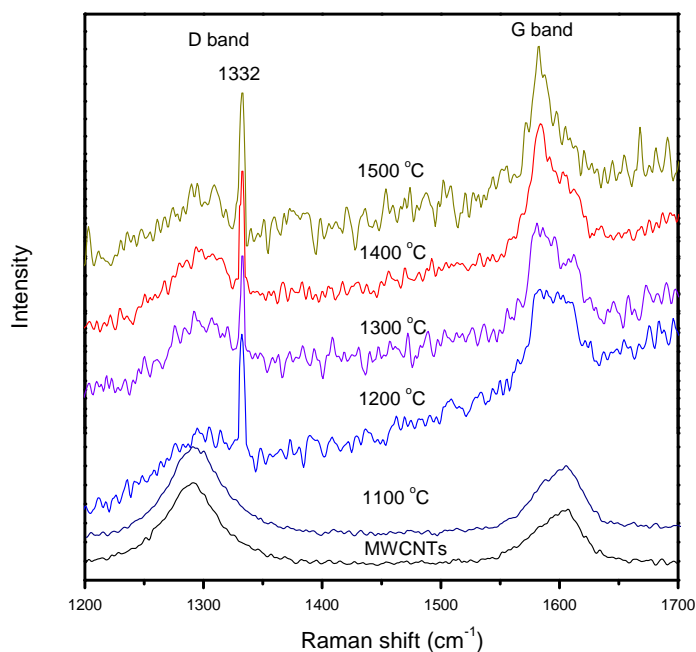


Figure 3-3 Raman spectra of the starting MWCNTs and the spark plasma sintered MWCNTs/Fe35Ni samples at (1100-1500) °C after etching.

The G band is due to the E_{2g} mode of graphite band (G band) relating to the sp^2 bonded carbon vibrations in a 2-dimensional graphitic hexagonal lattice. The G bands appeared at 1606 cm^{-1} in the starting MWCNTs and 1100 °C sample, has shifted to 1584 cm^{-1} around in the samples of (1200-1500) °C, which implied the formation of

graphite phase besides the diamond formation from the carbon nanotubes above the SPS temperature of 1200 °C. The Raman results indicated that diamonds have been converted from the MWCNTs/Fe35Ni in the temperature range of (1200-1500) °C. The XRD and Raman results confirmed the diamond formation in the (1200-1500) °C sintered samples.

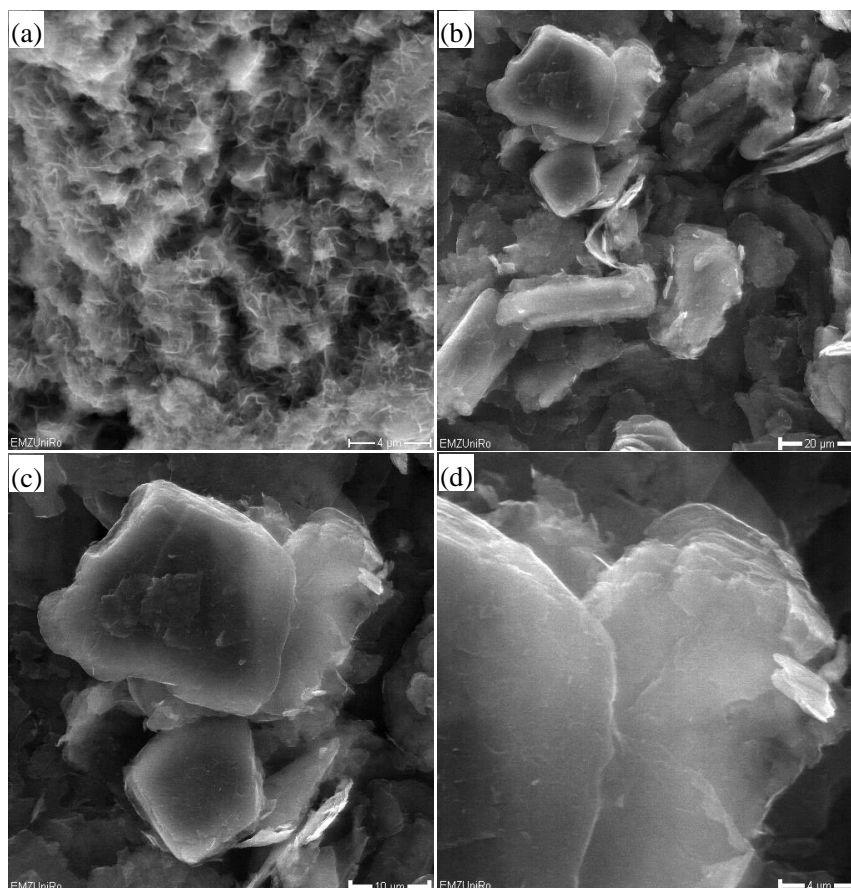


Figure 3-4 SEM micrographs of the spark plasma sintered MWCNTs/Fe35Ni samples at 1100 °C (a), 1200 °C (b-d) after etching, exhibiting the growing process of diamond.

The SEM micrographs of the spark plasma sintered MWCNTs/FeNi samples at 1100 °C and 1200 °C after etching are shown in Figure 3-4. Compared with the starting CNTs (Figure 3-1b), the MWCNTs in the 1100 °C sample are almost melted and adhered together, but the tubular structure of the CNTs are noticeable in the growing diamond (Figure 3-4a). After sintering at 1200 °C, diamond crystals with sizes of (10-40) μm are observed in the samples (Figure 3-4b). These diamond crystals are in the shape of hexahedron. Some flake-like carbons are noticed in the

sample, as indicated by circles. The higher magnification SEM micrograph showed that the diamond crystals without residual CNTs left on their surface (Figure 3-4c). The high magnification micrograph in Figure 3-4 (d) indicated the layer-by-layer texture on the diamond crystals.

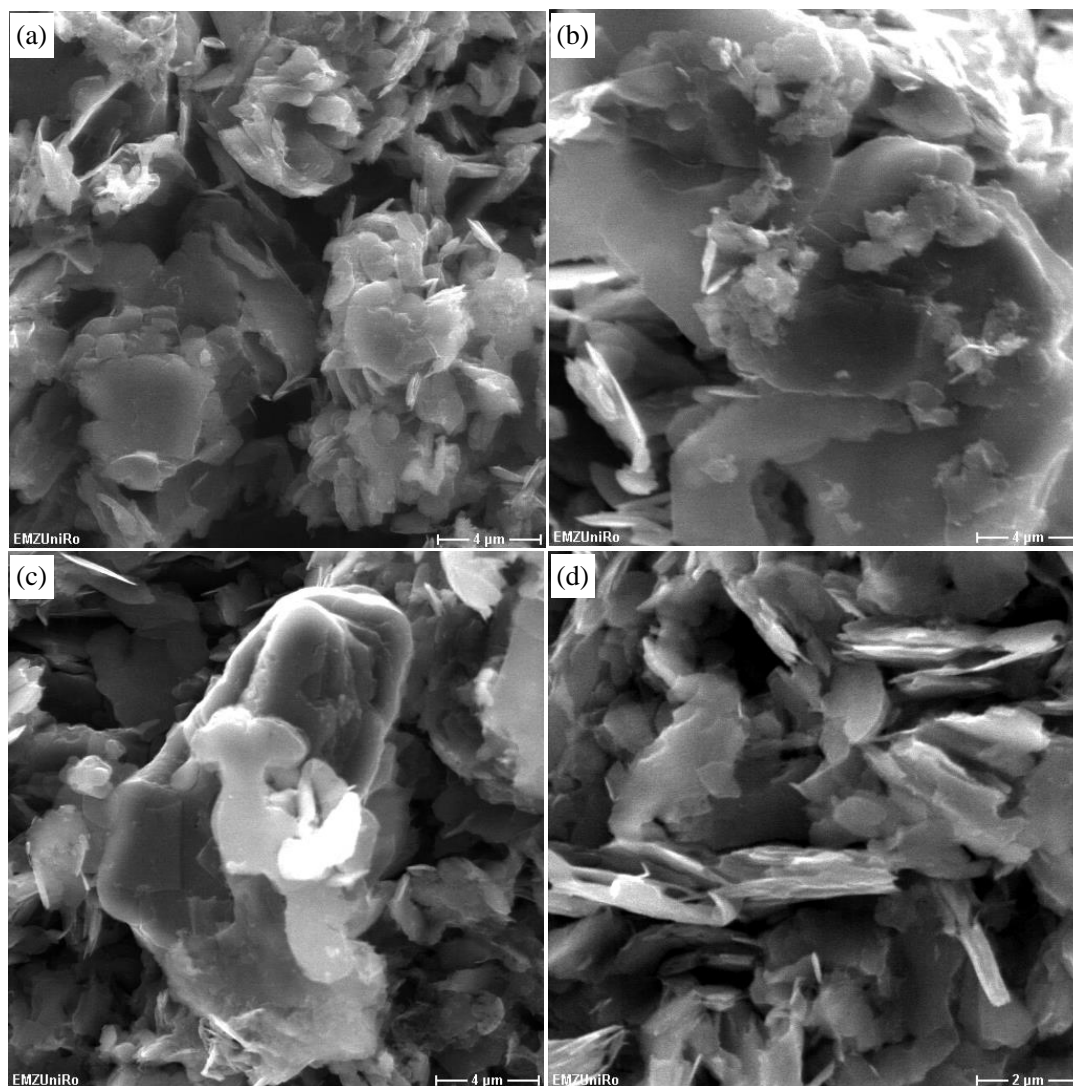


Figure 3-5 SEM micrographs of the spark plasma sintered MWCNTs/Fe35Ni at 1300 °C (a), 1400 °C (b), 1500 °C (c, d) after etching, showing the diamond crystals and flakes.

Figure 3-5 shows the SEM micrographs of the spark plasma sintered MWCNTs/FeNi samples from 1300 °C to 1500 °C after etching. The particle sizes of the diamond crystals did not increase with the increasing sintering temperatures (Figure 3-5a-c). A 1500 °C synthesized diamond with crystal size of about 20 μm also showed clear layer-by-layer textures (Figure 3-5c). On the matrix of this diamond

crystal, there are many flake-like carbons as shown in Figure 3-5(d). Such flake-like carbons were found in all these samples from 1300 °C to 1500 °C. The carbon flakes in these higher temperature sintered samples are similar to those in the 1200 °C sintered one. These flakes also showed layer-by-layer microstructures. The SEM observations agree well with the XRD and Raman results.

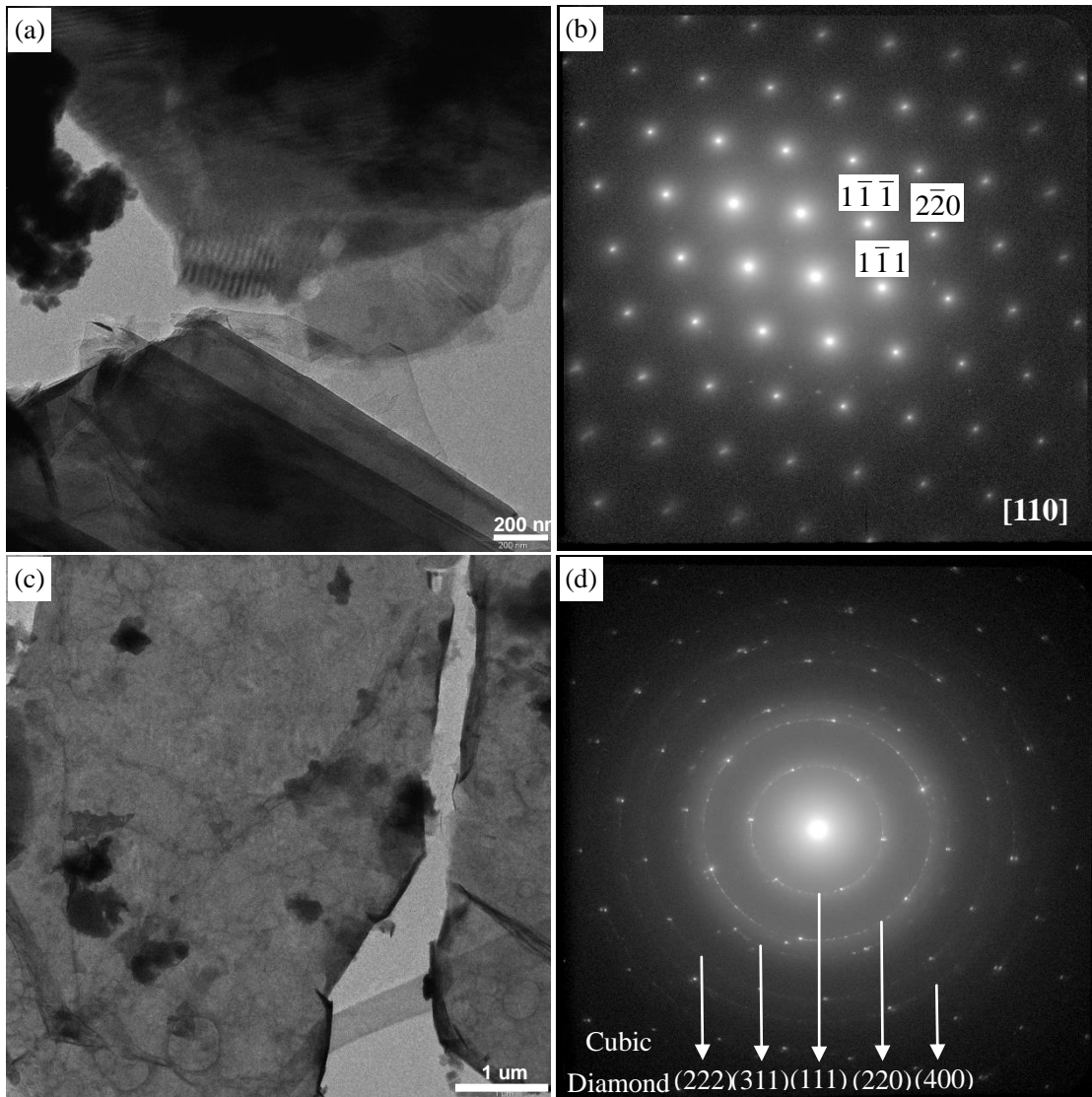


Figure 3-6 TEM micrographs with selected area diffraction patterns (SADP) of the 1200 °C spark plasma sintered MWCNTs/Fe35Ni sample after etching, showing the monocrystalline diamond (a, b) and polycrystalline diamond (c, d).

Figure 3-6 show the TEM micrographs and selected area diffraction patterns of the spark plasma sintered MWCNTs/Fe35Ni sample at 1200 °C after etching. There are some mono-crystal and poly-crystal diamonds in the samples (Figure 3-6 a-d). The monocrystalline diamond also shows the layer-by-layer structure (Figure 3-6a), which is consistent with the results of the SEM. The selected area diffraction pattern of the crystal in the bottom of the Figure 3-6 (a) confirmed the diamond is mono-crystalline along [110] direction (Figure 3-6b). The poly-crystal diamond is in size of tens of micrometers (Figure 3-6c). The selected area diffraction pattern with diffraction rings were calculated and confirmed that the diamonds are cubic poly-crystals (Figure 3-6d). The Raman, XRD, SEM, and TEM identification results have confirmed the diamond formation in MWCNTs with Fe35Ni as catalysts at a lower temperature of 1200 °C.

The Raman, XRD, SEM and TEM results confirmed that monocrystalline and polycrystalline diamonds were synthesized in the MWCNTs/Fe35Ni sample after SPS at temperatures above 1200 °C. The SEM results showed better diamond crystal shapes in the 1200 °C sintered samples. The TEM with selected area diffraction patterns showed the existence of diamond mono-crystals and poly-crystals in the 1200 °C sintered samples. Higher temperatures (1300-1500 °C) did not lead to larger diamond crystals as seen in the SEM images. The temperature 1200 °C is the optimal SPS temperature for the MWCNTs/Fe35Ni samples. This temperature 1200 °C for the diamond synthesis is much lower than that of the MWCNTs without catalyst (1500 °C) in our previous research [7]. It indicates that the FeNi catalysts are effective to enhance the diamond conversion from MWCNTs in the SPS technique. The melting point of Fe35Ni alloy is about 1460 °C as measured in its phase diagram. During the SPS processing, the melting point of this Fe35Ni powder has been decreased due to the pulsed current induced powder activation, and the applied pressures. There is usually some temperature difference between the mold surface and the actual temperature in the SPS sample. The temperature measurement design in the FCT spark plasma sintering system allowed a very accurate temperature control since the temperature difference between the centre of the sample and the controlling pyrometer

was always below 5 °C [8]. The catalysts of Fe35Ni alloy powders were melted at SPS temperature of 1200 °C, which was noticed during the SPS of the MWCNTs/Fe35Ni sample. It reduced the SPS temperature to 1200 °C and the pressure to 70 MPa for the diamond synthesis as well as increased the diamond transition rate using the MWCNTs as carbon sources. In general, milder conditions were realized for the diamond synthesis by using the Fe35Ni catalysts in this study. In the HPHT method, the carbon-carbon diagram for the diamond synthesis is crucial [9]. In this SPS method, there will be a new carbon-carbon diagram for the diamond synthesis, which can predict the optimal temperature, pressure regions for the diamond synthesis in this SPS method.

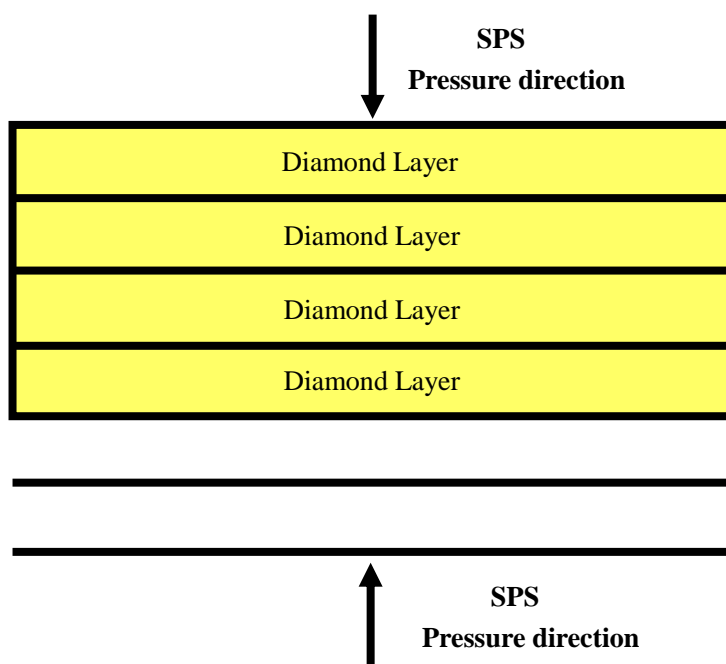


Figure 3-7 Schematic illustration of the growth model of diamond crystals from MWCNTs in SPS.

The layer-by-layer structure of diamond crystals are found in the SEM and TEM micrographs. Our previous research revealed the initial diamond growth mechanism from MWCNTs to diamond in SPS without catalysts, that is from CNTs to intermediate phase carbon onions, and finally to diamond [10]. The diamond crystals in the samples without FeNi catalysts are also shown the similar layer-by-layer

structures. Many flake-carbons with layers structures were found in the samples of (1200-1500) °C. These indicate that the diamonds were grown up from these carbon flakes. Based on the above analysis, a model for the growth of diamond crystals during the SPS is proposed in Figure 3-7. The direction of pressure during the SPS is in uniaxial directions, but not in six directions as the HPHT six-anvil press. Therefore, the diamonds are easier to grow in the direction without pressures. As a result, the MWCNTs are grown to layered diamond flakes vertically to the direction of pressure. Finally, several diamond flakes are reacted together and formed a three-dimensional diamond crystal. In a word, the growth mechanism of diamond from MWCNTs is a layer-by-layer growth model in the SPS method. This model is available for the MWCNTs to diamond with and without catalysts. This mechanism will be constructive and helpful for the large diamond crystals synthesis by using the SPS technique.

3.1.3 Effects of the CNTs diameters on the diamond sizes by the SPS

The kinetic mechanism for the phase transformation of carbon nanotube to diamond is proposed that the CNTs transformed to carbon nano-onions, and the nucleation and growth of the diamond phase within the onion cores [10]. A model for the diamond nucleation at the internal surface of carbon onion is established, as shown in Fig.3-8.

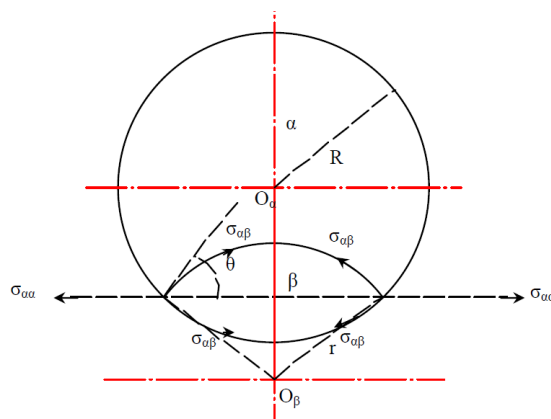


Fig. 3-8 Model for diamond (β) nucleation at the internal surface of carbon onion (α).

Based on this model, the energy need for the nucleation of diamond at the internal surface of carbon onion can be formulized based on theory of thermal dynamics:

$$\Delta G = \Delta G_V + \Delta G_S + \Delta G_E \quad (3-1)$$

Where ΔG — Difference of Free energy for the nucleation of diamond;

ΔG_v — Difference of Volume Free energy for the nucleation of diamond;

ΔG_s — Difference of Surface Free energy for the nucleation of diamond;

ΔG_E — Difference of Elastic strain energy for the nucleation of diamond.

In the equation of (3-1), each type of energy difference can be formulized:

$$\Delta G_v = \frac{4}{3}\pi R^3 \Delta G_v \quad (3-2)$$

$$\Delta G_s = 4\pi R^2 \Delta G_s \quad (3-3)$$

$$\Delta G_E = \frac{4}{3}\pi R^3 \Delta G_E \quad (3-4)$$

Nucleation energy of diamond from carbon anion ΔG ,

$$\Delta G = \frac{4}{3}\pi R^3 \Delta G_v - 4\pi R^2 \Delta G_s + \frac{4}{3}\pi R^3 \Delta G_E \quad (3-5)$$

The above equation shows the reduction of R leads to the decrease of ΔG . The value of R is the inner radius of CNTs. It means that reducing the diameter of CNTs could decrease the energy for the diamond nucleation ΔG . The lower ΔG leads to higher transition rate and larger particle size of diamond. This will be validated by the following experiments.

The MWCNTs with diameters from 10-100 nm were mixed with Fe35Ni catalyst at a weight ratio of 1:1 by ball milling, and pressed into a graphite die for SPS treatment to form disk-shaped samples. The raw materials those used in this experiment is shown in Table 1 with internal diameters of (10-20) nm, (20-40) nm, (40-60) nm and (60-100) nm. The SPSed samples after etching were subjected to the SEM analysis. Figure 3-9 shows the SEM micrographs of the diamond crystals obtained from different MWCNTs. It really shows various diamond sizes. The (10-20) nm MWCNTs generated (15-30) μm diamond crystals. The (20-40) nm MWCNTs generated (10-20) μm diamond. The (40-60) nm MWCNTs produced (7-10) μm diamonds, and the (60-100) nm MWCNTs formed (4-10) μm diamonds. The results are summarized in Table 2. Smaller diameters MWCNTs could produce larger diamond particles.

Table 1 The raw materials those used in this experiments.

Main range of diameter of	(10-20) nm	(20-40) nm	(40-60) nm	(60-100) nm
MWCNTs				
Length	(5-15) μm	(5-15) μm	(5-15) μm	(5-15) μm
Purity	>95%	>95%	>95%	>95%
Ash	<0.2 wt%	<0.2 wt%	<0.2 wt%	<0.2 wt%
Specific surface area	(40-300) m^2/g	(40-300) m^2/g	(40-300) m^2/g	(40-300) m^2/g
Amorphous carbon	<3%	<3%	<3%	<3%

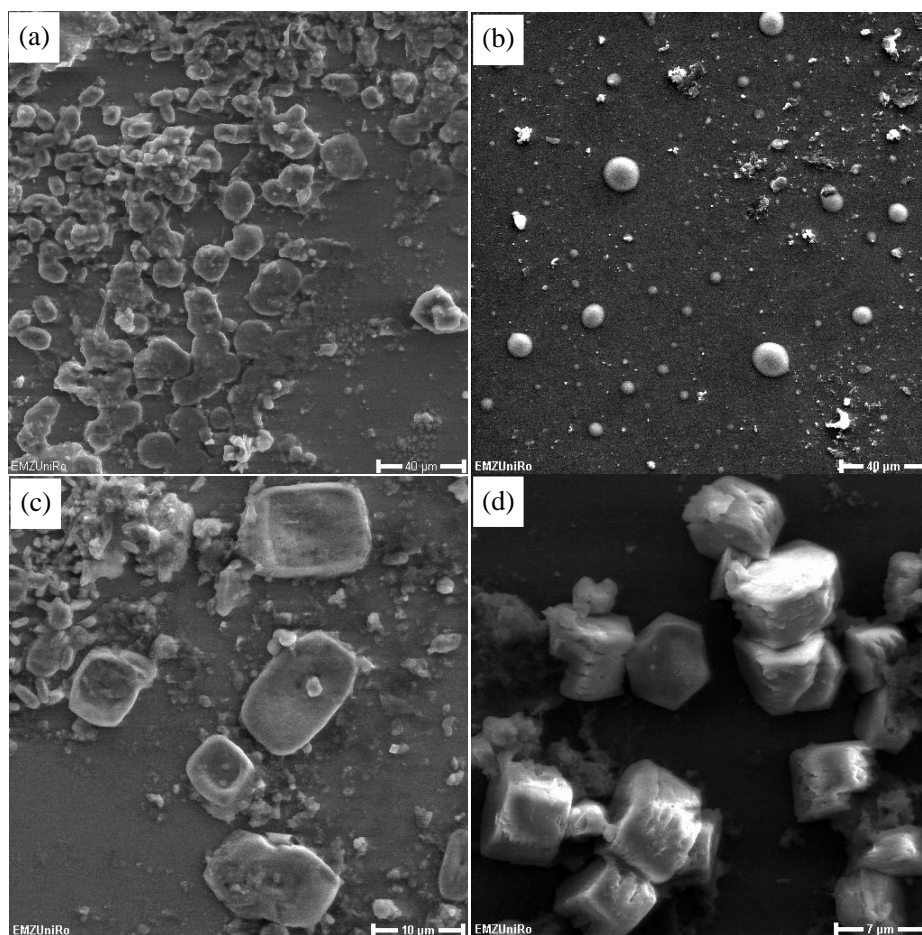


Fig.3-9. SEM micrographs of the SPSed MWCNT/FeNi samples with various internal nanotube diameters of (10-20) nm (a), (20-40) nm (b), (40-60) nm (c) and (60-100) nm (d) showing the different diamond sizes.

Table 2 The diamond particle size from various MWCNTs.

Main range of diameter of MWCNTs	(10-20) nm	(20-40) nm	(40-60) nm	(60-100) nm
Diamond particle size	(15-30) μm	(10-20) μm	(7-15) μm	(4-10) μm

The experiments validated the theoretical assumption. Herein, the MWCNTs have been transformed to diamond under SPS conditions in presence of a FeNi catalyst at pressures of 50MPa and temperatures of 1200 °C. The diamond particle size depends on the diameter of the MWCNTs. The MWCNTs with diameters (60-100) nm produced diamond particle (4-10) μm , while in the sample of MWCNTs with diameters (10-20) nm generated diamond particle sizes (15-30) μm .

3.1.4 Summary

Fe₃₅Ni solvent catalyst has been involved to synthesize diamond from MWCNTs by using the SPS technique. Cubic diamond crystals were synthesized from the MWCNTs/Fe₃₅Ni mixtures at lower SPS temperature of 1200 °C under pressure of 70 MPa. In the sample, well-crystallized diamond mono-crystals and poly-crystals consisted particle sizes of (10-40) μm . The Fe₃₅Ni catalysts achieved an effective reduction of the SPS temperature to 1200 °C and the SPS pressure to 70 MPa for the diamond synthesis, as well as an increment of diamond transition rate from MWCNTs in the SPS. A model was also proposed to describe the diamond growth as a layer-by-layer growth mechanism. The diamond particle size depends on the diameter of the MWCNTs.

3.2. Synthesis of diamond from fullerene C₆₀ by SPS

Due to its unique physical and chemical properties, fullerene C₆₀ is a promising candidate substance for many novel applications in industry. Therefore, it is very important to deeply understand the stability and phase transformation behavior under

extreme physical conditions. Duclos et al [11] reported that the C60 molecules are extremely stable at room temperature, withstanding hydrostatic pressure of up to about 20 GPa. It is transformed irreversibly into a new hard carbon phase above hydrostatic pressure of 27 GPa [12, 13]. Under non-hydrostatic high pressures (20±5GPa), the C60 is unstable to collapse into a diamond phase at room temperature [14]. At high temperatures above 1500 °C, C60 crystals are transformed into diamond in a pressure range of 9-15 GPa [15]. Nanocrystalline cubic diamond with crystallite sizes of 5–12 nm could be synthesized from fullerene C60 at 20 GPa and 2000 °C using a multi-anvil apparatus [16]. Microcrystalline diamonds up to 6 µm were produced from fullerenes C60-C150 using a shock-wave synthesis under pressures ranged 24-40 GPa [17]. In general, it needs solely superhigh pressure or high pressure (in several GPa) and high temperature for the phase transition of C60 to diamond.

Since the C60 has a higher sp^3 hybridization fraction than that of carbon nanotubes, it makes the transformation of C60 into diamond easier. Therefore, it is postulated that the C60 may be able to increase the diamond size and transition rate in the SPS diamond synthetic method. In this study, the diamond growth from C60 was studied under the pulsed electric field of the SPS system to increase the size and transition rate of diamond. The spark plasma sintered carbon samples were analyzed by using micro-Raman spectroscopy, Synchrotron X-ray, scanning electron microscopy (SEM) and transmission electron microscopy (TEM) techniques. Its phase transformation mechanism is also discussed.

3.2.1 Experimental

The fullerene C60 was purchased from SES research, Houston, USA. The purity of the pristine C60 was claimed by the producer to be about 99.5%. The pure C60 powders were pressed into a graphite die for SPS treatment to form disk-shaped samples. The SPS experiments were conducted using a Model of HP-D5 FCT spark plasma sintering system installed at the Tycho Sinter Lab in the University of Rostock, under an axial pressure of (50-80) MPa at temperatures of (1100-1500) °C in vacuum (<6 Pa). A heating rate of 100 K/min was used, and the sintering process lasted typically 20 minutes. The applied direct current for SPS was about 1000 A with a

pulse duration of 12 ms and an interval of 2 ms leading to disk-shaped samples with a diameter of 20 mm and a thickness of 5 mm.

The sintered samples were etched in a solution of concentrated H_2SO_4 (90 vol.%) and HNO_3 (10 vol.%) at room temperature for 12 h. The etched samples were washed using de-ionized water repeatedly, and dried in an oven. The identification was performed with a Renishaw-2000 Laser Raman spectroscopy system with a He-Ne laser excited at 514 nm with a power density of 4.7 mW and a spot diameter of about 5 μm . Further identification was performed with a high-energy X-ray diffraction at beamline BW5 (DESY/HASYLAB Hamburger Synchrotron Laboratory) with a wavelength of 0.123984 Å (100.0 keV). Scanning electron microscope (SEM, Zeiss Supra 25, Germany) and transmission electron microscope (TEM, Zeiss-Libra120, Germany) operating at 120 keV, were employed to characterize the starting materials and the products following the SPS treatment.

3.2.2 Results and discussions

Figure 3-10 (a) shows the TEM micrograph of the fullerene C60 powder with particle sizes from 40 nm to 100 nm. There are some agglomerates in the particles. The inserted selected area diffraction pattern on a specific C60 particle indicates that the C60 is a single crystal along [110] direction. Figure 1(b) shows the SEM micrograph of the C60 powder. The particle agglomerates are from nanometer to 4 micrometers.

Figure 3-11(a) shows the Raman spectra of the raw C60 and the spark plasma sintered (SPSed) C60 samples after etching. The raw C60 shows a sharp peak appeared at 1460 cm^{-1} and two weak broad peaks centered at 1568 cm^{-1} and 1413 cm^{-1} . Previous study [12] demonstrated that SPS processing of C60 with a pressure of 80 MPa and a temperature of $1500\text{ }^\circ\text{C}$ is leading to the formation of diamond. Hereby, the SPS pressure was reduced to 50 MPa. As expected, the cubic diamond peaks can also be detected at 1333 cm^{-1} in the Raman spectra taken for the samples SPS processed in the temperature range from $1150\text{ }^\circ\text{C}$ to $1500\text{ }^\circ\text{C}$. However, the diamond band of the samples sintered at $1150\text{ }^\circ\text{C}$ is very broad having the lowest height. Its graphite band at 1568 cm^{-1} is at the same value as that of the raw C60. It indicates that

there is only a small fraction of diamond in this 1150 °C SPSed sample. With an increase in temperature to 1200 °C, 1300 °C and 1500 °C, the diamond band at 1333 cm^{-1} gets sharper and sharper, as well as the graphite band is shifted to a higher value of 1576 cm^{-1} . The result of the 1300 °C SPSed C60 shows a Raman spectrum similar to the 1500 °C SPSed sample. The main peak in the pure C60 spectrum at 1460 cm^{-1} disappears in all the spectra of the samples processed in the temperature range (1150-1500) °C. This indicates that the C60 is completely transformed into diamond and graphite phases after SPS at above temperatures of 1150 °C.

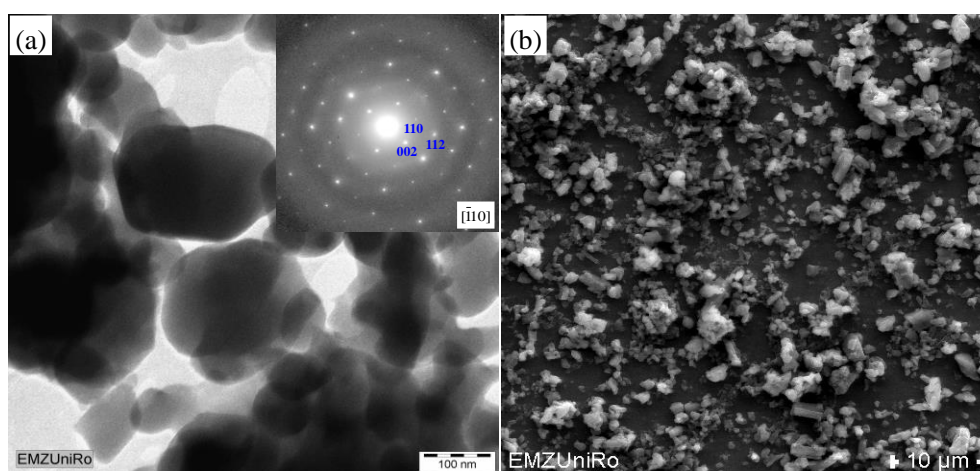


Figure 3-10 TEM micrograph with inserted selected area diffraction pattern (a) and SEM micrograph of the raw fullerene C60 powder (b).

Figure 3-11(b) shows the synchrotron radiation-high energy X-ray diffraction patterns of the raw C60 and the SPSed C60 samples after etching. In the 1150 °C sintered C60 sample, very weak diamond peaks at d spacing of 2.06 Å and 1.26 Å are noticeable. The C60 after SPS at temperatures above 1200 °C show sharper cubic diamond diffraction peaks at d spacing of 2.06 Å and 1.26 Å and broad graphite peaks. The peaks of graphite are very broad indicating its amorphous structure. Amorphous graphite is the least graphitic of the graphite types where none of the common crystal faces are visible. The C60 diffraction peaks disappeared indicating the C60 has completely transformed into diamond and amorphous graphite phases after the SPS processing at temperatures from 1150 °C to 1500 °C. The Raman and Synchrotron X-ray results confirmed the diamond formation in the C60 samples. However, the

FWHMs of the diamond peaks in the Raman spectra and Synchrotron X-ray diffraction patterns are all broad. Such broad peaks are known to be a sign of fine diamond crystallites. It is calculated from the peak-area ratio in the Raman results that the fractions of the sp^3 hybridized carbon in the final products are about 50 vol.% in the samples of (1200-1500) °C. As calculated from the peak-area ratio in the Synchrotron X-ray results, the fractions of the diamond in the final products are about 30 vol.% in the samples processed at 1300 °C and 1500 °C. Combining both of them, the transition rate of diamond from C60 is at least 30 vol.% in the SPSed samples at 1300 °C and 1500 °C.

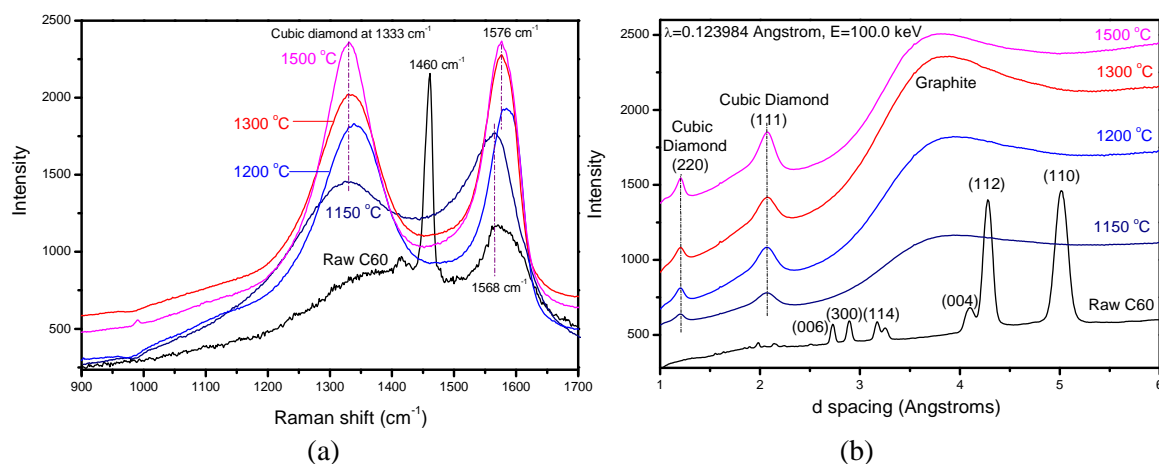


Figure 3-11 Raman spectra (a) and synchrotron radiation-high energy X-ray diffraction patterns (b) of the raw C60 and the spark plasma sintered C60 at different temperatures under pressure of 50 MPa.

Figure 3-12 shows the SEM micrographs of the SPSed C60 samples after etching. In the 1150 °C SPSed sample, it is found few small diamond particles, as marked by circles (Figure 3a). Some diamond crystals with hexagonal, tetragonal or triangular shapes are found in Figure 3-12(b) of the 1200 °C SPSed sample. The particle sizes of the diamond crystals are from tens of micrometers up to 200 μm, as marked by circles. The diamond crystals with perfect hexahedron shapes are clearly observed in the 1300 °C sintered sample (Figure 3-12 c). The diamond sizes range from 100 μm to 250 μm, and they are larger than those of the sample sintered at 1200 °C. Some fine diamond crystals are noticeable on one big diamond crystal. The micrographs of the

1500 °C sintered C60 sample show that the big diamond crystals are almost melted (Figure 3-12 d). There are many fine diamond crystals below 4 μm on the big crystals (Figure 3-12 e). It is obvious that the diamond crystal sizes do not increase with the increase in temperature. A processing temperature of 1300 °C is the best for the phase transformation of C60 directly to diamond, according to this study. The particle size of the diamond crystals made from C60 is up to 250 μm. It is a very large size for such conversion without any catalyst being involved in the process.

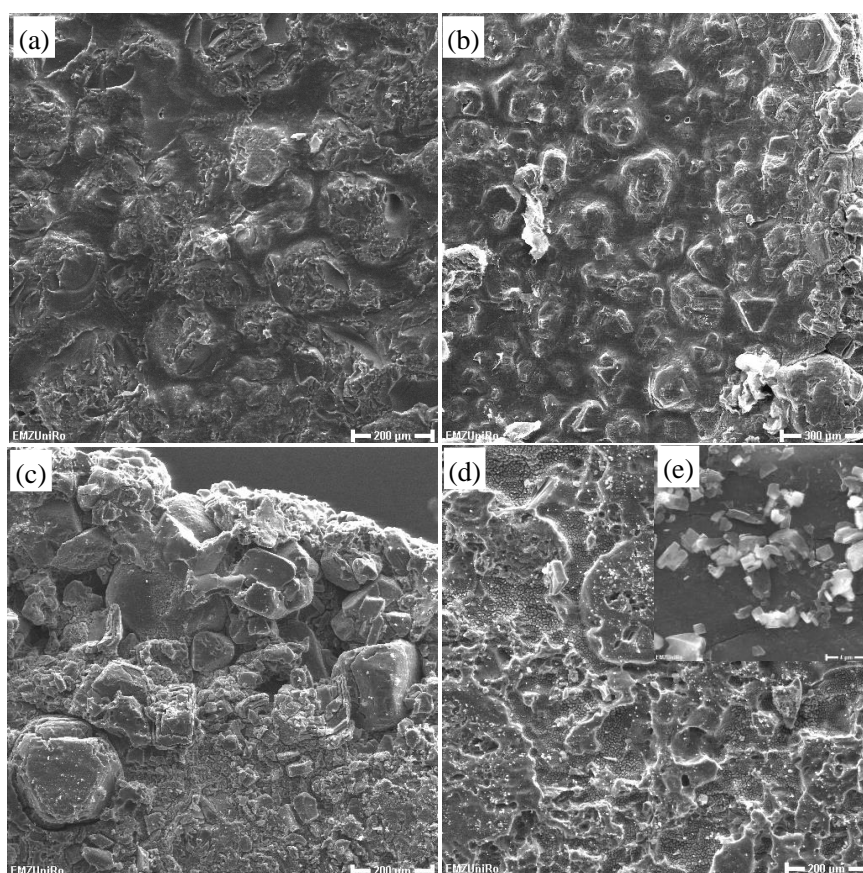


Figure 3-12 SEM micrographs of spark plasma sintered C60 samples at 1150 °C (a), 1200 °C (b), 1300 °C (c) and 1500 °C (d, e) after etching, showing the growth of diamond crystals.

The TEM micrograph of the 1200 °C spark plasma sintered C60 sample is shown in Figure 3-13. Figure 3-13 (a) shows a big diamond crystal with some pure C60 particles. The particle size of the C60 in this SPSed sample lies in the range of (40-100) nm. It is identically to that of the pure C60. The C60 particles are present with the diamond crystal together. This indicates that the diamond is directly

transformed from these C60 particles. The selected area diffraction pattern with diffraction rings were calculated and confirmed that the diamonds are cubic polycrystals (Figure 3-13b). It is noted that there are two sets of diffraction patterns indicating the presence of two cubic polycrystals in the selected area. No formation of an intermediate phase was observed for the C60 transformation into diamond in the TEM micrograph. The transformation from C60 to diamond seems to be a direct carbon transformation process with structural reconstruction without the production of any intermediate phase.

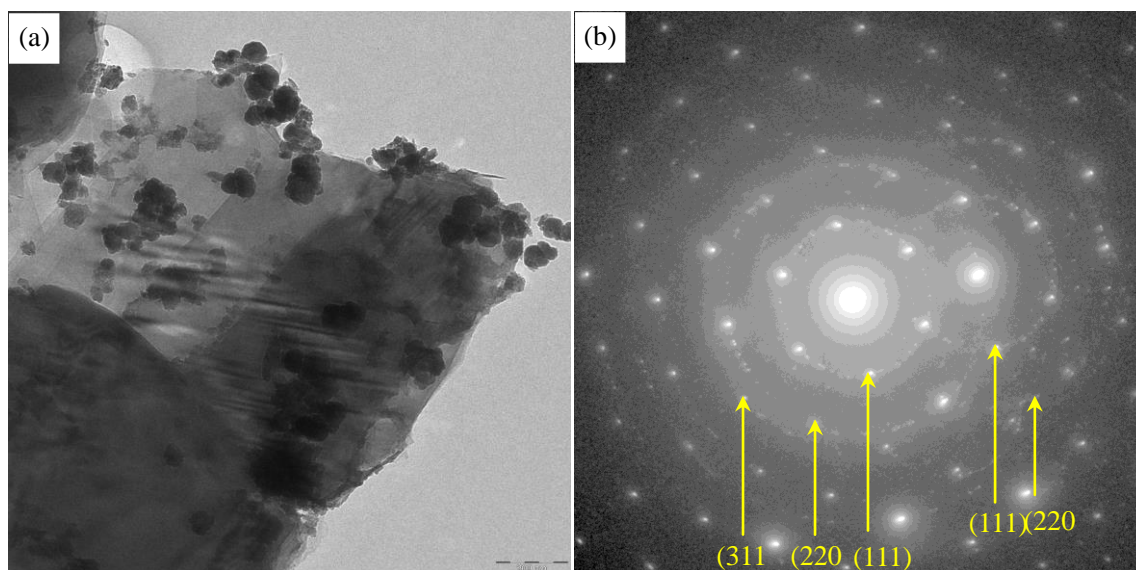


Figure 3-13 TEM micrograph of a diamond crystal formed in the 1200 °C spark plasma sintered C60 sample (a) with the selected area diffraction pattern (b), exhibiting the polycrystalline diamonds.

The Raman, Synchrotron X-ray, SEM, and TEM identifications have confirmed the diamond formation in the C60 by the SPS at milder conditions. The diamond particle size and transition rate both increased using the C60 as carbon source for diamond synthesis. The experimental results validated the hypothesis in the introduction. Due to the high price of the C60, conversion of C60 to diamond by SPS has more theoretical impact than practical application for the growth of diamond. For its practical use, this study suggests that the C60 may be able to be used as a doping catalyst to promote the diamond transitions. Vul et al [18] have studied the effects of

fullerene on the high-pressure high temperature synthesis of diamond from graphite and found that the fullerenes increased the percentage graphite to diamond conversion by a factor of 1.8 and allowed the pressure and temperature of the synthesis to be decreased. Therefore, the application of C60 as one type of catalyst or doping catalyst for diamond synthesis in the SPS or other techniques has some practical prospects. The theoretical impact of the conversion of C60 into diamond by the SPS at such milder condition is very constructive. The carbon atoms in C60 are sp^2 hybridized with a high fraction of sp^3 hybridized structure due to angular strain. It is a bit difficult to transform the planar sp^2 structure to the diamond sp^3 network. Our previous results confirmed that the graphite with pure sp^2 structure cannot be converted to diamond in the SPS. The C60 can be considered as a folded graphite sheet with the predominant hybridization sp^3 in the pentagons. This makes the transformation of C60 into diamond easier. A dense assembly of C60 spheroids, where 48 out of 60 carbon atoms have quasi-tetrahedral coordination, is sterically fairly close to that of the diamond [11, 14]. It implies that a small rearrangement of the atoms of C60 can result in the change of its structure. However, it still needs solely superhigh pressure or high pressure and high temperatures for the phase transition from C60 to diamond [11-16]. In the pulsed electric field of the SPS, the DC currents were passed through the graphite die and the C60 sample. The pulsed electric field in the SPS utilizes high currents up to thousands of Ampere and low voltages up to 10 Volt eventually generating spark plasmas provides most of the energy for the diamond formation under such low temperatures and low pressure. Our previous research has validated the presence of plasmas during SPS of these conductive and high surface area nanocarbon materials. Finally, the C60 gets unstable under such pulsed electric field and can be transformed into diamond at temperature as low as 1150 °C. In a word, the mechanism for the conversion of C60 to diamond owns to the special structure of the C60 and the unique SPS technique.

3.2.3 Summary

Fullerene C60 is unstable and can be transformed into crystalline diamond by spark plasma sintering under a pressure of 50 MPa above temperatures of 1150 °C without

any catalysts being involved. Well-defined diamonds with particle sizes up to 250 μm and transition rate about 30 vol.% are obtained at 1300 $^{\circ}\text{C}$ and no further growth in particle size is seen beyond this temperature. The mechanism analysis indicates that the high sp^3 hybrid fraction in the C60 and the generated plasmas in the pulsed electric field lead to the transformation to diamond. It is a direct transition process from C60 to diamond with a structural reconstruction of carbon atoms without intermediate phases being involved.

3.3 Synthesis of diamond from graphite with catalysts

3.3.1 Diamond from graphite with various catalysts

Graphite has been used as the main carbon source for the diamond synthesis in the HPHT technique. In this study, the Ni, MnNi, MnNiFe and AlCuFe quasicrystal powders were tested as the catalysts for the diamond synthesis from the graphite by the SPS technique. Each catalyst was weighted and mixed with the graphite powder in the mass ratio of 4:6. The mixture powders were mixed homogeneously by high energy ball milling for 5 hours. Then, the mixtures were subjected to the SPS machine. The samples were sintered at SPS temperatures of (1200-1500) $^{\circ}\text{C}$ and under pressures of (10-80) MPa. The results show that diamond crystals can be converted from graphite at the SPS temperature of 1300 $^{\circ}\text{C}$ for soaking time of 20 min under the pressure of 50 MPa.

Figure 3-14 shows the SEM micrographs of the spark plasma sintered graphite samples at 1300 $^{\circ}\text{C}$ for 20 min under 50 MPa with Ni, AlCuFe quasicrystal, MnNi, and MnNiFe powder catalysts after etching. It is interesting that we got diamond nano- and micro-rods with the Ni catalysts from the graphite (Figure 3-14a) by the SPS. The diameter of the diamond rods are from 80 nm to 2 μm . It is noted that the SPS also can be used as a new method to synthesize of diamond nano- and micro-rods. The AlCuFe quasicrystal was introduced as the catalyst for the graphite to diamond in the SPS. It is noticed that the diamond crystals with good diamond shapes from 1 μm to 3 μm were converted from the graphite with the AlCuFe catalyst. It indicates that

the AlCuFe quasicrystal powder also can be used as catalyst for the conversion from graphite to diamond in the SPS. With MnNi catalysts, some short rod like diamond crystals are found in the sample (Figure 3-14c). However, in the sample of graphite/MnNiFe, there are no good diamond crystals visible (Figure 3-14d).

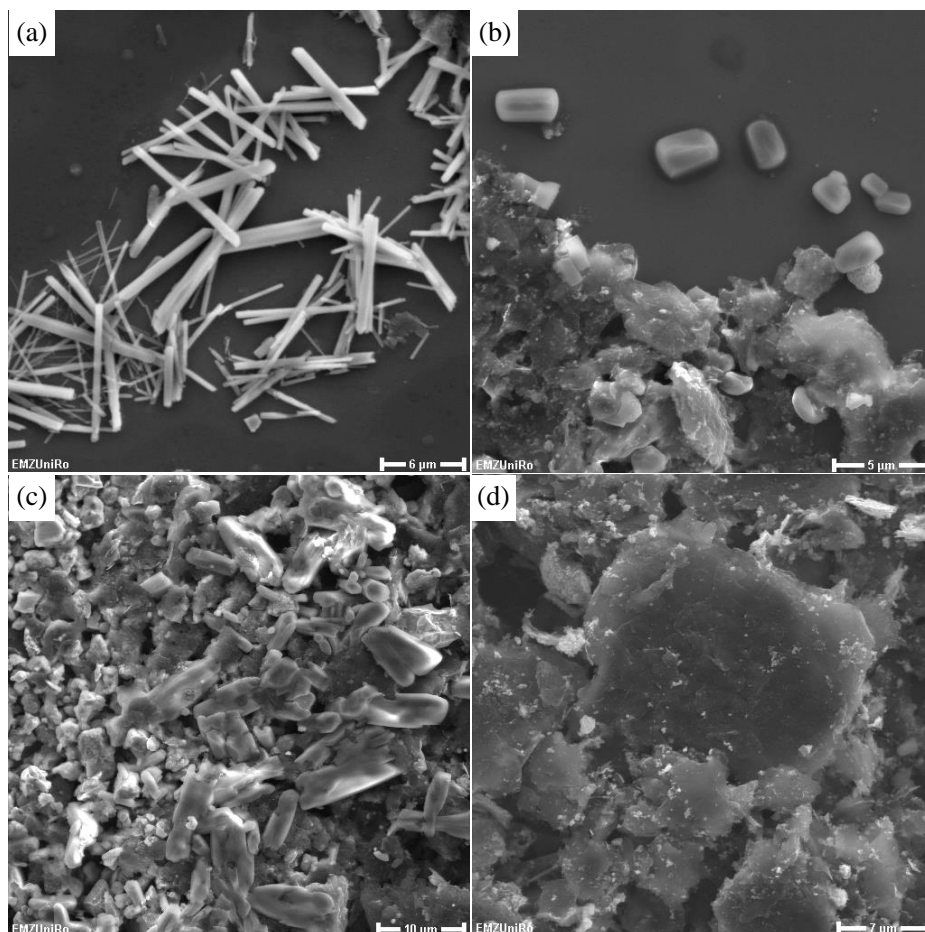


Figure 3-14. SEM micrographs of the spark plasma sintered graphite samples at 1300 °C, 50 MPa with Ni (a), AlCuFe quasicrystal (b), MnNi (c), and MnNiFe powder catalysts (d) exhibiting the different diamonds

Additionally, the diamond phase was identified by the X-ray diffraction. Figure 3-15 shows the synchrotron radiation-high energy X-ray diffraction patterns of the spark plasma sintered graphite samples at 1300 °C, 50 MPa with Ni, AlCuFe quasicrystal, MnNi, and MnNiFe powder catalysts after etching. The Graphite/Ni sample show strong cubic diamond peaks at d-spacing of 2.06 Å, 1.26 Å and 1.07 Å. The Graphite/AlCuFe samples show the strong diamond peaks at d-spacing of 2.06 Å

and 1.26 Å. The Graphite/MnNi and Graphite/MnNiFe samples showed weak diamond peaks at d-spacing of 2.06 Å, 1.26 Å and 1.07 Å. The XRD results agree well with the SEM results that good crystalline diamonds have been successfully synthesized from the graphite with catalysts of Ni and AlCuFe.

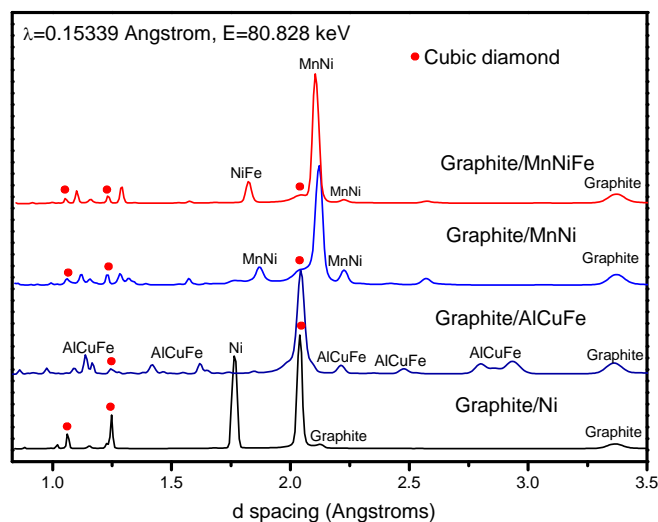


Figure 3-15 Synchrotron radiation-high energy X-ray diffraction patterns of the spark plasma sintered graphite samples at 1300 °C, 50 MPa with Ni (a), AlCuFe quasicrystal (b), MnNi (c), and MnNiFe powder catalysts (d).

3.3.2 Diamond/copper composites

The parameters for the diamond synthesis from graphite/quasicrystals mixtures are modified. Larger diamond crystals up to 30 μm are prepared at 1300 °C and 80 MPa for 30 min soaking time. After purification with strong acid treatments, the diamond particles were mixed with copper powder and then sintered by the SPS in vacuum at 720 °C and 50 MPa for 5 min soaking time. The SEM image of the surface of the copper-3.0 wt.% diamond composites is shown in Figure 3-16. The diamond crystals are embedded and dispersed in the soft copper matrix. The nanoindenter result of the copper/diamond composite shows the hardness of diamond is (15.1±1.6) GPa, Young's modulus is (92.1±4.8) GPa, and the matrix Cu hardness is (1.45±0.2) GPa and Young's modulus is (32.8±3.8) GPa. The diamond/copper composites have a possibility to be used as wear resistance parts and high thermal conductivity required components.

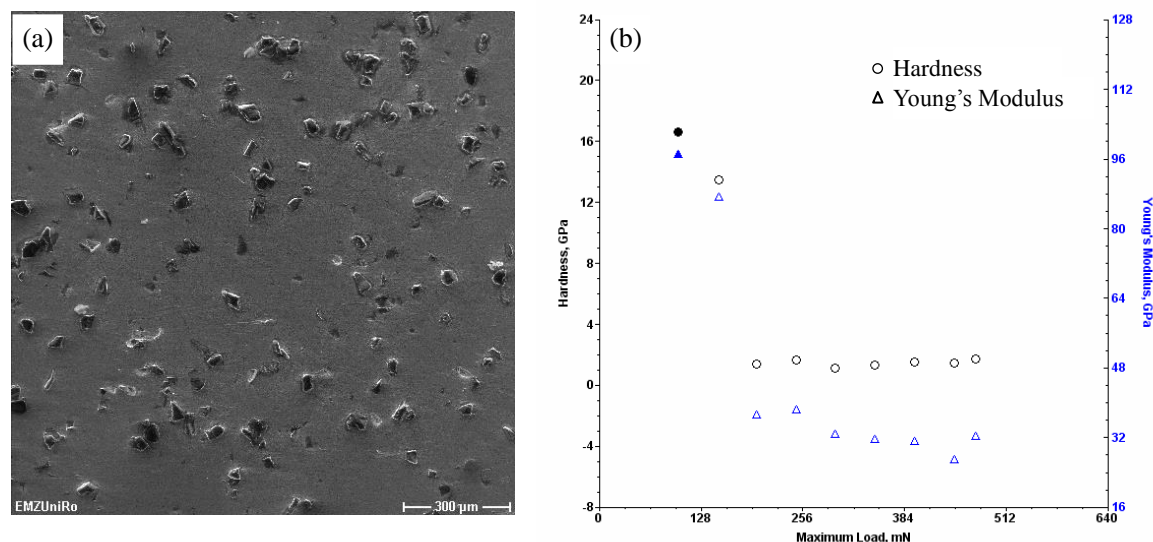


Figure 3-16 SEM image of the surface of the Diamond/Cu composite (a) and the nanoindentation results of the diamond and copper matrix (b).

3.3.4 Summary

Diamond crystals have been converted from graphite at the SPS condition of 1300 °C, 50 MPa for 20 min. Diamond nano- and micro-rods (80 nm-2 μm) have been obtained with the Ni catalysts from the graphite by the SPS. Diamond crystals with good diamond shapes from 1 μm to 3 μm have been converted from the graphite with the AlCuFe catalyst. The diamond/copper composites are prepared by SPS. The composite shows the hard diamond phase with hardness of (15.1 ± 1.6) GPa embedded in the soft copper matrix with hardness of (1.45 ± 0.2) GPa with a uniform distribution.

References

- [1] S. Naka, K. Horii, Y. Takeda, T. Hanawa. Direct Conversion of graphite to diamond under static pressure. *Nature*. 1976;259(5538):38-39.
- [2] Y. Z. Ma, G. T. Zou, H.B. Yang, J.F. Meng. Conversion of fullerenes to diamond under high-pressure and high-temperature. *Applied Physics Letters*. 1994, 65(7): 822-823.
- [3] L. Cao. Synthesis of diamond from carbon nanotubes under high pressure and high temperature. *Carbon*. 2001, 39:311-314.
- [4] X. Yan, H. Kanda, T. Ohsawa, S. Yamaoka, O. Fukunaga. Behaviour of graphite-diamond conversion using Ni-Cu and Ni-Zn alloys as catalyst-solvent. *Journal of Materials Science*. 1990, 25:1585-1589.
- [5] J. Sung. Graphite - diamond transition under high pressure: A kinetics approach. *Journal of Materials Science*. 2000, 35(23): 6041-6054.

- [6] C. M. Sun, inventor, Diamond growth devices and methods. USA Patent US2008/0313968 A1.
- [7] F. Zhang, J. Shen, J.F. Sun, Y.Q. Zhu, G. Wang, G. McCartney. Conversion of carbon nanotubes to diamond by spark plasma sintering. *Carbon*. 2005, 43(6):1254-1258.
- [8] K. Vanmeensel, A. Laptev, J. Hennicke, J. Vleugels, O. Van der Biest. Modelling of the temperature distribution during field assisted sintering. *Acta Materialia*, 2005, 53, 4379-4388.
- [9] N.V. Novikov. New trends in high-pressure synthesis of diamond. *Diamond and Related Materials*. 1999, 8(8-9):1427-1432.
- [10] J. Shen, F. Zhang, J.F. Sun, Y.Q. Sun, D.G. McCartney. Spark plasma sintering assisted diamond formation from carbon nanotubes at very low pressure. *Nanotechnology*. 2006, 17(9):2187-2191.
- [11] S. J. Duclos, K. Brister, R.C. Haddon, A.R. Kortan, F.A. Thiel, Effects of pressure and stress on C60 fullerite to 20 GPa, *Nature*, 1991, 351: 380-382.
- [12] F. Mosshary, N.H. Chen, L.F. Silvera, C.A. Brown, H.C. Dorn, M.S.d. Veies, D.S. Bethune, Gap reduction and the collapse of solid C60 to a new phase of carbon under pressure. *Phys. Rev. Lett.* 1992, 69: 446-469.
- [13] V. Brazhkin, A. Lyapin. Hard Carbon Phases Prepared from Fullerite C60 under High Pressure. *New Diamond and Frontier Carbon Technology*. 2004, 14(5):259-278.
- [14] M. N. Regueiro, P. Monceau, J.L. Hodeau. Crushing C60 to diamond at room temperature. *Nature* 1992, 355: 237-239.
- [15] V. D. Blank, S.G. Buga, N.R. Serebryanaya, G.A. Dubitsky, S.N. Sulyanov, M.Y. Popov, V.N. Denisov, A.N. Ivlev, B. Mavrin. Phase transformations in solid C60 at high-pressure-high-temperature treatment and the structure of 3D polymerized fullerenes. *Phys Lett. A* 1996, 220(1-3): 149-157.
- [16] N. Dubrovinskaia, L. Dubrovinsky, F. Langenhorst, S. Jacobsen, C. Liebske. Nanocrystalline diamond synthesized from C60, *Diamond & Related Materials*, 2005, 14:16-22.
- [17] O. G. Epanchintsev, A. S. Zubchenko, A. E. Korneyev, V. A. Simonov, Highly-efficient shock-wave diamond synthesis from fullerenes, *J. Phys. Chem Solids*, 1997, 58(11):1785-1788.
- [18] A. Ya. Vul, V. M. Davidenko, S. V. Kidalov, S. S. Ordan'yan, and V. A. Yashin. Fullerenes catalyze the graphite-diamond phase transition, *Technical Physics Letters* 2001, 27(5): 384-386.

Chapter 4 SPS of titanium alloys for biomedical applications

4.1 Preparation and properties of TiMn Alloys for biomedical applications

4.1.1 Introduction

The exploration of high strength new Ti alloys without Al and V for medical implants has gained great attentions in the past years and is still ongoing. Manganese (Mn) is one of the essential trace elements in human body. The Mn is beneficial to the normal skeletal growth and development, and is important for enzymes in the body like the superoxide dismutase therefore involved in the elimination of radicals [1, 2]. Thus the Mn element should have less toxicity than the Al and V. The Mn was doped in magnesium alloy to improve its corrosion resistance and mechanical properties for biomedical applications [3]. The Mn was incorporated to tri-calcium phosphate bioceramics which resulted in a sufficient cell compatibility [4]. The preliminary results in our group showed that the Mn incorporation into the Ti alloys could enhance the cell adhesion properties [5].

The Ti8Mn alloys have been used in aerospace field and the TiMn₂ Laves phase has been used for hydrogen storage already [6, 7]. Nevertheless, few studies were on the exploration of TiMn alloys for biomedical applications. The TiMn alloys were generally fabricated by traditional casting or powder metallurgy techniques. Due to high melting point, high reactive activity at high temperature and contamination susceptibility, the Ti alloys are difficult to be produced from the liquid state. The production of Ti alloys via a powder metallurgy (PM) route is attractive due to the ability to produce net-shape components. Because of their stable surface oxide film (TiO₂), the Ti alloys are difficult to be sintered by traditional PM sintering techniques. Thus, the spark plasma sintering (SPS), a pulsed electric current field assisted sintering technique has been used to prepare the Ti alloys. In this study, the Mn element was incorporated into the Ti and TiMn alloys with 2, 5, 8, 12 wt. % Mn amounts were prepared by MA and SPS techniques. The preparation process, microstructures, mechanical properties, cytotoxicity and cell proliferation properties

of the TiMn alloys were investigated for exploration of their biomedical applications. Pure Ti, Mn metals and Ti6Al4V alloys were also fabricated at the same conditions for a comparison.

2.1.2 Experimental

The raw Ti and Mn powders were prepared by gas atomization method with 99.0% purities (Fluka Co., Germany). TiMn alloys were designed by varying the amount of Mn in the Ti with 2, 5, 8 and 12 (wt.%) compositions on the base of the binary phase diagram of TiMn alloys in Figure 4-1 showing the phases of the Ti-2, 5, 8, 12 (wt.%) Mn alloys. With Mn below 12 wt.%, the phase composition of the TiMn alloy is Ti₂Mn₂ phase. After weighting, each component of the designed composition was mechanical alloyed with a high energy planetary ball milling machine (Retsch PM400, Germany). Chromium hardened steel vials and balls were used as grinding media, with ball to powder ratio of 15:1. Wet-milling in hexane was performed for different hours at 250 rpm. Hexane was used as process control agent to prevent oxidation and excessive contamination from the grinding media.

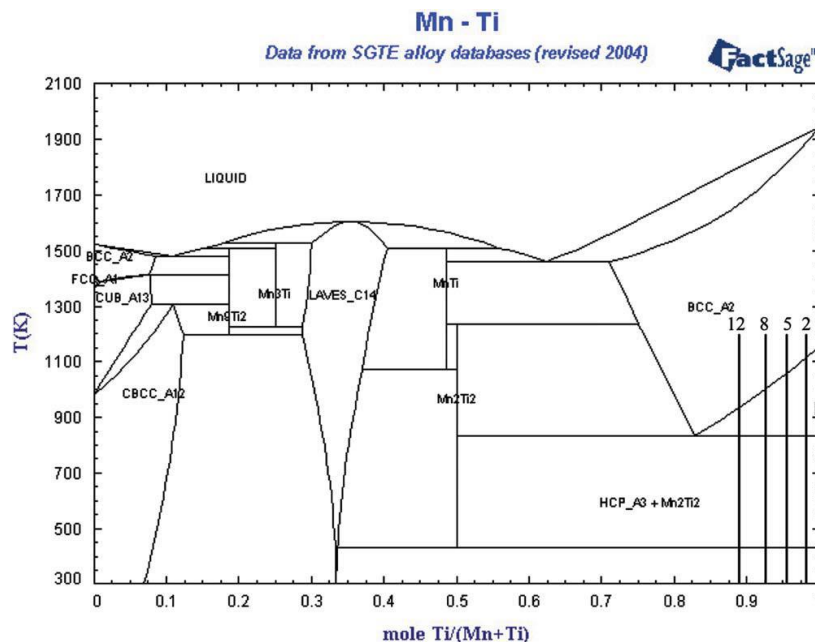


Figure 4-1 Binary phase diagram of TiMn alloy showing the phases of the Ti-2, 5, 8, 12 wt.% Mn alloys.

The sintering was accomplished using a Model HPD-25/1 FCT spark plasma sintering system (FCT systeme GmbH, Rauenstein, Germany) at a temperature of (500-800) °C for various times. The powders were loaded into graphite die to sinter disc-shaped pellets (20 mm diameter, thickness (5-6) mm). The SPS experiments were conducted in vacuum (<6 Pa) under uniaxial pressure 50 MPa. The heating rate was maintained at 100 °C/min.

X-ray diffraction (XRD, Bruker D8, Germany) was used to characterize the phase composition of the powders and sintered alloys. The phase transformation of the alloys was performed with a differential scanning calorimetry (DSC, Netzsch Pegasus 404C, Germany). Scanning electron microscopy (SEM, Zeiss Supra 25, Germany) was employed to analyze the microstructures of the powders and sintered alloys. The densities of the sintered alloys were determined by the Archimedes method using water immersion. Hardness and elastic modulus were measured by Universal CETR Nano+Micro tester with a model UNMT-1 multi-specimen test system. The measurements were measured with micro-head at various forces up to 5 N. 15 indents were done on one sample for an average value. The ductility of the TiMn alloys under compressive load was performed on an Instron 5566 testing machine at room temperature with a compression speed of 0.5 mm/min.

Before cell cultivation TiMn alloys were sterilized in 70 % ethanol for 15 min. The human osteoblastic cells MG-63 (osteosarcoma cell line, ATCC, LGC Promochem) were cultivated on TiMn alloys in 12-well plates (Greiner Bio-One, Germany) in Dulbecco's modified Eagle medium (DMEM, Invitrogen, USA) with 10 % fetal calf serum (FCS, PAA, Austria), 4500 mg/l glucose (high glucose), GlutaMAX, pyruvate, 1% gentamicin (Ratiopharm, Germany), 0.02 % plasmocin (Invivogen, USA) at 37 °C and in a 5 % CO₂ atmosphere. The tissue culture polystyrene (TCPS) was used as an additional control.

The inhibitory influence of the TiMn alloys was studied by measuring osteoblast MG-63 cell's metabolism. The CellTiter 96® Aqueous One Solution Cell Proliferation Assay (Promega) was used. The principle of the test is an enzymatic cleavage of the methyltetrazolium salt (3-(4,5-dimethylthiazol-2-yl)-5 -(3-carboxy

-methoxyphenyl)) (MTS) by active cells into violet Formosan product. The amount of Formosan product is directly proportional to the number of living cells. 100 μ l of the MTS solution were added to each well and incubated for 2 h at 37 °C and in a 5 % CO₂ atmosphere. The spectrophotometric absorption was analyzed in a 96-well plate by an ELISA reader (Anthos 2010, Anthos Labtec Instruments) at 490 nm.

For flow cytometry, cells were suspended using 0.05 % trypsin/0.02 % EDTA solution (5 min at 37 °C). Then, cells were washed in phosphate buffered saline (PBS), fixed with 70 % ethanol over night at -20 °C, and intensively washed again. After treatment with 1 % RNase (Sigma, Germany) for 20 min at 37 °C, the DNA of the cells was labelled with propidium iodide (50 μ g/ml, Sigma, Germany) over night at 4 °C. Cells were measured in a FACSCalibur™ flow cytometer (BD Biosciences) equipped with a 488 nm argon-ion laser and a Macintosh Power PC (G4). In general, 25,000 events were acquired using CellQuest Pro 4.0.1. Percentage of proliferating cells was then calculated in percent using ModFIT version 3.0 (BD Biosciences).

Statistical analysis was performed with SPSS 14.0 for Windows (SPSS Inc., Chicago, IL). The differences between the concentrations were evaluated using Students t-test for independent samples because variables present normal distribution (Kolmogorov-Smirnov test). Data were expressed as mean and standard error of the mean. A probability value of $p < 0.05$ was considered as significant.

4.1.3 Results

The TiMn alloy powders with 2, 5, 8 and 12 (wt.%) Mn compositions were mixed and mechanical alloyed for various hours in a high energy ball milling machine. Figure 4-2 shows the XRD patterns of the pure Ti, Mn powders, and TiMn alloy powders after 60 hours mechanical alloying. Pure Ti and Mn peaks completely disappeared and TiMn phases were formed after 60 hours mechanical alloying. The pure Ti powders are α -Ti phase (ICDD No. 65-3362) with hexagonal structure and the pure Mn powders are α -Mn phase (ICDD No. 32-0637) with cubic structure. The synthetic TiMn powders are α -TiMn phase (ICDD No. 07-0132) with tetragonal structure. There are no obvious changes in the phase compositions with increasing of Mn amount up to 12 wt% in Ti.

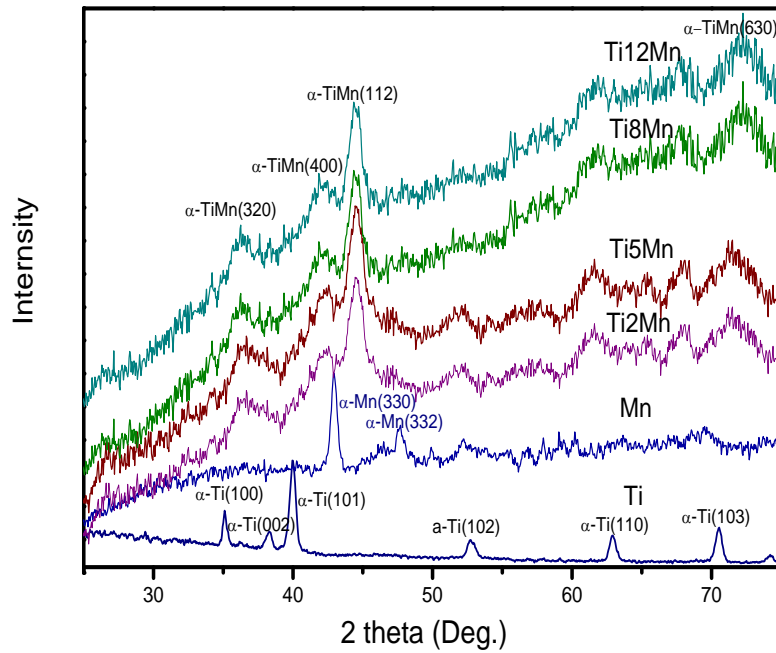


Figure 4-2 XRD patterns of the Ti, Mn powders, and TiMn alloy powders prepared by mechanical alloying showing the formation of α -TiMn phases.

Figure 4-3 shows the SEM micrograph and EDX of the Ti8Mn powders prepared by mechanical alloying. The powders are agglomerates with mean particle sizes of (4-5) μm in diameter with a narrow size distribution (Figure 4-3 a). The EDX spectra show that the Ti, Mn peaks belong to the TiMn powder, the C and O peaks are from adsorption of air, and the small Fe peak is the contamination from the steel balls and vials during the mechanical alloying.

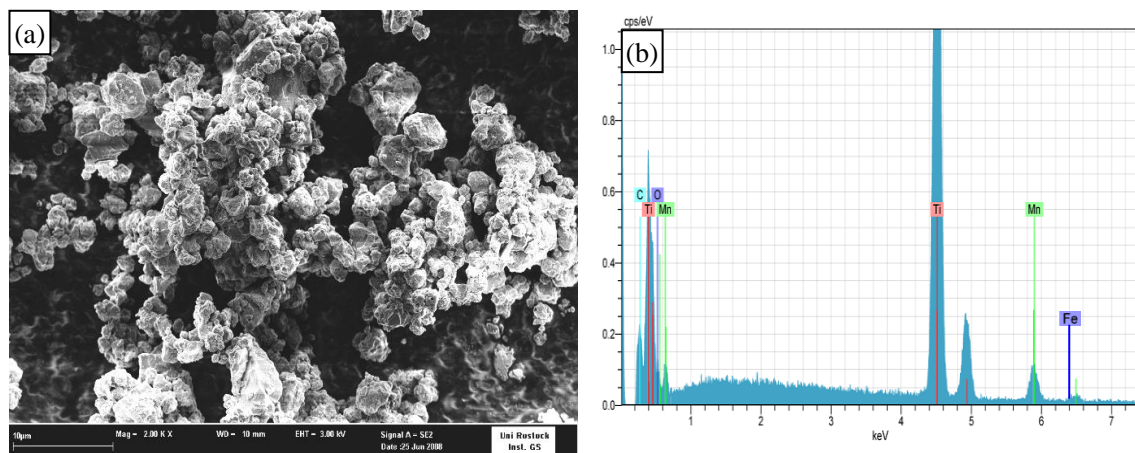


Figure 4-3 SEM micrograph (a) and EDX (b) of the Ti8Mn powder prepared by mechanical alloying showing the morphology and composition of the powder.

The phase transformation behaviors of the TiMn alloy powders were analyzed by using differential scanning calorimetry. Figure 4-4 shows the transformation temperatures of the TiMn alloys in comparison with the pure Ti. In the case of pure Ti, the transformation temperature from α to β phase occurs at about 840 °C. The transformation temperature in Ti2Mn is 735 °C while that of in Ti5Mn alloys is 700 °C. The transformation temperatures are 665 °C and 660 °C in Ti8Mn and Ti12Mn alloys, respectively. As the amount of Mn increased, the transformation temperature decreased to a relative lower temperature. The addition of Mn in Ti has depressed their transformation temperature from α to β phase.

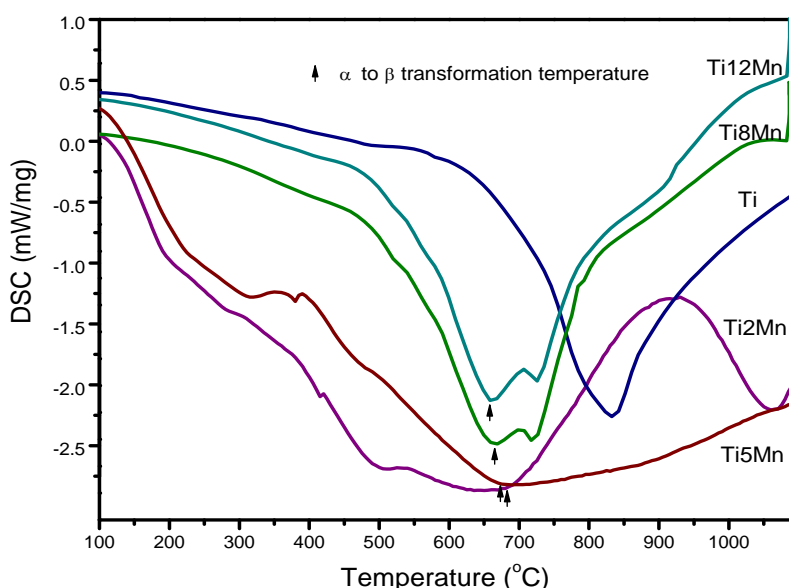


Figure 4-4 Phase transformation behaviours of the TiMn alloys measured by DSC showing the decrease of α to β transformation temperature with increase of Mn amounts in Ti.

After characterization, the alloy powders were subjected to the SPS furnace. Figure 4-5 shows the relative density of spark plasma sintered Ti at different temperatures and TiMn alloys with various Mn amounts. With temperature increase from 550 °C to 800 °C, the relative density of the Ti metal increased from 68% to 99% (Figure 5a). The relative density of TiMn alloys increased as the Mn contents increased at 650 °C and 700 °C, respectively (Figure 4-5b). The Ti8Mn alloys showed

99% relative density at 700 °C for 5 min. The SPS decreased the sintering temperature of Ti and TiMn alloys. The Mn addition increased the relative density of Ti metal during SPS.

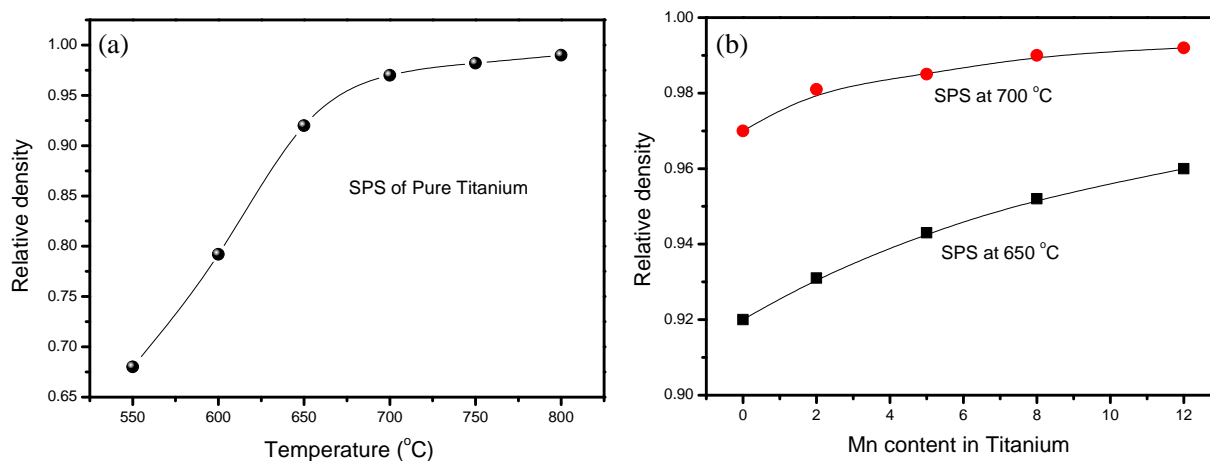


Figure 4-5 Relative density of spark plasma sintered Ti at different temperatures (a) and TiMn alloys with various Mn amounts (b) showing the variation of Ti relative density with the SPS temperature and the enhancement of relative density with increase of Mn amounts in Ti.

Figure 4-6 shows XRD patterns of the spark plasma sintered Ti, Mn metals and TiMn alloys. The Ti and Mn still retain α -Ti and α -Mn phases because of the lower sintering temperature in SPS (700 °C). However, all the TiMn alloys are mostly β -TiMn phase (ICDD No. 11-0514) with cubic structure. There is still a small amount of α -TiMn phase in the alloy; therefore, the TiMn alloy is a $\alpha+\beta$ phase alloy. The synthesized alloy has $\alpha+\beta$ microstructures which is similar to that of Ti6Al4V alloy. In Figure 4-7, the SEM micrographs of the fracture surfaces of the spark plasma sintered Ti8Mn and Ti12Mn alloys are demonstrated. There are few micropores on the fracture surface of the TiMn alloys. The grain size of the Ti8Mn alloys is about 500 nm in ultrafine microstructure and the fracture mode of the alloy is primary intergranular cracking (Figure 4-7a). There are some large size grains in the Ti12Mn alloy which may due to the sintering of powder agglomerates (Figure 4-7b).

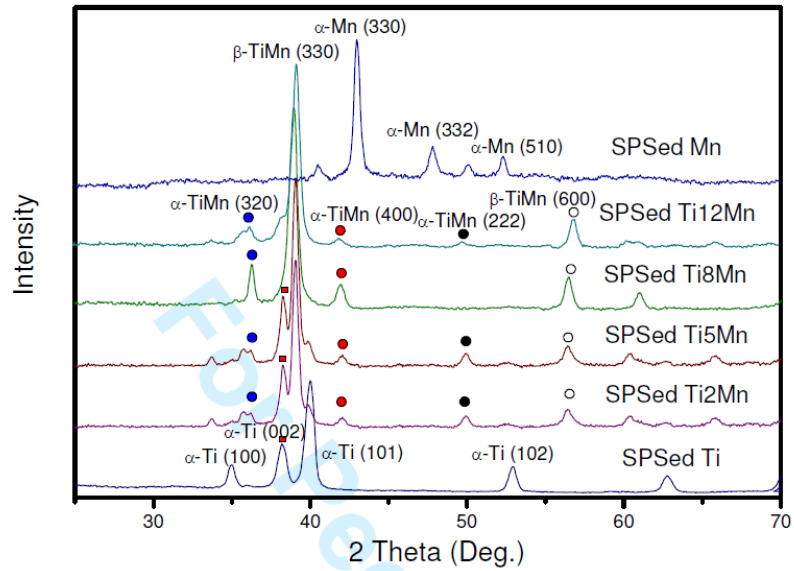


Figure 4-6 XRD patterns of the spark plasma sintered Ti, Mn and TiMn alloys showing the TiMn alloys are $\alpha+\beta$ phase alloy.

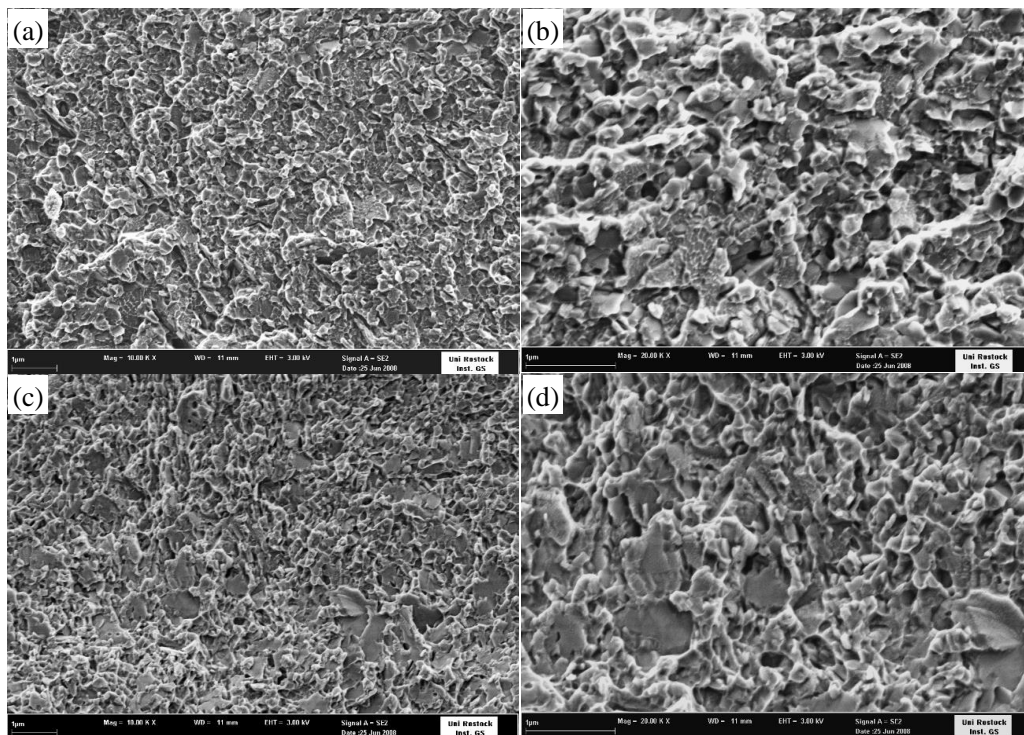


Figure 4-7 SEM micrographs of the fracture surfaces of Ti8Mn (a, b) and Ti12Mn (c, d) alloys prepared by SPS showing the superfine microstructures (Bar 1 μm , magnification 10 kx, 20 kx).

Figure 4-8 shows the mechanical properties of the TiMn alloys. The 3D image indicates the depth and dimension of the indent by the microindentation technique (Figure 4-8a). The depth of the indent is 20 μm around; the dimension is about 110 μm in width and length. The hardness results show that the hardness value tended to rise with increasing Mn contents (Figure 4-8b). The hardness values of all TiMn alloys are significantly higher than that of pure Ti. The pure Ti shows a hardness of (1.60 \pm 0.20) GPa; Ti2Mn, (2.40 \pm 0.25), Ti5Mn, (3.65 \pm 0.30); Ti8Mn, (4.98 \pm 0.32); Ti12Mn, (5.28 \pm 0.36) GPa. The hardness of Ti12Mn alloy is comparable to that of the pure Mn (5.44 \pm 0.34) GPa. From statistical analysis, the hardness values of the TiMn alloys are significantly higher than that of pure Ti. The elastic modulus results show that they are also increased as shown in Figure 3-8(c). The pure Ti is (105.2 \pm 6.0) GPa, Ti2Mn (83.3 \pm 3.0) GPa, Ti5Mn (95.0 \pm 5.0) GPa, Ti8Mn (106 \pm 4.0) GPa, and Ti12Mn (122 \pm 6.0) GPa, Mn (68.72 \pm 4.3) GPa. The increment magnitude of the elastic modulus is lower than that of the hardness. The ductility results of the TiMn alloys are shown in Figure 3-8 (d). The pure Ti exhibits (25.0 \pm 2.0)% ductility, Ti2Mn (21.3 \pm 2.4)%, Ti5Mn (18.2 \pm 2.2)%, Ti8Mn (15.0 \pm 1.3)% and Ti12Mn (11.7 \pm 2.0)%. The ductility decreased with increase of Mn amounts in Ti. The mechanical properties of the Ti6Al4V alloy were also measured with the same methods. It shows hardness: (4.3 \pm 0.3) GPa, elastic modulus: (122 \pm 4.0) GPa, and ductility: (14.0 \pm 1.5)% which are almost identical to the reported values²¹. The Ti2Mn, Ti5Mn and Ti8Mn alloy possess lower elastic modulus and higher ductility than those of the Ti6Al4V alloy.

Figure 4-9 represent the cytotoxicity and cell proliferation properties of the TiMn alloys. The tissue culture polystyrene (TCPS) was used as a control material. The MG-63 osteoblast cell viability (%) of the pure Ti and TiMn alloys by MTS assay is shown in Figure 9(a). The cytotoxicity increases with increasing amount of the Mn contents in the Ti alloy. Cell's viability on pure Mn and Ti12Mn was about 50 % and 72 %, respectively ($p < 0.05$). However, cells on the Ti5Mn and Ti8Mn alloys were also influenced concerning viability without statistical difference ($p > 0.05$), but it reached comparative high values (89%, 86%, respectively) comparable with that of pure Ti (93%).

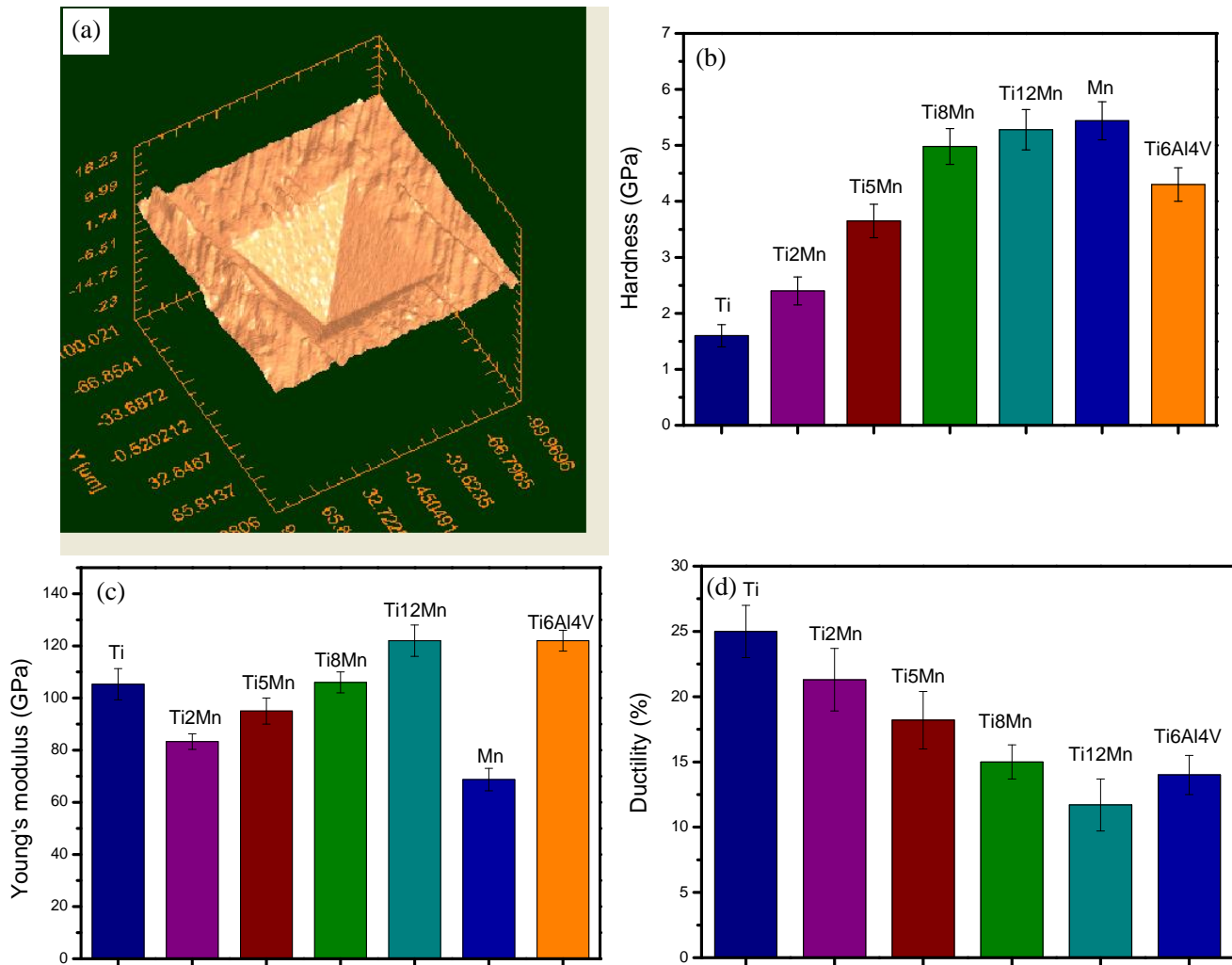


Figure 4-8 3D (a) image of an indent obtained after microindentation test on the TiMn alloys, hardness (b) and elastic modulus (c) of the Ti, Mn and TiMn alloys by the microindentation, as well as ductility (d) of the TiMn alloys showing the increase of hardness and elastic modulus but decrease of ductility with increase of Mn amounts in Ti.

The proliferation of MG-63 osteoblasts on the TiMn alloys using flow cytometric cell proliferation analysis is demonstrated in Figure 4-9 (b). The percentage of cells on the pure Ti and TiMn alloys decrease in contrast to the TCPS control (53.67 %). Proliferating cells on TiMn alloys (Ti2Mn 41.17%, Ti5Mn 40.50%, Ti8Mn 41.57% and Ti12Mn 39.99%) are decreased compared with that of pure Ti (48.93%), but are not significant with $p > 0.05$ and all acceptable for biomedical applications. However, the percentage of proliferating cells grown on pure Mn is significantly reduced to

35.87 % ($p < 0.05$). The student t-test, that is an established statistical method, shows that the proliferation of MG-63 osteoblast cells on TiMn alloys is not remarkably inhibited, and only Mn is significantly decreased ($p < 0.05$). The decrease in pure Mn is about 27% from the Ti value. It is indicated that only very high amount of Mn inhibits cell proliferation. Combining the cytotoxicity and cell proliferation results, it can say that the amount of Mn below 8 wt.% has a negligible effect on the cytotoxicity and cell proliferation of all Ti alloys tested.

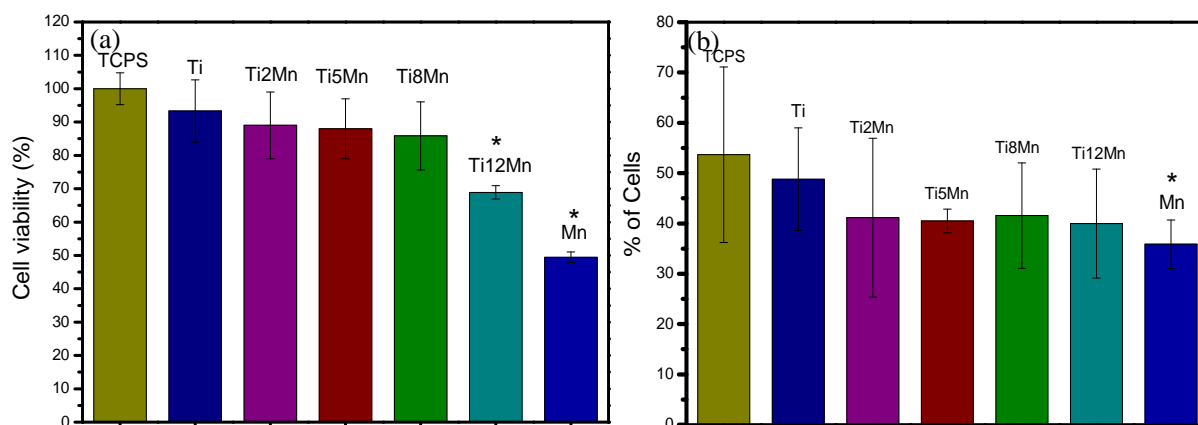


Figure 4-9 Cytotoxicity (a) and cell proliferation (b) of MG-63 osteoblasts on the Ti and TiMn alloys showing the comparable cell viability of Ti2Mn, Ti5Mn and Ti8Mn alloys with that of pure Ti, and the proliferation of osteoblasts was not inhibited on TiMn alloys but only significantly on pure Mn. Mean \pm SD, $n=5$, Student t-test * $p < 0.05$.

4.1.3 Discussions

The TiMn alloy powders were prepared by MA for 60 hours. The MA is a high energy ball milling process which involved repeated welding, fracturing, rewelding operations leading to microstructure refinement and alloy formation. MA also has the advantage of not involving melting; allowing alloying of elements with significantly different melting points, and it is a process scalable to commercial sizes [8]. Many Ti based alloy powders have been produced by MA method. The melting point of Ti is 1668 °C and that of Mn is 1246 °C. α -TiMn alloy powders were prepared at a solid state by MA with 422 °C difference of melting points. The contamination during MA is a main problem of this technique. In this study, hexane was used as control agent to prevent oxidation and excessive contamination of the TiMn powders from the

grinding balls and vial. Therefore, only a small Fe contamination peak is detected in the EDX spectra of the TiMn powder (Figure 4-3b).

High density Ti metal was prepared by using SPS at 750 °C for 5 min, and high density TiMn alloys were fabricated at 700 °C for 5 min (Figure 4-5). By using the traditional sintering techniques, high temperatures of (1100-1300) °C were required to get a high density Ti and its alloy [9]. The SPS has decreased the sintering temperature of Ti and TiMn alloys. The Mn has increased the relative density of Ti alloy, which is due to the lower β transformation temperatures in TiMn alloys. The low sintering temperature is ascribed to the ionization of particles by local sparks during SPS. A pulsed current generated plasmas in SPS that lead to a surface activation of the powder particles, which melted the titanium oxide films and formed neck junctions among powder particles at a lower temperature [10,11]. A simultaneous pressure impact causes a plastic flow of the powders, which enables the creation of the dense Ti alloys with ultrafine microstructures at high heating rates, lower temperature and short soaking time. Because of the high reactivity of Ti metal above 1000 °C, the sintering of Ti avoiding chemical reaction between Ti and die is difficult to be performed. The low sintering temperature used in the SPS allows the use of graphite dies in this study.

The V, Mo, Nb, Fe, Cr, etc are all β stabilizers and additions of these elements depress the β transitional temperature. The results in Figure 4-4 show that the Mn has decreased the transformation temperature from the α to the β phase. The effect of manganese on the α to β transition temperature is significant. With only 2wt.% Mn addition in the Ti, the transition temperature reduced from 840 °C to 735 °C. It decreased ranging from 735 °C (Ti2Mn) to 660 °C (Ti12Mn) with increase of Mn amount in Ti. It is confirmed that the Mn is a β stabilizing addition element for Ti metal. Additionally, the Mn could increase the hardness and elastic modulus of the Ti alloy (Figure 4-8b, c). The TiMn alloys provide higher hardness and elastic modulus than those of the pure Ti. The Ti5Mn and Ti8Mn alloys possess comparable hardness but lower elastic modulus comparing with Ti6Al4V alloy. The increment of the hardness and elastic modulus of TiMn alloys is ascribed to the formation $\alpha+\beta$ TiMn

phases which are intermetallic phases with excellent mechanical properties. The Ti6Al4V alloy was chosen for orthopedic implant for several reasons. Excellent ductility is one of the most important reasons for its wide use in biomedical industry. The ductility of Ti6Al4V alloy is measured to be 14% at room temperature. The ductility of the TiMn alloy decreased from 21.3% (Ti2Mn) to 11.7% (Ti12Mn) with increase of Mn amount (Figure 8d). However, the Ti2Mn (21.3%), Ti5Mn (18.2%), Ti8Mn (15.0%) alloys have higher ductility than that of the Ti6Al4V. Compared with the Ti6Al4V, the Ti2Mn alloy presents lower hardness (2.4 GPa), but better elastic modulus (83.3 GPa) and ductility (21.3%), the Ti5Mn alloy exhibits comparable hardness (3.65 GPa) but better elastic modulus (95.0 GPa) and ductility (18.2%), the Ti8Mn alloy shows better hardness (4.98 GPa) and elastic modulus (106 GPa) with a comparable ductility (15.0%). The Ti2Mn, Ti5Mn and Ti8Mn alloy could be used as biomedical implants in light of their mechanical properties.

Some commercial Ti alloys also contain Mn as an alloying component. The Mn was doped in magnesium alloy with 1.2 wt. % and found the Mn has no toxicity and can improve the corrosion resistance and mechanical properties of Mg [3]. The Mn was doped to tri-calcium phosphate bioceramics and showed good cell compatibility [4]. Recently, Fe-35Mn alloy was prepared and showed higher strength and ductility, degradable properties, which make it suitable for biodegradable stent applications [12]. The values concerning cytotoxicity and cell proliferation of the TiMn alloys demonstrate a dependency on the Mn concentration. A lower Mn concentration (<8 wt.%) in Ti has a low effect on the cytotoxicity and cell proliferation properties ($p > 0.05$). In general, the Ti2Mn, Ti5Mn and Ti8Mn were comparable in viability and cell proliferation properties with pure Ti. The Ti6Al4V alloy was firstly used in aerospace industry, and then applied in biomedical field as bone and dental implants. Until now, the Ti8Mn alloy as one of the typical $\alpha + \beta$ Ti alloys has been extensively used in aerospace industry because of its excellent mechanical properties [13]. Our research here suggest that the application of the Ti8Mn alloy could be extended to biomedical field. As well as the Ti2Mn and Ti5Mn alloys, they exhibit higher ductility and lower elastic modulus than those of Ti6Al4V. The lower elastic modulus

of metals for joint prosthesis could decrease the stress-shielding effect in bone-implant coupling [14]. The Ti2Mn, Ti5Mn and Ti8Mn alloys all exhibit acceptable cytotoxicity and cell proliferation of the human osteoblasts. Consequently, the Ti2Mn, Ti5Mn and Ti8Mn alloys all have a potential for the use in the biomedical field as new bone substitutes and dental implants.

2.1.5 Summary

The $\alpha+\beta$ type TiMn alloys with high relative density and ultrafine microstructures were prepared by using mechanical alloying for 60 hours and spark plasma sintering at 700 °C for 5 min. The Mn reduced the α to β transformation temperature of Ti and was confirmed as a β stabilizer element. The hardness increased significantly ranging from 2.4 GPa (Ti2Mn) to 5.28 GPa (Ti12Mn), the elastic modulus as well ranging from 83.3 GPa (Ti2Mn) to 122 GPa (Ti12Mn) and the ductility decreased ranging from 21.3% (Ti2Mn) to 11.7% (Ti12Mn) with increasing manganese content in the Ti. Concentrations of Mn below 8 wt.% in titanium reveal negligible effects on the metabolic activity and the cell proliferation of human osteoblasts. Therefore, the Mn could be used in lower concentrations as an alloying element for biomedical titanium.

4.2 Modification of Ti6Al4V alloys by rapid cooling SPS

4.2.1 Introduction

Titanium alloys such as Ti6Al4V offer high strength-to-weight ratio, high toughness, super-corrosion resistance, and bio-compatibility are increasingly used in aerospace and biomedical fields [15,16]. The Ti6Al4V alloys have long been a main medical titanium alloy and are the favourable implant materials for uncemented knee and hip arthroplasties [17]. Additionally, the Ti6Al4V alloys are also preferred for intramedullary rods, spinal clamps, self-drilling bone screws and other implants [18]. One of the main problems of this alloy in biomedical applications is the insufficient ductility which lead to the difficulty in their contouring as required for pelvic and mandibular plates [19].

Sinter hardening has become a process of high importance in powder metallurgy (PM) in the past years because of the time- and cost- effective manufacturing which it

permits [20]. It is a hardening method applicable only for PM parts in which the parts are sintered and quenched directly after the sintering step saving energy and costs connected to conventional hardening where the parts have to be reheated to hardening temperature [21,22]. Furthermore, sinter hardening is performed by gas quenching instead of oil quenching being beneficial in terms of dimensional stability and cleanliness of the specimen. Due to poor thermal transfer characteristics (lower cooling rate) of gases under normal conditions, they have to be optimized by proper adjustment of gas pressure and flow speed. In principle, gas quenching can be performed in two ways [23, 24], namely: at low or atmosphere pressure with high gas velocity or at high pressure with limited gas velocities. In the present work, the $\alpha+\beta$ Ti6Al4V alloy was prepared by the SPS technique integrated with a novel gas quenching system. The heat transfer coefficient and temperature distribution of the Ti6Al4V alloy during quenching was numerical simulated by a finite element method. The effects of the cooling rate on the mechanical properties and microstructure of the Ti6Al4V alloy were investigated.

2.2.2 Experimental

The Ti6Al4V powder with a particle size about 20 microns is obtained from TLS Technik GmbH & Co, Germany. The element contents have aluminum 5.9%, vanadium 3.9%, carbon 0.01%, oxygen 0.12%, iron 0.19%, nitrogen 0.01% and hydrogen 0.004% (wt.%).

The SPS experiments were conducted using a Model HP D-125 FCT spark plasma sintering system (FCT systeme GmbH, Rauenstein, Germany) installed at the Tycho Sinter Lab in the University of Rostock. Fig. 4-1(a, b) shows the schematic diagram and image of the gas quenching system in the SPS. In the system, six nozzles in one group and eight groups up to 48 nozzles arranged rotational symmetric around the sintered component. The gas is distributed evenly on all nozzles. The gas nozzle field is positioned inside the SPS chamber and quenches the sintered component together with the graphite tool directly after sintering without any movement of the component. The core temperature is measured by a central pyrometer with a focus

point at the bottom of the central borehole of the graphite up-punch (Label 6). The Ti6Al4V powders were firstly pressed into a $\text{Ø}40$ mm graphite die, and sintered at $850\text{ }^{\circ}\text{C}$ and 50 MPa in vacuum. A heating rate of 100 K/min was adopted, and the sintering process lasted typically 6 min. The applied direct current for SPS was 1000-2000 A with pulse duration of 10 ms and an interval of 5 ms. During the cooling, the SPS furnace was flooded with argon gas to 40 mbar at rate of 10 l/min keeping the sintering temperature. Additionally, it was quenched from $850\text{ }^{\circ}\text{C}$ with room temperature nitrogen gas at very high flowing rate of 8000 l/min out of the nozzles. Afterwards the nitrogen gas was released out the chamber to an internal gas pressure of 1-2 mbar. The various cooling rates are achieved by changing the thickness of the graphite dies. Finally, the sample dimensions are 40 mm in diameter and 10-12 mm in height.

The heat transfer coefficients are of interest for the characterization of the nozzle field's cooling effect. These were determined by means of cooling curve measurement and inverse thermal simulation by finite element software MSC.MARC 2010.1.0. In the quenching experiments, the temperature of four sites of the system is measured with pyrometer and thermal couples. As shown in Fig. 4-10 (a), the center of the sample (A) is measured by the pyrometer; the surface of the sample (B) is by the thermal couple T_1 , the temperature in the middle of the graphite form (C) is by T_2 , the temperature of the lower graphite cone is by T_3 . The numerical simulations used a rotation-symmetric finite-element-model considering the axial symmetry. Fig. 4-11 shows the rotation-symmetric FE-Model and boundary conditions for thermal simulation of the Ti6Al4V sample and graphite die. The discretization of the model has 1100 elements and 1176 nodes. The red part is the Ti alloy (radius dimension), the blue part below the sample is the graphite stamp and right of the sample is the graphite form. The length of the bars of gas nozzle field is 110 mm and larger than the sample dimension (40 mm). The bottom surfaces of graphite die and stamp were also supplied with quenching gas. The thermal properties of graphite form and stamps are chosen according to the information from the manufacturer (Density: 1.8 g/cm^3 ,

Thermal conductivity: 80 W/m °C, Coefficient of thermal expansion: $6.0 \times 10^{-6}/\text{°C}$). The thermal properties of the Ti6Al4V sample are from a handbook [25]. A constant heat-flow from the stamps into the sintering machine of 35 W was assumed for all simulations based on the SPS running raw data. An initial value for the heat transfer coefficient was based on the results of former quenching tests in external gas nozzle fields [26]. This coefficient was adjusted iteratively until the calculated cooling curves corresponded to the measured ones.

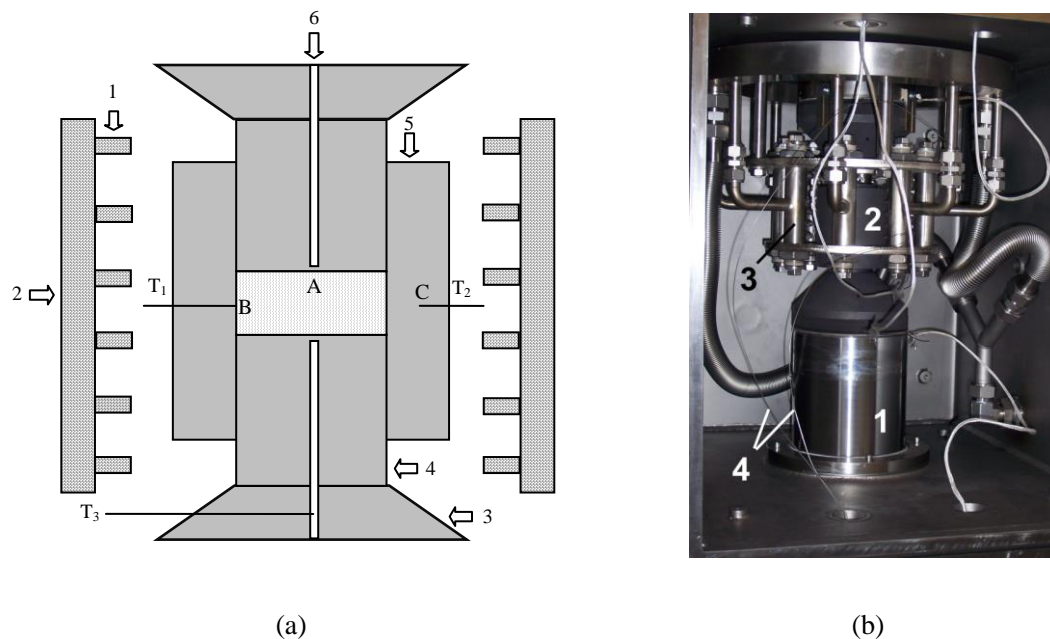


Figure 4-10. Schematic diagram (a) of the apparatus for spark plasma sintering with gas quenching system (1, gas nozzles; 2, gas tube; 3, graphite cone; 4, graphite punch; 5, graphite form; 6, Pyrometer hole for temperature measurement of the sample center A; T_1 , T_2 and T_3 , Thermal couples for temperature measurement of the sample surface B, graphite form C, and graphite cone, respectively), and image (b) of SPS vacuum chamber (1, machine stamp, 2, sample block, 3, gas nozzle field, 4, thermocouples).

After SPS, the density of the sintered alloys was determined by the Archimedes method using water immersion. Then, the samples were machined into small cylinders with 8 mm in diameter and (10-12) mm in height. Cross sections were polished and part of them etched by Weck's reagent (2 g ammonium acid, 100 ml

distilled water, 50 ml alcohol) for 20 seconds and subjected to optical microscopy to observe metallographic morphologies. The hardness of the polished samples was measured with a SHIMADAZU Micro Hardness tester HMV at HV1 (9.81 N). Their compressive strength and ductility was performed according to standard DIN 50106 on an Instron 8502 testing machine at room temperature with a compression speed of 0.5 mm/min. The sample surfaces have been prepared according to standard DIN 50106, top and bottom parallel grinded, circumference polished. In the compressive tests, five samples for one group were tested to get statistic results. The fracture surface of the compressed samples was analyzed using scanning electron microscope (SEM, Zeiss Supra 25, Germany) at 20 keV. The phase analysis of the Ti alloys was performed using synchrotron radiation high energy X-ray diffraction at Beamline P02.2 (DESY/ PETRA III) with a wavelength of 0.29118 Å (42.58 keV).

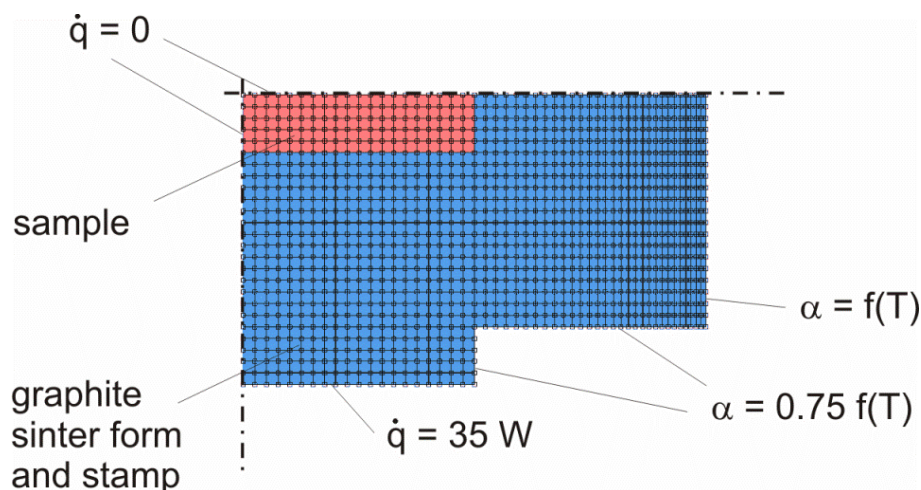


Figure 4-11. Rotation-symmetric FE-Model and boundary conditions for thermal simulation of the Ti6Al4V sample and graphite die: (red) sample, (blue) graphite die.

4.2.3 Results

Various cooling rates are achieved by changing the thickness of the graphite forms. Fig. 4-12 shows the temperature-time cooling curve of the spark plasma sintered Ti6Al4V alloys with various cooling rates. Below 400 °C, the pyrometer cannot measure the temperature of the sample. From the cooling curves, the average cooling rates of samples 1.6 K/s, 4.8 K/s, 5.6 K/s and 6.9 K/s with an uncertainty of 0.1 K/s

were derived. The cooling rate 1.6 K/s was achieved with a 20 mm thick graphite die with a natural cooling, 4.8 K/s with the 20 mm die with gas quenching, and 5.6 K/s with the 10 mm die, also with gas quenching. The rate of 6.9 K/s was achieved in two steps. Hereby, the powder sample was firstly sintered in the SPS at 500 °C for 5 min at 50 MPa in die to get a 70-80% relative density, and then heated to a sintering temperature of 850 °C to get full density without die and directly gas quenched to the specimen, later on. Finally, various cooling rates are achieved by this way.

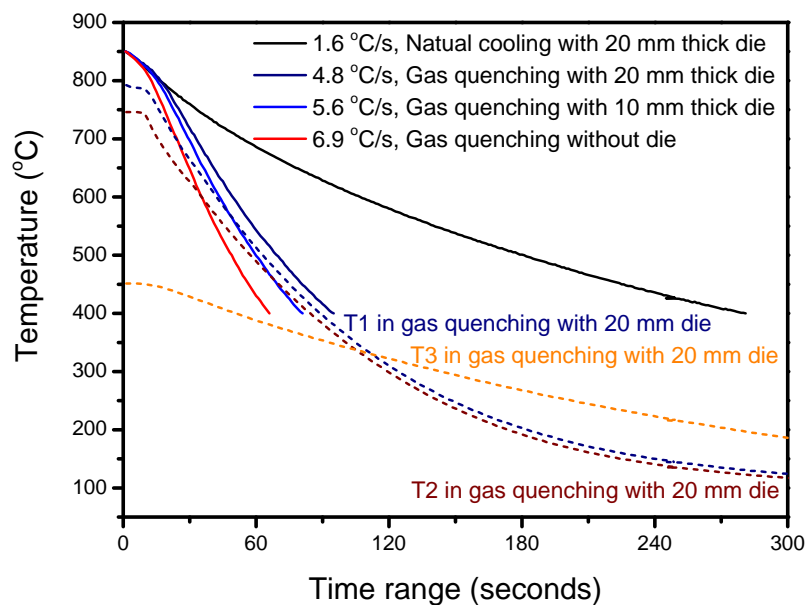


Figure 4-12. The cooling curves of the Ti6Al4V alloy as a function of time: (Solid lines) Pyrometer temperature values with various quenching rates and (Dash lines) thermal couple values (T1, T2, T3) in gas quenching with 20 mm thick die.

The dash lines show the temperature values by thermal couples during gas quenching with 20 mm die. At the sintering temperature, the temperature of the graphite form (T_2) is lower than that of the sample surface (T_1) and the T_1 is lower than the temperature in the center of the samples by the pyrometer. The temperature gradient existed during the sintering process as well as in the cooling process. The gas quenching started from outside surface of the graphite form. The temperature of the graphite cone (T_3) is reduced from 450 °C to about 200 °C at 300 s of gas quenching.

But the T_1 and T_2 have decreased to below $80\text{ }^\circ\text{C}$ already at 300 s. It indicates that the gas quenching is only effective to cool the graphite form and sample in the gas nozzle fields.

Fig. 4-13 shows the numerically determined heat transfer coefficients of gas quenching and natural cooling of the Ti6Al4V samples. The heat transfer coefficients reduced with the decreasing temperatures for the samples processed with natural cooling (20 mm thick die) and gas quenching with (20 mm thick die) and without dies. From $800\text{ }^\circ\text{C}$ to $400\text{ }^\circ\text{C}$, the coefficient values are higher than those below $400\text{ }^\circ\text{C}$. It indicates that the heat transfer and dissipation are faster at higher temperatures above $400\text{ }^\circ\text{C}$. The natural cooling sample exhibits heat transfer coefficient of $80\text{ W}/(\text{m}^2\text{K})$ at $800\text{ }^\circ\text{C}$ and gradually reduced to $50\text{ W}/(\text{m}^2\text{K})$ at room temperature. The gas quenched sample with die shows heat transfer coefficient of about $400\text{ W}/(\text{m}^2\text{K})$ at $800\text{ }^\circ\text{C}$ and dropped to about $300\text{ W}/(\text{m}^2\text{K})$ at room temperature. The quenching without die presents heat transfer coefficient of about $810\text{ W}/(\text{m}^2\text{K})$ at $800\text{ }^\circ\text{C}$ and $400\text{ W}/(\text{m}^2\text{K})$ at room temperature. The quenching intensity without die is about 2 times higher than that with die.

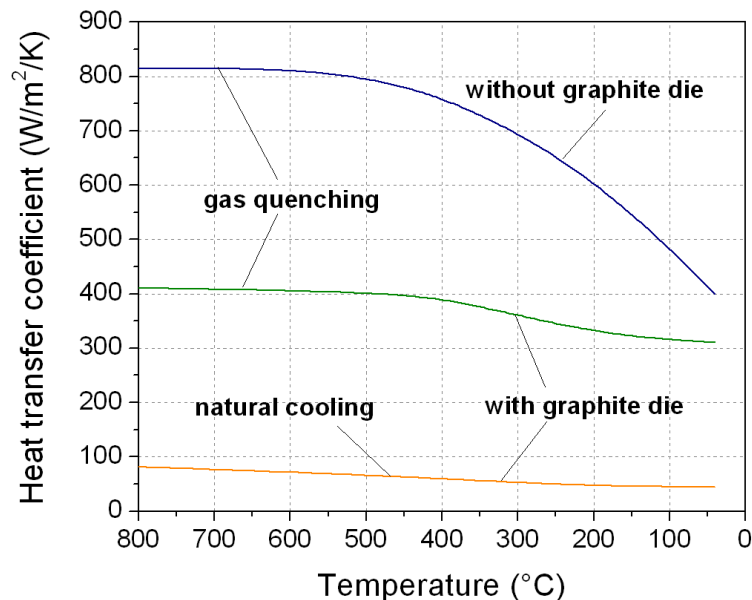


Figure 4-13 The determined heat transfer coefficients of natural cooling ($1.6\text{ }^\circ\text{C}/\text{s}$) and gas quenching of the Ti6Al4V alloys with 20 mm thick die ($4.8\text{ }^\circ\text{C}/\text{s}$) and without die ($6.9\text{ }^\circ\text{C}/\text{s}$).

However, the gas quenching with die is also effective to increase the heat transfer coefficients up to (5-7) times higher than the natural cooling. The heat transfer coefficient is defined as the ratio of heat lost due to the flow to the product of area and temperature difference. Higher heat transfer coefficients can cool the sample faster. Hence, the Ti alloys can be cooled rapidly with the gas quenching due to the higher heat transfer coefficients. The sintering and quenching heat-treatment have been completed by one step SPS process without a separate heat treatment operation.

Fig. 4-14 shows the simulation results of the temperature distribution in the Ti6Al4V sample and graphite die at 60 s of cooling time. The wall thickness of the graphite form used for the simulation is 20 mm. The position A is the center and B is the surface of the sample, B to D is the graphite form. The top of the Fig. contains the temperature distribution in case of a natural cooling of the Ti6Al4V inside the graphite form. At 60 s of cooling time, the center of the sample is 704 °C, the surface of the sample is 692 °C, and the outside surface of the graphite form is 682 °C. In natural cooling, the temperature gradient of the sample at 60 s is 12 °C and the graphite form is 10 °C. By a comparison, the center of the sample after gas quenching for 60 s is 502 °C, the surface of the sample is 458 °C, and the outside surface of the graphite form is 432 °C. In the gas quenching, the temperature dropped very fast, the temperature gradient of the sample is 44 °C and the graphite form is 26 °C. Therefore, a lower temperature level and a higher temperature gradient are observed in the simulation results. The temperature distribution reflects the different thermal behavior of the Ti6Al4V and the graphite. The heat of the Ti alloy is transferred considerably through the outside surface of the graphite form being cooled by gas nozzle field. Large proportions of heat in the Ti alloy have been dissipated by the gas quenching. It was cooled from outside surface to the center of the sample. The temperature gradients of the Ti alloy and the graphite form have been increased by the gas quenching using high velocity nitrogen, but the gradients are not large.

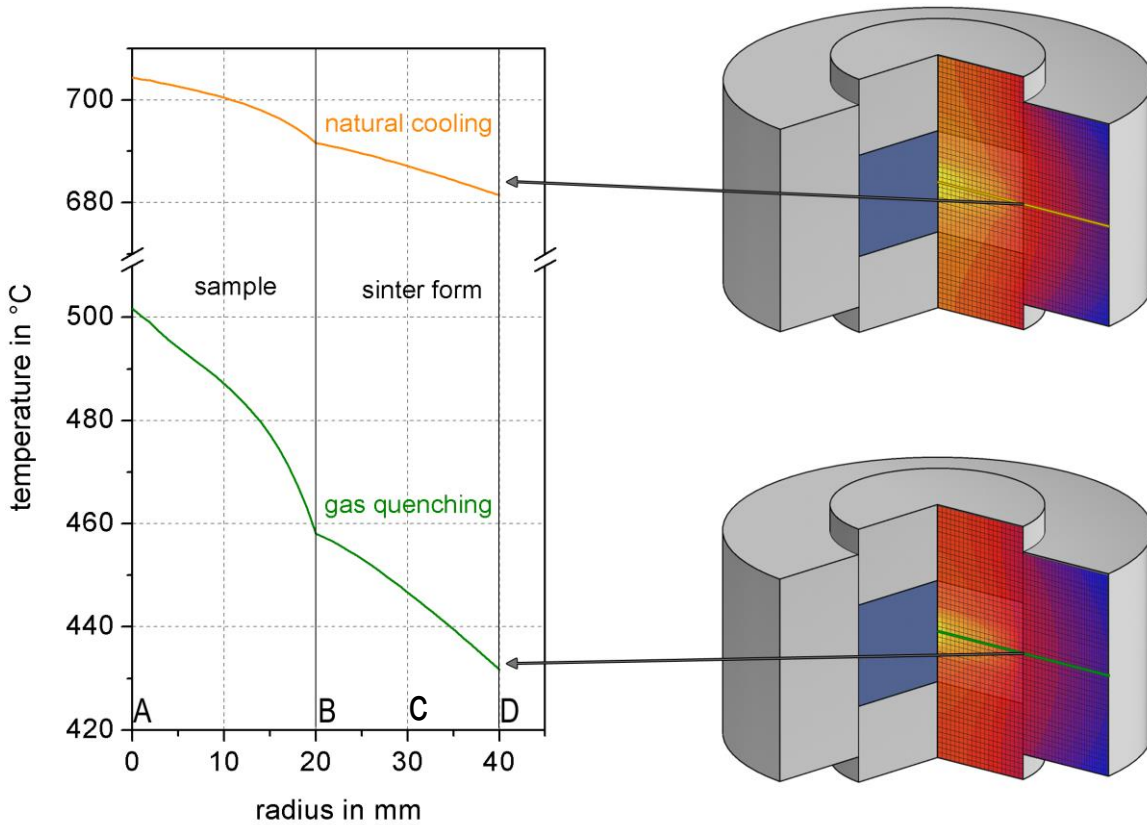


Figure 4-14. Temperature distribution in the Ti6Al4V alloys and graphite die at 60 s of cooling time: (up) natural cooling, (bottom) gas quenching.

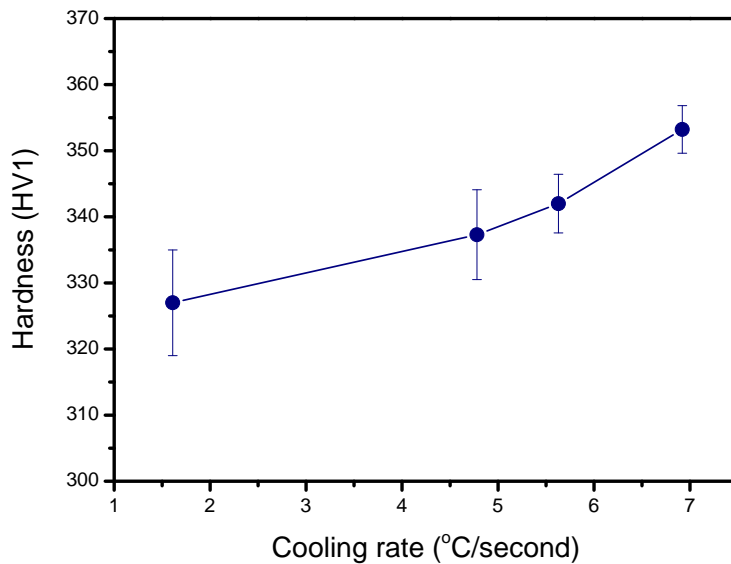


Figure 4-15 Hardness (HV1) of the Ti6Al4V alloys with various cooling rate.

Fig. 4-15 shows the hardness (HV1) of the sinter-hardened Ti6Al4V alloy with various cooling rates. All the Ti6Al4V alloys with various cooling rates have similar relative densities above 99.0%. The naturally cooled samples with the cooling rate of

1.6 K/s have hardness of 327 ± 8 . The gas quenched samples show hardness of 337 ± 7 , 342 ± 4 and 353 ± 4 for cooling rate of 4.8, 5.6 and 6.9 K/s, respectively. The hardness increases with higher cooling rate. Thus, sinter hardening of the Ti6Al4V alloys has been realized by the SPS with gas quenching.

Fig. 4-16 (a) shows the compressive stress-strain curves of the Ti6Al4V alloys with various cooling rates. The stress-strain curves show the elastic deformation, plastic deformation and fracture stages. The insert image shows one of the fractured Ti6Al4V specimens. It is found that the fracture takes places at an angle of about 45 degree to the direction of the compressive load. The compressive yield strengths for all the samples are around 1100 MPa, which is higher than the reported values [8] (about 902 MPa). But the ultimate compressive strength has increased with higher cooling rate, as well as the compressive strains.

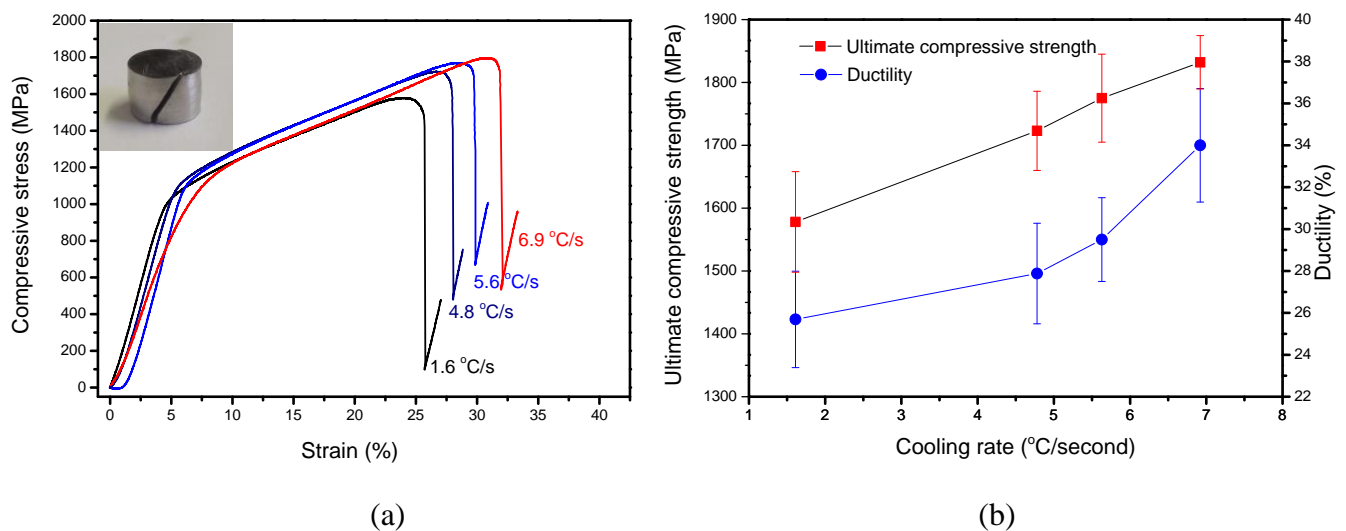


Figure 4-16 Compressive stress-strain curves with inserted image of fractured sample (a), and ultimate compressive strength and ductility of the Ti6Al4V alloys (b) with various cooling rates.

Fig. 4-16 (b) shows the effects of cooling rate on the ultimate compressive strength and ductility of the Ti6Al4V alloys. The ultimate compressive strength goes up with the increase of the cooling rate. The samples of natural cooling rate 1.6 K/s show the ultimate compressive strength of (1578 ± 80) MPa. At a cooling rate of 4.8 K/s, it reaches to (1723 ± 63) MPa. At 5.6 K/s cooling rate, it is increased to

(1775±70) MPa and at 6.9 K/s, it rises to (1832±43) MPa. The rapid cooling has increased the ultimate compressive strength of the Ti6Al4V alloy. The ductility increased with higher cooling rate. The samples with natural cooling rate 1.6 K/s show a ductility of (26±2) %. At a cooling rate of 4.8 K/s, it reaches to (28±2)%, at 5.6 K/s to (30±2)%, and at 6.9 K/s to (34.0±3)%. The ductility measured in this study is under compressive stress. The rapid cooling in the SPS has enhanced the ductility of the Ti6Al4V alloy.

Fig. 4-17 shows the SEM micrographs of the fracture surface of the Ti6Al4V alloys after SPS with various cooling rates. The samples all present a ductile fracture mode with a large amount of plastic deformation undergoing transgranular fracture with typical dimples. However, the fracture surfaces present more and more dimples with increase of the cooling rate (Fig. 4-17a-d). In Fig. 4-17 (d), the sample with cooling rate of 6.9 k/s has much more pronounced dimples and shows more ductile than the sample with cooling rate of 1.6 K/s in Fig. 4-17 (a). It indicates that the sample becomes more ductile after the rapid cooling in the SPS. The SEM fracture surfaces are consistent with the mechanical results.

Fig. 4-18 demonstrates the synchrotron radiation high energy X-ray diffraction of the Ti6Al4V alloys with various cooling rates. The raw Ti6Al4V powder and natural cooling sample in Fig. 4-18 (a, b) showed both of α and β -Ti phases and weak diffractions in α -Ti (112) and (201) lattice planes. The gas quenched Ti6Al4V alloys exhibit sharper crystalline diffraction peaks corresponding to Ti-rich phases with β -Ti phase, as well as new broad peak of intermetallic phase of Al_2Ti (ICDD No. 42-1136) appeared in Fig. 4-18(b-d). The impurity peaks are invisible in the high energy XRD patterns since the synchrotron radiation can penetrate the thick samples. The gas quenching in the SPS resulted in the formation of nanocrystalline intermetallic phase of Al_2Ti in the alloys.

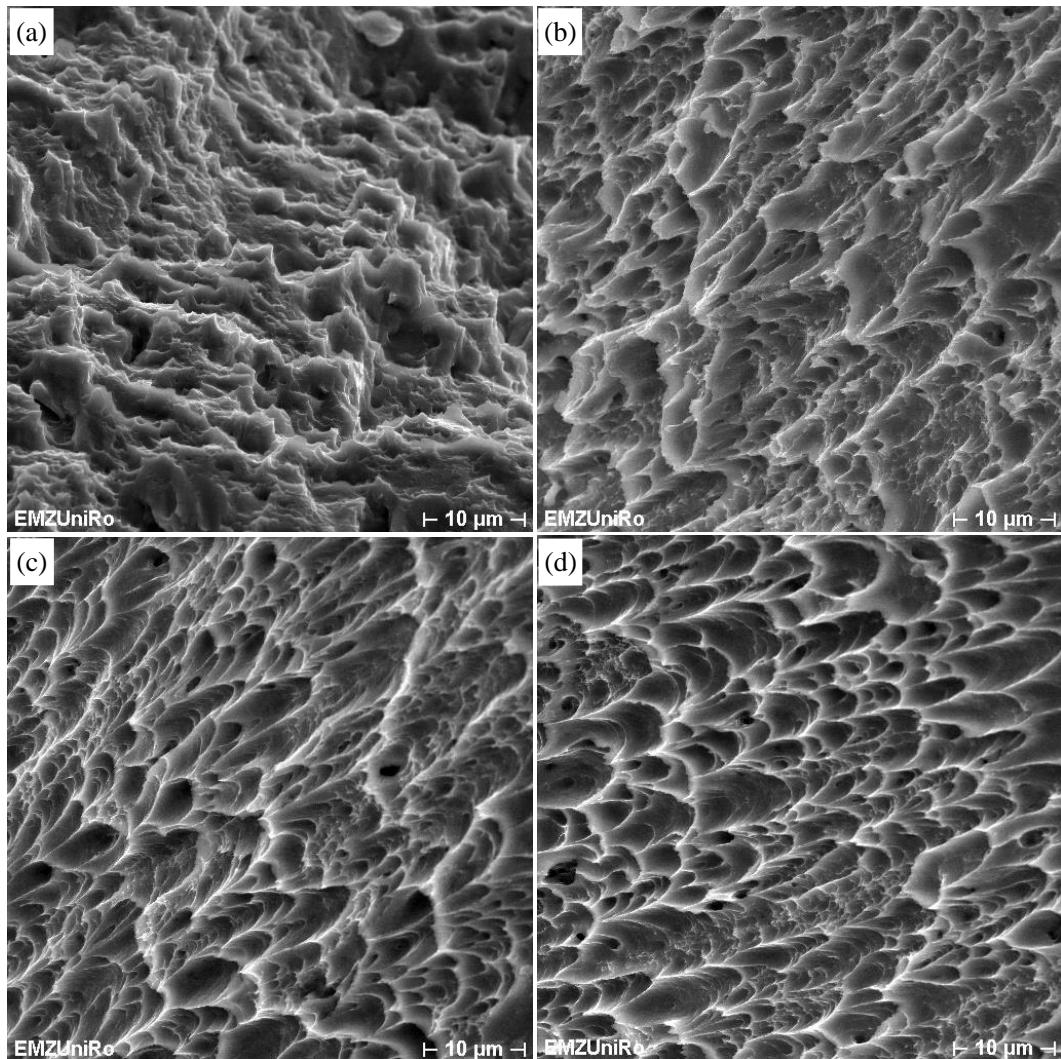


Figure 4-17. SEM micrographs of the fracture surfaces of the Ti6Al4V alloys with various cooling rates: (a) 1.6 °C/s, (b) 4.8 °C/s, (c) 5.6 °C/s, (d) 6.9 °C/s.

Fig. 4-19 provides the metallographic morphology of the Ti6Al4V alloys with various cooling rates. In the etched metallographic images, the β -Ti phase (bcc) appears in white color and α -Ti phase (hcp) in dark color. The samples all show both phases in the microstructures. The microstructures form during sintering at 850 °C and subsequent cooling with different rates.

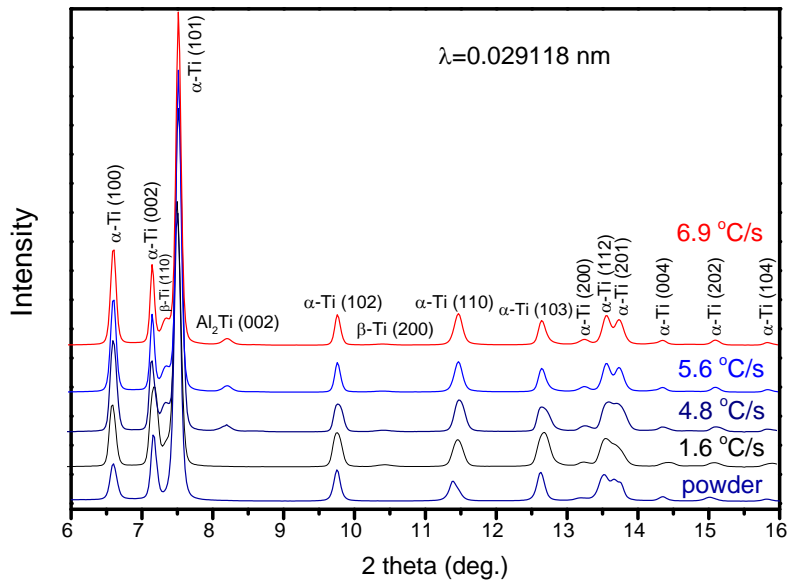


Figure 4-18. Synchrotron radiation high energy X-ray diffraction pattern of the Ti6Al4V raw powder (a) and sintered alloys with various cooling rates: 1.6 °C/s, 4.8 °C/s, 5.6 °C/s and 6.9 °C/s.

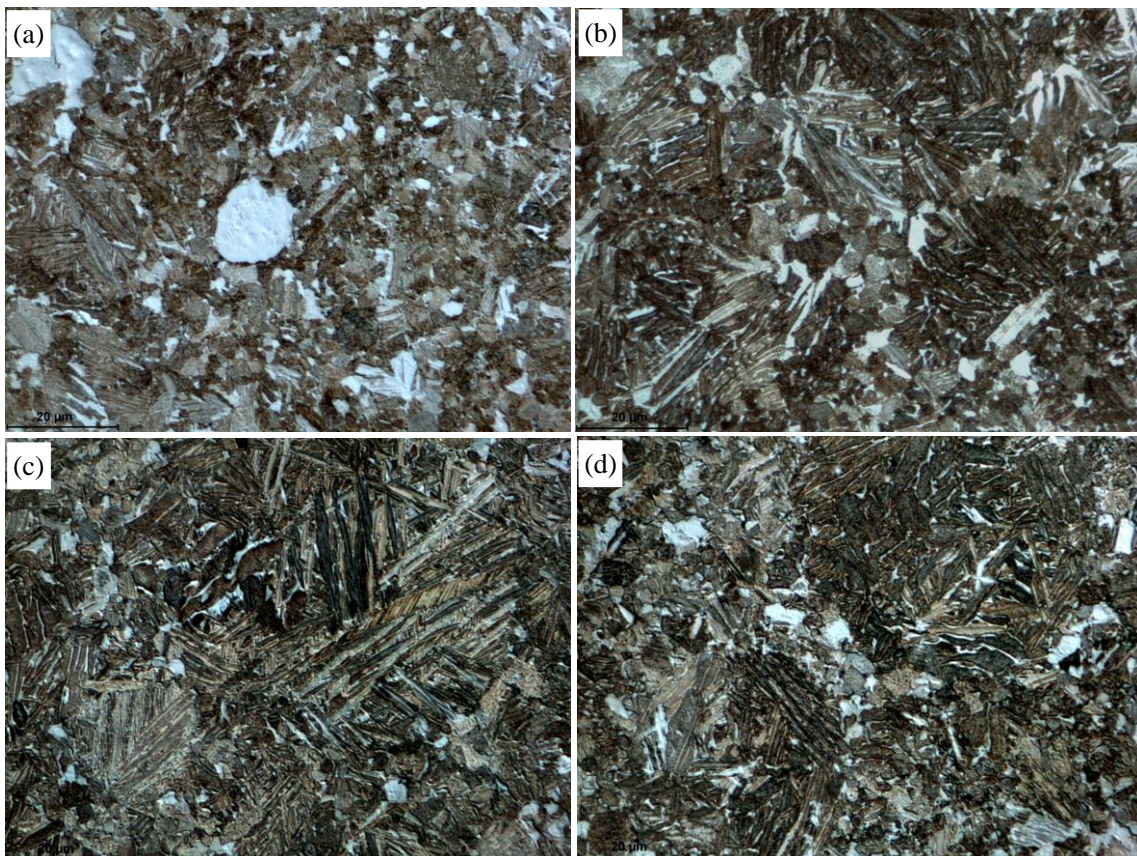


Figure 4-19. Metallographic micrographs of the surfaces of the Ti6Al4V alloys with various cooling rates: (a) 1.6 °C/s, (b) 4.8 °C/s, (c) 5.6 °C/s, (d) 6.9 °C/s. (Scar bar 20 μm).

At sintering temperature of 850 °C, the microstructure consists of a lower amount of α and a higher amount of β . During cooling β partially transforms to α . After cooling the microstructure consists of former α , retained β and newly formed α . The cooling rate mainly influences on the morphology of the newly formed α . The naturally cooled sample with 1.6 K/s cooling rate shows a relative homogeneous globular $\alpha+\beta$ microstructure (Fig. 4-19a). The rapidly cooled sample shows a different microstructure with a morphological change to lamellar α phase (Fig. 4-19b). As the cooling rate increases, the 5.6 °C/s cooled sample in Fig. 4-19(c) has even more lamellar α phase. In Fig. 4-19(d), α phase is getting much more lamellar. In general, gas quenching in the SPS resulted in a morphological change to lamellar α -Ti phase.

4.2.3 Discussions

The results of numerical simulation of the temperature distribution inside of the graphite die indicate that the temperature gradient is larger in the gas quenching Ti6Al4V than in the natural cooling one. The temperature gradient existed during SPS of various samples: ceramics, metals and composites [27-29]. The amount of gradients depends on thermal conductivity of the materials, dimensions and heating rate. Usually, larger diameter samples have higher temperature gradient and higher heating rates result in higher gradient [30-31]. The investigations in this study show that the cooling rate also can influence the temperature gradient of the sample. Higher cooling rates lead to larger temperature gradients. However, the temperature gradient of the sample is not large (44 °C). Such amount of gradient cannot result in obvious differences in mechanical properties and microstructures of the Ti6Al4V alloy. The heat transfer coefficient is defined as the ratio of heat lost due to the flow to the product of area and temperature difference. Higher heat transfer coefficients can cool the sample faster. The gas quenching is effective to increase the heat transfer coefficients up to 5-7 times higher than the natural cooling. Therefore, the Ti6Al4V alloy can be quenched through the outside surface of the graphite form being cooled by gas nozzle field of nitrogen gas. The sintering and quenching heat-treatment have been completed by one step SPS process without a separate heat treatment operation. The cooling rates have been tailored by changing the thickness of the graphite die in

this study. Besides variation of cooling rate by die wall thickness, further variation of cooling rate will become possible by adjusting gas flow rate and gas nozzle field geometry in the future.

The hardness, ultimate compressive strength and ductility of the Ti6Al4V alloys have been increased due to the gas quenching. Sinter hardening is applicable for the Ti6Al4V alloy in which the samples are spark plasma sintered and gas quenched directly after the sintering. It saved energy and costs when compared with the conventional hardening in which the parts must be reheated to the hardening temperature. The gas quenching induced the precipitation of intermetallic phase of Al₂Ti, and a morphological change to lamellar α -Ti phase. The SPS is a nonequilibrium sintering process. The Ti6Al4V powders were sintered in the SPS, and then directly quenched from the sintering temperature. Due to the higher cooling rates, the soluble Al, V elements in Ti had not enough time to diffuse, and then precipitated as a second phase in the Ti6Al4V alloy. Potez et al reported that the Al₂Ti precipitation has an important hardening effect [32]. It can be seen from Fig. 4-18 that the peak of Al₂Ti is broad indicating their nanocrystalline structure. The precipitated nanocrystalline Al₂Ti can play a role of hardening and dispersion reinforcing of the Ti6Al4V alloys. Therefore, the hardness and ultimate compressive strength of the Ti6Al4V alloy are increased. The alloys were sintered and gas quenched from 850 °C by the SPS which is between the α and β transus line (in $\alpha+\beta$ field), and below the martensitic transformation (Ms) line in the phase diagram. Quenching from the $\alpha+\beta$ phase field can produce microstructure consisted of primary α phase, retained β -Ti, new α -Ti formed during quenching and intermetallic precipitates. With increasing cooling rate, the newly formed α -Ti becomes more lamellar. The morphological change to lamellar structured α -Ti phase can lead to the increase in ductility of the Ti6Al4V alloy [33].

The use of industrial gases for quenching of high value parts offered significant environmental and performance advantages over liquid quenching (water, oil, etc.). Gas quenched parts are clean thus eliminating the need for post-cleaning operations. Due to poor thermal transfer characteristics (lower cooling rate) of gases under normal conditions, they have to be optimized by proper adjustment of gas pressure

and flow speed. Gas quenching can be performed in two methods, namely: at low atmosphere pressure with high gas velocity or at high pressure with limited gas velocities. In this study, we used the first technique in the SPS that at low or atmosphere pressure with high gas velocity. The flowing rate of the nitrogen gas from nozzles is 8000 l/min. The pressure of gas is only slightly above normal atmosphere pressure. The thermo-physical properties of the gas are also an important issue. Based on availability, and thermo-physical properties, hydrogen would appear to be good choice as a quench agent [34]. However, because of the explosive risks associated with hydrogen, it is seldom used as a quench gas in commercial heat treating. Helium is almost as fast as hydrogen, not explosive, but significant more expensive. Nitrogen is the most popular choice, primarily because it is readily available and inexpensive. Argon is used in some special applications but does not quench as effectively as nitrogen and is considerably more expensive. In this study, the SPS vacuum furnace was flooded with argon gas to 40 mbar with keeping the sintering temperature of 850 °C , and then quenched with nitrogen gas at high velocity. The achieved heat transfer coefficients of about 400 W/m² K are much higher than that of the natural cooling of 80 W/m² K (Fig. 3). However, it is still lower than that in comparable external gas nozzle fields of about 1000 W/m² K with flowing rate of 8000 l/min [26]. This is mainly due to the relation between sample/die geometry and nozzle field geometry, which still can be improved in the next step research.

Manipulating the morphology of the two phases in Ti6Al4V yielded excellent combinations of hardness, strength and ductility. The Ti6Al4V alloys have been used in medical applications for several decades already. As mentioned, one of the main problems of this alloy in biomedical applications is its insufficient ductility. This investigation indicates that the traditional Ti6Al4V alloy can be modified by SPS with gas quenching leading to various mechanical properties and microstructures. The high ductility of the Ti6Al4V achieved by SPS with gas quenching leads to the easy fabrication of complex shape and plates for the medical applications. Thanks to controlling the cooling rates, microstructures of the Ti6Al4V can be designed to obtain the desired mechanical properties. It can be expected that the Ti6Al4V alloys

would be used widely as bone substitutes and dental implants. The rapid cooling-SPS combining sintering and gas quenching provides a novel method to tailor the mechanical properties and microstructure of the Ti6Al4V alloys. This processing approach could be applied to a wide range of metallic materials and metal matrix composites for biomedical applications, where the parts can be rapidly sintered and rapidly quenched directly after the sintering step saving energy and costs.

4.2.5 Summary

The Ti6Al4V alloys were prepared by the spark plasma sintering equipped with a novel nitrogen gas quenching system. Cooling curve measurement and inverse thermal Finite element simulation reveal that the gas quenching can increase the heat transfer coefficient up to 5-7 times higher and magnify the temperature gradient of the Ti6Al4V. The cooling rate ranged from 1.6 °C/s to 6.9 °C/s was achieved by changing the thickness of the graphite dies. Sinter-hardening of the Ti6Al4V alloy has been achieved, where the hardness rises from 327 HV1 to 353 HV1. The gas quenching has increased the ultimate compressive strength and ductility of the Ti6Al4V alloy from 1578 MPa to 1832 MPa and from 26% to 34%, respectively. The rapid cooling leads to much more pronounced dimples in fracture surfaces, the precipitation of intermetallic phase (Al₂Ti), and a morphological change to lamellar α -Ti phase in metallography. The high ductile Ti6Al4V alloys could be used widely as bone substitutes and dental implants. The rapid cooling-SPS combining sintering and gas quenching provides a novel method to tailor the mechanical properties and microstructures of the Ti6Al4V alloys.

References

- [1] E. Blaurock-Busch, Mineral & Trace Element Analysis, Laboratory and Clinical Application. Tmi 1997.
- [2] L. Miao, D. K. St Clair. Regulation of superoxide dismutase genes: Implications in disease. Free Radical Biology and Medicine 2009, 47(4):344-356.
- [3] L.P. Xu, G. Yu, E. Zhang, F. Pan, K. Yang. In vivo corrosion behavior of Mg-Mn-Zn alloy for bone implant application. J Biomed Mater Res 2007; 83A: 703–711.
- [4] F. Sima, G. Socol, E. Axente, I. N. Mihailescu, L. Zdrentu, S. M. Petrescu, I. Mayer, Biocompatible and bioactive coatings of Mn²⁺-doped β -tricalcium phosphate synthesized by

- pulsed laser deposition. *Applied Surface Science* 2007, 254: 1155-1159.
- [5] R. Nicula, R. Lüthen, M. Stir, B. Nebe, E. Burkel. Spark plasma sintering synthesis of porous nanocrystalline titanium alloys for biomedical applications. *Biomolecular Engineering* 2007, 24: 564-567.
- [6] O. M. Ivasishin. Cost-effective manufacturing of titanium parts with powder metallurgy approach. *Materials Forum* 2005, 29:1-8.
- [7] S. Semboshi, N. Masahashi and S. Hanada. Degradation of hydrogen absorbing capacity in cyclically hydrogenated TiMn₂. *Acta Mater* 2001, 49: 927-935.
- [8] I. S. Polkin, A. B. Borzov. New materials produced by mechanical alloying. *Advanced Performance Materials* 1995, 2: 99-109.
- [9] D.R. Santosa, V.A.R. Henriquesb, C.A.A. Cairob, M.S. Pereiraa. Production of a low Young modulus titanium alloy by powder metallurgy. *Materials Research* 2005, 8: 439-442.
- [10] D. Handtrack, F. Despang, C. Sauer, B. Kieback, N. Reinfried N, Y. Grin. Fabrication of ultra-fine grained and dispersion-strengthened titanium materials by spark plasma sintering. *Materials Science and Engineering A* 2006, 437: 423-429.
- [11] K. Masayuki, M. H. Luciana, A. Kenzo. Porous Ti-6Al-4V alloy fabricated by spark plasma sintering for biomimetic surface modification. *J. Biomedical Mater Res. B* 2004, 68B: 88-93.
- [12] H. Hermawan, D. Dube, D. Mantovani. Development of degradable Fe-35Mn alloy for biomedical applications. *Advanced Materials Research* 2007, 15-17: 107-122.
- [13] A. K. Ghosh, C. H. Hamilton. Superplastic forming and diffusion bonding of titanium alloys. *Defence Science Journal* 1986, 36: 153-177.
- [14] M. Arciniegas, C. Aparicio, J. M. Manero and F. J. Gil. Low elastic modulus metals for joint prosthesis: Tantalum and nickel–titanium foams. *Journal of the European Ceramic Society* 2007, 27: 3391-3398.
- [15] A. Guitar, G. Vigna, M. I. Luppò, Microstructure and tensile properties after thermohydrogen processing of Ti–6Al–4V. *Journal of the Mechanical Behavior of Biomedical Materials*, 2009, 2(2),156–163.
- [16] E. Bertrand, T. Gloriant, D. M. Gordin, E. Vasilescu, P. Drob, C. Vasilescu, S. I. Drob, Synthesis and characterisation of a new superelastic Ti–25Ta–25Nb biomedical alloy. *Journal of the Mechanical Behavior of Biomedical Materials* 2010, 3(8): 559–564.
- [17] C. N. Elias, J. H. C. Lima, R. Valiev, M.A. Meyers, Biomedical Applications of Titanium and its Alloys. *JOM*, 2008.3: 46-49.
- [18] V.K. Ganesh, K. Ramakrishna, D. N. Ghista, Biomechanics of bone-fracture fixation by stiffness-graded plates in comparison with stainless-steel plates. *BioMedical Engineering OnLine* 2005, 4: 46.
- [19] K.H. Frosch, K. M. Stürmer, Metallic biomaterials in skeletal repair. *European Journal of Trauma* 2006, 32:149–159.
- [20] M. Dlapka, H. Danniger, C. Gierl, B. Lindqvist, Sinter hardening – a special heat treatment for powder metallurgy precision parts. *Journal of Heat Treatment and Materials* 2012, 67(3): 223-231.
- [21] S. N. Thakur, J.W. Newkirk, G.B. Fillari, I.F. Murphy, K.S. Narasimhan, Mechanical Properties of Sinter-Hardened Steels. *International Journal of Powder Metallurgy* 2004, 40(3):45-56.
- [22] L.A. Dobrzanski, M. Musztyfaga, Effect of cooling rates on sinter-hardened steels. *Journal of Achievements in Materials and Manufacturing Engineering* 2009, 37(2): 630-638.

- [23] N. Lior, The cooling process in gas quenching. *Journal of Materials Processing Technology* 2004, 155–156: 1881-1888.
- [24] M. Reich, S. Schöne, O. Keßler, M. Nowak, O. Grydin, F. Nürnberger, M. Schaper, Simulation of gas and spray quenching during extrusion of aluminium alloys. *Key Engineering Materials* 2010, 424: 57-64.
- [25] R. Boyer, G. Welsch, E.W. Collings, *Materials Properties Handbook: Titanium Alloys*, ASM International, Materials Park, OH 1994.
- [26] S. Schöne, M. Reich, O. Keßler, Gas nozzle field quenching of aluminium extrusion profiles – a feasibility study. *HTM Journal of Heat Treatment and Materials* 2011, 66(3):175-181.
- [27] K. Vanmeensel, A. Laptev, J. Hennicke, J. Vleugels, O. Van der Biest, Modelling of the temperature distribution during field assisted sintering. *Acta Materialia* 2005, 53(16):4379-4388.
- [28] K. Vanmeensel, A. Laptev, O. Van der Biest, J. Vleugels, Field assisted sintering of electro-conductive ZrO₂-based composites. *Journal of the European Ceramic Society* 2007, 27(2-3):979-985.
- [29] U. Anselmi-Tamburini, S. Gennari, J. E. Garay, Z.A. Munir, Fundamental investigations on the spark plasma sintering/synthesis process II. Modeling of current and temperature distributions. *Materials Science and Engineering A* 2005, 394(1-2):139-148.
- [30] Y. Wang, Z. Fu, Study of temperature field in spark plasma sintering. *Materials Science and Engineering B*. 2002, 90(1-2):34-37.
- [31] G. Salvatore, S. Yoshio, M. Giovanni, Effects of initial punch-die clearance in spark plasma sintering process. *Materials Transactions*, 2008, 49(12): 2899-2906.
- [32] L. Poteza, A. Loiseau, S. Nakaa, G. Lapassetta, A study of Al₂Ti precipitation in a Cu-modified Al₃Ti alloy. *Journal of Materials Research* 1992, 7(4): 876-882.
- [33] J. H. Kim, S.L. Semiatin, C.S. Lee, Constitutive analysis of the high-temperature deformation of Ti–6Al–4V with a transformed microstructure. *Acta Materialia* 2003, 51(18):5613-5626.
- [34] B. Xiao, G. Wang, Y. Rong, R. Sisson, Influencing factors of heat transfer coefficient in air and gas quenching. *Journal of ASTM International*. 2011, 8(4):103403.

Chapter 5 SPS of titanium foams for biomedical applications

5.1 SPS of macroporous pure titanium foams

5.1.1 Introduction

Porous titanium (Ti) and its alloys were widely used in the biomedical field due to their outstanding mechanical properties, low density, chemical resistance and biocompatibility. As a kind of long-term load-bearing implant, the porous structures of Ti and its alloy could lead to a reliable anchoring of metal implants into host tissue, and allow mechanical interlocking between bone and implant [1]. The SPS studies on porous Ti alloys were mainly using low temperature and low pressure to decrease the relative density of samples [2-6]. The samples exhibited pore sizes of some tens of micrometers and a porosity in the range of 20-45%. Nevertheless, macroporous Ti foams with higher porosity (>50%) and larger macropore size (>200 μm) by SPS were scarcely reported. In fact, Ti has a much higher melting point (1660.0 $^{\circ}\text{C}$) than aluminium (660.3 $^{\circ}\text{C}$). Therefore, it is a great challenge to fabricate Ti foams by using the SPS and NaCl spacer methods. The objective of this study is to develop macroporous Ti foams with controlled architectures using the SPS in combination with the NaCl spacer methods. The major parameters involved in the preparation process were studied. The microstructures of the prepared foams were analyzed by using 3D X-ray microcomputed tomography (micro-CT) and scanning electron microscopy (SEM) techniques. The relationship between the mechanical properties and the porous architectures were analyzed and discussed.

5.1.2 Experimental

The precursor Ti powders were prepared by gas atomization method with 99.5% purities (Alfa Aesar, Germany). The space holder material consisted NaCl crystalline powders with 99.0% purity (Alfa Aesar, Germany) sieved in the range of 100 μm to 1000 μm .

The Ti powders and NaCl powders were homogenously mixed in different weight ratios in a blender. The mixtures were loaded into graphite die to sinter disc-shaped pellets (20 mm diameter, thickness about 7 mm). The SPS experiments were

performed using a FCT spark plasma sintering system (FCT systeme GmbH, Rauenstein, Germany) at temperatures of (600-800) °C lasting for various time. The applied direct current for SPS was about (1000-2000) A (voltage < 5 V) with a pulse duration of 12 ms and an interval of 2 ms. The SPS experiments were conducted in vacuum (<6 Pa) under an uniaxial pressure of 30-50 MPa. The heating rate was maintained at 100 °C/min. The SPSed samples were then suspended in circulating hot water (80 °C) to dissolve the NaCl space holder for 12 hours. The leached Ti forms were cleaned in an ultrasonic water bath for 15 min, rinsed with ethanol and furnace dried at 120 °C for 10 hours.

X-ray diffraction (XRD, Bruker D8, Germany) was used to characterize the phase composition of the powders and sintered foams with CuK α radiation (0.154178 nm). The pore structure of the titanium foam was examined by using X-ray microcomputed tomography (Micro-CT, GE, USA). The specimens were mounted on a rotary stage and scanned in their entirety, being rotated by 360° in 1400 equiangular steps (4 pics per 1°). The detector size is 2284 pixel in x and y and 2304 pixel in z direction. The voxel size of the images is 10.2 μ m in all three axes. The macroporous structures and the microstructures of the obtained Ti foams were analyzed by using a scanning electron microscopy (SEM, Zeiss Supra 25, Germany) equipped with EDX.

The porosities and densities of the sintered porous Ti samples were determined by the Archimedes principal method, i.e. the porosity was calculated from the dry weight of the specimen in ambient air, the wet weight of the specimen in ambient air after boiling water impregnation, and the wet weight of the specimen under water after boiling water impregnation. The mechanical behaviour of the porous Ti foams was investigated by uniaxial compression experiments at room temperature. The plateau stress measurements were carried out on a universal testing machine Zwick Roell Z050, equipped with a 50 kN load cell at 0.5mm/min. The strain was measured with a strain gauge. The Young's modulus was calculated by dividing the plateau stress by the plateau strain.

5.1.3 Results

Figure 5-1 shows the SEM micrograph and XRD pattern of the starting titanium

powders. The titanium powders have irregular morphologies and particle sizes of (10-30) μm (Figure 5-1 a). The XRD result shows that the precursor titanium powders are in the α -Ti phase with hexagonal structure (Figure 5-1 b).

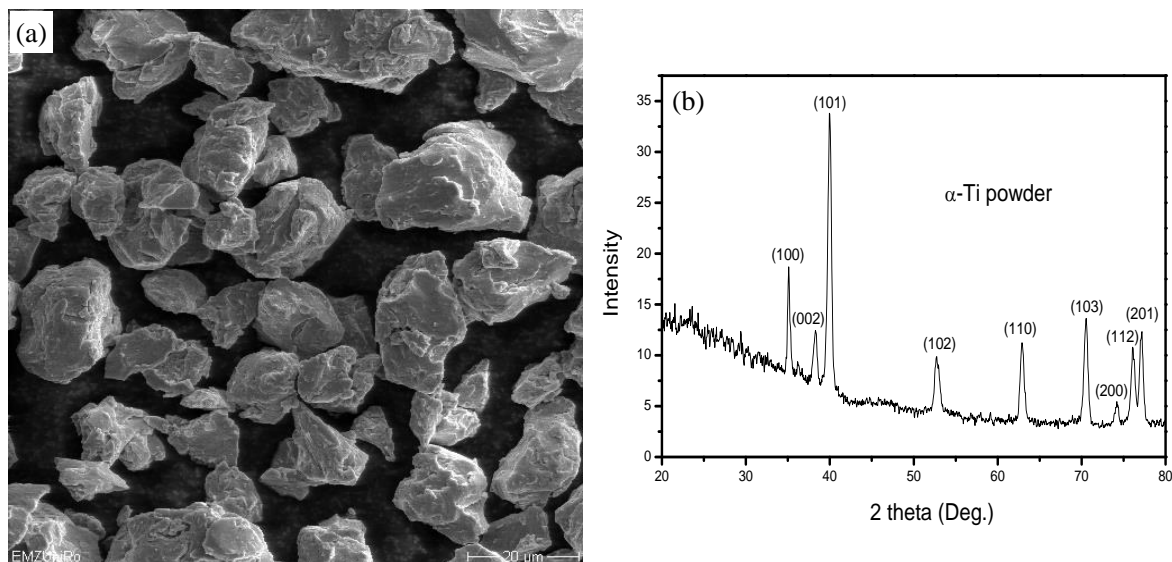


Figure 5-1 SEM micrograph (a) and XRD pattern (b) of the precursor titanium powders.

Figure 5-2 shows the schematic illustration of the pore forming process by using the SPS and NaCl dissolution methods. The Ti and NaCl powders were sieved to the required particle size, firstly (Figure 5-2a). Then, the Ti and NaCl powders with different weight ratios were mixed thoroughly (Figure 5-2b). Additionally, the Ti/NaCl mixtures were subjected to spark plasma sintering at various parameters (Figure 5-2c). The spark plasma sintered samples were suspended in circulating hot water (80 $^{\circ}\text{C}$) for as long as 12 hours (Figure 5-2d). After cleaning and drying, the porous Ti foams were obtained finally (Figure 5-2e).

The influence of the weight ratio and particle size of NaCl on the porosity and pore size of Ti foam samples is shown in Table 5-1. The pore sizes of the sintered foams were measured from the SEM images. It shows mean pore sizes about 125 μm in the foams with a NaCl spacing material in the range of 88-149 μm , mean pore size about 250 μm with NaCl of (224-297) μm , 400 μm with NaCl of (388-500) μm sizes, 800 μm with NaCl of (784-1000) μm sizes. After porosity characterization by the Archimedes method, it is noticed that more NaCl particles were needed to obtain the

same porosity in the large pore sized foams. To achieve a porosity of 55% in the 125 μm foams, the weight ratio of Ti:NaCl is 1:1.28. However, the weight ratio of Ti:NaCl is 1:1.75 in the 800 μm foams for the same porosity. It may be due to the decreased specific surface area in the large sized NaCl particles as spacer materials. It also noticed that more NaCl particles were needed to get high porosity in the equal sized foams. The weight ratio of Ti:NaCl is 1:0.72 to get a porosity of 30% in the 250 μm sized Ti foams, in contrast to 1:1.64 for porosity of 70% at the same pore size.

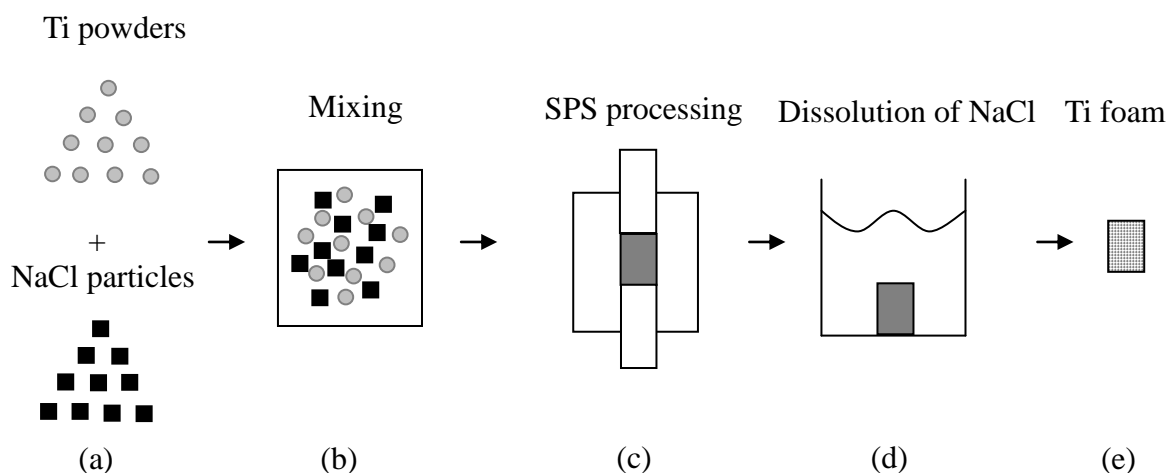


Figure 5-2 Schematic illustration of the pore forming process by using the SPS and NaCl dissolution: sieving of the Ti and NaCl powders (a), mixing of the Ti and NaCl powders (b), processing by the SPS (c), dissolution of the NaCl in water (d), obtaining of the Ti foams (e).

The Ti/NaCl mixtures were spark plasma sintered at temperatures of (550-800) $^{\circ}\text{C}$ under a pressure of (30-50) MPa. The SPSed sample at 750 $^{\circ}\text{C}$ was failed because of the melting of NaCl particulates resulting in an explanation of the mixture and breakage of the graphite die. The parameters were adjusted, and the Ti foams were prepared by the SPS at conditions of 730 $^{\circ}\text{C}$ for 8 min under 30 MPa. However, the XRD result in Figure 5-3 shows that there are some rutile TiO_2 phases (ICDD No. 21-1276) and few TiCl_2 phase (ICDD No.10-0315) in the 730 $^{\circ}\text{C}$ sintered foams. The presences of TiO_2 and TiCl_2 are due to the reaction of the Ti with oxygen and dissociated Cl in NaCl by the sparks of SPS. High purity Ti foams were prepared at

700 °C for 8 min under 50 MPa.

Table 5-1 The influence of the weight ratio and particle size of NaCl on the porosity and pore size of the Ti foams.

.Ti powder	NaCl particles	Weight ratio (Ti: NaCl)	Porosity of foam	Mean pore size
(10-30) μm	(88-149) μm	1:1.28	~55%	~125 μm
		1:0.72	~30%	~250 μm
(10-30) μm	(224-297) μm	1:0.93	~45%	~250 μm
		1:1.32	~55%	~250 μm
		1:1.64	~70%	~250 μm
(10-30) μm	(388-500) μm	1:1.46	~55%	~400 μm
(10-30) μm	(784-1000) μm	1:1.75	~55%	~800 μm

The XRD results in Figure 5-3 show that the Ti remains are in the α -Ti phase structure without any impurities when the SPS process temperatures are below 700 °C. There is usually some temperature difference between the mold surface and the actual temperature in the SPS sample. The temperature difference in the FCT spark plasma sintering system is about 50 °C as investigated by the FCT Company. The sintering temperature of 700 °C plus the temperature difference 50 °C was still lower than the melting point of NaCl (801 °C). Thus, high purity Ti foams can be prepared at the SPS temperature of 700 °C. It took about 40 min to prepare one sample including heating, soaking and cooling time. Compared with hot pressing and traditional vacuum sintering, SPS is capable of sintering at lower temperature within shorter periods. The SPS was originally designed to prepare nanostructured bulk inorganic materials utilizing its merits of fast heating and lower sintering temperatures. There were a number of attempts to synthesize porous Ti metals by using SPS in recent years [2-6]. From the present study, it can be stated that the SPS technique is effective for the

fabrication of porous Ti too. Due to directly applied on-off DC pulse voltage and current, the sintering rate is greatly increased. The SPS is a rapid energy transfer and less energy consumption technique to prepare Ti foams.

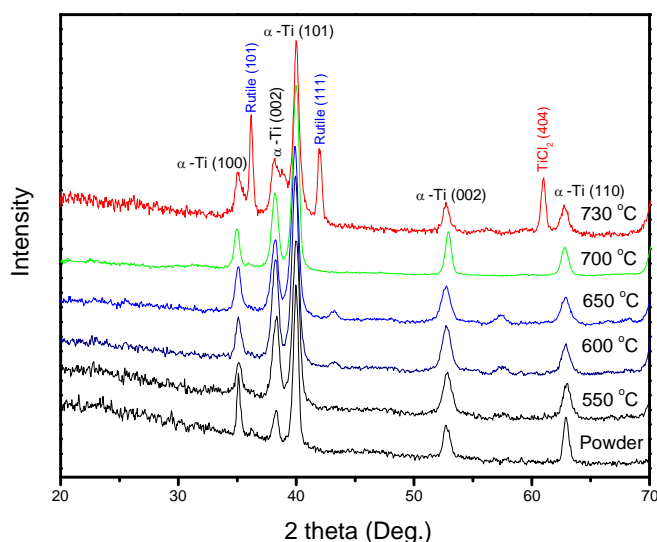


Figure 5-3 XRD patterns of the raw Ti powder and Ti foams processed by SPS at 550, 600, 650, 700 and 730 °C.

The 3D reconstruction by topographical methods is the most realistic way to get space information about the internal structure of the foams in a non-destructive way. The Micro-CT three-dimensional reconstructions of the spark plasma sintered titanium foams with 55% porosity and 250 μm pore size are shown in Figure 5-4. The 3D reconstruction image with isometric view is shown in Figure 5-4 (a). It shows the uniform pore distribution and interconnected 3D porous structures with a high porosity. The Micro-CT 2D top view and side views of the Ti foam sample are shown in Figure 5-4(b-d). It shows that the macropore shapes are in quadratic cross sections, uniform distribution of pore sizes in 250 μm around, and high interconnectivity with cell wall average thickness about 20 μm . The 3-D surface, cell wall thickness and connectivity were examined by the micro-CT in a non-destructive way.

The SEM micrographs of the Ti foams with the same porosity of 55% but different pore sizes of 125 μm , 250 μm , 400 μm , and 800 μm is shown Figure 5-5. All the foams from (125 to 800) μm exhibit highly interconnected porous structures and

uniform pore distributions. It is found that the pores have irregular quadratic cross sections. They are similar to those of the initial NaCl particles of cuboid shapes.

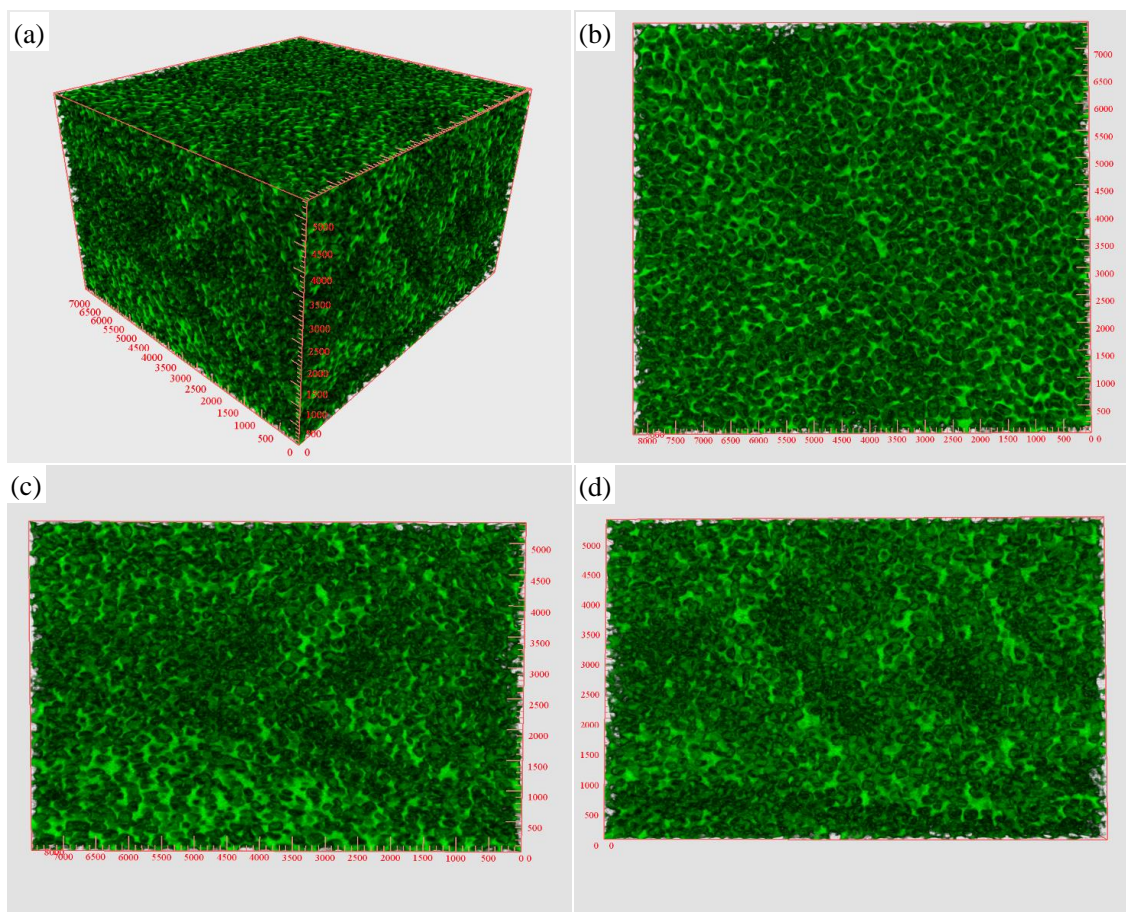


Figure 5-4 Micro-CT three-dimensional 3D reconstructions of the Ti foam (250 μm of pore size, 55% of porosity) with an isometric view (a), 2D top view (b), left side view (c), and right side view (d). Scale spacing, 500 μm .

Figure 5-6 shows the SEM micrographs of the porous Ti foams with the same pore size of 250 μm but different porosity of 30 %, 45%, 55% and 70%. The thickness of the pore walls of the foams decreases with the increase in porosity. The thickness of the pore walls in the 30% porosity foams is about 100 μm , decreasing to 50 μm in 45% porosity foams, and to 20 μm in 55%, finally ending at 10 μm in 70% porosity foams. The interconnectivity was also enhanced with the increase in porosity. The 30% and 45% porosity foams show poor interconnectivity because of the lower porosity (Figure 5-6a, b). But the 55% and 70% higher porosity samples showed good

interconnectivity (Figure 5-6c, d). The macropores are in quadrate cross sections in all the Ti foams with different porosities. The 3D Micro-CT and SEM microstructures show that the pore size and porosity can be well controlled by the SPS process and the NaCl spacer materials with uniform internal structure.

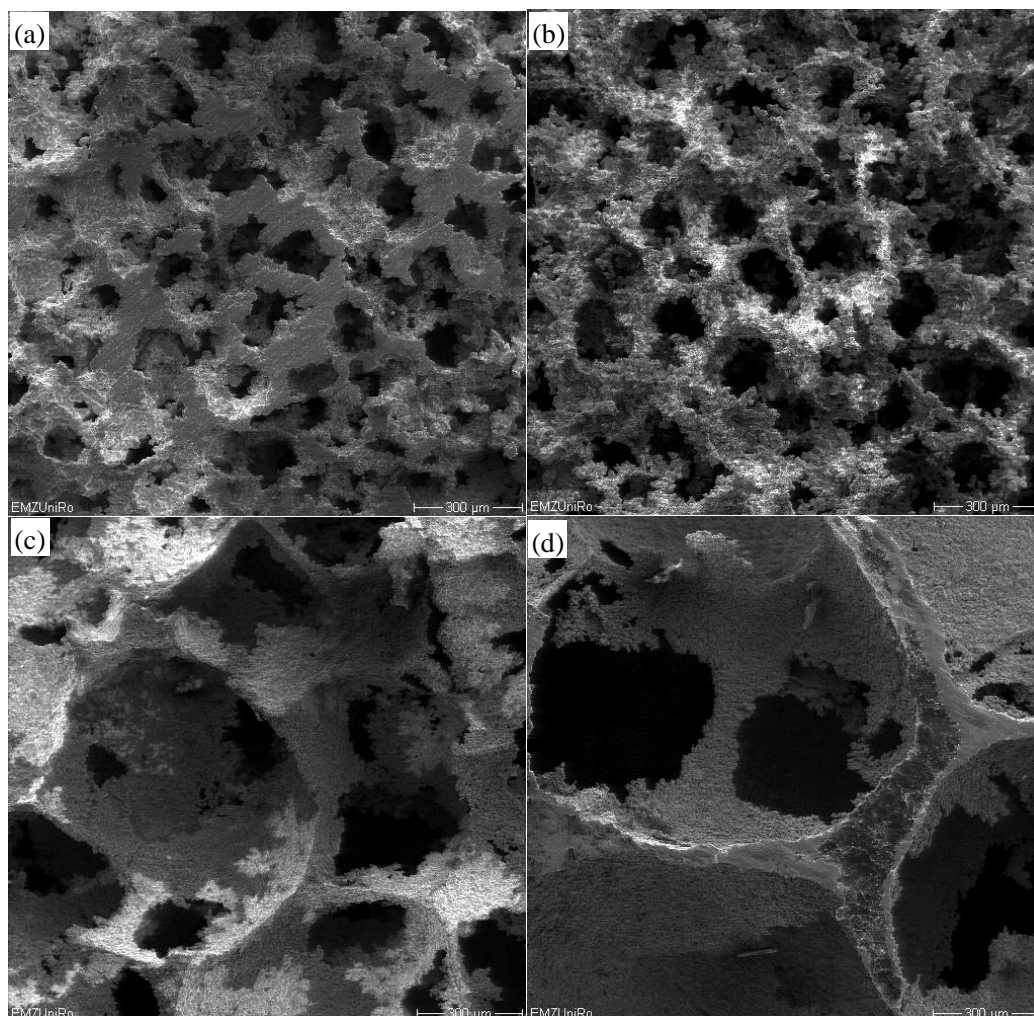


Figure 5-5 SEM micrographs of the Ti foams with the same porosity of 55% but different pore sizes of 125 (a), 250 (b), 400 (c) and 800 μm (d). Scale bars, 300 μm .

Figure 5-7 shows the SEM microstructures of the polished cross-section, pore edge and pore wall of the Ti foams, and EDX analysis on the pore matrix. Few micropores ranged (1-2) μm were detected in the the SEM micrograph of the polished cross-section of the Ti foam. It is indicated that the Ti foams have been densified after spark plasma sintering at 700 $^{\circ}\text{C}$ for 8 min under 50 MPa. The typical pore edge and wall of the Ti foams are shown in Figure 5-7 (b, c). The grain sizes of the Ti foams

still range from about (10 to 30) μm which indicates the absence of rapid grain growth thanks to the rapid heating rate during the SPS process. There are some micropores smaller than 10 μm on the pore walls. The micropores could allow body fluid circulation whereas the macropores may provide a scaffold for bone-cell colonization. The surfaces of the pore walls of the macropores of the porous Ti are relatively rough. The EDX analysis shows that the matrix of the pore wall contains only Ti elements without O element (Figure 5-7d). It is accordingly to the XRD results in Figure 3 that high purity Ti foams were prepared by SPS at 700 $^{\circ}\text{C}$.

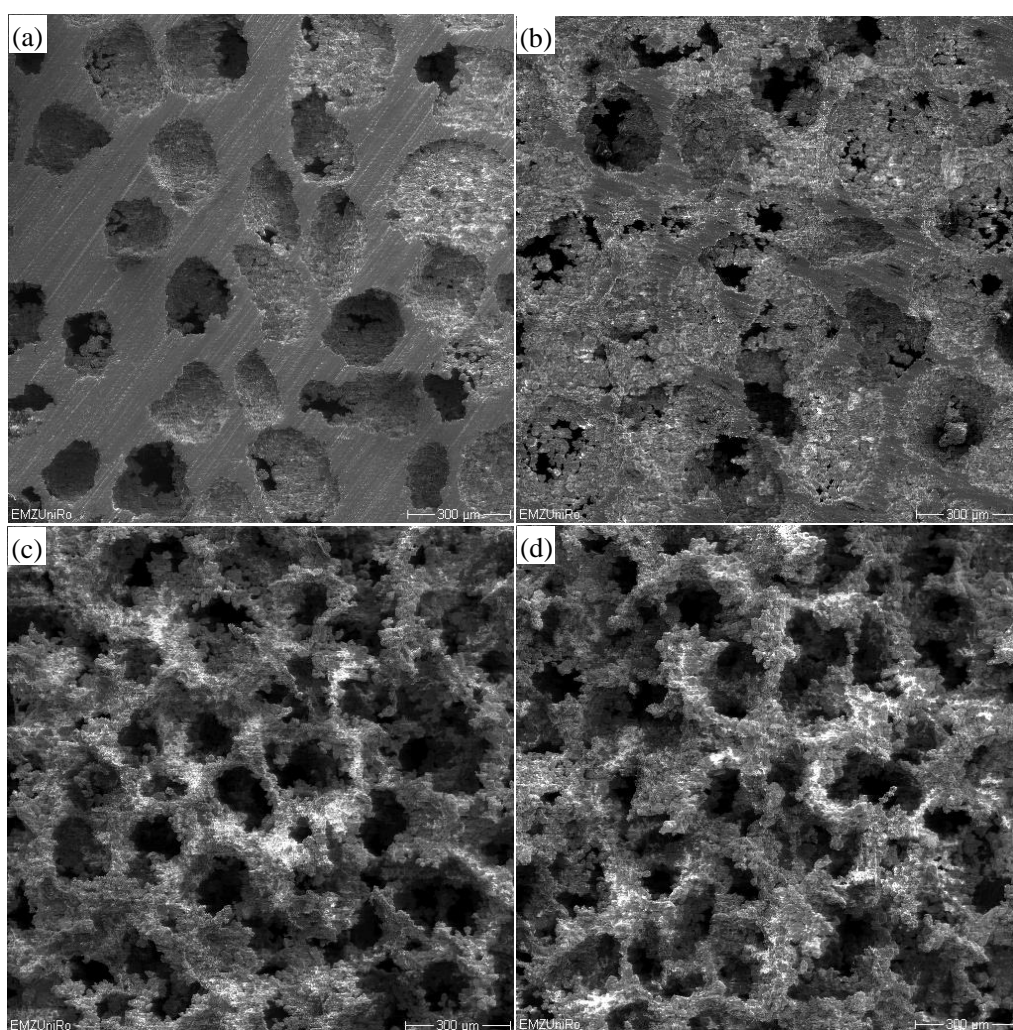


Figure 5-6 SEM micrographs of the Ti foams with the same pore size of 250 μm but different porosities of 30 % (a), 45% (b), 55% (c) and 70% (d). Scale bars, 300 μm .

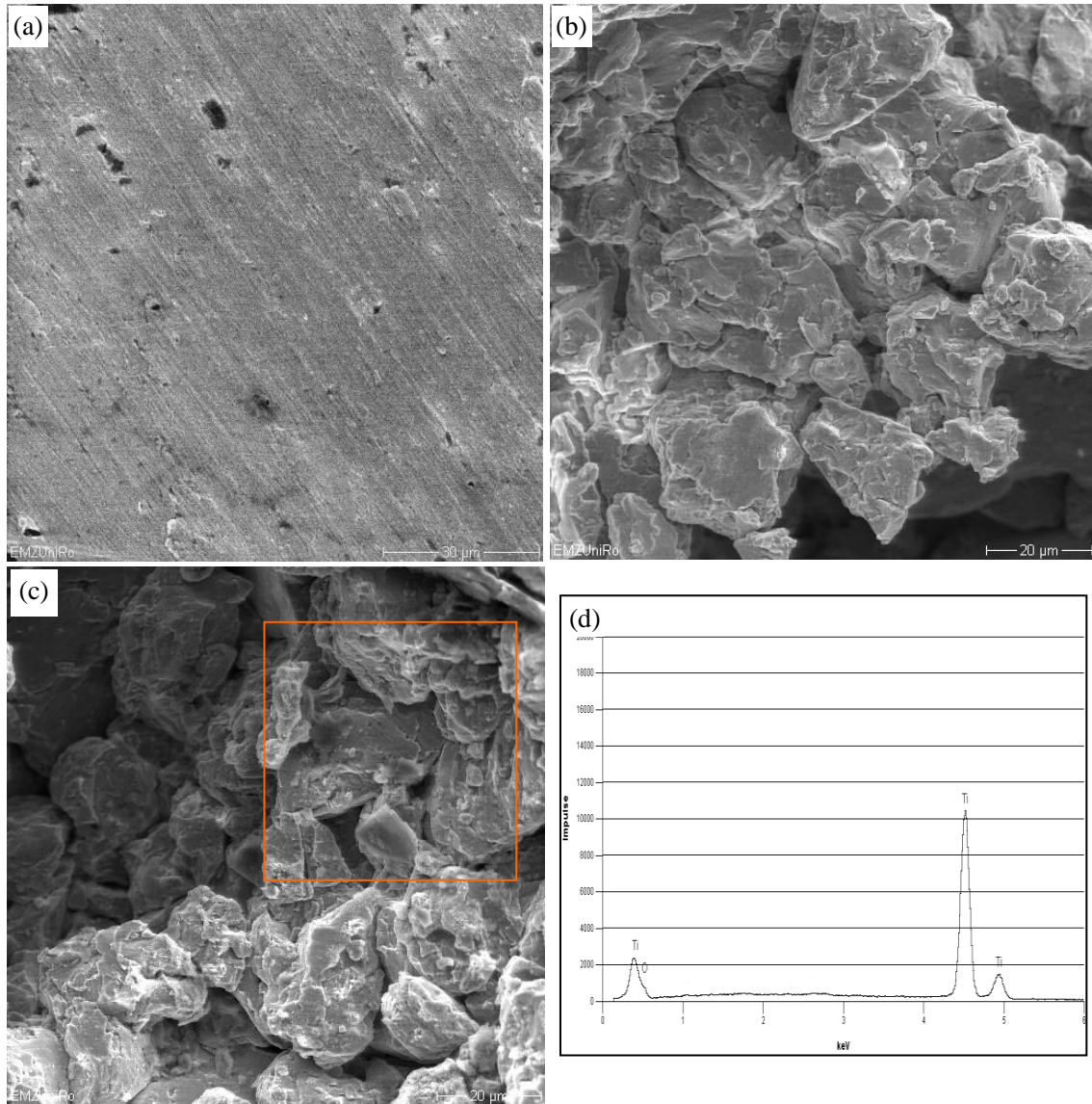


Figure 5-7 SEM micrographs of the microstructure of the polished cross-section (a), pore edge (b) and pore wall (c) of the Ti foams, and EDX analysis on the pore matrix (d). Scale bars, 30 μm in (a), 20 μm in (b, c).

Figure 5-8 shows the effect of pore size and porosity on the plateau stress and Young's modulus of the porous Ti foams. The measured plateau stress and Young's modulus of the Ti foams were compared with the theoretical values that calculated from Gibson-Ashby model. According to the Gibson-Ashby model, the relationship between the relative plateau stress and relative density is given by [7]:

$$\sigma_{pl}/\sigma_{ys} = C(\rho/\rho_s)^{3/2} \quad (1)$$

where σ_{pl} is the plateau stress of the foams, σ_{ys} is the yield stress of the dense material; C is a constant 0.3 from the data of cellular metals and polymers. The density of the pure Ti is 4.5 g/cm³ with yield stress of 692 MPa [8, 8]. The density of the Ti foam with 55% porosity and 250 μ m pore size is 1.69 g/cm³. Substituting these values in Equation 1, the theoretical value was calculated to be 47.78 MPa, which is comparable to the measured plateau stress (45.1 \pm 3.0) MPa. According to the Gibson-Ashby model, the relationship between the relative Young's modules and relative density is given by [7]:

$$E/E_s = A(\rho/\rho_s)^2 \quad (2)$$

where E is the Young's modulus of the foams, E_s is the Young's modulus of the dense materials, A is a constant of 1 including data of metals, rigid polymers, elastomers and glasses. The Young's modulus of the pure Ti is 105 GPa according to the Equation 2 [8, 9]. The measured Young's modulus of the above Ti foams with 55% porosity is (13.46 \pm 1.4) GPa. Substituting the values into Equation 2, it is calculated that the theoretical value is 14.81 GPa which is also comparable to the measured one. All the Ti foams prepared by the SPS were measured and calculated. As seen from the Figure, it can be deduced that all the experimental data agrees with the Gibson-Ashby model (1) and (2) in the present study. The relationship between the pore sizes and the mechanical properties of the Ti foams is shown in Figure 5-8 (a, b). The plateau stress decreased from (49.7 \pm 3.8) MPa to (27.2 \pm 3.0) MPa with the pore size increase (Figure 5-8a). The Young's modulus reduced from (18.3 \pm 2.0) GPa to (8.9 \pm 1.5) GPa with the pore size increase (Figure 5-8b). It coarsely obeys a linear decay with the pore size increase. The effect of the porosity on the mechanical properties of the Ti foams is shown in Figure 5-8 (c, d). The plateau stress decreased from (94.2 \pm 5.9) MPa to (28.8 \pm 3.3) MPa, and the Young's modulus decreased from (36.1 \pm 3.5) GPa to (6.2 \pm 1.8) GPa with porosity increase. It generally obeys the rule of exponential decline with the porosity increase.

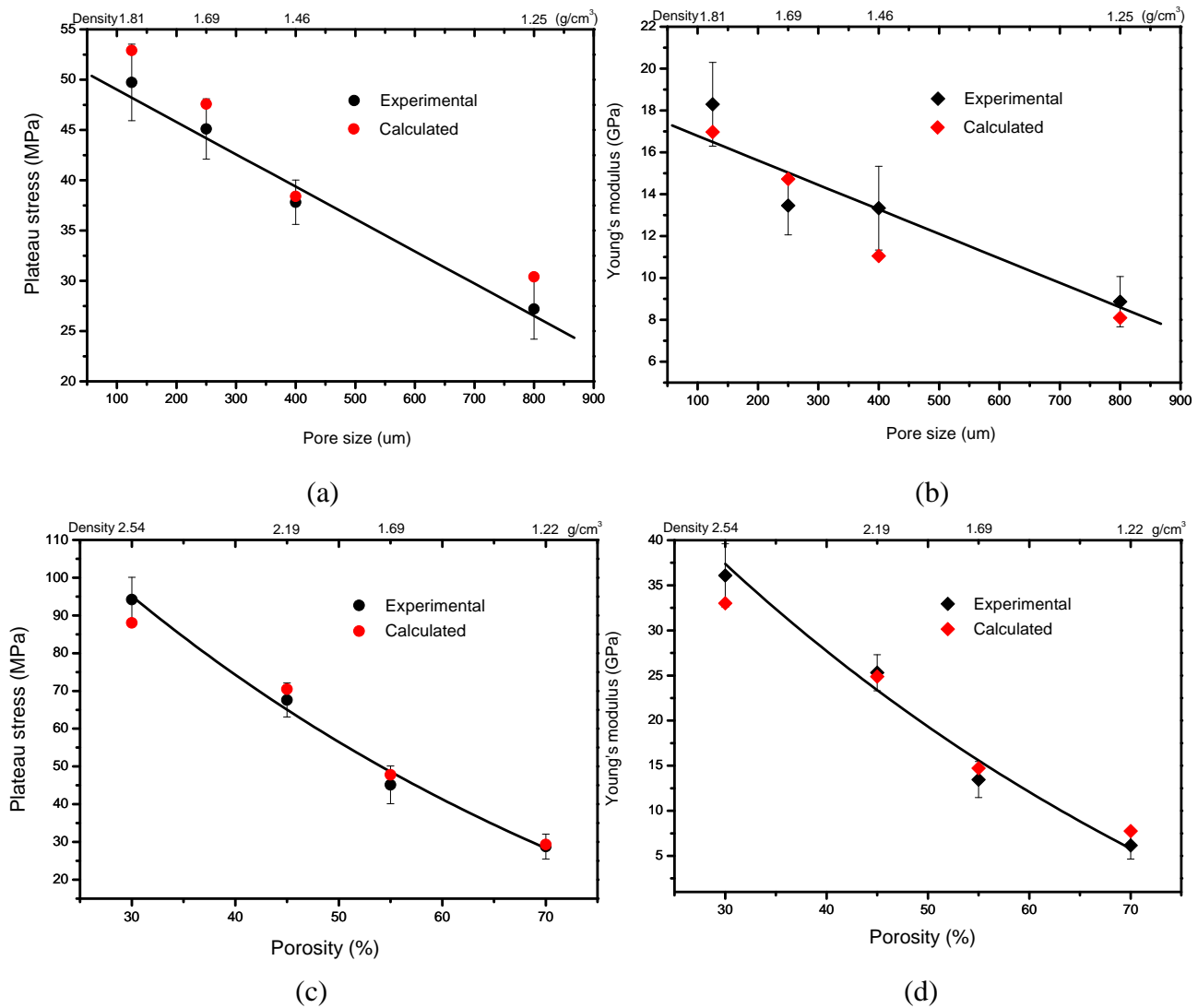


Figure 5-8 The effects of pore sizes (a, b) and porosities (c, d) on the plateau stress and Young's modulus of the Ti foams.

The plateau stress and Young's modulus coarsely obey linear declines with the pore size increase and exponential decay with the porosity increase. Liu et al found that the plateau stress of the porous hydroxylapatite ceramics decreases linearly with increasing macropore size for a given total porosity [10]. In this study, we found that the plateau stress and Young's modulus coarsely obey linear declines with the pore size increase. Rice RW [11] has proposed a function on the relationship of porosity with strength of porous solids,

$$\sigma = \sigma_0 \exp(-cp) \quad (3)$$

where σ_0 is zero-porosity strength, σ is the strength at pore volume fraction p , and the constant c is related directly to the pore characteristics such as pore shape and size. In this study, we used the same NaCl spacer material; therefore, σ_0 and c can be considered as constant. According to the above function, the strength (σ) should decrease exponentially as the pore volume fraction (p) increases. Our results in Fig. 8 (c, d) are well in accordance with the above function.

5.1.3 Discussions

It is reported that powder sintered pure Ti foams with porosity of (55-75)% showed plateau stress and Young's modulus are in the range of (10-35) MPa and (3-6.4) GPa [12]. Plateau stress of (30-65) MPa and Young's modulus of (1.2-2.8) GPa were reported for commercial titanium foams with (70-80) % porosity produced by a solid sacrificial template [13]. In this study, the 250 μm pore sized Ti foams with 55% porosity shows plateau stress of (45.1 ± 3.0) MPa and Young's modulus of (13.46 ± 1.4) GPa. The same pore sized Ti foams with 70% porosity exhibit plateau strength of (28.8 ± 3.3) MPa and Young's modulus of (6.15 ± 1.5) GPa. The results are comparable to the above reported values. The Ti powders used in this study are coarse particles in the range of (10-30) μm . The sintering activity and density could be enhanced by ball milling of the raw Ti powders. It is believed that pure Ti foams with higher mechanical properties can be prepared by using the ball milling, SPS and NaCl dissolution methods. Additionally, the phase structure in these Ti foams is the low temperature α -Ti phase but not the high temperature β -Ti phase because of the lower SPS temperature of 700 °C. The β -Ti phase has a cubic body centred crystalline structure, while the α -Ti phase has a hexagonal crystalline structure which provides β -alloys with an improved notched fatigue resistance and a superior resistance to wear and abrasion [14]. The doping of β phase stabilized elements in Ti, for example Fe, V, Ta, Nb, Mn, Mo, Ni, Cr, Cu, etc could decrease the phase transformation temperature from α to β phase to below 700 °C. It can be predicted that β -Ti alloy foams with much higher mechanical properties could be produced by using the SPS and NaCl dissolution methods.

Implants sometimes are used to substitute bone defects in tumour or spine surgery.

Porous Ti foam with its osteoconductive properties is an ideal alternative bone graft. The porous structure with pore sizes of (200-500) μm of the Ti foams may be able to permit bone cell penetration and tissue integration. The plateau stress of the human vertebral bone (load-bearing site) ranges from (24 to 43) MPa, and femoral cancellous bone (load-bearing site) is in the range of (48-80) MPa [15]. The average Young's modulus of compact bone of human ranges (7-30) GPa [15]. The plateau stress of the presented Ti foams in the range of (27.2-94.2) MPa is comparable to that of the cancellous bone which is enough for biomedical applications. For biomedical applications, the main problem of Ti and Ti alloys in clinical view is their high Young's modulus. Stress shielding is known to lead to bone resorption and eventual loosening of the implant [16]. The dense Ti generally showed much higher Young's modulus of (70-120) GPa than that of human bone. Thus, the porous structures were incorporated in the Ti and Ti alloys. In this study, the porous Ti foams show lower Young's modulus values (6.2-36.1) GPa than that of dense ones which are comparable to those of natural compact bone (7-30) GPa. The macroporous Ti foams with plateau stress (27.2-94.2) MPa and Young's modulus (6.2-36.1) GPa have a potential to be used as bone implants. The low Young's modulus of titanium foams is desirable to reduce the amount of stress shielding of the bone into which the foam is implanted. Combining the good biocompatibility of the pure Ti and the high interconnected porous structure, the Ti foams achieved by the SPS and NaCl dissolution methods with mechanical properties comparable to those of human bone makes these materials to be ideal bone implant foams.

2.1.5 Summary

Macroporous pure titanium foams with porosities of (30-70)% and pore sizes of (125-800) μm were prepared by using SPS and NaCl dissolution methods for bone implant applications. The Ti foams prepared by SPS at 700 °C for 8 min under 50 MPa showed pure α -Ti phase structure. The Ti foams consist of interconnected macropores with quadrature cross sections. The plateau stress and Young's modulus agree with the Gibson-Ashby models, and coarsely obey linear declines with the pore size increase and exponential decays with the increase of porosity. The Ti foams

processed by SPS and NaCl dissolution methods show mechanical properties comparable to those of human bone making these materials to ideal bone implant foams.

5.2 Ti6Al4V foams prepared by spark plasma sintering with post heat treatment

5.2.1 Introduction

Ti6Al4V alloys have interesting mechanical properties, as well as inherent biocompatibility and corrosion resistance due to its native oxide layer. As indicated in above research, open-celled pure titanium foams were fabricated by vacuum hot pressing of a blend of Ti and NaCl powders followed by NaCl removal in water. However, the Ti6Al4V/NaCl mixture is difficult to be densified by the hot pressing due to the higher creep resistance of this alloy at 790 °C [17]. Promising approach to produce Ti alloys is SPS process. The SPS can easily sinter Ti and Ti alloy powders applying pressure and high pulsed DC currents. Thus the local surfaces of the particles melt, allowing junctions to be formed between particles in contact. The present work focuses on the preparation of Ti6Al4V foams by the SPS with post heat treatment using NaCl space holder. The microstructures of the fabricated foams are investigated by scanning electron microscopy, X-ray micro-CT, X-ray diffraction. Their Young's moduli and yield strengths are examined by compression tests. The human osteoblast cell line MG-63 was used to evaluate the cellular acceptance of the foam surfaces.

5.3.2 Experimental procedures

As a basis of the powder mixtures, the Ti6Al4V powder with particle sizes of (5-35) μm and a chemical purity of 99.0% (TLS Technik GmbH & Co, Germany) was blended with 99.0% pure NaCl powders of sizes of the grains between 125 μm and 250 μm with poly (vinyl alcohol) as a binder.

The SPS experiments were performed using the SPS system installed at the Tycho Sinter Lab in the University of Rostock. All blends were SPS treated under vacuum in cylindrical graphite dies. After heating the samples with a rate of 100°C/min up to 700°C, a pressure of 50 MPa was applied for 8 minutes to get disc-shaped pellets (20 mm diameter, thickness (5-7) mm). Porous Ti6Al4V foams were obtained through

dissolution of the NaCl phase in renewed deionized water for 72 hours at room temperature. The alloy foams were cleaned in an ultrasonic water bath for 30 minutes and furnace dried at 120°C for 12 hours. By changing the weight ratio of NaCl, a series of samples with different porosities were obtained. In addition, a SPS post heat treatment was used to increase the density and strength of the foams. It was carried out by a pressureless mode of the SPS. The set-up of the pressureless SPS is shown in Figure 5-9. A small gap d greater than or equal to 0 mm was designed to avoid damaging the porous materials. The foams after the NaCl being removed were spark plasma sintered at 1100 °C for 5 minutes in this pressureless mode.

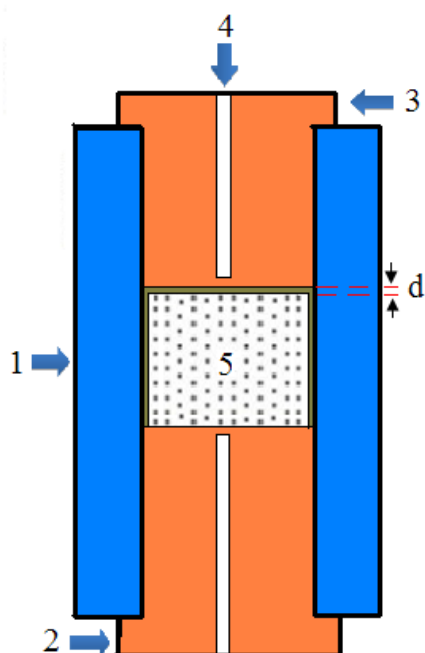


Figure 5-9 Schematic diagram of the graphite die set-up for the pressureless mode of the SPS (1. graphite form, 2. graphite bottom punch, 3. graphite up punch, 4. Pyrometer measurement hole, 5. sample, d . gap ≥ 0 mm).

The density of the samples was measured by the Archimedes method in water. The mass of the samples was measured on a balance. The sample was attached to a thread and fully immersed in a small beaker with water, without touching the bottom of the beaker. The weight of the sample in water was measured, whereby the loss of weight of a sample when suspended in water is equal to the mass of fluid displaced, from which its volume and hence density can be calculated. The microstructures of the

porous Ti6Al4V were analyzed by using a scanning electron microscope (Zeiss Supra 25, Germany). The pore structure of the sample was analyzed with an X-ray micro-CT (GE, USA). The specimens were mounted on a rotary stage and scanned over the whole volume, being rotated by 360° in 1400 equiangular steps (4 pics per 1°). The detector size is 2284 pixel in x and y and 2304 pixel in z direction. The voxel size of the images is 10.2 μm in all three axes. The phase composition was analyzed using high energy synchrotron radiation (42.58 keV) at Beamline P02.2 (Petra III/ Desy). Mechanical tests were conducted by uniaxial compression experiments at room temperature. The standard specimens were 20 mm in diameter and height. The stress measurements were carried out on a universal testing machine Instron 8520, equipped with a 250 kN load cell at 0.5 mm/min. The strain was measured with the travel distance of the testing machine. The compressive yield strength was determined from the stress-strain curve according to the 0.2% offset method [18].

The human osteoblast-like cell line MG-63 (ATCC, CRL-1427, LGC Promochem, Wesel, Germany) was used for the evaluation of the cellular acceptance of the surfaces [19]. In general, the cells were cultured in Dulbecco's modified Eagle's medium (DMEM) with 10% fetal calf serum (FCS, PAA), and 1% gentamicin (Ratiopharm GmbH, Ulm, Germany) at 37 °C in a humidified atmosphere with 5% CO₂. For cell analyses, 1x10⁵ cells were grown on the porous Ti6Al4V plates for 24 hours, fixed with 4% glutaraldehyde (1 h), dehydrated through a graded series of acetone, dried in a critical point dryer (K 850, EMITECH, Taunusstein, Germany) and sputtered with a coater (SCD 004, BAL-TEC, Balzers, Lichtenstein). The samples were investigated with a SEM DSM 960A (Zeiss, Germany).

5.2.3 Results

The Ti6Al4V powders have spherical morphologies and size distributions of (5-35) μm. The cuboidal sodium chloride powders have round angles and a size distribution of (125-250) μm. In the preparation process, the size of the metal powder should be smaller than the average powder size of the space holder. By choosing the size, shape and quantity of the space holder material, the mechanical properties of the metal foams can be adjusted.

Table 5-2 shows a summary of the Ti6Al4V foam parameters after spark plasma sintering. Different weight ratios of NaCl powders were mixed with the Ti6Al4V powders to get various porosities. After the foams were SPSed at 700°C, they show porosities of 47.6%, 57.6%, 63.9% and 72.5% (± 1.0)%, respectively. When they were post heat treated at 1100°C, they display porosities of 44.7%, 54.4%, 60.7% and 70.0% (± 1.0)%. The densities of the foams have been increased 5.5%, 7.5%, 8.9% and 9.1% at above specific porosities after the heat treatments.

Table 1 Summary of parameters of the Ti6Al4V foams after spark plasma sintering.

Parameters	3 g Ti6Al4V /1.02g NaCl	3 g Ti6Al4V /1.6 g NaCl	3 g Ti6Al4V /2.2 g NaCl	3 g Ti6Al4V /3.4 g NaCl
Density after SPS at 700 °C (g/cm ³)	2.32	1.88	1.60	1.22
Density after heat treatment at 1100 °C(g/cm ³)	2.45	2.02	1.74	1.33
Porosity after SPS at 700 °C (%)	47.6	57.6	63.9	72.5
Porosity after SPS at 1100 °C (%)	44.7	54.4	60.7	70.0
Relative density after SPS at 700 °C (%)	52.4	42.4	36.1	27.5
Relative density after heat treatment at 1100 °C (%)	55.3	45.6	39.3	30.0
Increments in density	5.5 %	7.5%	8.9%	9.1%

Density of dense Ti6Al4V 4.43 g/cm³

Detailed microstructural views of the Ti6Al4V foam with 70.0% porosity are shown in Figure 5-10. Figure 5-10a and b display the foams fabricated at 700°C and 50 MPa. They show the porous structure and pore walls, revealing relatively uniformly shaped macropores having rough surfaces, with many micropores (<10 μ m) and the shapes and the sizes of the original alloy powders being visible. This indicates that the Ti6Al4V/NaCl mixture is difficult to be densified and, as expected, the diffusion at 700°C was not sufficient to smooth the micropores due to the very high melting point of Ti6Al4V. Figure 5-10c, d display the Ti6Al4V foams post heat

treated at 1100°C at a pressureless mode. After the heat treatment, the junctions between the Ti6Al4V powder grains are formed with only few micropores left. As seen in Figure 5-10d, most of the micropores disappeared due to the heat treatment. This indicates that the pressureless heat treatment contributes to reduce the microporosity of the foams, since no pressure was applied and only diffusion dominated the SPS process. Thus, Ti6Al4V foams with higher density of the walls have been fabricated by the SPS at 700°C and the post heat treatment at 1100°C.

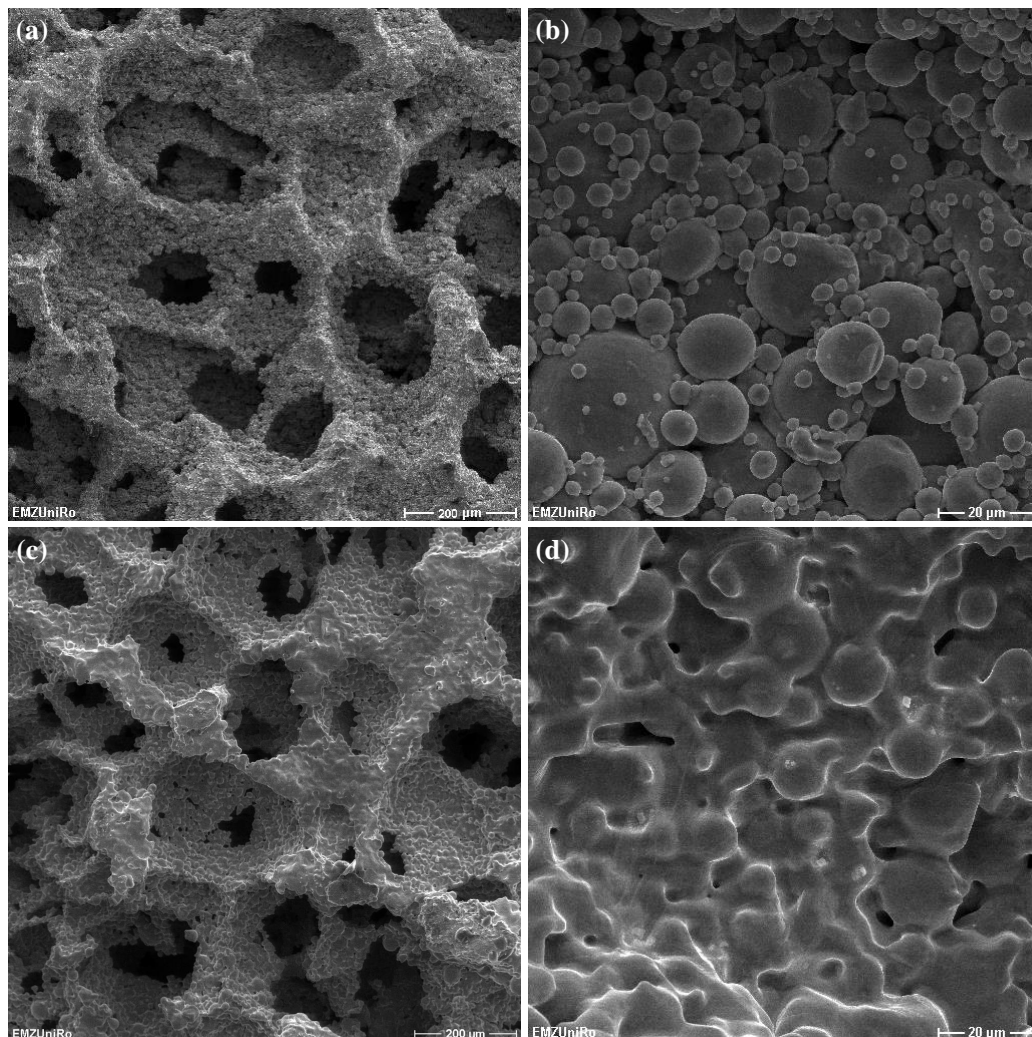


Figure 5-10 SEM images of the porous structures and pore walls of the Ti6Al4V foams with 70% porosity of the spark plasma sintered at 700°C, 50 MPa (a, b), and SPS post heat treatment at 1100°C (c, d).

The outer shape of the Ti6Al4V foam with 54.4% porosity fabricated by the SPS with post heat treatment is shown in Figure 5-11a. Figure 5-11b, c, d display the

micro-CT 3D reconstructions of the foam. The 3D cropped isometric view of cross sections in the Ti6Al4V foam shows the relative uniform pore distribution and interconnected 3D porous structures. The Micro-CT 2D top view and side views show that the macropore shapes are in square cross sections with a relative uniform distribution of pore sizes of $(210 \pm 40) \mu\text{m}$ with an average cell wall thickness of $(22.1 \pm 5) \mu\text{m}$.

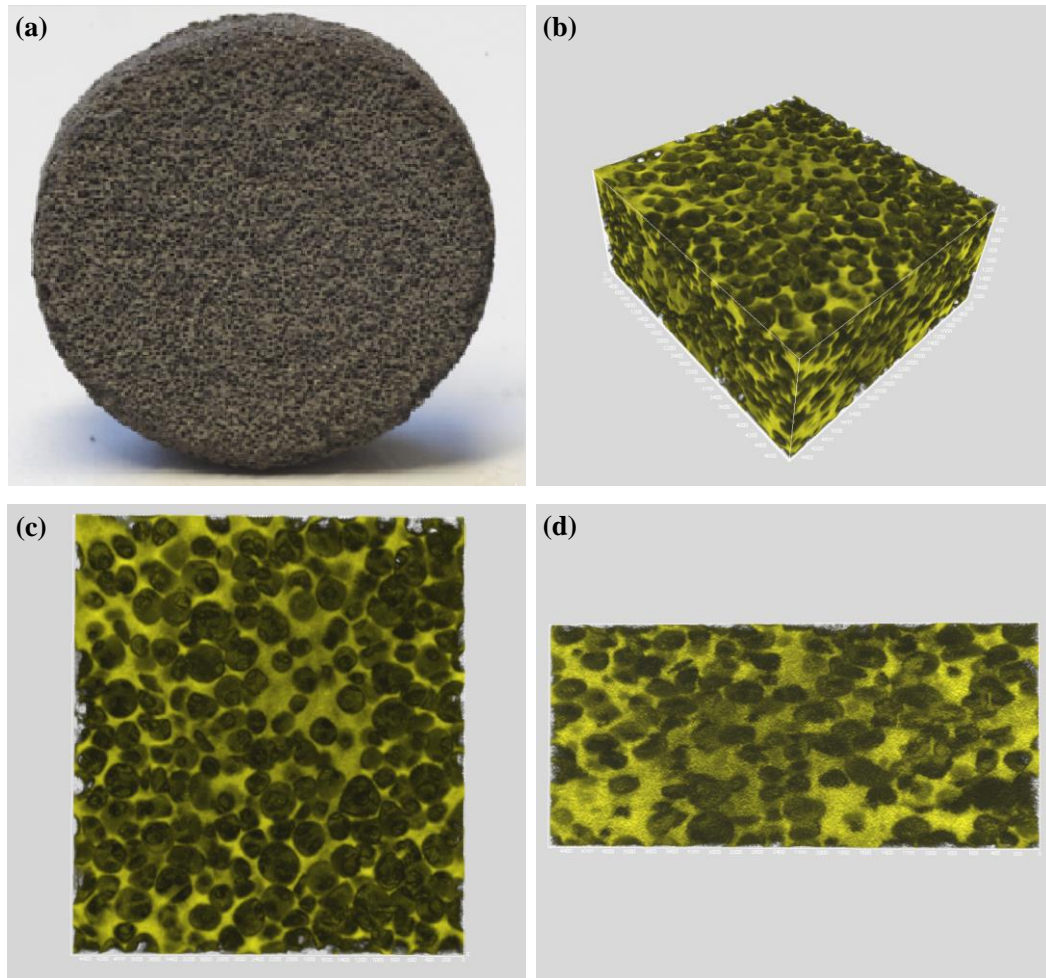


Figure 5-11 Micro-CT three-dimensional 3D reconstructions of the Ti6Al4V foam (54.4% of porosity) with outer shape of the alloy foam (a), an isometric view (b), 2D top view (c), left side view (d) (scale bar $200 \mu\text{m}$).

Figure 5-12 shows the SEM micrographs of the porous Ti6Al4V foams with different porosities of 44.7%, 54.4%, 60.7% and 70.0% (± 1.0)% fabricated by the SPS with post heat treatment. The macrostructure of the foam is composed of

homogeneously dispersed porous cavities and continuously connected Ti6Al4V struts. It shows mean pores with a size of 150 μm to 250 μm achieved with a NaCl spacing material in the range of 125 μm to 260 μm . The thickness of the pore walls decrease with increasing porosity. The higher porosity samples show good interconnectivity. The primary pores replicate the size and shape of the angular NaCl particles with rounded corners. Thus, pore shapes can be controlled by using NaCl powders with various shapes. Finally, interconnected pores are visible either as black pores or as necks between adjacent pores in cross sections. These interconnected pores usually ranged (20-150) μm in sizes, indicating that osteoblasts may be able to penetrate into the porous structure.

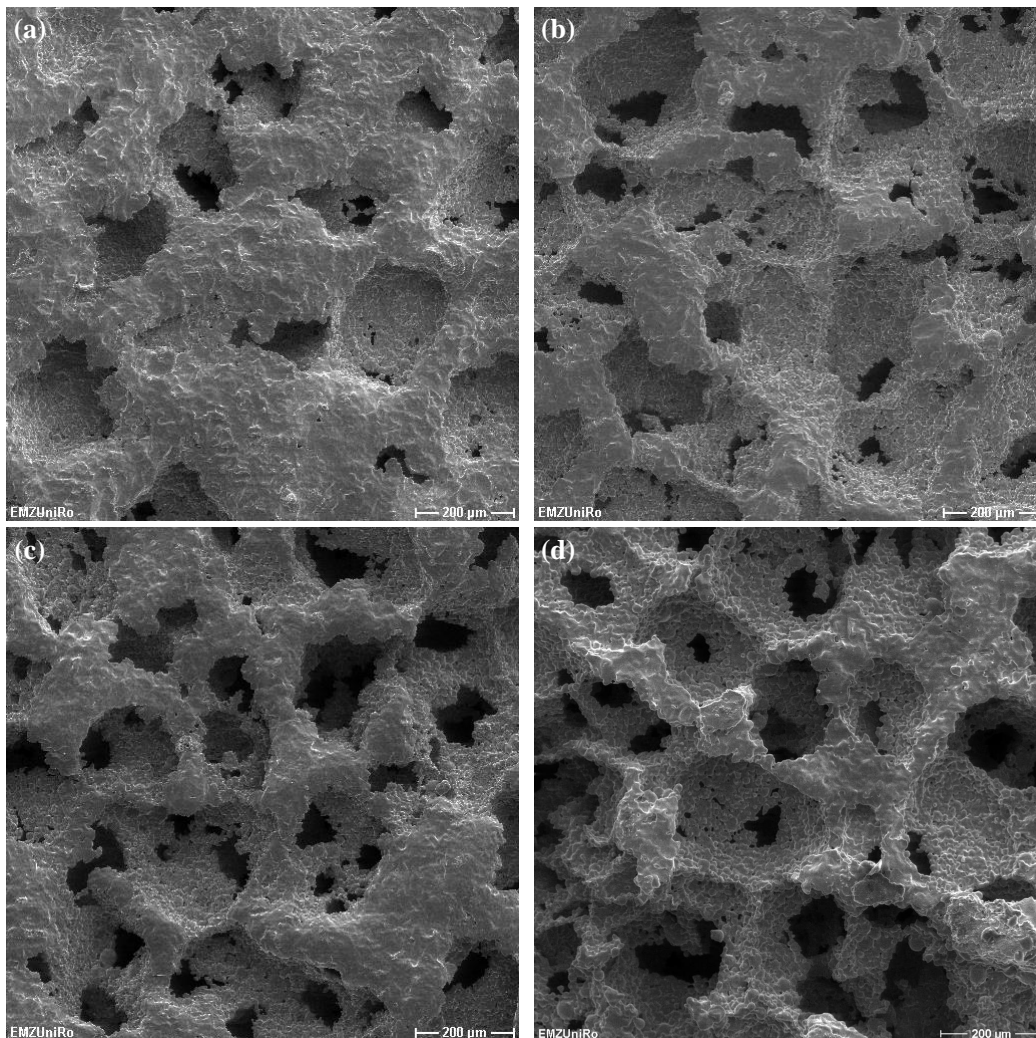


Figure 5-12 SEM images of the Ti6Al4V foams prepared by SPS with post heat treatment with different porosities of (a) 44.7%, (b) 54.4%, (c) 60.7%, (d) 70.0% (± 1.0)%.

Figure 5-13 demonstrates the synchrotron radiation high energy X-ray diffraction of Ti6Al4V foams produced by SPS. The diffraction pattern confirms the α -Ti phase in the Ti6Al4V powder. The α -Ti phase is still present in the Ti6Al4V foams after the SPS process at 700°C. In addition to the crystalline diffraction peaks of the α -Ti phase, peak of β -Ti (110) phase are visible. After the post heat treatment by the SPS at 1100°C, it shows that the intensity of the α -Ti (002) peaks is weaker and the peak of β -Ti (110) phase is stronger than those in the 700°C sintered sample. Additionally, β -Ti (211) plane was detected in the 1100°C sintered sample. However, there are no impurity peaks visible in the XRD patterns. The X-ray diffraction obtained from the porous Ti6Al4V in Figure 5-13 proved that the space holder NaCl phase was removed completely. The post heat treatment has increased the ratio of the β -Ti phase in the microstructures.

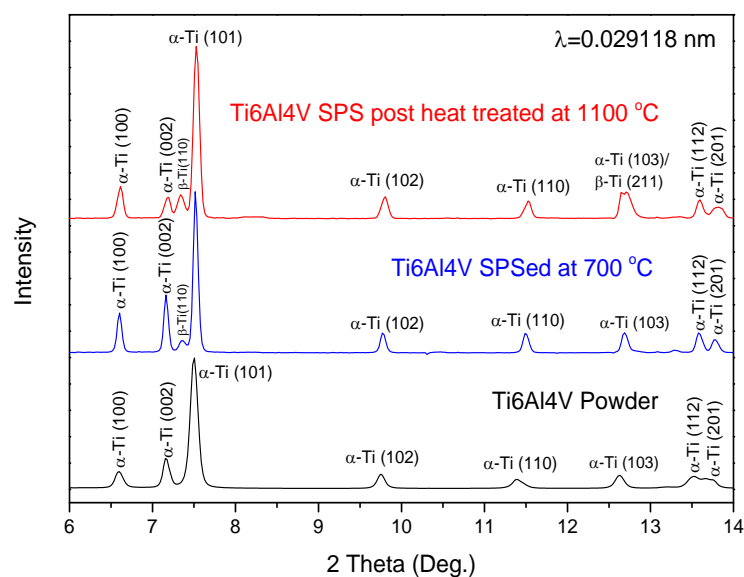


Figure 5-13 Synchrotron Radiation high energy X-ray diffraction patterns of the Ti6Al4V powder and spark plasma sintered Ti6Al4V foams.

For the evaluation of the mechanical properties of the porous samples, compression tests were performed. Figure 5-14a shows the Young's modulus and compressive yield strength as a function of relative density for the Ti6Al4V foams and the predicted theoretical values. The Young's modulus of the porous metals is compared

with a prediction according to the Gibson and Ashby model. The estimated Young's moduli ranging from 34.11GPa to 9.84GPa obey exponential decays with the increase of porosity, and the actual measured Young's moduli of the foams are comparable with the calculated Young's modulus based on the density of the Ti6Al4V foam. Besides the Young's modulus, the strength is an important property of orthopedic implants, in particular in load bearing applications. According to the Gibson-Ashby model, the yield strength of Ti6Al4V foams and predicted theoretical values for open porous material are given in Figure 5-14b. It can be seen that the measured values for porous Ti6Al4V are slightly higher than the analytical predictions by Gibson and Ashby for open structures, also much higher than the compressive strength of cancellous bone (10-50MPa). The experimental values are all comparable with the calculated data obeying the Gibson and Ashby model.

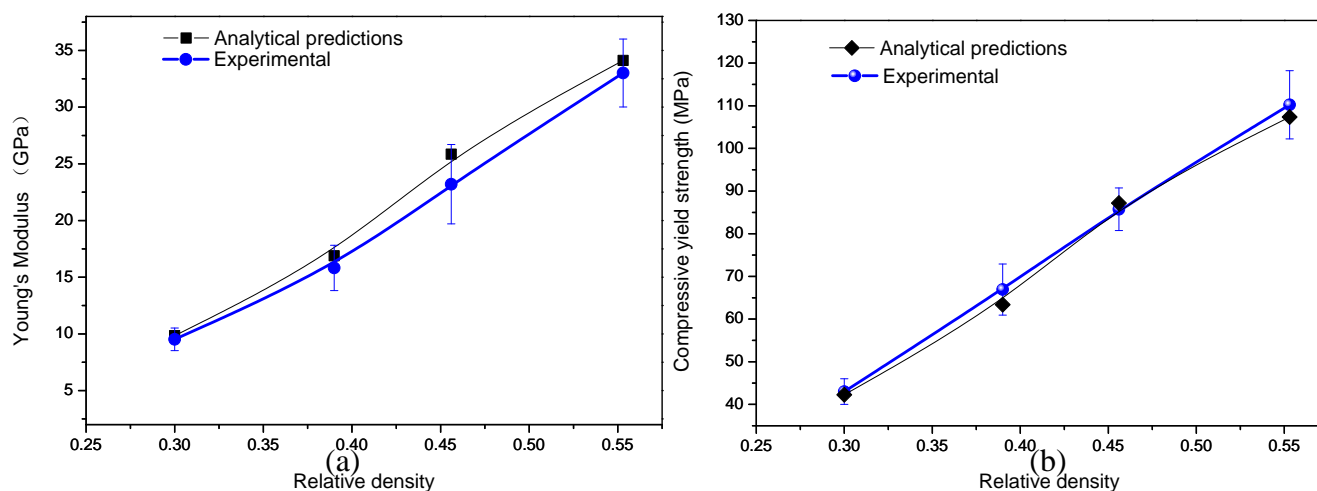


Figure 5-14 Young's modulus (a) and yield strength (b) of the Ti6Al4V foams and theoretically predicted values.

Figure 5-15 shows the SEM images of the Ti6Al4V foams (44.7%porosity) after the compressive tests. The macropores have been compressed to a crushed shape. However, there were no bulk cracks been observed. By this way, it can adsorbe a large amount of energy. The strength of the foams depends on the thickness of the struts. The 44.7%porosity foam has the largest yield strength and Young's modulus (Figure 16) due to the the thickest struts in this group of the prepared samples.

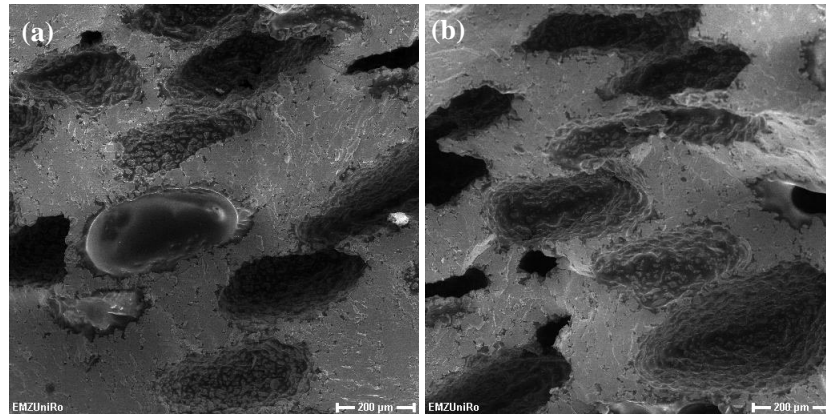


Figure 5-15 SEM images of the Ti6Al4V foams (44.7% porosity) after the compressive tests showing the crushed shape pores of different places (a) and (b).

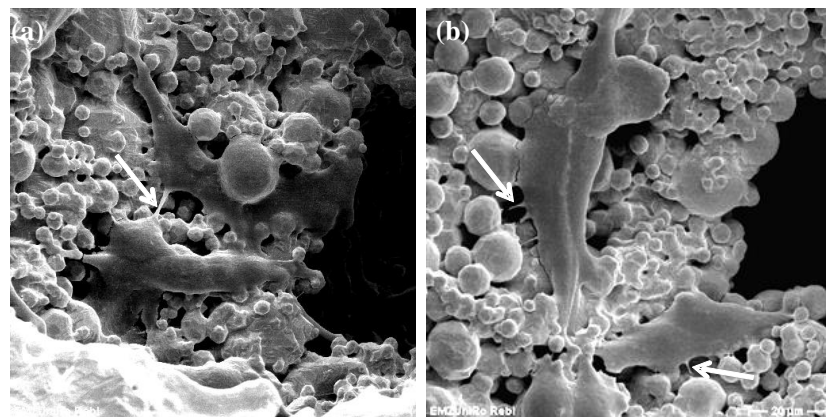


Figure 5-16 SEM of human bone-like MG-63 cells on porous Ti6Al4V foams (a) 54.4%, (b) 60.7%. The cells display a well spread morphology and moreover the cells extend various filopodia to the adjacent grains (arrow).

Human osteoblast like cells (MG-63) were cultured on the porous Ti6Al4V samples. Figure 5-16 shows the SEM images of human bone-like MG-63 cells on porous Ti6Al4V foams with 44.7%, 54.4%, 60.7%, and 70.0 % (± 1.0)%. After 24 hours they exhibit a well spread morphology and excellent bonding to the surface. The cells form filopodia to reach the adjacent grains of the Ti6Al4V structure. The cells grow inside the pores to a large extent implying a good integration when implanted into the bone. For a better interconnectivity, higher porosity Ti6Al4V foams (above 60%) are recommended for the biomedical applications. This cell tests display that the pore sizes and porous surface of the Ti6Al4V foams fabricated by the SPS are suitable for the osteoblasts in-growth.

5.2.4 Discussion

In this study, the Ti6Al4V foams were fabricated by using SPS at 700 °C with controlled porosity followed by dissolution of NaCl phase and post heat treatment at 1100°C. The NaCl has a melting point of 801 °C. In the actual experiments, the temperatures of 650 °C, 700 °C, 720 °C, 750 °C have been tested in the first step of SPS. At 720 °C, a little NaCl melted and reacted with Ti resulted in some impurities formation. At 750 °C, most of NaCl spacer melted and the expansion of the sample destroyed the graphite die. The sintering temperature was determined as 700 °C finally. A relative higher pressure of 50 MPa allows the use of pressure to enhance the densification of the Ti6Al4V/NaCl mixture. The higher pressures from 60 to 80 MPa have been tested. At these pressures, the graphite dies were easy to break due to the thermal expansion of the Ti6Al4V/NaCl mixture during sintering. In the end, the parameters of 700°C and 50 MPa were selected. Previous investigations showed that high-density pure Ti foams can be fabricated with NaCl as space holder by the SPS at 700 °C and 50 MPa. However, the Ti6Al4V/NaCl mixture cannot be densified at the same condition. It indicates that this Ti6Al4V/NaCl mixture is difficult to be consolidated either in the hot pressing [17] or in the SPS. The Ti6Al4V foams were post heat treated by the pressureless SPS method at 1100°C for 5 minutes. The alpha-beta transus temperature of the Ti6Al4V alloy is about 1000 °C. In the second run, several temperatures (1050 °C, 1100 °C, 1150 °C and 1200 °C) over the transus temperature were tested. The results indicated that at 1050 °C it cannot densify the foam walls well. At 1150 °C and 1200 °C, the samples were overheated with melting of grain boundaries. Hence, the 1100 °C as the optimal heat treatment temperature was confirmed. The densities of the foams have been increased as shown in Table 1. The relative density values can give the information of macroporosity and microporosity in the foams. The macroporosity determined by the fraction of NaCl spacer after the SPS at 700°C and dissolution in water. The post heat treatment by pressureless SPS at 1100°C will contribute to reduce the microporosity of the foams. As the schematic diagram of the graphite die set-up for the pressureless SPS in Figure 1 indicated, the gap d is greater than or equal to 0 mm between the top punch and the sample. When

the gap is zero, the current can pass through the sample at the beginning of sintering. After densification and shrinkage of the sample, it became into an open circuit again. When the gap is greater than zero, it is an open circuit. The current can only pass through the graphite punch and outer form, but not the sample. The sample was heated by the temperature field of the graphite die. There was no pressure being applied; therefore, the surface diffusion, volume diffusion and grain boundary diffusion dominated the densification process in the pressureless SPS. These diffusions mainly play roles of reducing the microporosities in the foams. This pressureless SPS is similar to a conventional pressureless sintering. The only difference between them is the efficiency where the pressureless SPS is much faster with a faster heating rate and a shorter soaking time. This post heat treatment by the pressureless SPS is similar to the technique of hot isostatic pressing (HIP) used to reduce the microporosity of metals and to increase the density of many ceramic materials, thus improving the material's mechanical properties. The post heat treatment by the pressureless SPS can be done in vacuum and argon gas up to 40 hPa. The results in this study indicate that this pressureless SPS method can be used for post heat treatment of Ti6Al4V foams, and possibly for all the metallic foams, dense metals and ceramics.

Because of the passive oxide film that formed at room temperature, the Ti alloys has very good corrosion resistance. The oxide films on the powder surfaces would probably have some effects on the sintering temperatures; however, it is not noticeable during the SPS process. In another side, the biological properties of a Ti implant depend on its surface oxide film [20]. The TiO₂ has good cell biocompatibility and it is already used as a coating on many Ti alloys [21]. In this study, there are no bad effects been observed for the oxide films interaction with the MG-63 cells. Consequently, this method using SPS by dissolution of NaCl spacer and post heat treatment provides a foamed structure with a close to homogenous pore structure, high levels of porosity and improved mechanical properties. The mechanical properties of the metal foam can be adjusted by choosing the size, shape and quantity of the space holder material used. The highly porous nature of the alloys

combining improved mechanical properties with osteoconductivity makes these materials ideal for bone scaffolds. The future highlights will be net-shape processing of foams with complex forms by the SPS method. Prospectively, this kind of Ti6Al4V foams is potential to alleviate the problem of mechanical mismatch between the bones and the Ti alloy implants and may provide a new candidate as a long-term bone substitute for biomedical applications.

5.2.5. Summary

Ti6Al4V foams were fabricated by the SPS with post heat treatment using a blend of Ti6Al4V and sodium chloride powders. The Ti6Al4V foams fabricated at 700°C and 50 MPa in SPS cannot achieve high relative densities. The sintered foams were post heat treated in a pressureless mode of the SPS at 1100°C for 5 minutes. This heat treatment is very effective to reduce microporosity and to densify the foam walls. Young's moduli of the foams were in the range of (33.0 ± 3.2) GPa to (9.5 ± 1.0) GPa and the yield strengths ranged from (110.2 ± 8.0) MPa to (43.0 ± 2.8) MPa with porosity values from 44.7% to 70.0% (±1.0)% obeying the Gibson-Ashby models. The human osteoblast cell line MG-63 validated the cellular acceptance of the foam surfaces. This pressureless SPS method can be used for post heat treatment of Ti6Al4V foams, and possibly for all the metallic foams and dense solids.

5.3 Other methods for preparation of titanium foams by SPS and surface modification

5.3.1 Other methods for preparation of Ti foams by SPS

Besides NaCl particles as spacer material, some other ways to fabricate Ti foams by the SPS were also tried and studied. Fig.5-17 shows the SEM images of the Ti6Al4V foams prepared by SPS using Cu spacer. The Ti6Al4V powders and Cu powders were mixed and sintered by SPS at 800 °C and 50 MPa for 5 min soaking time. Then the Cu spacers were removed by high concentration HNO₃ acid washing. Finally, they were washed in deionized water to get a neutral PH value. The porous foams were obtained. The porous structures at various magnifications show that the pores are

interconnected with pore sizes from 10 to 200 micrometers. The pore walls show that there are many TiO_2 nanostructures formed on the surfaces. Its formation is due to the strong acid oxidation. The TiO_2 nanostructures could increase the bioactivity and cell adhesion property of the Ti6Al4V foams.

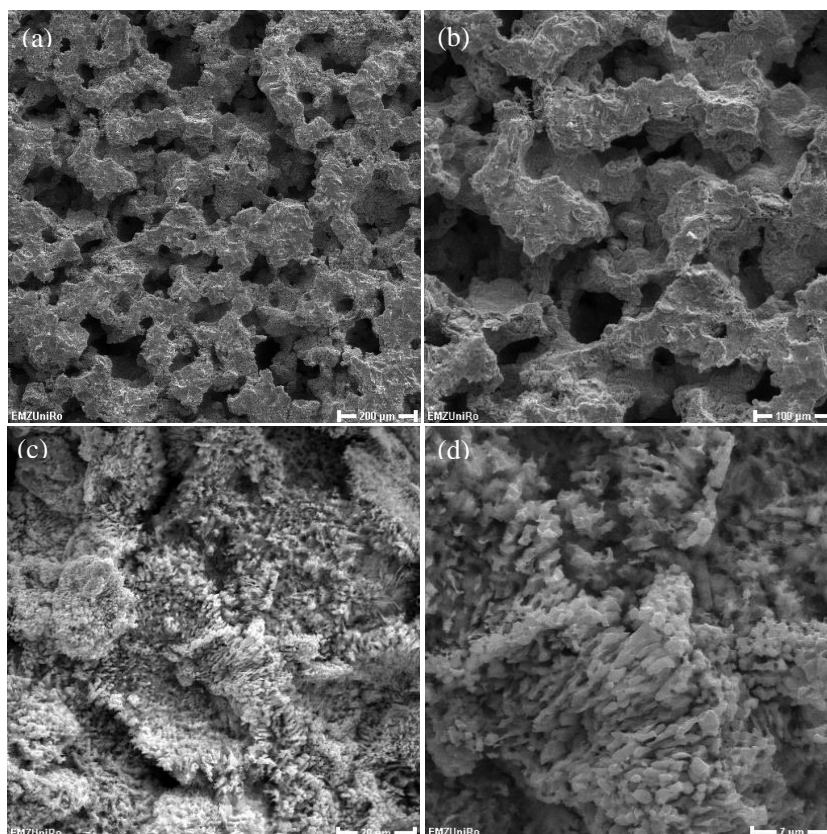


Figure 5-17 SEM images of the Ti6Al4V foams prepared by the PECS using Cu spacer: (a, b) porous structure at various magnifications and (c, d) pore walls shows the TiO_2 nanostructures.

Another method to prepare the Ti foams is the simulated body fluid soaking of the sintered TiMg solids. It is an in-situ pore formation method. The TiMg solids were prepared by ball milling of Ti and Mg powders and SPS at 600 °C and 50 MPa for 5 min. Figure 5-18(a) shows the XRD diffraction results of the TiMg solids with 10-40 wt% fraction of Mg. It exhibits pure Ti and Mg phases, no intermetallic phases. Afterwards, they were immersed in the simulated body fluid for several weeks. Figure 5-18(b) exhibits the surface of the Ti-40 wt%Mg solids before the body fluid soaking. Figure 5-18(c) shows the in-situ formed macropores after 4 weeks soaking in the

simulated body fluid. The pore sizes are about 500-700 μm in dimension. The pore wall in Figure 5-18(d) shows the microstructures after body fluid soaking and some hints of corrosions can be found. The dense TiMg solids can load higher forces than the porous Ti foams. After they were implanted *in vivo*, the Mg composition in the TiMg solids will be degraded by body fluid immersion to form porous foams with time going. The bone tissue would grow into the foams simultaneously with the pore forming progress. The key issue of this method is how to match the growth rate of the bone tissue. It can be realized by tailoring the fraction of Mg in the Ti alloy and the alloying elements in the Mg phase (e.g. Zr, Ag etc.).

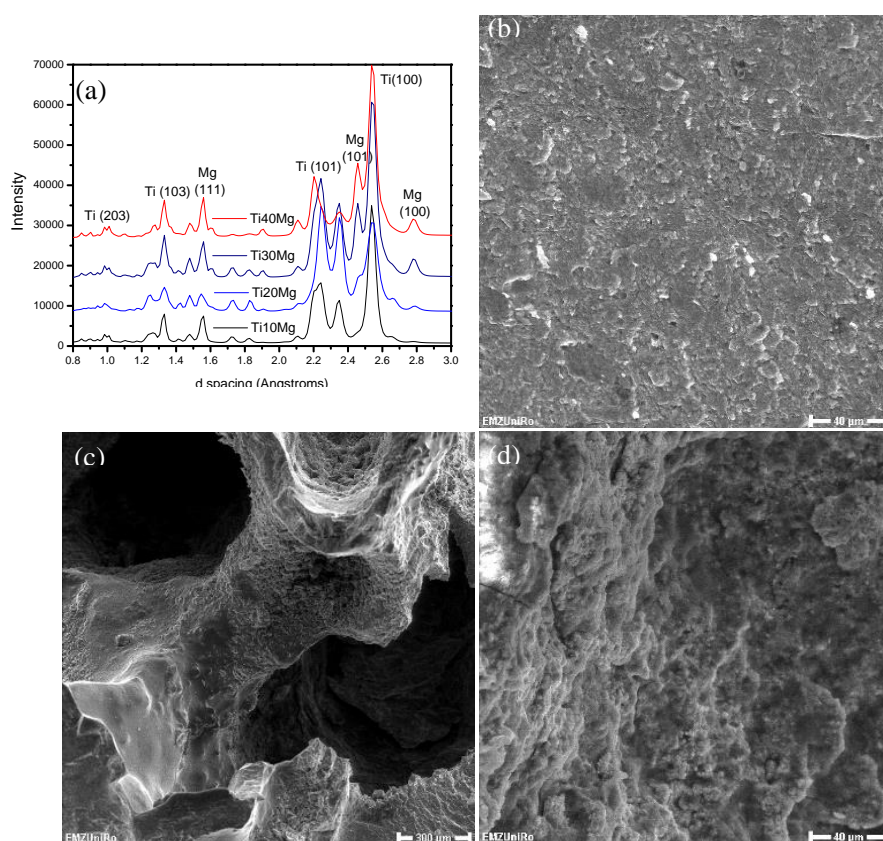


Figure 5-18 XRD results of the SPS prepared TiMg system (a) and SEM images the surface of the Ti40Mg sample (b), in-situ formed macropores in the simulated body fluid (c) and pore wall structure (d).

5.3.2 Surface modification

Our previous research indicated that TiMn alloys with superior mechanical properties and acceptable cytocompatibility could be used as bone implants. In this part, porous TiMn foams were prepared by using the spark plasma sintering technique and the surface was subsequently modified with TiO₂ nanostructures. The in vitro bioactivity of the TiO₂ modified Ti8Mn foams was investigated in a simulated body fluid.

The TiMn foams were prepared with NaCl spacer by the SPS and then surface modified by immersing in a NaOH solution at 60 °C for several hours. The foams were washed and heat treated at 600 °C. The surface modified TiMn foams were suspended in polystyrene bottles containing simulated body fluid solution at 37.0 °C in a shaking bath. At certain times, the samples were taken out, rinsed with deionized water, and dried in an oven. X-ray diffraction (XRD, Bruker D8, Germany) was used to characterize the phase composition of the sintered foams. Scanning electron microscopy (SEM, Zeiss Supra 25, Germany) equipped with EDX was employed to analyze the microstructures of the sintered foams.

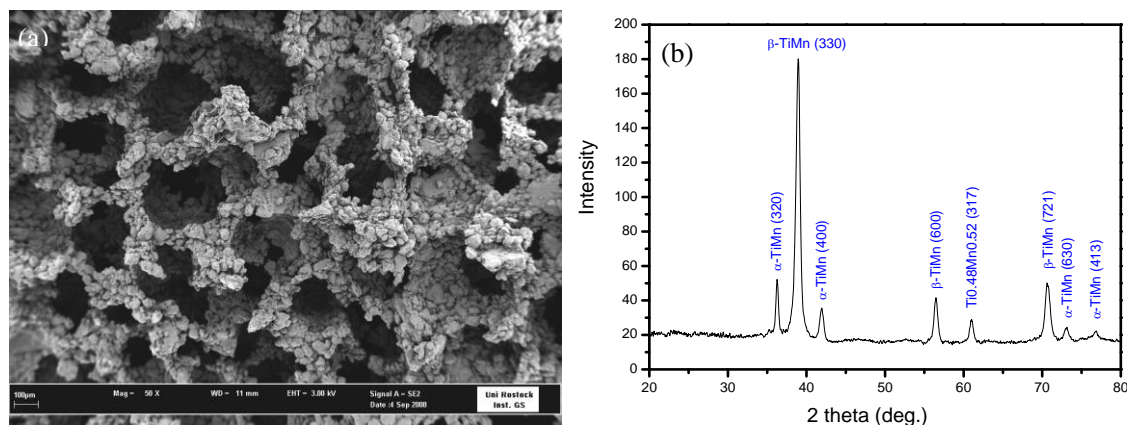


Figure 5-19 SEM micrograph of the TiMn foam (a) and X-ray diffraction pattern of the TiMn foam showing the phase compositions (b).

The SEM micrograph of the TiMn foams prepared by spark plasma sintering at a temperature of 700 °C under 50MPa is shown in Fig. 5-19 (a). This TiMn foam shows a measured porosity of 65%, and pore sizes of about 300 μm with interconnected pore distributions. The X-ray diffraction pattern in Fig. 5-19 (b) shows that the TiMn foam

consists mainly of β -TiMn phase in cubic structure. There is still a small amount of an α -TiMn phase in the foam. This shows that the synthesized TiMn alloy foam has $\alpha+\beta$ microstructures similar to those of the standard Ti6Al4V alloys.

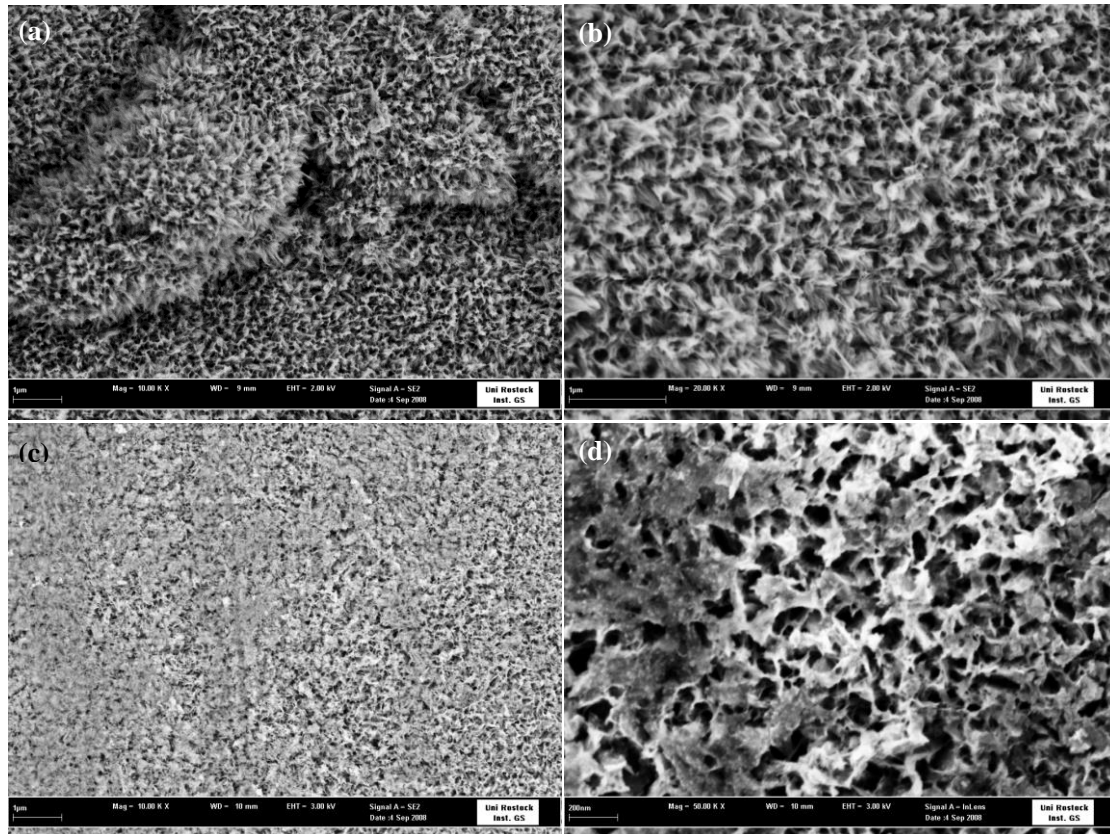


Figure 5-20 SEM micrographs of the surface modified TiMn foam with TiO₂ anatase/rutile nanostructures showing the uniform oriented nanofibers (a,b) and immersed in simulated body fluid for 3 days with EDX indicating the apatite formation (c-e).

The SEM micrographs of a TiMn foam sample with through TiO₂ nanostructures modified surface are shown in Fig. 5-20. The oriented nanofibers structures cover all the pore walls of the TiMn foams with a uniform distribution (Fig. 5-20a, b). X-ray diffraction confirmed the TiO₂ nanostructures as anatase/rutile phases [22]. After only 3 days soaking in the simulated body fluid, the SEM micrographs exhibited that some particles were covered on the nanofibers of the foams (Fig. 5-20c, d). The EDX identification in Fig.5-20(e) confirmed that these particles are bone-like apatite (hydroxyapatite) with elements of Ca, P, O, Mg, Na, K and C. The deposition of the apatite on the pore walls is a biomineralization process. It is indicated that the nano-TiO₂ surface modified Ti8Mn foams have a high *in vitro* bioactivity, which can lead to a high bone-bonding ability of these foams *in vivo*.

5.3.3 Summary

The Ti6Al4V foams with Cu spacer were prepared by the SPS. The pore walls were modified with TiO₂ nanostructures. The in-situ pore forming method by soaking of the TiMg solids in the simulated body fluid was also introduced. Ti8Mn foams with porosity of 65% and pore size of 300 μm were prepared by using the spark plasma sintering technique. Ti8Mn foams with porosity of 65% and pore size of 300 μm were prepared by using the SPS technique. The TiMn foam showed α+β microstructures. TiO₂ nanostructures in anatase/rutile phases were created on the pore walls of the TiMn foams. The surface modified TiMn foams exhibited high *in vitro* bioactivity with apatite formation in the simulated body fluid after 3 days soaking.

References

- [1] J.P. Li, S. H. Li, C.A. Van Blitterswijk, K. de Groot, A novel porous Ti6Al4V: characterization and cell attachment, *J Biomed Mater Res A* 2005, 73(2): 223-233.
- [2] K. Masayuki, L.M. Hirakata, K. Asaoka, Porous Ti-6Al-4V alloy fabricated by spark plasma sintering for biomimetic surface modification, *J. Biomed. Mater. Res. B* 2003, 68(1): 88-93.
- [3] Y. Sakamoto, K. Asaoka, M. Kon, T. Matsubara, K.Yoshida, Chemical surface modification of high-strength porous Ti compacts by spark plasma sintering, *Bio-Med. Mater. Eng.* 2006, 16(2): 83-91.
- [4] R. Nicula, R. Lüthen, M. Stir, B. Nebe, E. Burkel, Spark plasma sintering synthesis of porous nanocrystalline titanium alloys for biomedical applications, *Biomolec. Eng.* 2007, 24(5):564-567.
- [5] I.H. Oh, H.T. Son, C.S. Kang, J.S. Lee, J.I. Cho, J.C. Bae, B.T. Lee et al. Mechanical properties and biocompatibility of porous titanium prepared by powder sintering. *Materials Science Forum* 2007,

539-543: 635-640.

- [6] T. Chandra, J.M. Torralba, T. Sakai. Sintered porous titanium and titanium alloys as advanced biomaterials. *Materials Science Forum* 2003, 426-4: 3079-3084.
- [7] L. J. Gibson, M. F. Ashby, *Cellular Solids: Structure and Properties 2nd*, Cambridge. 1997, pp. 175–281.
- [8] C. E. Wen, Y. Yamada, K. Shimojima, Y. Chino, T. Asahina, M. Mabuchi. Processing and mechanical properties of autogenous titanium implant materials. *J. Mater. Sci.: Mater. Med.* 2002,13(4): 397-401.
- [9] M. Long, H.J. Rack, Titanium alloys in total joint replacement--a materials science perspective. *Biomaterials* 1998, 19(18):1621-1639.
- [10] D.M. Liu, Influence of porosity and pore size on the compressive strength of porous hydroxyapatite ceramic. *Ceramics International* 1997; 23:135-139.
- [11] R.W. Rice, Comparison of physical property-porosity behaviour with minimum solid area models. *Journal of Materials Science* 1993; 28(8): 2187-2190.
- [12] W. Niu, C. Bai, G. Qiu, Q. Wang, Processing and properties of porous titanium using space holder technique, *Mater. Sci. .Eng. A* 2009, 506: 148-151.
- [13] A. Schuh, J.L.R. Vidael, W. Hoenle, T. Schmichal. Porous titanium implant materials and their potential in orthopedic surgery, *Materialwissenschaft und Werkstofftechnik* 2007, 12,1015-1018.
- [14] E. Eisenbarth, D. Velten, M. Mueller, R. Thull, J. Breme, Biocompatibility of beta-stabilizing elements of titanium alloys, *Biomaterials* 2004, 25(26): 5705-5713.
- [15] F. Zhang, J. Chang, J. Lu, K. Lin and C. Ning. Bioinspired structure of bioceramics for bone regeneration in load-bearing sites, *Acta Biomaterialia* 2007, 3(6): 896-904.
- [16] M. Geetha, A.K. Singh, R. Asokamani, A.K. Gogia. Ti based biomaterials, the ultimate choice for orthopaedic implants – A review *Export. Progress in Materials Science* 2009; 54(3): 397-425.
- [17] B. Ye, D. C. Dunand, Titanium foams produced by solid-state replication of NaCl powders, *Materials Science and Engineering A*. 2010, 528 (2): 691-697.
- [18] Testing metallic materials; compression test. DIN 50106, Issue:1978-12
- [19] H. Rebl, B. Finke, R. Lange, K-D. Weltmann, J. B. Nebe, Impact of plasma chemistry versus titanium surface topography on osteoblast orientation, *Acta Biomater.* 2012, 8(10):3840-3851.
- [20] B. Feng, J.Y. Chen, S.K. Qi, L. He, J. Z. Zhao, X. D. Zhang. Characterization of surface oxide films on titanium and bioactivity, *J Mater Sci Mater Med.* 2002, 13(5):457-464.
- [21] D.Y. Kim, M. Kim, H.E. Kim, Y. H. Koh, H.W. Kim, J. H. Jang. Formation of hydroxyapatite within porous TiO₂ layer by micro-arc oxidation coupled with electrophoretic deposition, *Acta Biomaterialia* 2009, 5(6): 2196-2205.
- [22] F. Zhang, E. Otterstein, G. Rott, U. Beck, D. G. Weiss, E. Burkel. Preparation and surface modification of TiMn foams for bone implants. *BMT2010*, 5-8, Oct. 2010, Warnamunde, Germany.

Chapter 6 Conclusions and outlook

The indirect evidences for the presence of plasmas in SPS were revealed. The thermal stability of MWCNTs, C60, graphene and graphite has been investigated under the pulsed DC field in a SPS furnace. Cubic diamonds have been converted from pure MWCNTs, pure C60 and graphene without catalysts being involved by the SPS at conditions of 1500 °C, 80 MPa for 20 min. There was no notice of diamond formation in the case of pure graphite sample processed by SPS at this condition. The graphite is the most stable crystalline modification of carbon among the MWCNTs, C60, graphene and graphite allotropes under the SPS. The parallel investigations by using the synchrotron radiation in situ high temperature (AC field) X-ray diffraction show that there is no diamond formation in the MWCNTs, C60 and graphene samples at the same pressure (80 MPa) and temperature (1500 °C). Their phase transitional mechanism from MWCNTs, C60, graphene to diamond indicated the high localized temperatures between particles due to the presence of momentary plasmas during the SPS process. In addition, the SPS experiments are conducted in vacuum and argon atmosphere with carbon nanotubes based materials. Some fractions of sp^3 hydride carbon in the transition stage to diamond are obtained from the pure MWCNTs by SPS at 1500 °C and 9.55 MPa in vacuum and Ar atmosphere. Crystalline cubic diamond crystals are generated from the MWCNTs/FeNi by SPS at 1200 °C and 9.55MPa in vacuum and Ar atmosphere. Flower-like structured carbon and high quality diamond crystals with hexahedron structures are produced only in the Ar atmosphere. Such low pressure diamond formation in both vacuum and Ar gas atmospheres provides an important indirect evidence for the existence of plasma during the SPS. The Ar atmospheres lead to higher currents and voltages during SPS. It is assumed to promote the plasma generation and sizes. The plasmas momentary generated from ionized gas produced temperatures up to thousands of degree and thus promote the diamond transition.

The synthesis of diamond from nanocarbon and graphite by SPS was investigated. MWCNTs with Fe35Ni powders as solvent catalysts were used to synthesize diamond

by SPS. Cubic diamond crystals were synthesized from the MWCNTs/Fe35Ni mixtures at lower SPS temperature of 1200 °C under the pressure of 70 MPa. In the sample, well-crystallized diamond mono-crystals and poly-crystals consisted particle sizes ranged (10–40) μm. The Fe35Ni catalysts achieved an effective reduction of the SPS temperature to 1200 °C and the SPS pressure to 70 MPa for the diamond synthesis, as well as an increment in diamond transitional rate from MWCNTs in the SPS. A model was also proposed to describe the diamond growth and revealed as a layer-by-layer growth mechanism. Fullerene C60 can be transformed into crystalline diamond by SPS under a pressure of 50 MPa above temperatures of 1150 °C without any catalysts being involved. Well-defined diamonds with particle sizes up to 250 nm and transition rate about 30 vol% are obtained at 1300 °C and no further growth in particle size is seen beyond this temperature. The mechanism analysis indicates that the high sp³ hybrid fraction in the C60 and the generated plasmas in the pulsed electric field lead to its transformation to diamond. It is a direct transition process from C60 to diamond with a structural reconstruction of carbon atoms without intermediate phases being involved. Additionally, the Ni, MnNi, MnNiFe and AlCuFe quasicrystal powders were used as the catalysts for the diamond synthesis from graphite by the SPS. Diamond crystals have been converted from the graphite at the SPS condition of 1300 °C, 50 MPa for 20 min. Diamond nano- and micro-rods (80 nm–2 μm) have been obtained with the Ni catalysts from the graphite by the SPS. Diamond crystals with good diamond shapes in the range of (1–3) μm have been converted from the graphite with the AlCuFe catalyst. The diamond/copper composites are prepared by SPS. The composite shows the hard diamond phase with Hardness of (15.1 ± 1.6) GPa embedded in the soft copper matrix with Hardness of (1.45 ± 0.2) GPa with a uniform distribution. .

SPS of titanium alloys for biomedical applications was studied. The α+β type TiMn alloys with high relative density and ultrafine microstructures were prepared by using mechanical alloying for 60 hours and spark plasma sintering at 700 °C for 5 min. The Mn reduced the α to β transformation temperature of Ti and was confirmed as a β stabilizer element. The hardness increased significantly ranging from 2.4 GPa (Ti2Mn)

to 5.28 GPa (Ti12Mn), the elastic modulus ranging from 83.3 GPa (Ti2Mn) to 122 GPa (Ti12Mn) and the ductility decreased ranging from 21.3% (Ti2Mn) to 11.7% (Ti12Mn) with increasing manganese content in the Ti. Concentrations of Mn below 8 wt.% in titanium reveal negligible effects on the metabolic activity and the cell proliferation of human osteoblasts. Therefore, the Mn could be used in lower concentrations as an alloying element for biomedical titanium. The Ti2Mn, Ti5Mn and Ti8Mn alloys all have a potential for use as new bone substitutes and dental implants. Additionally, the SPS has been modified and integrated with a novel nitrogen gas quenching system. The Ti6Al4V alloy is used as a model material for the study of this modified SPS. Finite element simulation results reveal that the gas quenching can increase the heat transfer coefficient up to (5-7) times higher and magnify the temperature gradient of the sample. Experimental results show that sinter-hardening of the Ti6Al4V alloy has been achieved, where the hardness rises from 327 HV1 to 353 HV1 with the cooling rate ranging from 1.6 °C/s to 6.9 °C/s. The ultimate compressive strength and the ductility have increased up to 1832 MPa and 34%, respectively. The gas quenching leads to much more pronounced dimples in fracture surfaces, the precipitation of intermetallic phase and a morphological change to lamellar α -Ti phase in metallography. The rapid cooling-SPS combining sintering and gas quenching provides a novel method to tailor the mechanical properties and microstructures of the Ti6Al4V alloys. The Ti6Al4V alloys could be used widely as bone substitutes and dental implants.

SPS of titanium foams for biomedical applications was investigated. Macroporous pure titanium (Ti) foams with porosity of (30-70) % and pore size of (125-800) μm were fabricated by SPS for bone implant applications. A mixture of Ti and sodium chloride (NaCl) powders were spark plasma sintered at 700 °C under pressure of 50 MPa and the NaCl phase was then dissolved in water. The resulting Ti foams consist of pure α -Ti phase with interconnected macropores in quadratic cross sections. The plateau stress and Young's modulus agree with the Gibson-Ashby models, and coarsely follow a linear decline with the increase of the pore sizes, and exponential decay with the increase of the porosity. The macroporous Ti foams with plateau stress

(27.2-94.2) MPa and Young's modulus (6.2-36.1) GPa have a potential to be used as bone implants. In addition, Ti6Al4V foams were fabricated by SPS with post heat treatment using a blend of Ti6Al4V and NaCl powders. The Ti6Al4V foams fabricated at 700 °C and 50 MPa in SPS cannot get high relative densities. These sintered foams were post heat treated in a pressureless mode of the SPS at 1100 °C for 5 min. This heat treatment is very effective to reduce the microporosity and to fully densify the foam walls. Young's modulus of the foams was in the range of 33.0 GPa to 9.5 GPa and yield strength ranged from 110.2 MPa to 43.0 MPa with porosity values from 44.7% to 70.0% obeying the Gibson-Ashby models. The human osteoblast cell line MG-63 validated the cellular acceptance of the foam surfaces. The pressureless SPS provides a new method for the heat treatment of metallic foams. The Ti6Al4V foams with Cu spacer were prepared by the SPS with a strong acid etching afterwards. The pore walls were modified with TiO₂ nanostructures. The in-situ pore forming method by soaking of the TiMg solids in the simulated body fluid was also introduced. Finally, the Ti8Mn foams with porosity of 65% and pore size of 300 μm were prepared by using the SPS. TiO₂ nanostructures in anatase/rutile phases were modified on the pore walls of the Ti8Mn foam uniformly by NaOH solution soaking and heat treatment. This surface modified TiMn foam exhibited high *in vitro* bioactivity with a fast apatite-forming ability in the simulated body fluid. The Ti, Ti6Al4V and TiMn foams processed by SPS have a potential to be used as ideal bone implants.

What makes the SPS so interesting for the diamond synthesis is the fact that only relatively low pressures of (9-80) MPa are needed. The SPS possesses a wide range of sintering temperatures from a few hundreds up to 2000 °C, controllable heating rates which can be set to several hundred degrees per minute for extremely rapid processing, as well as the capacity to process large samples up to 100 mm in diameter and 20 mm thick. As we know, the HPHT technique only can prepare very small samples in order to achieve the several GPa level high pressures. Therefore, the SPS is a highly efficient and energy saving technique for diamond synthesis. The investigations in this thesis indicate that the SPS, a pulsed electric field processing

technique, has great potential to be used as an alternative and novel method for high-efficiency diamond generation. The diamond generation at such low pressures also provided some indirect evidences for the presence of plasmas during the SPS operation. However, it still needs further investigations to promote the SPS method to be used as a large-scale synthetic diamond production technique. The future highlights will be the development of diamond purification methods to get high purity diamond crystals from the SPSed carbon compacts and the synthesis of millimetre sized diamond crystals and achieving much higher diamond transition rates by using the SPS technique. The functional properties including electrical, thermal, optical, magnetic properties etc. of the SPSed diamond particles and the SPSed carbon samples with in-situ formed diamonds need to be investigated. The in-situ synthesis of diamond/ceramics or diamond/metals composites from CNTs/ceramics or CNTs/metals by the SPS is also a very interesting subject for future researches.

As load bearing and long term hard tissue repair materials, Ti and its alloys are the most outstanding metallic materials nowadays. The modification (processing and/or surface) of the clinic used Ti alloys, and the exploration of new Ti alloy systems for biomedical applications are still the tasks for the future. The sinter hardening by the SPS, in which the parts are sintered and quenched directly after the sintering step, has a perspective future in the powder metallurgy industry due to energy saving and cleanness. For the Ti foams, the development of processing techniques to create controlled porosity, pore sizes and interconnectivity is still required. The relationship between the relative density and mechanical properties of the Ti foams can be predicted well with the Gibson-Ashby model. However, the relationships between the porosity-functional properties (thermal, flow, transport, absorption and so on) are not well modelled yet. The effects of pore architecture, pore size, pore interconnectivity, inter-connective pore size on the mechanical and functional properties of Ti foams are still not clear, and need more investigations. The post heat treatment of materials in the pressureless SPS possibly should be suitable for all the porous materials and dense solids. The in-situ pore forming method represents the tendency of the future in the field of cellular solids. The future highlights will be the preparation of nanostructured

Ti alloys and composites, the processing of Ti alloy foams with complex shapes by using the SPS technique. The application of the SPS in preparation of the biomedical Ti alloys and foams has perspective future.

Acknowledgments

First of all, I would like to thank Prof. Dr. Eberhard Burkel. I can clearly remember five years ago in a cold December, he went to the railway station of Rostock to pick me and my wife up there. I express my gratitude to him for his supports and trusts in research, teaching and laboratory management. He gave me so much freedom to explore new topics and interesting fields. He led me enter the field of synchrotron radiation. He also gave me lots of help and care to my family and children. The time passes gradually, years like shuttle. I have worked with him for over 5 years already. This five years' time is very important for my career. In my life, I will always remember this harvest period time in University of Rostock. Additionally, I would like to thank Prof. Dr. Olaf Kessler for his supports in my Habilitation application in the Faculty of Mechanical Engineering and Marine Technology. I appreciate him for his supports in sample treatments and measurements in the past five years and taking me into the teaching in the Faculty. I have nice experiences collaborating with him in research of gas quenching-SPS and mechanical tests.

Secondly, I would like to acknowledge the financial supports from DFG with Grant No. BU547/10-1, BU547/10-2, and Venture Cup-MV 2011 with No. UR 11007 VC-2011 for the researches in nanocarbon and diamond, and DFG with Grant No. GRK1505/1 (Welisa) for the researches in titanium based biomaterials. I also acknowledge the DESY Projects of II-20090264 and I-20110661 for the synchrotron radiation researches.

I would like to extend my gratitude to all my old and new colleagues in the group of Physics of new materials, Institute of physics. The colleagues are the secretary Mrs. Ulrike Schröder, the technicians Mr. Stephan Flor, Mrs. Christine Benkner and Mrs. Bärbel Przybill, and colleagues of Dipl.-Phys. Eileen Otterstein, M.Sc. Carmen Mihoc, M.Sc. Karina Porath, Dipl.-Phys. Enrico Buchholz, Dipl.-Phys. Matthias Lütgens, Dipl.-Phys. Daniel Schick, Dipl.-Phys. Sebastian Helm, Dipl.-Phys. Gunnar Rott, Dipl.-Phys. Peter Säger, Dipl.-Phys. Kerstin Witte, Dr. Wiktor Bodnar, Mr. Frank Eisenhut, M.Sc. Yujie Quan, M.Sc. Wenwei Gu, M.Sc. Lijun Jing, M.Sc. Qingqing Xu, M.Sc. Rico Schnierer, M.Sc. Dieter Skroblin.

I appreciate the help from all the colleagues in the group of Materials science,

Mechanical engineering department, especially to Dr.-Ing. Wolfgang Kowalski, Dr.-Ing. Michael Reich, Mr. Christoph Schweigel and Mrs. Carola Ladewig for their help in the experiments.

I thank the collaborators involved in the researches. The Raman spectra of diamonds were tested by Dr. Furqan Ahmed in University of Erlangen-Nürnberg University. The TEM of diamonds was partly performed by Dr. Gerd Holzhuter and Mr. Martin Adam in the group of Prof. Thomas Gerber. I thank Prof. Ludwig Jonas, Mr. Fulda Gerhard, Mr. Labs Wolfgang and PD. Dr. Frank Marcus in Elektronenmikroskopisches Zentrum (EMZ) for their supports in the SEM and TEM measurements. The cell experiments were conducted by Dr. Arne Weidman and Ms. Henrike Rebl in the group of Prof. Dr. Barbara Nebe in Medicine Faculty. The compressive tests of porous materials were done in the group of Prof. Rainer Bader. I thank Prof. Dr. Christoph Schick for his supports in the thermal analysis of my samples in past years. I also thank the scientists in DESY Hamburg: Dr. Christian Lathe, Dr. Martin von Zimmermann, Dr. Jozef Bednarcik, Dr. H. P. Liermann for their supports in the beamlines.

My thesis is covered part of my research. Other researches collaborated with Prof. Herman Seitz in porous materials and electron beam melting, with Prof. Detlef Behrend in dental materials are acknowledged.

My Special thanks would go to my beloved family: my wife and two children. I own a great deal of my accomplishments to my wife Ms. Shanshan Wang. Her measureless love, endless support and meticulous consideration give me the power to keep going forward. I would like to thank my parents, parents in law, my two sisters and brother in law for their encouragement and great confidences in me.

Dr. Faming Zhang

Institut für Physik, Universität Rostock

August Bebel Str. 55, 18055 Rostock

Habilitationskommission

Fakultät für Maschinenbau und Schiffstechnik

und

Mathematisch-Naturwissenschaftliche Fakultät

Universität Rostock

02-04-2013

Eidesstattliche Erklärung

Im Rahmen des von mir gestellten Antrages auf Habilitation durch die Fakultät für Maschinenbau und Schiffstechnik und Mathematisch-Naturwissenschaftliche Fakultät der Universität Rostock erkläre ich an Eides statt, die vorgelegte Habilitationsschrift mit dem Titel ‘Spark Plasma Sintern von Nanomaterialien und Biomaterialien’ selbständig abgefasst und dabei keine fremden, nicht erwähnten Hilfen verwendet zu haben.

Faming Zhang

Dr. Faming Zhang

APPENDIX

Curriculum vitae

Name: Faming Zhang

Nickname: Fames

Born: Dec. 1st, 1978 in Hebei

Nationality: China

Home address: Neue Bleicherstr.7, 18055 Rostock

Permanent email: fames.zhang@hotmail.com, star.zhang@163.com

EDUCATION

Ph.D., Materials Engineering, **Sept., 2005**, Harbin Institute of Technology (HIT), Harbin, China

M.E., Materials Engineering, **Jul., 2002**, Harbin Institute of Technology (HIT), Harbin, China

B.E., Foundry Engineering, **Jul., 2000**, Hebei University of Science and Technology (HEBUST), Shijiazhuang, China

WORK EXPERIENCES

Aug. 2002- Sept. 2005

Research Associate, School of Materials Science and Engineering, Harbin Institute of Technology, Harbin, China.

Oct., 2005 - Nov., 2007 Postdoc research fellow

Biomaterials and Tissue Engineering Research Center, Shanghai Institute of Ceramics, Chinese Academy of Sciences (CAS), Shanghai, China

Dec., 2007 - July, 2013, Faculty staff, Wissenschaftlicher Mitarbeiter, (Haushaltsstelle)

Physics of new materials, Institute for Physics, University of Rostock, D-18055 Rostock, Germany

Sept., 2013 Habilitation Degree, in Faculty of Mechanical Engineering and Marine Technology, University of Rostock, Germany. Thesis title: 'Spark plasma sintering of nanomaterials and biomaterials'.

RESEARCH INTERESTS

- Nanomaterials: nanocarbon, nanocomposites;
- Biomaterials: bone and teeth repair materials, porous cellular solids;
- Field assisted processing techniques and theory;
- Structural stability and phase transformation by Synchrotron-X rays.
- Industrial, biomedical, environmental and sustainable development applications.

PROJECTS & FUNDING

- PI: Venture Cup 2011, MV. Diamantsynthese durch Spark-Plasma-Sinterung. UR 11 007 VC 2011.
- Co-PI: DFG (Germany research foundation). Pulsed electric field Induced diamond synthesis and mechanisms. Grant No. BU 547/10-1.
- Co-PI: DFG (Germany research foundation). Pulsed electric field Induced Phase transformation from Graphene. Grant No. BU 547/10-2.
- Co-PI: DESY Project in Hamburg, Temperature and pressure induced phase transformation of carbon materials by synchrotron radiation. II-20090264.
- Co-PI: DESY Project in Hamburg, Stability and phase transformations of graphene under extreme physical conditions. I-20110661.
- Participating in DFG (Germany research foundation) Welisa Project. Analyse und Simulation elektrischer Wechselwirkungen zwischen Implantaten und Biosystemen. Grant No. DFG GRK1505/1 (01.10.2008 – 31.03.2013).
- Participating in BMBF Project. Werkstoffentwicklung für Pumpenrotoren mittels Spark Plasma Sintern. 01.07.2011 -30.06.2014
- PI: Postdoctoral key Project of Shanghai government (Granted No.06R214201) entitled “Bioinspired design and fabrication of calcium phosphate bioceramics for load bearing bone regeneration application” (Schedule: Oct., 2005-Oct., 2007).
- PI: China Postdoctoral Science Foundation (Granted No.20060390648) entitled “Fabrication, mechanical property and degradability of porous calcium phosphate scaffolds by spark plasma sintering”(Schedule: Oct.,2005-Oct., 2007).
- Project composer, participating in applying, researching and completing one NSFC project (No.50374035) on carbon nanotubes WC matrix composite materials, and one key project of Heilongjiang Province on nanostructured WC/Co cemented carbides (2001-2005).

TEACHING COURSES

- Übung: Advanced Experimental Physics: solid state (WS2012/13)
- Übung: Experimentalphysik für Wirtschaftsingenieure (SS2012)
- Vorlesung: Nanomaterialien (WS2012/13)
- Übung: Nanomaterialien (WS2012/13)
- Übung: Nanotechnologie in der Materialsynthese, 20W (WS2012/13)
- Übung: Nanotechnologie in der Materialsynthese, 20W (WS2010/11)
- Übung: Nanotechnologie in der Materialsynthese, 20W (WS2011/12)
- Übung: Untersuchungsmethoden der Struktur und Dynamik (Methods to investigate structure and dynamics), 21 S (SS2011)
- Übung: Untersuchungsmethoden der Struktur und Dynamik (Methods to investigate structure and dynamics), 21 S (SS2012)
- Solid state Physics, International Master’s course (WS2010).
- Physics, chemistry and biology of new Materials, International Master’s course (SS2009, WS2009).
- Praktikum, Bachelor’s course (WS2008)

PROFESSIONAL AFFILIATION

- Lead guest editor in special issue ‘Nanomaterials processed by spark plasma sintering’ of Journal of Nanomaterials.
<http://www.hindawi.com/journals/jnm/si/853959/cfp/>
- Editorial Board, Journal of Nanoscience.
[\(http://www.hindawi.com/journals/nanoscience/editors/\)](http://www.hindawi.com/journals/nanoscience/editors/)
- Associate editor in Material chemistry, in Versita Publisher
[\(http://versita.com/Book_Author/Chemistry/\)](http://versita.com/Book_Author/Chemistry/)
- Mitglieds-Nr. 167578, Deutsche Gesellschaft für Materialkunde, DGM
- ASM International Member, No.704555, ASM Society, USA.
- Member, No. 484040, The Minerals Metals & Materials Society (TMS), USA
- Member, No.064642, The American Ceramic Society (ACerS), USA
- Member, No.6165315, VDE Verband der Elektrotechnik, Germany
- Member, Chinese Materials Research Society (C-MRS), China.
- Member, Chinese Society for Biomaterials (CCB), China.
- Reviewer and Referee of : “Advanced Materials”, “Advanced Functional Materials”, “Advanced Engineering Materials”, “Expert Review of Medical Devices”, “Chemical Engineering and Technology”, “Materials Science and Engineering B”, “Materials Letters” “Materials” “Journal of Nanomaterials” “Materials and Design”, “Modern Physics Letters B”, “Surface Review and Letters”, “Journal of Central South University of China” etc.

STUDENTS SUPERVISION

1. Frank Essenhut. (Germany). Master Science, University of Rostock, Germany. Stability and phase transformation of graphene under extreme physical field. (April.2012-Sep.,2013).
2. Yujie Quan (China), Ph.D, University of Rostock, Germany. Nanostructured Ti alloys and foams for biomedical applications. (Sep. 2010-Sep. 2014) with Prof. Burkel.
3. Lijun Jing (China), Ph.D, University of Rostock, Germany. Ti-CaTiO₃ nanocomposites for biomedical applications. University of Rostock, Germany. (April. 2012-Sep. 2015) with Prof. Burkel.
4. Sudheer Aanam (India). Master Science, University of Rostock, Germany. Numerical simulation of frequencies of pulsed current on the diamond formation. (2010)
5. Gunnar Adreas Rott (Germany), Dipl, Physics, University of Rostock, Germany. Preparation and dielectric properties of porous calcium titanates. (2009).
6. Yahya Obeid (Yemen), Master Science, University of Rostock, Germany. TiMn₂ alloys by balling and sintering for hydrogen storage. (2009).
7. Thomas Orłowski (Germany), Bachelor, University of Rostock, Germany. Erzeugung und Charakterisierung vom Nanostrukturiertem Titan-Aluminium. Sep. 2011
8. Frank Eisenhut (Germany), Bachelor, University of Rostock, Germany.

Dielektrische Eigenschaften von Calciumtitanat. .

9. Christopher Jacob (Germany), Bachelor, University of Rostock, Germany. Messung von Oberflächenpotentialen. Sep. 2011
10. Wang Dongjun (China), BS, Harbin Institute of Technology, China. Preparation of carbon nanotubes-WC-Co nanocomposites. (2005).
11. Fan Jun (China), BS, Harbin Institute of Technology, China. Wear properties of nanostructured WC-Co composites. (2004)
12. Guo Shu (China), BS, Harbin Institute of Technology, China. Microstructure analysis of nanostructured WC-Co composites. (2002).

HONOURS & AWARDS

- Venture Cup Winner in Mecklenburg-Vorpommern, Germany. (Jan. 2012)
- Lead guest editor in special issue (Nanomaterials processed by spark plasma sintering) of Journal of Nanomaterials. 2012-2013.
- Invited project referee for MATETPRO 2011 program of the French National Research Agency, France. 2011
- Invited project referee for 2012 Council of the National Fund for Scientific & Technological Development (FONDECYT), Chile. 2012
- The excellent Ph.D thesis of Harbin Institute of Technology. (July, 2007).
- The Postdoctoral key Project Gainer of Shanghai government (The first Postdoctoral key Project of Shanghai Institute of Ceramics, CAS).(July, 2006)
- The China Postdoctoral Science Foundation Gainer. (Oct., 2006)
- The 10 best postgraduates of HIT in 2005 (June, 2005).
- Excellent Scientific Research Paper of HIT (Nov., 2004).
- A “Three Good” Student of HIT (Sep., 2004,).
- Guanghua Scholarship (Taiwan, China) of HIT (Sep., 2003).
- The Best Graduated Postgraduates of HIT (Jul., 2002).
- Chairman of Students Union in HBUST (1998-2000)

Publications:

Book chapters: 4

Peer reviewed articles: 40

Patents: 6

Conferences presentations and posters: 30

Full publication list

INVITED BOOK CHAPTERS

- [1] Faming Zhang, Eberhard Burkel. Chapter 9: Novel titanium manganese alloys and their macroporous foams for biomedical applications prepared by field assisted sintering. In the book of “Biomedical Engineering, Trends, Researches and Technologies” ISBN 978-953-7619. Edited by Anthony N. Laskovski, Published by InTech. 02.2011
- [2] Faming Zhang, Eberhard Burkel. Chapter 2 Synthesis of diamond using spark plasma sintering. In the book of “Sintering of ceramics-new emerging techniques”. ISBN 978-953-308-4-8. Published by InTech. Book edited by Dr. Arunachalam Lakshmanan. 02.2012.
- [3] F. Zhang, Y. Quan. R. Reich, O. Kessler, E. Burkel. Chapter 11: Sintering and heat treatment of titanium alloys by pulsed electric current sintering. In the Book 'Sintering Applications'. ISBN 978-953-51-0974-7, Edited by: Burcu Ertuğ, Published by InTech. 02.2013.
- [4] Rott, G. A., Zhang, F., Haba, Y., Kruger, W. and Burkel E. Chapter 10. (2011) Dielectric Properties of Porous Calcium Titanate (CaTiO₃), in Biomaterials Science-Processing, Properties, and Applications, Volume 228 (eds R. Narayan, A. Bandyopadhyay and S. Bose), John Wiley & Sons, Inc., Hoboken, NJ, USA. doi: 10.1002/9781118144565.ch10.

JOURNAL PUBLICATIONS

- [1] Q. Xu, F. Zhang, E. Burkel. Carbon dioxide adsorption behaviors in various carbon materials. Energy & Fuels. 2013 (In review).
- [2] Y. Quan, P. Drescher, F. Zhang, E. Burkel, H. Seitz. Selective beam melting of carbon nanotube structured titanium foams. Rapid Prototyping Journal. (Accepted) .
- [3] F. Zhang, M. Reich, O. Kessler, E. Burkel. Potential of rapid cooling spark plasma sintering for metallic materials. Materials Today. 2013, 16(5): 192-195.
- [4] F. Zhang, F. Essenhut, E. Burkel. Stability of graphene in high pressure-high temperature and spark plasma sintering. DESY Annual Report. 2013, 03.
- [5] Faming Zhang, Furqan Ahmed, Jozef Bednarcik, and Eberhard Burkel. Diamond synthesis through the generation of plasma during spark plasma sintering. Phys. Status Solidi A No. 11, 2241–2246 (2012)
- [6] Faming Zhang, Furqan Ahmed, Gerd Holzhter, Eberhard Burkel. Growth of diamond from fullerene C₆₀ by spark plasma sintering. Journal of Crystal Growth. 340 (2012) 1–5.
- [7] Quan Y, Zhang F., Rebl H., Nebe B. Kessler O., Burkel E. Ti₆Al₄V foams fabricated by spark plasma sintering with post heat treatment. Materials Science & Engineering A. vol. 565, pp. 118–125, 2013.

- [8] F. Zhang, C. Lathe, E. Burkel. Pulsed electric field induced phase transformation of nanocarbon materials. *Desy Annual Report*. 2012,02.
- [9] F. Zhang, C. Mihoc, F. Ahmed, C. Latte, E. Burkel. Thermal stability of carbon nanotubes, fullerene and graphite under spark plasma sintering. *Chemical Physics Letters* 510 (2011) 109-114
- [10] Ahmed Ibrahim, Faming Zhang, Eileen Otterstein, Eberhard Burkel. Processing of Porous Ti and Ti5Mn Foams by Spark Plasma sintering. *Materials and Design*. 2011, 32: 146-153.
- [11] Faming Zhang, Martin Adam, Eileen Otterstein, Eberhard Burkel. Pulsed Electric Field Induced Diamond Synthesis from Carbon Nanotubes with Solvent Catalysts. *Diamond and related Materials*. 20 (2011) 853-858.
- [12] Faming Zhang, Arne Weidmann, J. Barbara Nebe, Ulrich Beck, Eberhard Burkel. Preparation, Microstructures, Mechanical Properties and Cytocompatibility of TiMn Alloys for Biomedical Applications. *Journal of Biomedical Materials Research B*. 2010, 94B: 406-413.
- [13] Faming Zhang; Otterstein, E.; Rott, G.; Beck, U.; Weiss, D.G.; Burkel, E. Preparation and surface modification of TiMn foams for bone implants. *Biomedizinische Technik*. 2010, 55: 71-72.
- [14] Faming Zhang, Eileen Otterstein, Eberhard Burkel. Spark plasma sintering, microstructures and mechanical properties of macroporous titanium foams. *Advanced Engineering Materials*. 2010, 12 (9): 863-872.
- [15] F. Zhang, A. Weidmann, J. B. Nebe, E. Burkel. Cell Response to Surface Modified Carbon Nanotubes. *Materials Science and Engineering: C Volume 32, Issue 5*, 1 July 2012, Pages 1057–1061.
- [16] F. Zhang, J. Chang, E. Burkel. Dissolution Process and Mechanisms of Poly (Vinyl Alcohol) Modified Carbon Nanotubes. *New Carbon Materials*. 2010, 25(4): 1-7. *Carbon*, 49(2011)352-355.
- [17] Faming Zhang, Arne Weidmann, J. Barbara Nebe, Eberhard Burkel. Effect of Manganese on the in vitro biomedical properties of titanium alloy. *Biomaterialien*. 2009; 10(S1):129.
- [18] Faming Zhang, Eberhard Burkel. Preparation of tricalcium phosphate magnesium nanocomposites for load bearing bone regeneration applications. *Biomaterialien*. 2009; 10(S1):130.
- [19] F. Zhang, A. Weidmann, B. J. Nebe, E. Burkel. Preparation of TiMn alloy by mechanical alloying and spark plasma sintering for biomedical applications. *Journal of Physics: Con. Series 144* (2009) 012007.
- [20] Kuai Jicai, Zhang Feihu, Zhang Faming. Frictional Wear of Nano-cemented Carbide. *Journal of Northeast Forestry University*. 2009, 37(2): 120-125.
- [21] Faming Zhang, Jiang Chang, Jianxi Lu and Congqin Ning, Surface Modification of Beta-tricalcium Phosphate Scaffolds with Topological Nanoapatite Coatings. *Materials Science and Engineering: C*. 2009, Volume 28, Issue 8, 1 December 2008, Pages 1330-1339
- [22] Faming Zhang, Jiang Chang, Kaili Lin and Jianxi Lu; Preparation, mechanical properties and in vitro degradability of wollastonite/tricalcium phosphate

macroporous scaffolds from nanocomposite powders, *Journal of Materials Science: Materials in Medicine* 2008,19(1): 167-173.

- [23] Faming Zhang, Kaili Lin, Jiang Chang, Jianxi Lu and Congqin Ning; Spark plasma sintering of macroporous calcium phosphate scaffolds from nanocrystalline powders. *Journal of the European Ceramic Society*, Volume 28, Issue 3, 2008, Pages 539-545
- [24] Lihua Long, Faming Zhang, Lei Chen, Lidong Chen, Jiang Chang. Preparation and properties of β -CaSiO₃/ZrO₂ (3Y) nanocomposites. *Journal of the European Ceramic Society*, Volume 28, Issue 15, November 2008, Pages 2883-2887.
- [25] Faming Zhang, Jiang Chang, Jianxi Lu, Kaili Lin and Congqin Ning, Bioinspired structure of bioceramics for bone regeneration in load-bearing sites, *Acta Biomaterialia*, Volume 3, Issue 6, November 2007, Pages 896-904.
- [26] Faming Zhang, Jiang Chang, Jianxi Lu, Kaili Lin. Fabrication and Mechanical Properties of Dense/Porous β -Tricalcium Phosphate Bioceramics. *Key Engineering Materials*, Vols. 330-332 (2007) pp. 907-910.
- [27] Faming Zhang, Jun Shen, Jianfei Sun, D.G. McCartney. Direct Synthesis of Diamond from Low Purity Carbon Nanotubes. *Carbon*. 44 (2006) 3136-3138.
- [28] J Shen, F M Zhang, J F Sun, Y Q Zhu and G. McCartney. Spark plasma sintering assisted Diamond Formation from Carbon Nanotubes at very Low Pressure. *Nanotechnology*. 17 (2006) 2187-2191.
- [29] Shen Jun, Zhang Fa-ming, Sun Jian-fei. Preparation, properties and toughening mechanisms of carbon nanotubes reinforced ceramic matrix composites. *Materials Science and Technology*. 2006.14(2):165-169.
- [30] Faming Zhang, Jun Shen, Jianfei Sun, Yan Qiu Zhu, Gang Wang and G. McCartney. Conversion of Carbon Nanotubes to Diamond by a spark plasma sintering, *Carbon*. 2005, 43 (6): 1254-1258.
- [31] Faming Zhang, Jianfei Sun, Jun Shen. Effects of Carbon Nanotubes Incorporation on the Grain growth of Nanocrystalline WC-Co cermets. *Material Science Forum*. 475-479 (2005): 989-992.
- [32] Jun Shen, Faming Zhang, Jianfei Sun. Processing and Mechanical Properties of Spark Plasma Sintered WC-Co-Al₂O₃ Nanocomposites. *Transactions of Nonferrous Metals Society of China*. 2005.1:102-109.
- [33] ZHANG Fa-ming, SHEN Jun, SUN Jian-fei, GUO Shu. Microstructural Characterization of Nanostructured WC-Co Cemented Carbides. *Nonferrous Metals*. 2005.57(1):4-7.
- [34] Faming Zhang, Jun Shen, Jianfei Sun. Processing and Properties of Carbon Nanotubes-Nano-WC-Co composites. *Materials Science & Engineering A*. 381 (2004) 91-96.
- [35] Faming Zhang, Jun Shen, Jianfei Sun. The Effect of Phosphorus additions on

Densification, Grain growth and Properties of nanocrystalline WC/Co composites. *Journal of Alloys and Compounds*. 2004, 385(1-2): 96-103.

- [36] Jun SHEN, Jianfei SUN and Faming ZHANG. Synthesis and Characterizations of Nanocrystalline WC-Co Composite Powders by a Unique Ball Milling Process. *Journal of Materials Science and Technology*. 2004, 20(1): 7-10.
- [37] Jianfei Sun, Faming Zhang, Jun Shen. Characterization of ball-milled nanocrystalline WC-Co composite powders and subsequently rapid hot pressing sintered cermets. *Materials Letters*, 57(2003)3140-3148.
- [38] Shen, Jun; Zhang, Fa-Ming; Sun, Jian-Fei. Preparation of bulk nanostructured WC-Co cermets by high energy ball milling and rapid hot-pressing. *Mining and Metallurgical Engineering*, 2003, 23(5):89-92.
- [39] Sun Jianfei, Zhang Faming, Shen Jun, Xian Hengze. Characterizations of High Energy Ball Milled Nanocrystalline WC-Co Composite Powders. *Rare Metals*. 2003.27(6):665-670.
- [40] SUN Jian-fei, ZHANG Fa-ming, SHEN JUN. The Preparation and Sintering Characteristics of Nanocrystalline WC-Co Composites. *Rare Metals and Cemented Carbides*.2002, 30(1):33-37.

PATENTS

- [1] Faming Zhang, Eberhard Burkel, Gunnar Rott. Verfahren zur Synthese von Diamanten. Deutsches Patent, DE 10 2011 014 204 A1.
- [2] Jun Shen, Faming Zhang, Jianfei Sun and Gang Wang. Low pressure synthesis of diamonds from carbon nanotubes by a new process. China Patent. ZL 200410044157.0.(Authorized).
- [3] Jun Shen, Jianfei Sun, Faming Zhang. A new way to regulate the carbon contents in WC cemented carbides by incorporation of carbon nanotubes. China Patent. ZL200510009618.5(Authorized).
- [4] Zhang Faming, Chang Jiang, Lu Jianxi. A new method to prepare macroporous bioceramics with high interconnectivity. China Patent.CN200710047210.6.
- [5] Lu Jianxi, Chang Jiang, Lin Kaili, Zhang Faming. A bioinspiredBioceramics for Load bearing applications. China Patent. CN 200610026058.9. (Authorized).
- [6] Lu Jianxi, Chang Jiang, Lin Kaili, Zhang Faming. A bioinspiredBioceramics for Load bearing applications. International PCT Patent: PCT/CN2007/001124(Authorized).

CONFERENCE PUBLICATIONS

- [1] Dieter Schroblin, Faming Zhang, Eberhard Burkel. Residue stress of the rapid cooling SPS processed Titanium alloys by synchrotron radiation. International conference of Materials Day 2013, 05.24-26, Rostock, Germany. (Poster)

- [2] Kerstin Witte, Faming Zhang, Eberhard Burkel. Texture structures of the Ti-Ceramics graded materials Synchrotron radiation. International conference of Materials Day 2013, 05.24-26, Rostock, Germany. (Poster)
- [3] Faming Zhang, Eberhard Burkel. Diamond and Cu/Diamond composites by spark plasma sintering. International conference on diamond and carbon materials. 3-6, Sep. 2012. Granada, Spain. (Poster)
- [4] Faming Zhang. Ti alloys by SPS and selective electron beam melting. Materials Day 2012. Rostock. May 5-7, 2012(Oral Presentation)
- [5] Faming Zhang, Eberhard Burkel, SPS-Synthesis and in Vitro Studies of New Metallic 3D-Bone Replacement Materials. Workshop Neue Horizonte für Metallische Biomaterialien. 2-3, May, 2011 Helmholtz Zentrum Geesthacht. (Poster)
- [6] Faming Zhang. Ti scaffolds and graded composites by SPS. Materials Day 2011. Rostock. Oct. 8-9, 2012 (Oral Presentation)
- [7] Faming Zhang, Ahmed Ibrahim, Eileen Osterstein, Eberhard Burkel. Processing, structure and property relationships of Ti foams by spark plasma sintering. CELLMET 2010 Cellular Metals for Structural and Functional Applications. Oct. 26-30, 2010, Dresden, Germany (Presentation)
- [8] Faming Zhang, Carmen Mihoc, Eberhard Burke. Spark Plasma Sintering Assisted Carbon Conversion from Various Modifications to Diamond. MS&T10, Oct. 10-17, Huston, USA. (Presentation)
- [9] Faming Zhang, E. Otterstein, E. Burkel. Processing and mechanical properties of Ti foams by SPS. MS&T10, Oct.10-17, Huston, USA. (Presentation)
- [10] Rott G. A., Zhang F., Schlichting J., Haba Y., Kröger W., Burkel E. Dielectric properties of porous calcium titanate (CaTiO₃). MS&T10, Oct. 10-17, Huston, USA. (Presentation)
- [11] Faming Zhang, Martin Adam, Eileen Otterstein, Eberhard Burkel. Pulsed Electric Field Induced Diamond Synthesis from Carbon Nanotubes with Solvent Catalysts. Materials Science and Engineering, 24-26, Aug,2010, Darmstadt, Germany (Poster)
- [12] G. Rott, F. Zhang, J. Schlichting, J.Haba, W.Kroger, E.Burkel. Dielectric spectroscopy and microstructures of sintered calcium titanate samples with different porosities. Materials Science and Engineering, 24-26, Aug,2010, Darmstadt, Germany (Presentation)
- [13] Faming Zhang, Eileen Otterstein, Gunnar Rott, Ulrich Beck, Dieter G. Weiss, Eberhard Burkel. Preparation and surface modification of TiMn foams for bone implants. BMT2010 Warnamunde, Germany.(Presentation)
- [14] Rott G. A., Zhang F., Schlichting J., Haba Y., Kröger W., Burkel E. Dielektrische Eigenschaften von porösem Calciumtitanat (CaTiO₃). BMT2010 Warnamunde, Germany. (Presentation)
- [15] Evgeny Delyagina, Nan Ma, Weiwei Wang, Yue Zhang, Anna-Lena Kuhlo, Eva Flick, Hans-Heinrich Gatzert, Faming Zhang, Eberhard Burkel, Gustav Steinhoff, Wenzhong Li, Titaniumdioxide – mediated polyethylenimine forgene delivery. BMT2010 Warnamunde, Germany. (Presentation)

- [16] Evgeny Delyagina, Nan Ma, Weiwei Wang, Yue Zhang, Anna-Lena Kuhlo, Eva Flick, Hans-Heinrich Gatzert, Faming Zhang, Eberhard Burkel, Gustav Steinhoff, Wenzhong Li, Carbon nanotube – mediated polyethylenimine for gene delivery. BMT2010 Warnemünde, Germany. . (Presentation)
- [17] Faming Zhang, Eberhard Burkel. Workshop in sparkplasma sintering, Dresden, Germany, 23-25 April, 2010.
- [18] Faming Zhang, Arne Weidmann, Barbara Nebe, Eberhard Burkel. EFFECT OF MANGANESE ON THE IN VITRO BIOMEDICAL PROPERTIES OF TITANIUM ALLOY. International conference of Biomaterials Interface. 2009. Warnemünde, Germany. (Poster)
- [19] Faming Zhang, Eberhard Burkel. PREPARATION OF TRICALCIUM PHOSPHATE-MAGNESIUM NANOCOMPOSITES FOR LOAD-BEARING BONE REGENERATION APPLICATIONS. International conference of Biomaterials Interface. 2009. Warnemünde, Germany. (Poster)
- [20] F. Zhang, E. Burkel. Preparation of Ti-Mn Alloy by Mechanical Alloying and Spark Plasma Sintering for Biomedical Application. The 13th International Conference on Rapidly Quenched & Metal Stable Materials. Dresden, Germany, August, 2008. (Oral presentation)
- [21] F. Zhang, E. Burkel. Preparation of Titanium matrix nanocomposites by SPS for biomedical applications. International Workshop on SPS-Avignon, France. Oct.6-7, 2008. (Oral presentation).
- [22] F. Zhang, E. Burkel. Induced Structure Stability and Phase Transformation of Carbon Nanotubes, Materials Days 2008, Rostock (Germany), June 26-27, 2008 (Oral presentation)
- [23] Faming Zhang, Eberhard Burkel. Advanced Processing for Novel Functional Materials-APNFM 2008, Dresden, Germany, 23-25 January, 2008.
- [24] Faming Zhang, Jiang Chang, Jianxi Lu. Fabrication and Mechanical Properties of Dense/Porous β -Tricalcium Phosphate Bioceramics. 19th International Symposium on Ceramics in Medicine, Oct 10-13, 2006, Chengdu, China
- [25] Faming Zhang, Jiang Chang, Jianxi Lu. Bioinspired Structural Design, Preparation and Properties of Calcium Phosphates Scaffolds. 2006 Shanghai Conference on Biomaterials in Medicine. Shanghai Changzheng Hospital. Dec.16, 2006.
- [26] Faming Zhang, Jiang Chang, Jianxi Lu. Preparation, mechanical properties, bioactivity and biodegradability of Wollastonite/Tricalcium Phosphate Macroporous Scaffolds. 2005 Shanghai Conference on Biomaterials in Medicine. Shanghai Changzheng Hospital, Dec.17, 2005.
- [27] Faming Zhang, Jun Shen, Jianfei Sun. Reinforcing Mechanisms of Carbon Nanotubes in WC/Co Matrix Nanocomposites. The 12th International Conference on Rapidly Quenched & Metal Stable Materials. Jeju, Korea. Aug., 2005.
- [28] Faming Zhang, Jianfei Sun, Jun Shen. Effects of Carbon Nanotubes Incorporation on the Grain Growth and Properties of WC/Co Nanocomposites. The 5th Pacific Rim International Conference on Advanced Materials and Processing (PRICM-5),

Beijing, China. November 2-5, 2004.

- [29] Jianfei Sun, Faming Zhang, Jun Shen. Spark Plasma Sintering of Nanocrystalline WC-Co Cemented Carbides. Proceedings of the 1st International Conference on New Forming Technology, ICNFT, Harbin, China. Sep.6-9, 2004:499-504.
- [30] Faming Zhang, Jun Shen and Jianfei Sun. Spark plasma sintering of WC-Co-CNTs nanocomposites and their mechanical properties. 2004 Doctoral Forum of China, Harbin, China. Aug., 2004: 265-273.

Original publications included as part of the thesis

- [A] **F. Zhang**, C. Mihoc, F. Ahmed, C. Latte, E. Burkel. Thermal stability of carbon nanotubes, fullerene and graphite under spark plasma sintering. **Chemical Physics Letters** 2011,510 (1-3):109-114.
- [B] **F. Zhang**, F. Ahmed, J. Bednarcik, and E. Burkel. Diamond synthesis through the generation of plasma during spark plasma sintering. **Phys. Status Solidi A**. 2012, 209(11): 2241-2246.
- [C] **F. Zhang**, M. Adam, E. Otterstein, E. Burkel. Pulsed electric field induced diamond synthesis from carbon nanotubes with solvent catalysts. **Diamond and related Materials**. 2011, 20(5-6): 853-858.
- [D] **F. Zhang**, F. Ahmed, G. Hölzhuter, E. Burkel . Growth of diamond from fullerene C60 by spark plasma sintering. **Journal of Crystal Growth**. 2012, 340(1):1-5.
- [E] **F. Zhang**, A. Weidmann, J. B. Nebe, U. Beck, E. Burkel. Preparation, microstructures, mechanical properties and cytocompatibility of TiMn Alloys for biomedical applications. **Journal of Biomedical Materials Research B** 2010, 94B: 406-413.
- [F] **F. Zhang**, M. Reich, O. Kessler, E. Burkel. Potential of rapid cooling spark plasma sintering for metallic materials. **Materials Today**. 2013,16(5): 192-197.
- [G] **F. Zhang**, E. Otterstein, E. Burkel. Spark plasma sintering, microstructures and mechanical properties of macroporous titanium foams. **Advanced Engineering Materials** 2010, 12 (9): 863-872.
- [H] Y. Quan, **F. Zhang**, H. Rebl, B. Nebe, O. Kessler, E. Burkel. Ti6Al4V foams fabricated by spark plasma sintering with post heat treatment. **Materials Science and Engineering A**. 2013, 565:118-125.



Thermal stability of carbon nanotubes, fullerene and graphite under spark plasma sintering

Faming Zhang^{a,*}, Carmen Mihoc^a, Furqan Ahmed^{b,c}, Christian Lathe^d, Eberhard Burkel^a

^a Institute of Physics, University of Rostock, August Bebel Str. 55, Rostock 18055, Germany

^b Department of Materials Science and Engineering, University of Erlangen-Nürnberg, Martens Str. 5, Erlangen 91058, Germany

^c Department of Metallurgical and Materials Engineering, University of Engineering and Technology, Lahore, Pakistan

^d Helmholtz Centre Potsdam, GFZ German Research Centre for Geosciences, Centre for CO₂ Storage, Telegrafenberg, 14473 Potsdam, Germany

ARTICLE INFO

Article history:

Received 1 April 2011

In final form 8 May 2011

Available online 11 May 2011

ABSTRACT

The thermal stabilities of carbon nanotubes, fullerene and graphite were investigated under spark plasma sintering (SPS). Results were compared with data from synchrotron radiation in situ high temperature X-ray diffraction of these materials. Part of the nanotubes and fullerene transformed into diamond under SPS, but graphite kept stable. There was no diamond conversion in the in situ X-ray diffraction experiments under the same condition. Their phase transitional mechanism indicated the presence of plasmas during the SPS operation.

© 2011 Elsevier B.V. All rights reserved.

1. Introduction

The carbon nanotubes, fullerene (C60) and graphite have broad applications as structural and functional materials. Therefore, it is of great importance for a better in-depth understanding of their thermal stability under severe physical conditions [1,2]. Spark plasma sintering (SPS), also defined as field assisted sintering technique (FAST) or pulsed electric current sintering (PECS), is an electric field assisted sintering process utilizing ON-OFF DC pulse energizing [3]. During its treatment, pulsed DC current directly passes through the graphite die, as well as the powder compact, in case of conductive samples [4]. During study of the thermal stability of multi-walled carbon nanotubes (MWCNTs) under various SPS conditions, it was found that under SPS conditions of 1500 °C at very low pressure carbon nanotubes were unstable and transformed to diamonds without any catalysts being involved [5–7]. Recently, Inam et al. [8] reported that multiwall carbon nanotubes were not preserved for ceramic matrices that require high sintering temperatures (>1600 °C) and longer processing times (>13 min) in the SPS. We proposed that the spark plasmas may play a key role to provide most of the energy required in this diamond transition [5,6]. It indicates that the SPS has a potential to be used as an alternative method for diamond generation, and it also provides an indirect way to validate the existence of the plasmas during the SPS. However, at this point it needs further investigations due to the still on-going arguments about whether the spark plasmas actually occur during the SPS process [9,10]. In this study, we used an indirect way to prove the presence of plasmas during the SPS.

The thermal stability and phase transitional behavior of carbon nanotubes, C60 and graphite were investigated under the SPS (pulsed DC field). The pure MWCNTs, C60 and graphite powders were processed by using the SPS. Their phase constitutions were investigated by using synchrotron radiation–high energy X-ray diffraction and Raman spectroscopy. For a comparison study, these carbon materials were also studied using the in situ high temperature (AC field) synchrotron radiation X-ray diffraction. Their phase transitional mechanisms under such novel sintering technique were discussed.

2. Experimental

The MWCNTs (10–20 nm) with purity above 95% were obtained from Shenzhen Nanotech Port, Ltd., China. The C60 powders with purity of 99.5% were obtained from SES Research, Huston, USA. The graphite powders with purity of 99.0% were purchased from Alfa Aesar, Germany.

These carbon powders were pressed into a graphite die for SPS treatment to form disk-shaped samples of 20 mm diameter and 5 mm thickness. The SPS experiments were conducted using a Model HPD-25/1 FCT spark plasma sintering system (FCT systeme GmbH, Rauenstein, Germany), under an axial pressure of 80 MPa in vacuum (<6 Pa). A heating rate of 100 K/min was adopted, and the sintering process lasted typically 20 min. The applied direct current for SPS was about 1000 A, with a pulse duration of 12 ms and an interval of 2 ms.

The phase identification of the obtained carbon samples was performed using high-energy X-ray diffraction at beamline BW5 (DESY/HASYLAB Hamburger Synchrotron Laboratory) with a wavelength of 0.15339 Å (80.828 keV). The carbon samples were also

* Corresponding author. Fax: +49 381 4986862.

E-mail address: faming.zhang@uni-rostock.de (F. Zhang).

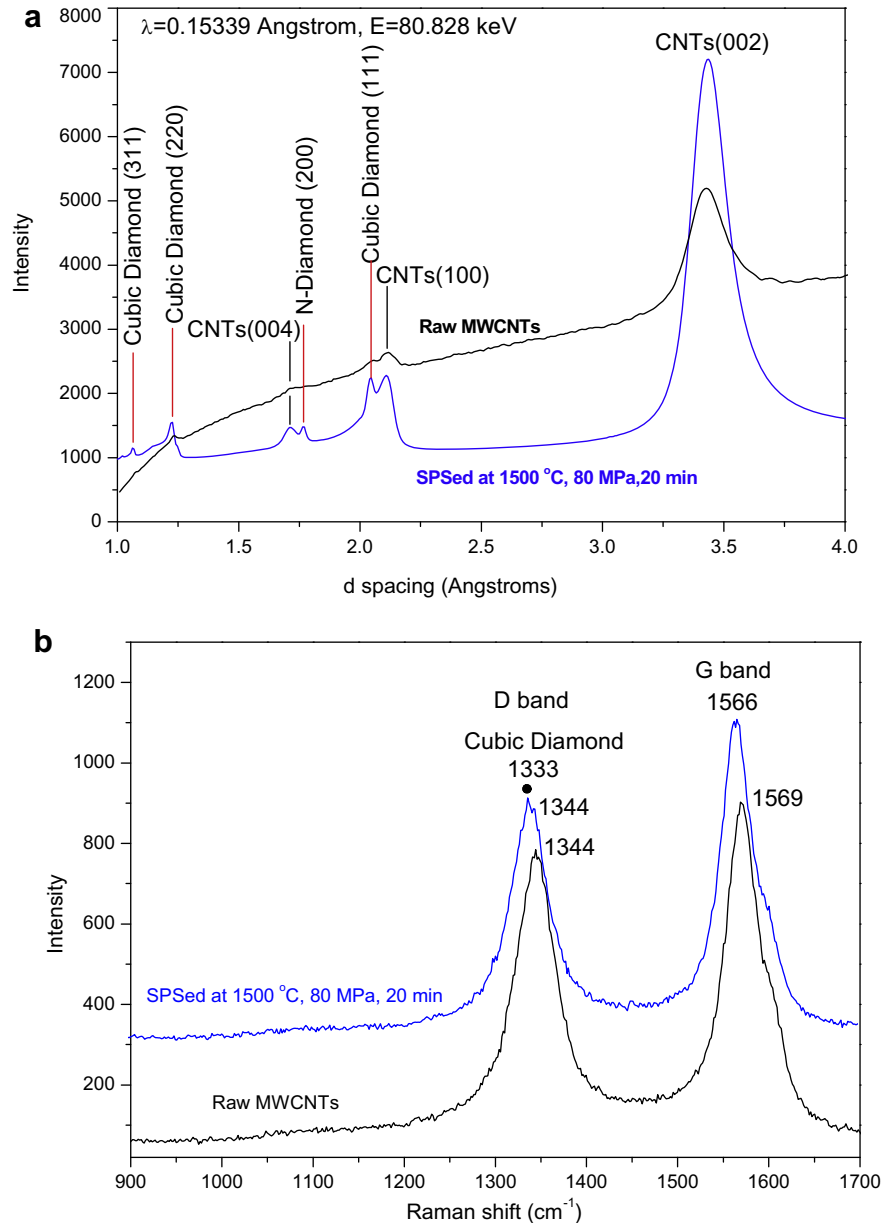


Figure 1. Synchrotron radiation-high energy X-ray diffraction patterns (a) and Raman spectra (b) of the raw MWCNTs and the spark plasma sintered MWCNTs at 1500 °C, 80 MPa for 20 min.

analyzed by a Renishaw-2000 Laser Raman spectroscopy system with a He–Ne laser excited at 514 nm. The stability of these carbon samples was investigated by the in situ high temperature X-ray diffraction at the MAX80/F2.1 high-pressure beamline of Helmholtz Centre Potsdam at HASYLAB/DESY. The MAX80 instrument uses a cubic-anvil-type press, which is known to provide better results for isotropic pressure generation compared to other multiple-anvil high-pressure devices [11]. The carbon samples were contained in cube cells made of a mixture of boron and epoxy resin with 4 mm edge length in a non-oxygen atmosphere. The pure MgO powder was used as a reference material in the cube cells. An in situ measurement comprises the room-temperature compression to the desired pressure, followed by isobaric constant-rate heating. X-ray diffraction patterns were acquired in energy-dispersive mode (EDX) during continuous specimen heating (up to 1500 °C) under an applied pressure of 80 MPa. The EDX method re-

lies on the use of a well-collimated and polychromatic (white) incident synchrotron radiation beam. The XRD patterns were collected each 10 °C during constant heating.

3. Results and discussion

The pure MWCNTs were SPSed at 1500 °C under pressure of 80 MPa for holding time of 20 min. Figure 1a shows the synchrotron radiation-high energy X-ray diffraction patterns of the raw MWCNTs and the spark plasma sintered (SPSed) MWCNTs. The raw MWCNTs show a main diffraction peak at 3.43 Å corresponding to the CNTs (0 0 2) plane spacing, and weak peaks at 2.10 and 1.70 Å corresponding to the CNTs (1 0 0) and (0 0 4) plane spacing, respectively. After SPS processing, the MWCNTs diffraction peaks are still presented in the sintered MWCNTs compacts, but the

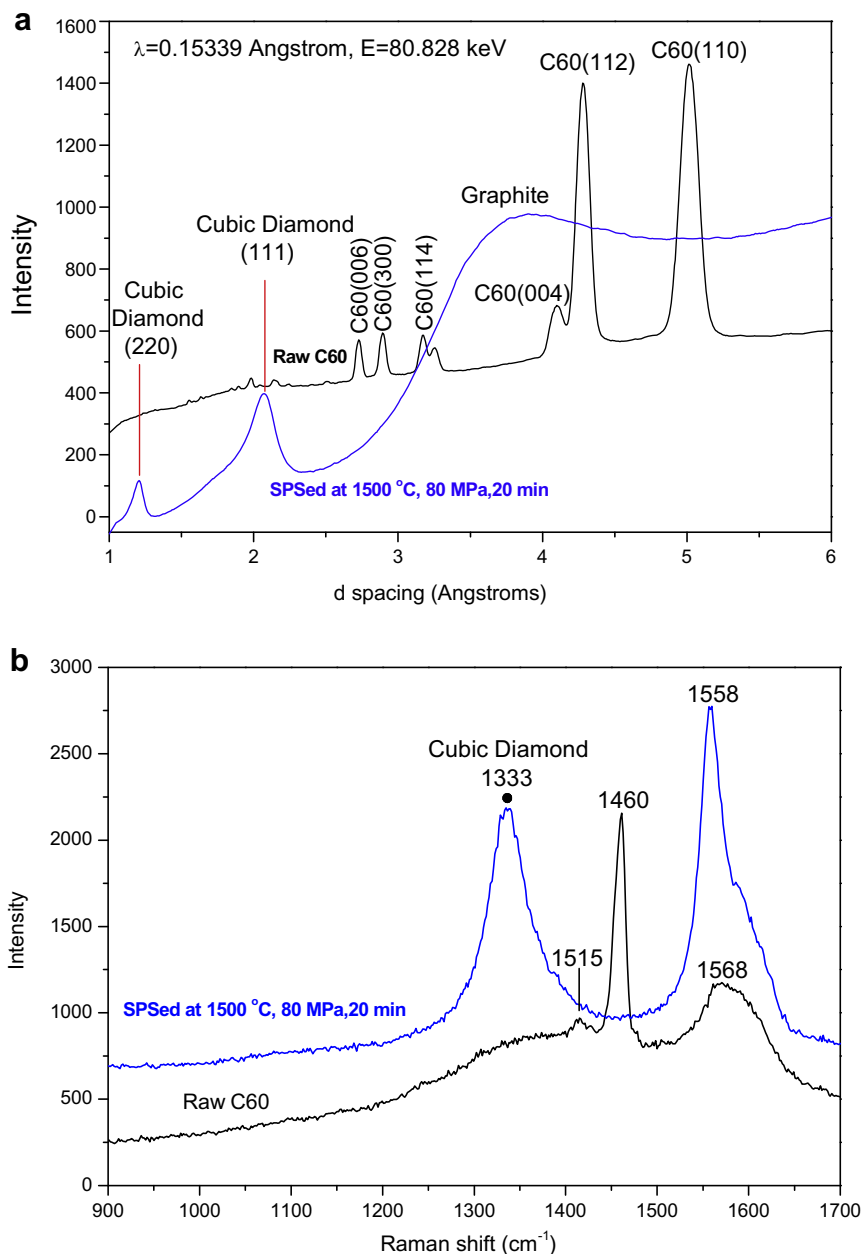


Figure 2. Synchrotron radiation-high energy X-ray diffraction patterns (a) and Raman spectra (b) of the raw C60 and the spark plasma sintered C60 at 1500 °C, 80 MPa for 20 min.

peaks of the CNTs (0 0 2), (1 0 0) and (0 0 4) are stronger than those in the raw MWCNTs. It indicates that the SPS process improved the crystallinity of the MWCNTs, which is consistent with the results of Yang et al. [12]. Additionally, new peaks were detected in the sample centered at 2.05, 1.23, 1.06 and 1.76 Å corresponding to the cubic diamond (ICDD No. 65-537) (1 1 1), (2 2 0), (3 1 1) and *n*-diamond (ICDD No. 43-1104) (2 0 0) plane spacing, respectively. Figure 1b shows Raman spectra of the raw MWCNTs and the SPSed MWCNTs. The result of the raw MWCNTs show that their D band appeared at 1344 cm⁻¹ and G band appeared at 1569 cm⁻¹. After SPS processing, the D peak shifted to 1333 cm⁻¹ corresponding to the cubic diamond but there was still a weak peak at 1344 cm⁻¹ belonging to the un-reacted MWCNTs, the G band shifted to 1566 cm⁻¹ relating to the sp² bonded carbon vibrations. The results of the X-ray diffraction and Raman spectroscopy confirmed

the diamond formation in the MWCNTs sample after SPS at 1500 °C, 80 MPa for 20 min.

Figure 2a shows the synchrotron radiation-high energy X-ray diffraction patterns of raw C60 and the SPSed C60 at 1500 °C, 80 MPa for 20 min. The raw C60 exhibits diffraction peaks at *d* spacing of 5.01, 4.28, 4.11, 3.18, 2.9, 2.74 Å belonging to C60 (1 1 0), (1 1 2), (0 0 4), (1 1 4), (3 0 0), (0 0 6) planes (ICDD No. 47-0787), respectively. The C60 after SPS shows the cubic diamond diffraction peaks at *d* spacing of 2.06 and 1.23 Å and a broad graphite peak. The C60 diffraction peaks disappeared indicating the C60 has completely transformed into diamond and graphite phases after the SPS processing. Figure 2b shows the Raman spectra of the raw C60 and the SPSed C60. The raw C60 shows a sharp peak appeared at 1460 cm⁻¹, and two weak, broad peaks centered at 1568 and 1515 cm⁻¹. After SPS processing, it shows the cubic dia-

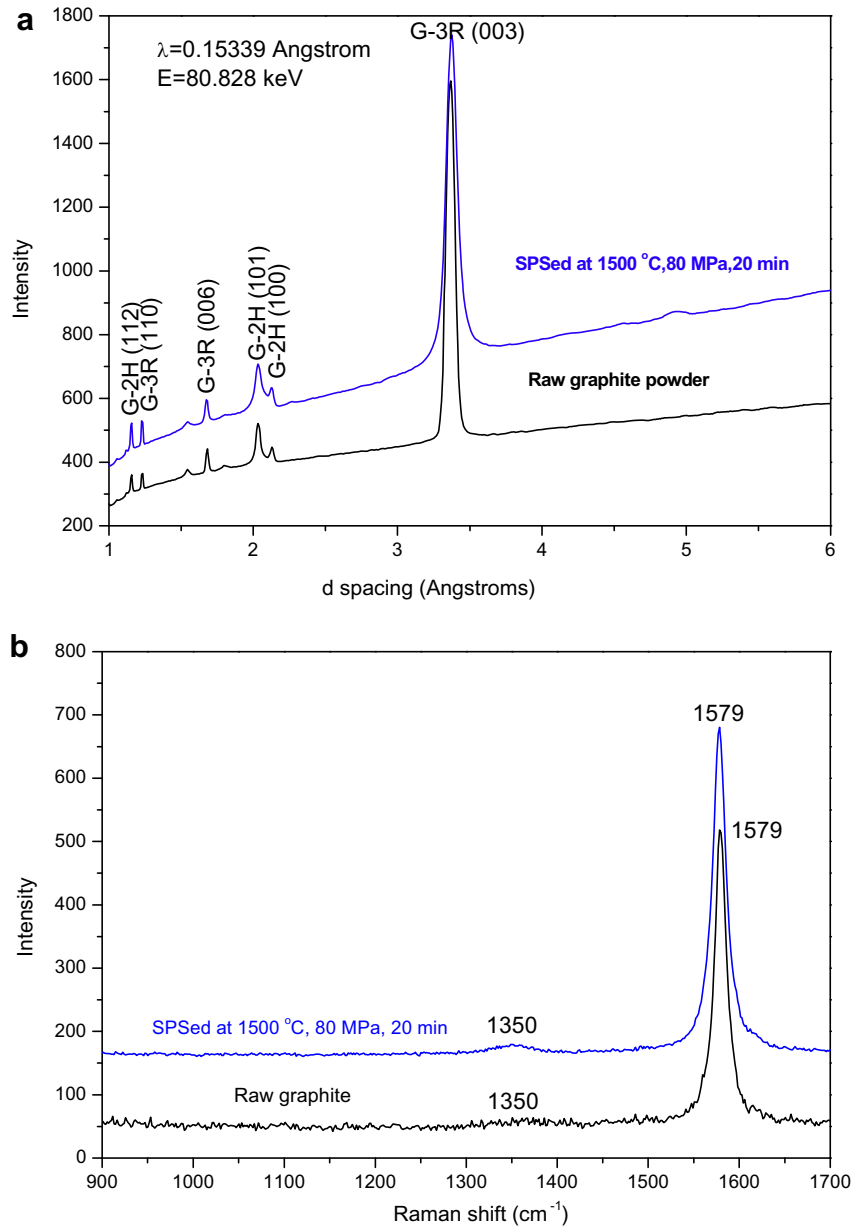


Figure 3. Synchrotron radiation-high energy X-ray diffraction patterns (a) and Raman spectra (b) of the raw graphite and the spark plasma sintered graphite at 1500 °C, 80 MPa for 20 min.

mond peak at 1333 cm⁻¹ and graphite peak at 1558 cm⁻¹, but the C60 peak at 1460 cm⁻¹ disappeared. It is consistent with X-ray diffraction results that the C60 has completely transformed into diamond and graphite phases after SPS at 1500 °C under 80 MPa for 20 min.

Figure 3a shows the synchrotron radiation diffraction patterns of the raw graphite and the SPSed graphite at 1500 °C, 80 MPa for 20 min. The raw graphite sample presents Graphite-3R and Graphite-2H diffraction peaks those are centered at 3.348 Å [G-3R(0 0 3)], 1.674 Å [G-3R(0 0 6)], 1.228 Å [G-3R(1 1 0)] (ICDD No. 26-1079), and 2.138 Å [G-2H(1 0 0)], 2.039 Å [G-2H(1 0 1)], 1.16 Å [G-2H(1 1 2)] (ICDD No. 41-1487). However, it didn't find the diamond phase in the graphite samples after the SPS processing. It only shows an increased intensity in the graphite peaks indicating the improved crystallinity. Figure 3b shows the Raman spectra of the raw graphite and the SPSed graphite. The raw graphite shows a sharp peak at 1579 cm⁻¹, and a weak peak at 1350 cm⁻¹. After

SPS processing, the intensity of the peak at 1350 cm⁻¹ has improved, but there is no diamond peak in the Raman spectra. The X-ray diffraction and Raman spectroscopy results confirmed that there is no diamond conversion from pure graphite after SPS at 1500 °C under 80 MPa for 20 min.

Figure 4a shows the synchrotron radiation-in situ X-ray diffraction patterns of the pure MWCNTs at 80 MPa under different temperatures. The combining peak of MWCNT and graphite has shifted to lower energy values. It indicates the thermal expansion of the nanotubes and graphite planes with the increase of temperature. The boron nitride (BN) peaks are from the container of the powder sample during the in situ high temperature X-ray experiments. However, there is no diamond formation at or below temperature of 1500 °C under 80 MPa. It means that the MWCNTs are dynamically stable at this 1500 °C temperature under 80 MPa in a non-oxygen atmosphere during the AC sintering. Figure 4b shows the synchrotron radiation-in situ X-ray diffraction patterns of the pure

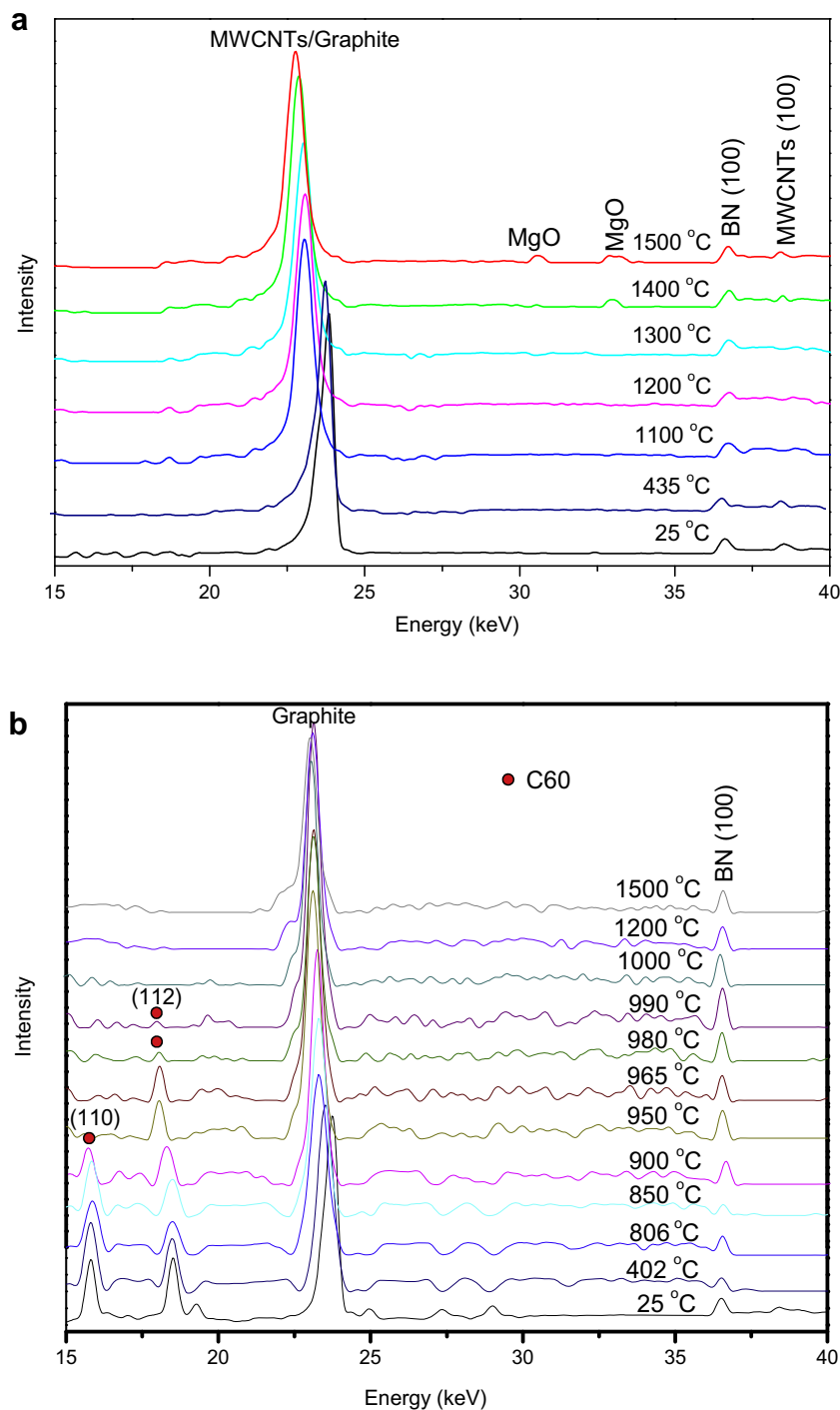


Figure 4. Synchrotron radiation-in situ X-ray diffraction patterns of the pure MWCNTs (a) and C60 (b) at 80 MPa under different temperatures.

C60 at 80 MPa under different temperatures. There is no diamond formation in the C60 sample. It shows that the C60 is stable below temperature of 900 °C. However, the C60 is unstable above that temperature point. The C60 (1 1 0) peak disappeared above temperature of 900 °C and C60 (1 1 2) peak disappeared above temperature of 990 °C. It is found that the graphite is very stable in the in situ high temperature X-ray experiments at or below temperature of 1500 °C under 80 MPa.

Synchrotron radiation-high energy X-ray diffraction [13] was used to identify the diamond phase in the carbon samples after SPS. In order to confirm the diamond formation, Raman spectroscopy

was also used to identify the formation of sp^3 bonded diamonds. By using the high energy X-ray diffraction and Raman spectroscopy, the cubic diamond phases were identified and confirmed in the SPSed MWCNTs and C60 samples. The n -diamond was also found in the SPSed MWCNTs sample. The n -diamond is a new kind of carbon allotrope, which was a metallic form of carbon with face-centred cubic structure [14]. It is a metastable and intermediate phase, can decompose slowly at room temperature, and has been synthesized accidentally by various processes [15]. This is noted that the n -diamond can also be synthesized by the SPS process. The standard d spacing of the cubic diamond (1 1 1),

(2 2 0) and (3 1 1) planes are centered at 2.059, 1.261 and 1.075 Å (ICDD No. 65-537). The cubic diamond in the SPSed MWCNTs centered at 2.05, 1.23 and 1.06 Å, and in the SPSed C60 appeared at 2.06 and 1.23 Å spacing. The diffraction peaks of the synthesized diamond from MWCNTs and C60 are very close to the standard diamond diffraction data, but there is a little shift. The diamond peak shifts are due to the existence of residual stress in the synthesized diamonds from MWCNTs and C60 by using the SPS. The residual stress of the diamond is because of the stress that remains after the original cause of the stresses (uniaxial forces, heat gradient) has been removed after the SPS processing. In this study, uniaxial force of 80 MPa was applied and there generally existed some temperature gradients during the operation of the SPS. Therefore, the diamond peaks in the SPSed MWCNTs and C60 have shifted a little. Combining the results of the Raman spectroscopy, the formation of diamond phases in these MWCNTs and C60 samples is confirmed. It is found that there are no C60 peaks in the X-ray diffraction and Raman results of the SPSed C60 sample, but there are strong unreacted MWCNTs peaks in the SPSed MWCNTs sample, and there are no diamond phases in the SPSed graphite sample. There exists a high activation barrier from the graphite, MWCNTs and C60 to diamond, the exact height of which is unknown. The results in this study indicated that the activation barrier between the C60 and diamond is lower than that of the MWCNTs with diamond, and this barrier between MWCNTs and diamond is lower than that of the graphite with diamond. The graphite is the most stable crystalline modification of carbon among the MWCNTs, C60 and graphite allotropes under the SPS processing.

The SPS is a remarkable technique to synthesize and consolidate a large variety of materials. The process typically uses moderate uniaxial pressures usually below 100 MPa in combination with a pulsing ON–OFF DC current during its operation. There are many mechanisms proposed to account for the enhanced sintering abilities of the SPS process; for example, field assisted diffusion [15], spark impact pressure [15,16], plasma cleaning of particle surfaces [17], Joule's heating [16,17], local melting and evaporation especially in metallic systems [16], surface activation on particles [18] and electron wind force [19]. The one that draws the most controversy of these mechanisms involves the presence of momentary plasma. In this study, the diamond converted from the MWCNTs and C60 without any catalysts being involved in the SPS. However, the parallel investigations by using the synchrotron radiation in situ high temperature X-ray diffraction show that there is no diamond formation in the MWCNTs and C60 samples in the AC sintering at the same pressure (80 MPa) and temperature (1500 °C). What is their phase transitional mechanism from MWCNTs and C60 to diamond in the SPS? Such a clear, significant difference in the products is due to the special sintering principle of SPS. It is a field activated sintering technique based on an DC electric spark discharge phenomenon, i.e. a high energy and low voltage spark pulse DC momentarily generates sparking plasma between particles, which causes localized high temperatures. It is an electric AC heating in the in situ high temperature experiments. Without plasma effect, it would need 8000–10,000 °C at pressure of 80 MPa to get diamond from the MWCNTs and C60, as we calculated. Therefore, super-high pressure (5–10 GPa) are required for the diamond formation in the hydrostatic HPHT technique. Since the SPS only needs MPa level pressure, it is believed that the plasma plays the key role for the diamond transformation from the MWCNTs and C60. The high current, low voltage, momentary pulsed plasma discharge have generated highly localized Joule's heating up to a few thousand degrees Celsius between particles in few minutes. The current density in the SPS is typically on the order of 10^2 A/cm² and is highly concentrated at the inter-granular contact or interface [12]. The momentary pulsed plasma provided energy equivalent to thousand degrees to help the nano-carbon

across their activation barriers to the diamond phase. It leads to the transformation of mainly sp² bonded MWCNTs and C60 to sp³ bonded diamonds. Despite the on-going argument about whether the spark plasmas actually occur during the SPS process, our present study, regarding on the generating diamond under such a low pressure, suggests that such spark plasmas indeed took place during SPS of these nano-carbon materials with excellent electrical conductivities and high surface areas. The plasmas generated very high localized temperatures up to about 8000–10,000 °C and dramatically reduced the pressures required for diamond formation from the GPa to the MPa level. Eventually, this research provided some new indirect evidences for the presence of plasmas during the SPS operation.

4. Conclusions

The thermal stability of MWCNTs, C60 and graphite has been investigated under the pulsed DC field in a SPS furnace. Cubic diamond and *n*-diamond have been converted from pure MWCNTs, cubic diamond has been converted from pure C60 without catalysts being involved by the SPS at conditions of 1500 °C, 80 MPa for 20 min. There was no notice of diamond formation in the case of pure graphite sample processed by SPS at this condition. The graphite is the most stable crystalline modification of carbon among the MWCNTs, C60 and graphite allotropes under the SPS. The parallel investigations by using the synchrotron radiation in situ high temperature (AC field) X-ray diffraction show that there is no diamond formation in the MWCNTs and C60 samples at the same pressure (80 MPa) and temperature (1500 °C). Their phase transitional mechanism from MWCNTs and C60 to diamond indicated the high localized temperatures between particles due to the presence of momentary plasmas during the SPS process.

Acknowledgements

This research was supported by the DFG-Deutschen Forschungsgemeinschaft (German Research Foundation) with Grant No. BU 547/10-1 and DESY Hasylab Project with Grant No. II-20090264.

References

- [1] K.M. Liew, C.H. Wong, X.Q. He, M.J. Tan, *Phys. Rev. B* 71 (2005) 075424.
- [2] Y.A. Kim, H. Muramatsu, T. Hayashi, M. Endo, M. Terrones, M.S. Dresselhaus, *Chem. Phys. Lett.* 398 (2004) 87.
- [3] Z.A. Munir, U. Anselmi-Tamburini, *J. Mater. Sci.* 41 (2006) 763.
- [4] J.R. Groza, A. Zavaliangos, *Mater. Sci. Eng., A* 287 (2000) 171.
- [5] F. Zhang, J. Shen, J. Sun, Y.Q. Zhu, G. Wang, G. McCartney, *Carbon* 43 (2005) 1254.
- [6] J. Shen, F.M. Zhang, J.F. Sun, Y.Q. Zhu, G. McCartney, *Nanotechnology* 17 (2006) 2187.
- [7] F. Zhang, J. Shen, J. Sun, D.G. McCartney, *Carbon* 44 (2006) 3136.
- [8] F. Inam, H. Yan, M.J. Reece, T. Peijs, *Adv. Appl. Ceram.* 109 (2010) 240.
- [9] U. Anselmi-Tamburini, S. Gennari, J.E. Garay, Z.A. Munir, *Mater. Sci. Eng., A* 394 (2005) 139.
- [10] D.M. Hulbert et al., *J. Appl. Phys.* 104 (2008) 033305.
- [11] R.J. Hemley, G.L. Chiarotti (Eds.), *High Pressure Phenomena*, IOS Press, Amsterdam, 2002.
- [12] K. Yang, J. He, Z. Su, J.B. Reppert, M.J. Skove, T.M. Tritt, A.M. Rao, *Carbon* 48 (2010) 756.
- [13] E. Burkel, *J. Phys. Condens. Matter* 13 (2001) 7477.
- [14] B. Wen et al., *J. Phys. Condens. Matter* 16 (2004) 2991.
- [15] G.D. Zhan, J. Kuntz, J. Wan, J. Garay, A.K. Mukherjee, *J. Am. Ceram. Soc.* 86 (2003) 200.
- [16] M. Omori, *Mater. Sci. Eng., A* 287 (2000) 183.
- [17] W. Chen, U. Anselmi-Tamburini, J.E. Garay, J.R. Groza, Z.A. Munir, *Mater. Sci. Eng., A* 394 (2005) 132.
- [18] N. Frage, S. Cohen, S. Meir, S. Kalabukhov, M. Dariel, *J. Mater. Sci.* 42 (2007) 3273.
- [19] P. Shewmon, *Diffusion in Solids*, second ed., Minerals Metals & Materials Society, Warrendale, PA, 1989. pp. 246.

Diamond synthesis through the generation of plasma during spark plasma sintering

Faming Zhang^{*1}, Furqan Ahmed^{2,3}, Jozef Bednarcik⁴, and Eberhard Burkel¹

¹Institute of Physics, University of Rostock, August Bebel Str. 55, Rostock 18055, Germany

²Department of Materials Science and Engineering, University of Erlangen-Nürnberg, Martens Str. 5, Erlangen 91058, Germany

³Department of Metallurgical and Materials Engineering, University of Engineering and Technology, Lahore, Pakistan

⁴HASYLAB at DESY, Notkestr. 85, 22603 Hamburg, Germany

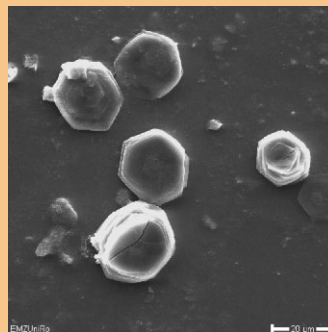
Received 18 May 2012, revised 27 June 2012, accepted 31 July 2012

Published online 24 August 2012

Keywords carbon nanotubes, phase transformations, Raman spectroscopy, spark plasma sintering, synchrotron radiation

^{*} Corresponding author: e-mail faming.zhang@uni-rostock.de, Phone: 49 381 4986864, Fax: 49 381 4986862

Spark plasma sintering (SPS) of carbon nanotubes based materials to diamond was conducted at a very low pressure in vacuum and argon atmospheres. The phases and microstructures of the sintered samples were analyzed by Synchrotron X-ray, Raman spectroscopy, and scanning electron microscopy. Diamond phases are created from carbon nanotubes/FeNi mixtures at pressure of 9.55 MPa in vacuum and argon atmospheres during SPS. At this pressure, carbon flowers, and perfect diamond crystals are obtained at 1200 °C only in the argon atmosphere. The consequences provide an indirect evidence for the existence of plasma during SPS. The argon atmosphere promotes the plasma generation and thus enhances the diamond transition.



Diamonds are obtained from carbon nanotubes/FeNi at 1200 °C and 9.55 MPa in argon atmosphere of SPS.

© 2012 WILEY-VCH Verlag GmbH & Co. KGaA, Weinheim

1 Introduction Spark plasma sintering (SPS), also defined as field assisted sintering technique (FAST) or pulsed electric current sintering (PECS), is an electric field assisted sintering process utilizing ON-OFF DC pulse energizing. The SPS is a remarkable technique to synthesize and consolidate a large variety of materials. There are many mechanisms proposed to account for the enhanced sintering abilities of the SPS process; for example, Joule's heating [1, 2], local melting, and evaporation especially in metallic systems [1], surface activation on particles [3], electron wind force [4], field assisted diffusion [5], spark impact pressure [1, 5], and plasma cleaning of particle surfaces [2]. The one that draws the most controversy of these mechanisms involves the presence of momentary plasma. There are on-going arguments about whether the spark plasmas actually occur during the SPS process [6–8].

In our previous research [9], we have provided an indirect way to validate the existence of the plasmas during the SPS. It is in the light of a thermal dynamic analysis of the phase transformation of nanocarbon materials. It was found that the diamond forms from pure carbon nanotubes (CNTs) and fullerenes C₆₀ at 1500 °C and 80 MPa [8, 9]. The thermal dynamic analysis suggests that the spark plasmas provide most of the energy required in such diamond formation [10]. The SPS process typically uses moderate uniaxial pressures below 100 MPa and commonly in vacuum. As indicated from the plasma spraying technique, gases like H₂, Ar, O₂, and so on can be used as plasma generating gases which can enhance the plasmas generation [11, 12]. In this study, the diamond synthesis from CNTs through the generation of plasmas during the SPS was investigated by very low pressure and various atmosphere SPS experiments. The pure multiwalled carbon nanotubes (MWCNTs) and MWCNTs/

FeNi mixture powders were degassed in the SPS and then sintered in vacuum and Ar gas atmospheres at 3 kN (9.55 MPa) which is the minimum pressure of the Model HP D-5 FCT SPS system. The sintered samples were etched and analyzed by Synchrotron X-ray diffraction, Raman spectroscopy, and scanning electron microscopy. The effect of the atmosphere on the diamond synthesis and plasma generation during the SPS is discussed.

2 Experimental The MWCNTs (10–20 nm) with purity above 95% were obtained from Shenzhen Nanotech Port, Ltd., China. The Fe₃₅Ni powders with 325 meshes were purchased from Alfa Aesar, Germany, which were prepared by gas atomization method with 99.0% purity. The MWCNTs were mixed uniformly with Fe₃₅Ni powders at a weight ratio of 1:1 by ball milling.

The SPS experiments were conducted using a Model HP D-5 FCT SPS system (FCT systeme GmbH, Rauenstein, Germany) installed at the Tycho Sinter Lab in the University of Rostock. The powders were pressed into a ϕ 20 mm graphite die at 3 kN pressure (9.55 MPa). They were degassed at 450 °C for 10 min in vacuum and then sintered in vacuum (1–3 Pa) and argon gas (20 hPa), respectively. A heating rate of 100 K min⁻¹ was adopted, and the sintering process lasted typically 20 min. The final temperatures were selected to be 1500 °C for pure MWCNTs and 1200 °C for MWCNTs/FeNi mixtures based on our previous researches [9, 13]. The applied direct current for SPS was 1000–1500 A with pulse duration of 12 ms and an interval of 2 ms. The final samples are disk-shaped samples of 20 mm diameter and 5 mm thickness. The sintered MWCNTs and MWCNTs/FeNi samples were etched in a boiling solution of concentrated H₂SO₄ (90 vol.%) and HNO₃ (10 vol.%) for 2 h. The etched samples were washed using deionized water repeatedly and dried in an oven. The phase identification of the etched carbon samples was performed by a high-energy X-ray diffraction at Beamline BW5 (DESY/HASYLAB Hamburger Synchrotron Laboratory) with a wavelength of 0.123984 Å (100.0 keV) and by a Renishaw-2000 Laser Raman spectroscopy system with a He–Ne laser excited at 514 nm. The samples were also analyzed using scanning electron microscope (SEM, Zeiss Supra 25, Germany) at 20 keV.

3 Results and discussion Figure 1a shows the synchrotron radiation-high energy X-ray diffraction patterns of the MWCNTs powder and the SPSed MWCNTs at 1500 °C under 9.55 MPa in vacuum and Ar gas atmospheres. The MWCNTs powder shows diffraction peaks at 3.43, 2.10, 1.70, and 1.22 (\pm 0.01) Å corresponding to the CNTs (002), (100), (004), and (110) plane spacing, respectively. After SPS processing, all the diffraction peaks of the CNTs are much sharper than before. However, no diamond peaks were found in the X-ray diffraction patterns. Figure 1b shows the Raman spectra of the MWCNTs powder and SPSed samples. The raw CNTs show *D* band at 1344 cm⁻¹ and *G* band at 1569 cm⁻¹. After SPS, the *G* bands shifted to the same value

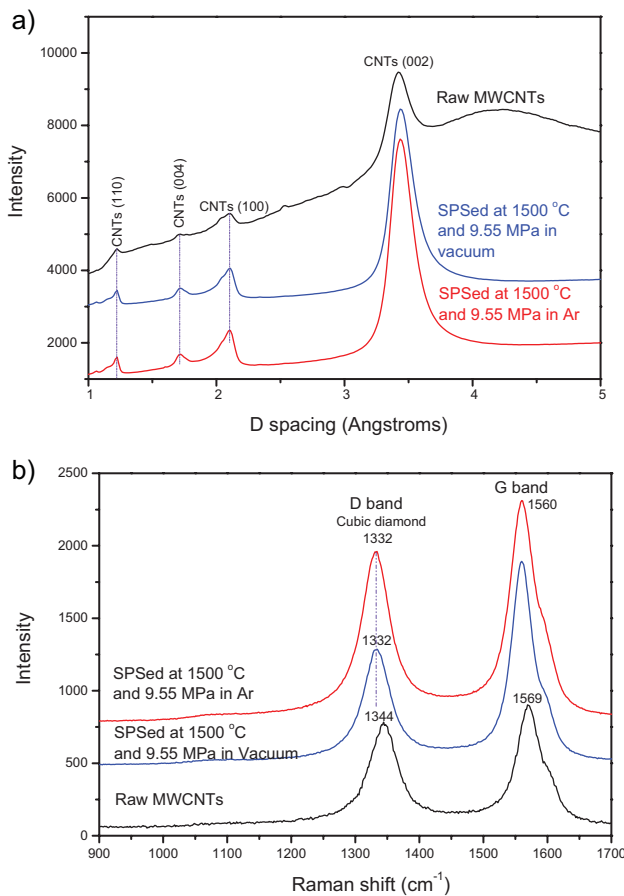


Figure 1 (online color at: www.pss-a.com) Synchrotron radiation-high energy X-ray diffraction patterns (a) and Raman spectra (b) of the raw MWCNTs and the spark plasma sintered MWCNTs at 1500 °C and 9.55 MPa in vacuum and Ar gas atmospheres.

of 1560 cm⁻¹ and the *D* bands shifted to 1332 cm⁻¹ indicating the diamond sp³ hybrid. The XRD results did not show the diamond peak so that only the Raman spectra results cannot confirm the diamond formation. The Raman spectra results only indicate that there are some sp³ carbon hybrids in the samples after the SPS. The peak area ratio of the *D* and *G* bands of the SPSed samples was calculated. The sample sintered in the Ar gas shows higher *D*/*G* ratio (0.77) than the vacuum sintered one (0.56). This indicates that there is a higher fraction of sp³ carbon hybrids in the Ar gas sintered sample.

Figure 2a and b shows the SEM micrographs of the MWCNTs samples SPSed at 1500 °C under 9.55 MPa in vacuum. At lower magnification, some particles can be seen on the surface of the sample (Fig. 2a). With a higher magnification, it is found that these particles are in a transition stage to diamond (Fig. 2b). Figure 2c and d shows the SEM micrographs of the MWCNTs samples SPSed at 1500 °C under 9.55 MPa in Ar gas. There are much more particles on the surface of the sample. A high magnification

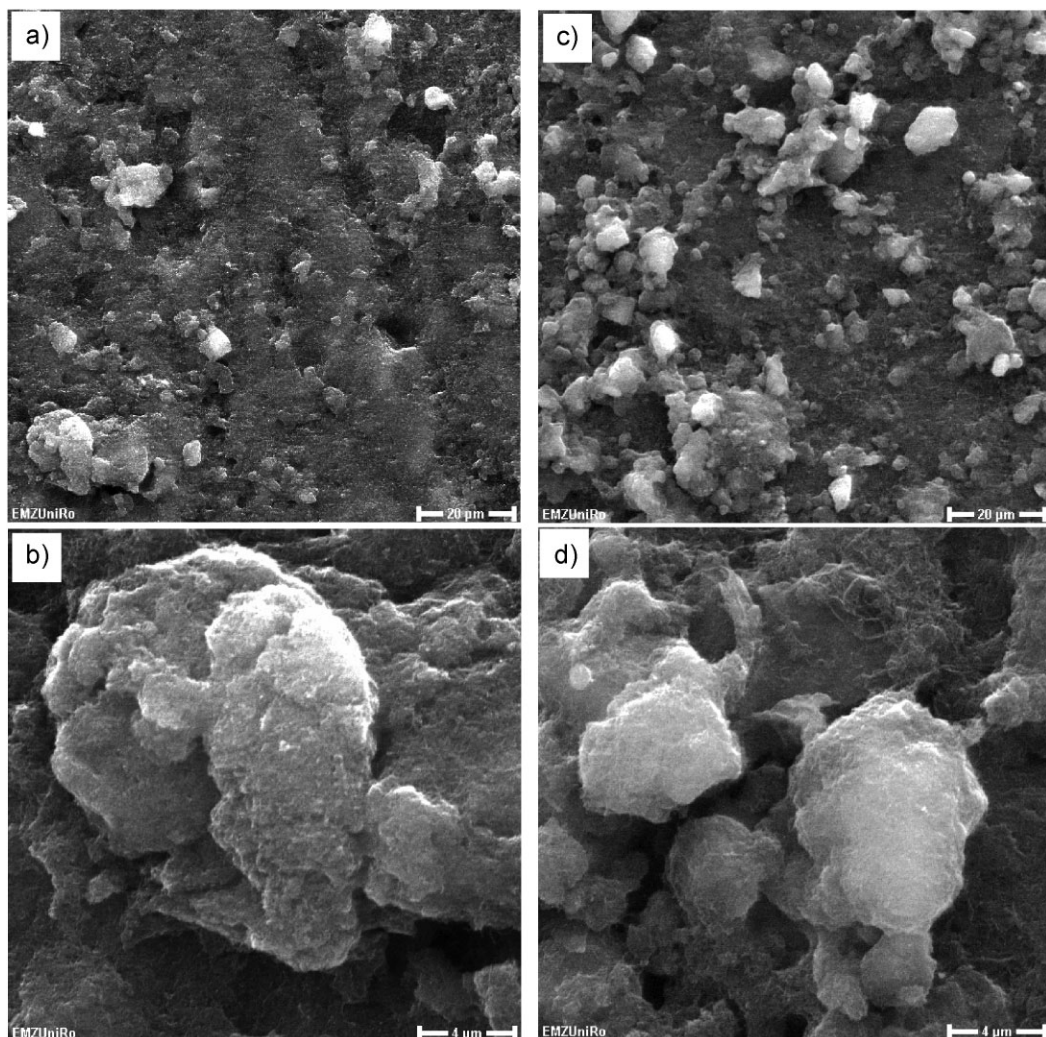


Figure 2 SEM micrographs of the spark plasma sintered MWCNTs at 1500 °C and 9.55 MPa in vacuum (a,b) and Ar gas atmospheres (c,d) with various magnifications.

micrograph shows that they are in the transition stage too. The SEM results are in accordance with the synchrotron X-ray diffraction and Raman results showing that the SPS processing of pure MWCNTs in Ar gas increased the fraction of sp^3 carbon hybrids, without forming crystalline diamonds in the samples.

Figure 3a shows the synchrotron radiation-high energy X-ray diffraction patterns of the raw MWCNTs and the SPSed MWCNTs/FeNi at 1200 °C under 9.55 MPa in vacuum and Ar gas. The MWCNTs powder shows a main diffraction peak at $3.43 (\pm 0.01) \text{ \AA}$ corresponding to the CNTs (002) plane spacing, and weak peaks at 2.10 and 1.70 (± 0.01) \AA corresponding to the CNTs (100) and (004) plane spacing, respectively. After SPS processing of the MWCNTs/NiFe, new peaks were detected in the etched sample and centered at 2.06, 1.25 (± 0.01) \AA corresponding to the cubic diamond (ICDD No. 65-537) (111) and (220). The diamond peaks in the Ar gas sintered sample with

WHM (full width at half maximum) value of 0.046 \AA are shaper than that in vacuum with WHM value of 0.090 \AA . Figure 3b shows the Raman spectra of the MWCNTs/FeNi samples SPSed at 1200 °C under 9.55 MPa in vacuum and Ar gas. Both of them show the cubic diamond peak at 1332 cm^{-1} . The vacuum SPSed sample shows very weak diamond peak ($D/G = 0.12$); however, the Ar gas SPSed sample exhibits a strong diamond peak ($D/G = 0.94$). Both of the G bands center at the same value of 1558 cm^{-1} after SPS. But these G bands are much sharper in the vacuum SPSed sample with WHM value of 19.1 cm^{-1} than that in the Ar gas with WHM value of 42.0 cm^{-1} indicating the higher fraction of MWCNTs. The results of the synchrotron X-ray diffraction and Raman spectra confirmed the cubic diamond formation in the MWCNTs/FeNi samples after SPS at 1200 °C and 9.55 MPa for 20 min in both vacuum and Ar atmospheres. The Ar gas enhanced the diamond transition in the SPS.

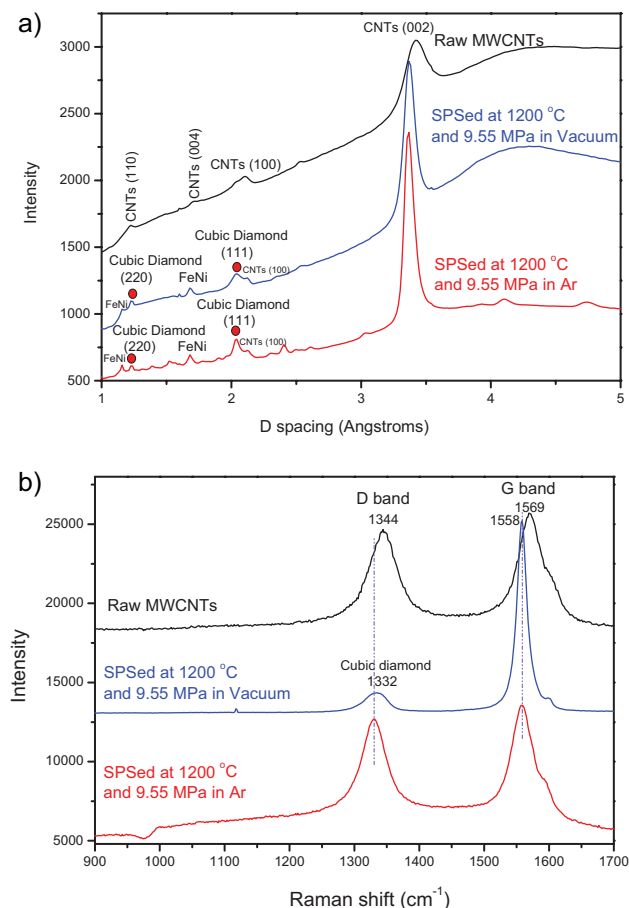


Figure 3 (online color at: www.pss-a.com) Synchrotron radiation-high energy X-ray diffraction patterns (a) and Raman spectra (b) of the raw MWCNTs and the spark plasma sintered MWCNTs/FeNi at 1200 °C and 9.55 MPa in vacuum and Ar gas atmospheres.

Figure 4a and b shows the SEM micrographs of the MWCNTs/FeNi samples SPSed at 1200 °C and 9.55 MPa in vacuum. There are only a few poor quality diamond crystals created in the vacuum atmosphere of the SPS (Fig. 4a). A cubic diamond crystal with an incomplete shape in the reacted MWCNTs matrix is shown in Fig. 4b. Figure 4c–f shows the SEM micrographs of the MWCNTs/FeNi samples SPSed at 1200 °C and 9.55 MPa in Ar gas. Some flower-like structured carbons are observable in the sample (Fig. 4c and d). This indicates that sparking plasmas may have happened and generated such carbon flowers. It is exciting that some high quality diamond crystals with hexahedron structures are found in the sample (Fig. 4e). A high magnification SEM micrograph of perfect diamond crystals is shown in Fig. 4f. The SEM results are in agreement with the synchrotron X-ray diffraction and Raman results that the Ar gas atmosphere in the SPS promoted the diamond formation.

Figure 5a and b shows the current and voltage during SPS of the pure MWCNTs and MWCNTs/FeNi in vacuum and Ar gas atmospheres. It is interesting to find that the current and voltage values in Ar atmosphere are all higher than those in

vacuum at the same temperatures using the same raw materials of MWCNTs and MWCNTs/FeNi, respectively. The Ar gas has high electrical resistance as well as it can adsorb some heats during the SPS. The MWCNTs have large surface areas and are sintered at the minimum pressure of the SPS. Some amounts of Ar gas can enter into and be adsorbed by the nanotubes. The resistance of the sample has been increased. Therefore, the SPS in Ar gas needs much higher current and voltages.

In this study, the SPS pressure is very low (9.55 MPa), so that the pressure effect is negligible for the diamond conversion. In both vacuum and Ar gas atmospheres, some fractions of sp^3 carbon hydrides have been obtained from the raw MWCNTs and crystalline cubic diamond crystals have been generated from the MWCNTs/FeNi by the SPS at such a low pressure. Where is the energy coming from for the transition of MWCNTs to diamond? The total energy for the diamond formation can be formulated [10]:

$$Q = \Delta H_T + Q_P + \Delta H_M, \quad (1)$$

where Q is the total energy, ΔH_T is the energy due to temperature difference, Q_P is the energy due to pressure difference, and ΔH_M is the energy due to plasma effect. The enthalpy of plasma is

$$H = H_E + H_K + H_D + H_I, \quad (2)$$

where H is the plasma contribution, H_E is the kinetic contribution, H_K is the excitation contribution, H_D is the dissolution contribution, and H_I is the electrolytic contribution. Then,

$$dS = \frac{\delta Q}{T}, \quad (3)$$

$$\Delta Q(T) - \Delta Q(T_0) = \Delta S(T_0 - T), \quad (4)$$

where T is the temperature, T_0 is the starting temperature, ΔQ is the difference of mol free energy, and ΔS is the difference of mol entropy. Only when $\Delta Q(T) < 0$ MWCNTs can be transformed into diamond. So, we can get the equation:

$$T > T_0 + \frac{\Delta Q(T_0)}{\Delta S}. \quad (5)$$

The effect of plasma in the SPS has increased the entropy ΔS of the whole SPS system resulting in a lower sintering temperature T for the diamond formation. As a result, diamonds were converted from MWCNTs with FeNi catalysts under very low pressure of 9.55 MPa. Based on the above thermal dynamic analysis, it is indicated that the plasma generated during the SPS operation plays the key role and provides most of the energy which is needed for the diamond formation. The momentary pulsed plasma provided energy equivalent to several thousands degree to help the MWCNTs across their activation barriers to form the diamond phase with the assistances from solvent catalyst-

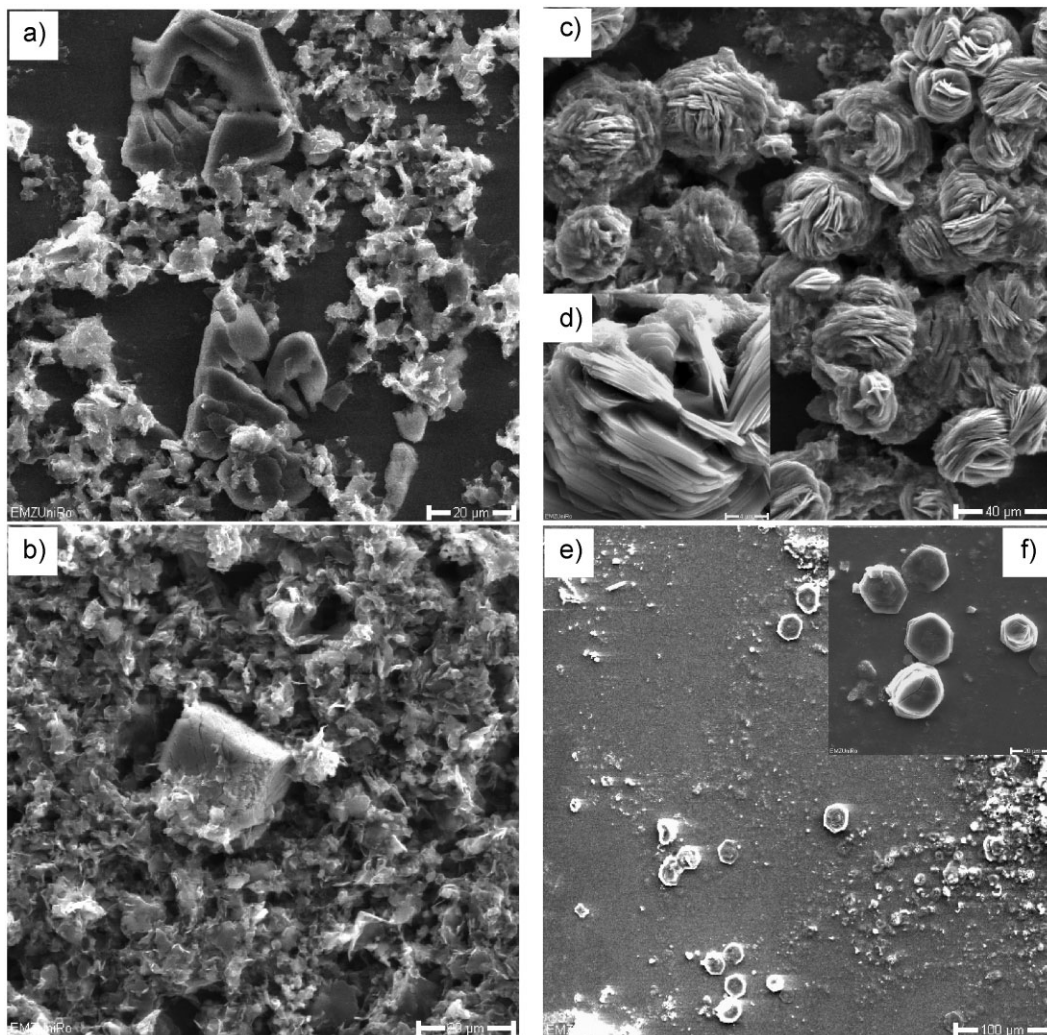


Figure 4 SEM micrographs of the spark plasma sintered MWCNTs/FeNi at 1200 °C and 9.55 MPa in vacuum (a,b) and Ar gas atmospheres (c–f) with various magnifications.

FeNi. It leads to the transformation of mainly sp^2 bonded MWCNTs to sp^3 bonded diamonds. Thus, this study provided another important evidence for the existence of plasma during the SPS at such low pressure diamond formation.

The Ar gas-SPS processed MWCNTs samples have higher fractions of sp^3 carbon hydrides than those treated in vacuum. The Ar gas atmosphere-SPS processed MWCNTs/NiFe samples have carbon flowers and perfect, high quality diamond crystals with hexahedron structures; however, only few incomplete shaped diamonds are found in the vacuum processed sample. Such an obvious difference indicates that the Ar gas atmosphere in the SPS operation enhanced the plasma generation and promoted the diamond transition. In present study, the MWCNTs samples were firstly degassed in vacuum at 450 °C for 10 min, and were sintered at the minimum pressure (3 kN) of FCT D-5 SPS system. Because of these special treatments, some amounts of Ar gas will

be adsorbed at gas pressure of 20 hPa during the SPS. The values of the voltage and current with function of temperature during SPS are plotted (Fig. 5). The results present that the current and voltage are much higher in Ar atmosphere of the SPS using the same temperature program and starting materials. The higher current and voltage in the Ar atmosphere of the SPS generated larger sparking plasmas, thus created more diamonds. It means that the Ar gas atmosphere should be selected when the enhancement of the plasma effect is needed in the SPS operation.

A plasma is an electrically conductive gas containing charged particles. The plasma generated for plasma spraying technique usually incorporates one or a mixture of the following gases: Ar, He, N_2 , H_2 , and Air [12, 14, 15]. Ar is probably the most favored primary plasma gas and is usually used with a secondary plasma gas (H_2 , He, and N_2) to increase its energy [15]. It is the easiest gas to form plasma and tends to be less aggressive toward electrode and nozzle

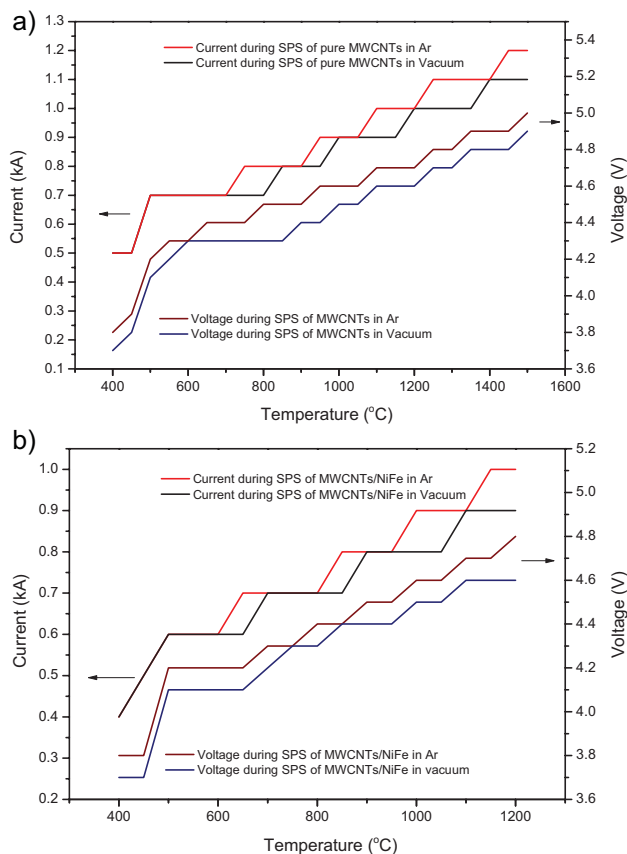


Figure 5 (online color at: www.pss-a.com) Current and voltage values during SPS of the pure MWCNTs (a) and MWCNTs/FeNi (b) in vacuum and Ar gas atmospheres.

hardware. Most plasmas are started up using pure Ar. The results in this study show that the Ar gas has a similar effect as in the plasma spraying process. The atoms of the Ar gas are excited to high energy levels during the SPS operation, the atoms become ionized producing a plasma containing electrically charged particles – ions and electrons. Monatomic molecule of Ar plus energy gives one free atom of Ar:



The reverse process provides most of the energy for heating without a dramatic drop in temperature. The momentary generated plasmas can produce temperatures around 7000–20 000 K. Therefore, the generated plasma during Ar gas-SPS supplies a high amount of energy, by which promoted the fraction of sp^3 hydride carbon in the MWCNTs and the diamond conversion from the MWCNTs/NiFe at a very low pressure of 9.55 MPa.

In summary, some fractions of sp^3 hydride carbon in the transition stage to diamond are obtained from the pure

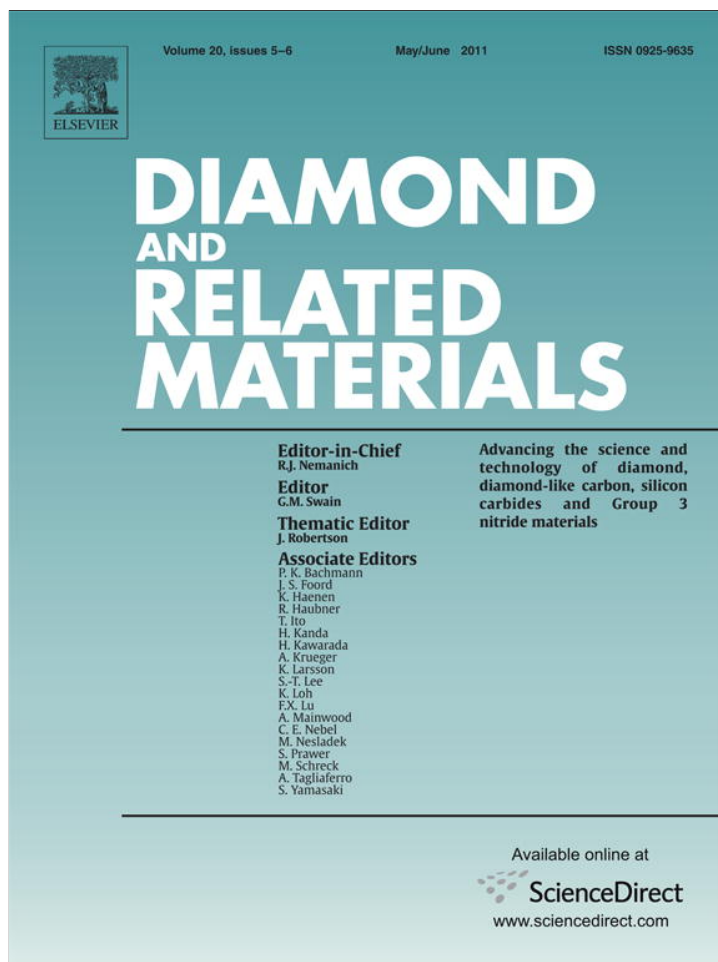
MWCNTs by SPS at 1500 °C and 9.55 MPa in vacuum and Ar atmosphere. Crystalline cubic diamond crystals are generated from the MWCNTs/FeNi by SPS at 1200 °C and 9.55 MPa in vacuum and Ar atmosphere. Carbon flowers and high quality diamond crystals with hexahedron structures are produced only in the Ar atmosphere. Such low pressure diamond formation in both vacuum and Ar gas atmospheres provides an important indirect evidence for the existence of plasma during the SPS. The Ar atmospheres lead to higher currents and voltages during SPS. It is assumed to promote the plasma generation and sizes. The plasmas momentary generated from ionized gas produced temperatures up to thousands of degree and thus promote the diamond transition.

Acknowledgements This research was supported by the DFG-Deutschen Forschungsgemeinschaft (German Research Foundation) with grant no. BU 547/10-1 and BU 547/10-2, as well as Venture Cup-MV 2011, Germany with grant no. UR 11 007 VC 2011, DESY Hasylab Project with grant no. II-20090264 and I-20110661. Portions of this research were carried out at the light source Hasylab at DESY, a member of the Helmholtz Association (HGF). We would like to thank Dr. Martin von Zimmermann for assistance in using Beamline BW5.

References

- [1] M. Omori, *Mater. Sci. Eng. A* **2871**, 83 (2000).
- [2] W. Chen, U. Anselmi-Tamburini, J. E. Garay, J. R. Groza, and Z. A. Munir, *Mater. Sci. Eng. A* **394**, 132 (2005).
- [3] N. Frage, S. Cohen, S. Meir, S. Kalabukhov, and M. Dariel, *J. Mater. Sci.* **42**, 3273 (2007).
- [4] P. Shewmon, in: *Diffusion in Solids (Minerals, Metals, Materials Society, Warrendale, PA, 1989)*, p. 246.
- [5] G. D. Zhan, J. Kuntz, J. Wan, J. Garay, and A. K. Mukherjee, *J. Am. Ceram. Soc.* **86**, 200 (2003).
- [6] U. Anselmi-Tamburini, S. Gennari, J. E. Garay, and Z. A. Munir, *Mater. Sci. Eng. A* **394**, 139 (2005).
- [7] D. M. Hulbert, A. Anders, D. V. Dudina, J. Andersson, D. Jiang, C. Unuvar, U. Anselmi-Tamburini, E. J. Lavernia, and A. K. Mukherjee, *J. Appl. Phys.* **104**, 033305 (2008).
- [8] F. Zhang, J. Shen, J. Sun, Y. Q. Zhu, G. Wang, and G. McCartney, *Carbon* **43**, 1254 (2005).
- [9] F. Zhang, C. Mihoc, F. Ahmed, C. Latte, and E. Burkel, *Chem. Phys. Lett.* **510**, 109 (2011).
- [10] F. Zhang, C. Mihoc, and E. Burkel, *Conf. Proc. Mater. Sci. Technol.* **10**, 2312 (2010).
- [11] Z. Zheng, L. Liao, B. Yan, J. X. Zhang, H. Gong, Z. X. Shen, and T. Yu, *Nanoscale Res. Lett.* **4**, 1115 (2009).
- [12] E. Nogues, M. Vardelle, P. Fauchais, and P. Granger, *Surf. Coat. Technol.* **202**, 4387 (2008).
- [13] F. Zhang, M. Adam, E. Otterstein, and E. Burkel, *Diam. Relat. Mater.* **20**, 853 (2011).
- [14] A. Rauf, Q. Yu, L. Jin, and C. Zhou, *Scr. Mater.* **66**, 109 (2012).
- [15] E. Pfender, *Surf. Coat. Technol.* **34**, 1 (1988).

Provided for non-commercial research and education use.
Not for reproduction, distribution or commercial use.



This article appeared in a journal published by Elsevier. The attached copy is furnished to the author for internal non-commercial research and education use, including for instruction at the authors institution and sharing with colleagues.

Other uses, including reproduction and distribution, or selling or licensing copies, or posting to personal, institutional or third party websites are prohibited.

In most cases authors are permitted to post their version of the article (e.g. in Word or Tex form) to their personal website or institutional repository. Authors requiring further information regarding Elsevier's archiving and manuscript policies are encouraged to visit:

<http://www.elsevier.com/copyright>



Pulsed electric field induced diamond synthesis from carbon nanotubes with solvent catalysts

Faming Zhang^a, Martin Adam^a, Furqan Ahmed^{b,c}, Eileen Otterstein^a, Eberhard Burkel^a

^a Institute of Physics, University of Rostock, August Bebel Str. 55, Rostock 18055, Germany

^b Department of Materials Science and Engineering, University of Erlangen-Nürnberg, Martens Str. 5, Erlangen 91058, Germany

^c Department of Metallurgical and Materials Engineering, University of Engineering and Technology, Lahore 54890, Pakistan

ARTICLE INFO

Article history:

Received 18 July 2010

Received in revised form 14 January 2011

Accepted 14 April 2011

Available online 19 April 2011

Keywords:

Diamond crystal

Carbon nanotubes

Spark plasma sintering

Synthetic diamond

Catalytic processes

ABSTRACT

Spark plasma sintering (SPS) was used to synthesize diamond from multiwalled carbon nanotubes (MWCNTs) with Fe₃₅Ni powders as solvent catalysts. The MWCNTs/Fe₃₅Ni mixtures were spark plasma sintered at various conditions. The microstructures and diamond phase were analyzed by using X-ray diffraction, Raman spectroscopy, scanning electron microscopy, and transmission electron microscope techniques. Experimental results showed that the diamond crystals can be synthesized from MWCNTs/Fe₃₅Ni by using the SPS at lower temperature of 1200 °C under very low pressure of 70 MPa. Well-crystallized cubic diamonds consisted of mono-crystals and poly-crystals exhibiting particle sizes ranged from 10 to 40 μm. The Fe₃₅Ni catalysts achieved an effective enhancement for diamond conversion from MWCNTs during the SPS. A model was also proposed to describe the diamond growth and revealed as a layer-by-layer growth mechanism.

© 2011 Elsevier B.V. All rights reserved.

1. Introduction

Diamond particles and diamond films have now been successfully obtained by many methods including high-pressure and high-temperature (HPHT) [1], detonation [2], combustion flames [3] and chemical vapour deposition (CVD) with RF plasma [4] or microwave plasma [5] etc., where the HPHT method is still the most popular commercial method for the diamond synthesis. The HPHT synthesis of diamond from graphite, fullerenes, and carbon nanotubes (CNTs) has been studied [6–8]; generally, pressures above 5.0 GPa and high temperature above 1300 °C are needed. Additionally, incorporation of solvent catalysts such as Ni, Co, Fe, other transition metals and their alloys is a crucial point for aid of the diamond synthesis in the HPHT method.

Spark plasma sintering (SPS), also defined as field assisted sintering technique (FAST) or pulsed electric current sintering (PECS), is an electric field assisted sintering process utilizing ON–OFF DC pulse energizing [9]. During the SPS treatment, pulsed DC current directly passes through the graphite die, as well as the powder compact, in case of conductive samples. When studying the thermal stability of multi-walled carbon nanotubes (MWCNTs) under the SPS, it was found that under SPS conditions of 1500 °C at pressure of

80 MPa CNTs are unstable and transform to diamonds without any catalysts being involved [10–12]. It is proposed that the spark plasmas play a key role to provide most of the energy required in this diamond transition. These studies indicate that the SPS has a potential to be used as an alternative method for diamond generation. But it needs further investigation to promote the SPS method to be used as a large-scale synthetic diamond production technique instead of the present hydrostatic HPHT method.

In the HPHT method, the involved solvent catalysts could decrease the energy barrier and affect the rate of a kinetics reaction for diamond nucleation and contribute to the formation of diamond from graphite [13,14]. Besides being able to reduce the transforming temperature and pressure from graphite to diamond, they can also affect the quality and crystal form of the diamond. It is indicated that the solvent catalysts may have the same effects to promote diamond growth from MWCNTs in the SPS method. Currently preferred metal catalyst materials are Fe–Ni alloys, such as Fe–35Ni, Fe–31Ni–5Co, Fe–30Ni, and other INVAR alloys, where Fe–35Ni being the most preferred and more readily available [15]. In order to increase the diamond transitional rate, the Fe₃₅Ni alloy powders were chosen as catalysts for diamond synthesis from MWCNTs by the SPS method in this study. The MWCNTs/Fe₃₅Ni mixtures were spark plasma sintered at various conditions. The microstructures and phases in the obtained carbon samples were analyzed by using X-ray diffraction (XRD), Raman spectroscopy (Raman), scanning electron microscopy (SEM), and transmission electron microscope (TEM) techniques. The growth model of the diamond crystals from the MWCNTs in the SPS process was proposed.

Corresponding author. Tel.: +49 381 4986864; fax: +49 381 4986862.

E-mail address: faming.zhang@uni-rostock.de (F. Zhang).

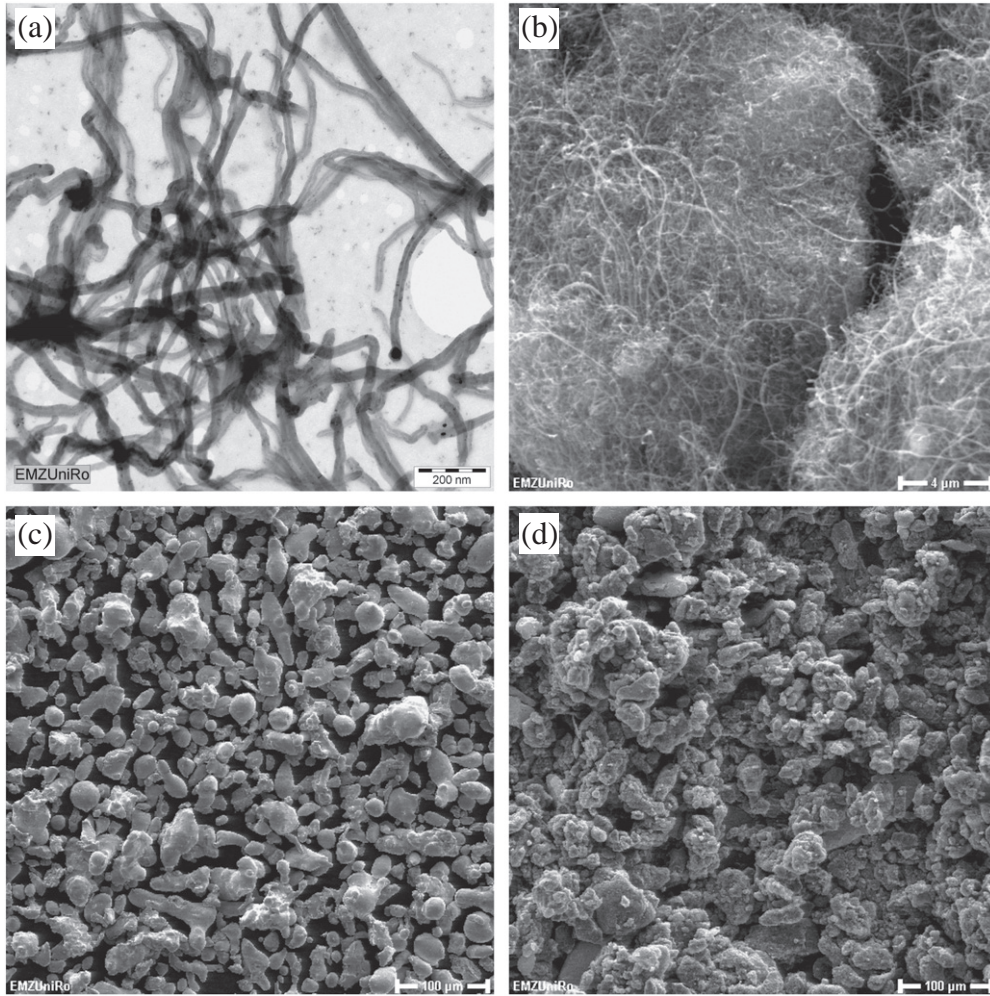


Fig. 1. TEM (a) and SEM (b) micrographs of the starting MWCNTs, as well as SEM micrographs of the Fe35Ni powder catalysts (c) and MWCNTs/Fe35Ni powder mixtures (d).

2. Materials and methods

The MWCNTs were obtained from Shenzhen Nanotech Port, Ltd., China, which were produced by catalytic chemical vapour deposition (CCVD) in which CH₄ was converted into CNTs at 1000 °C in the presence of Ni and La catalysts. The purity of the pristine MWCNTs

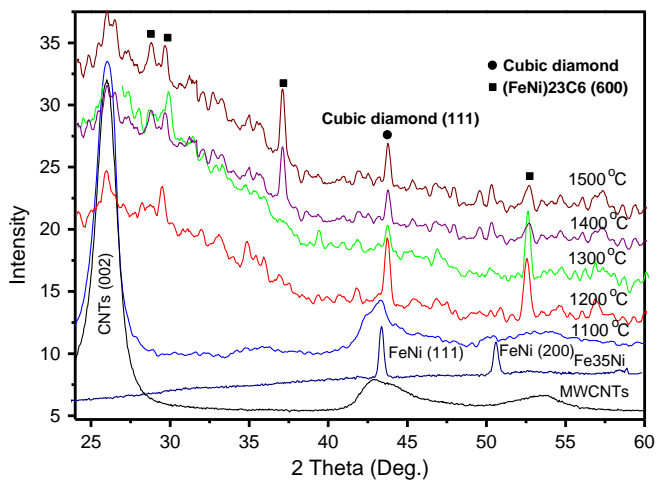


Fig. 2. X-ray diffraction patterns of the starting MWCNTs, Fe35Ni catalyst, and the spark plasma sintered MWCNTs/Fe35Ni samples at 1100–1500 °C after etching.

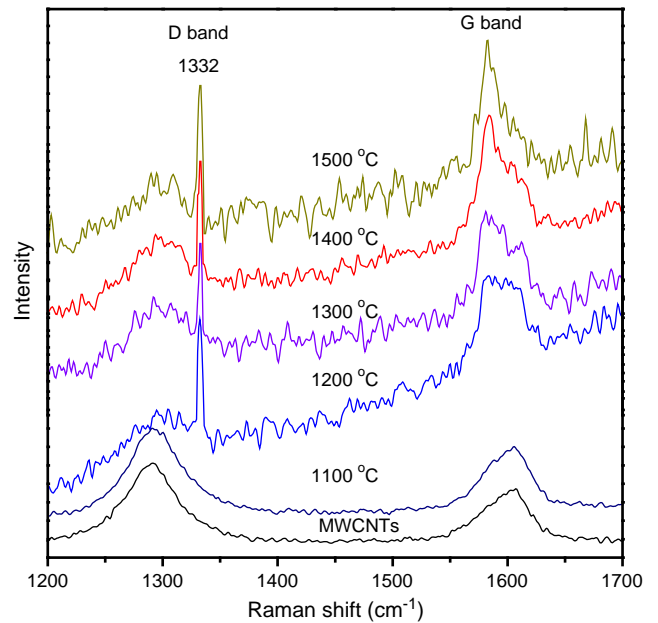


Fig. 3. Raman spectra of the starting MWCNTs and the spark plasma sintered MWCNTs/Fe35Ni samples at 1100–1500 °C after etching.

was claimed above 95% by the producer where presented less than 5% impurities of amorphous carbon and catalysts. The Fe35Ni powders with 325 meshes were purchased from Alfa Aesar, Germany, which were prepared by gas atomization method with 99% purity.

The MWCNTs were mixed with Fe35Ni powders at a weight ratio of 1:1 by ball milling, and pressed into a graphite die for SPS treatment to form disk-shaped samples. The SPS experiments were conducted using a Model HPD-25/1 FCT spark plasma sintering system (FCT systeme GmbH, Rauenstein, Germany) at temperatures of 1100–1500 °C for holding time of 20 min under an axial pressure of 70 MPa in a vacuum (<6 Pa). A heating rate of 100 K/min was adopted, and the sintering process lasted typically 20 min. The applied direct current for SPS was about 1000 A, with a pulse duration of 12 ms and an interval of 2 ms. The resulting disk-shaped samples with diameter of 20 mm and thickness of 6 mm were fabricated. The sintered MWCNTs/Fe35Ni samples were etched in a boiling solution of concentrated H₂SO₄ (90 vol.%) and HNO₃ (10 vol.%) for 2 h. The etched samples were washed using deionized water repeatedly, and dried in an oven. Further identification was performed with an X-ray diffraction (XRD, Bruker D8, Germany) with a CuK radiation (0.154178 nm). The etched samples were analyzed by a Bruker Fourier Transform (FT-) Raman Spectrometer uses a Bruker RAM II Raman module coupled to the VERTEX 70 optical path. The instrument comes with a Nd:YAG laser source with 1064 nm excitation wavelength and a maximum power output of 1500 mW. Scanning electron microscope (SEM, Zeiss Supra 25, Germany) and

transmission electron microscope (TEM, Zeiss-Libra120, Germany) operating at 120 keV were employed to characterize the starting materials and the products following the SPS treatment.

3. Results

The typical morphologies of the MWCNTs starting materials are shown in Fig. 1(a) and (b). They are found to exhibit an external and internal diameter of ca. 40 nm and 20 nm, respectively (Fig. 1a). No other forms of carbon and metal catalysts were identified during the TEM observations. The SEM micrograph shows that the MWCNTs appear entangled and agglomerated together (Fig. 1b). The SEM micrograph of the FeNi catalyst powders is shown in Fig. 1(c). The gas atomized powders present average particle sizes about 40 μm. After ball milling with the MWCNTs, the FeNi powders are mixed well with the nanotubes as shown in Fig. 1(d).

The MWCNTs/FeNi samples were sintered in the SPS furnace at various temperatures under 70 MPa for 20 min. All the obtained samples were etched in boiling acid to remove the FeNi catalysts and the un-reacted MWCNTs. Fig. 2 shows the X-ray diffraction patterns of the starting MWCNTs, Fe35Ni catalyst, and the spark plasma sintered MWCNTs/Fe35Ni samples at 1100–1500 °C after etching. The starting MWCNTs show the (002) plane at 2θ of 25.86° without Ni and La catalysts peaks. The Fe35Ni catalysts show diffraction peaks at 2θ of 43.60 and 50.79°. After etching of the obtained MWCNTs/Fe35Ni samples, no obvious Fe35Ni diffraction peaks were detected in the

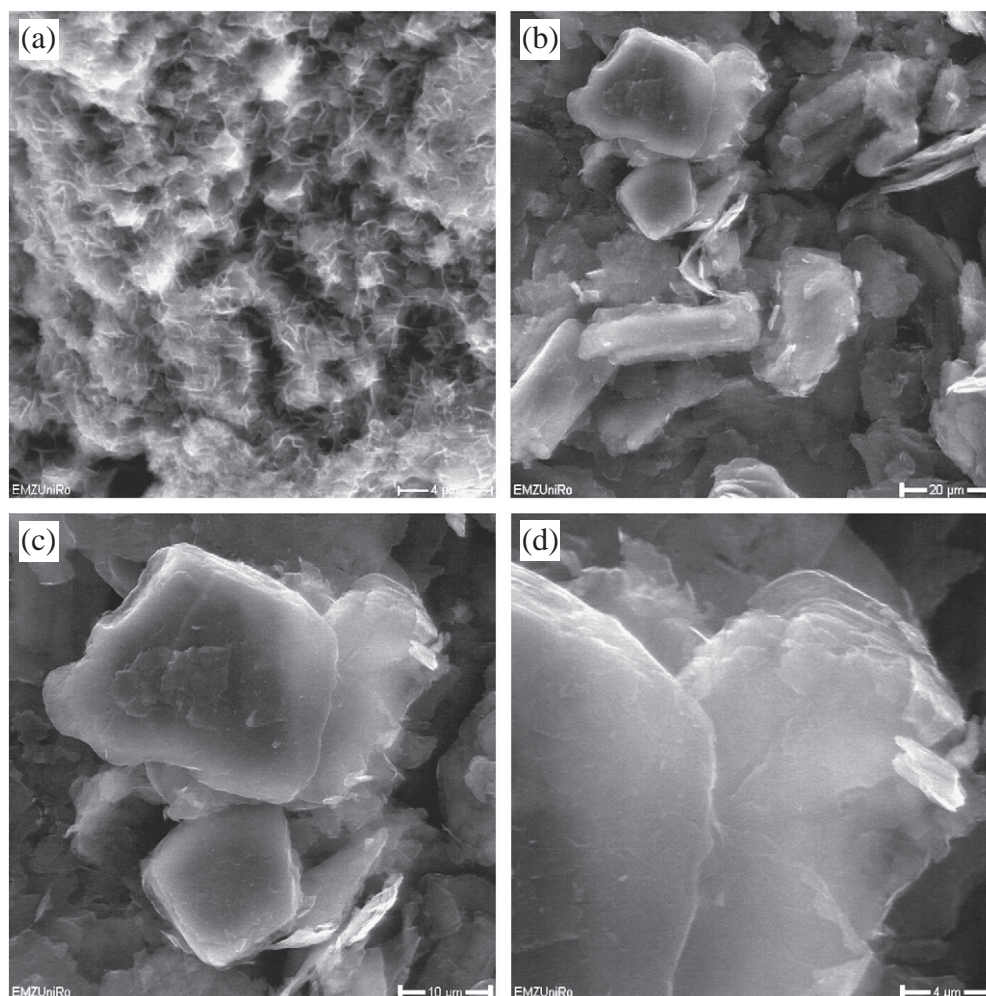


Fig. 4. SEM micrographs of the spark plasma sintered MWCNTs/Fe35Ni samples at 1100 °C (a), 1200 °C (b–d) after etching, exhibiting the growing process of diamonds.

1100–1500 °C sintered samples. It indicated that the FeNi catalysts have been completely removed from the carbon samples by the boiling acid treatment. The peak at 2θ of 42.90° in the raw CNTs has shifted to 43.37° in the 1100 °C sintered sample. It is noted that this sample is in the transitional stage from CNTs to diamond. It is identified that the cubic diamond peak at 2θ of 43.95° with d-spacing of 0.26 nm is present in the samples of 1200–1500 °C. There is still a broad CNTs (002) peak indicating that there are some un-reacted and un-removed CNTs in the samples. Additionally, haxonite (Fe,Ni)₂₃C₆ peaks are found in the XRD results of 1200–1500 °C sintered samples. With temperature increment from 1200 to 1500 °C, the haxonite peaks become stronger and stronger. It is due to the reaction between the FeNi catalysts and the MWCNTs at high temperatures.

Fig. 3 shows the Raman spectra of the starting MWCNTs and the spark plasma sintered MWCNTs/Fe35Ni samples at 1100–1500 °C after etching. The D band of the starting MWCNTs appeared at 1290 cm⁻¹. After spark plasma sintered at 1100 °C, the MWCNTs peak was still presented in the spectrum, but it appeared a new small peak centered at 1300 cm⁻¹. In the spectra of the 1200–1500 °C sintered samples, each of them exhibit a sharp and intense line with a frequency shift of 1332 cm⁻¹, which is the characteristic Raman shift of the cubic diamond. However, the MWCNTs peak (1290 cm⁻¹) still existed but became broader in the Raman spectra, which indicated the un-reacted nanotubes haven't been completely removed but their structures have been destroyed by the boiling-acid treatment. The D band shifted from the starting 1290 cm⁻¹ to 1332 cm⁻¹ indicating the cubic diamond formation above the temperatures of

1200 °C. The G band is due to the E_{2g} mode of graphite band (G band) relating to the sp² bonded carbon vibrations in a 2-dimensional graphitic hexagonal lattice. The G bands appeared at 1606 cm⁻¹ in the starting MWCNTs and 1100 °C sample, has shifted to 1584 cm⁻¹ around in the samples of 1200–1500 °C, which implied the formation of graphite phase besides the diamond formation from the carbon nanotubes above the SPS temperature of 1200 °C. The Raman results indicated that diamonds have been converted from the MWCNTs/Fe35Ni in the temperature range of 1200–1500 °C. The XRD and Raman results confirmed the diamond formation in the 1200–1500 °C sintered samples.

The SEM micrographs of the spark plasma sintered MWCNTs/FeNi samples at 1100 °C and 1200 °C after etching are shown in Fig. 4. Compared with the starting CNTs (Fig. 1b), the MWCNTs in the 1100 °C sample were almost melted and adhered together, but the tubular structure of the CNTs was noticeable in the growing diamond (Fig. 4a). After sintering at 1200 °C, diamond crystals with sizes of 10–40 μm are observed in the samples (Fig. 4b). These diamond crystals are in shape of hexahedron. Some flake-like carbons are noticed in the sample, as indicated by circles. The higher magnification SEM micrograph shows that the diamond crystals without residual CNTs left on their surface (Fig. 4c). The high magnification micrograph in Fig. 4(d) indicated the layer-by-layer texture on the diamond crystals.

Fig. 5 shows the SEM micrographs of the spark plasma sintered MWCNTs/FeNi samples from 1300 °C to 1500 °C after etching. The particle size of the diamond crystals did not increase with the increasing sintering temperatures (Fig. 5a–c). A 1500 °C synthesized

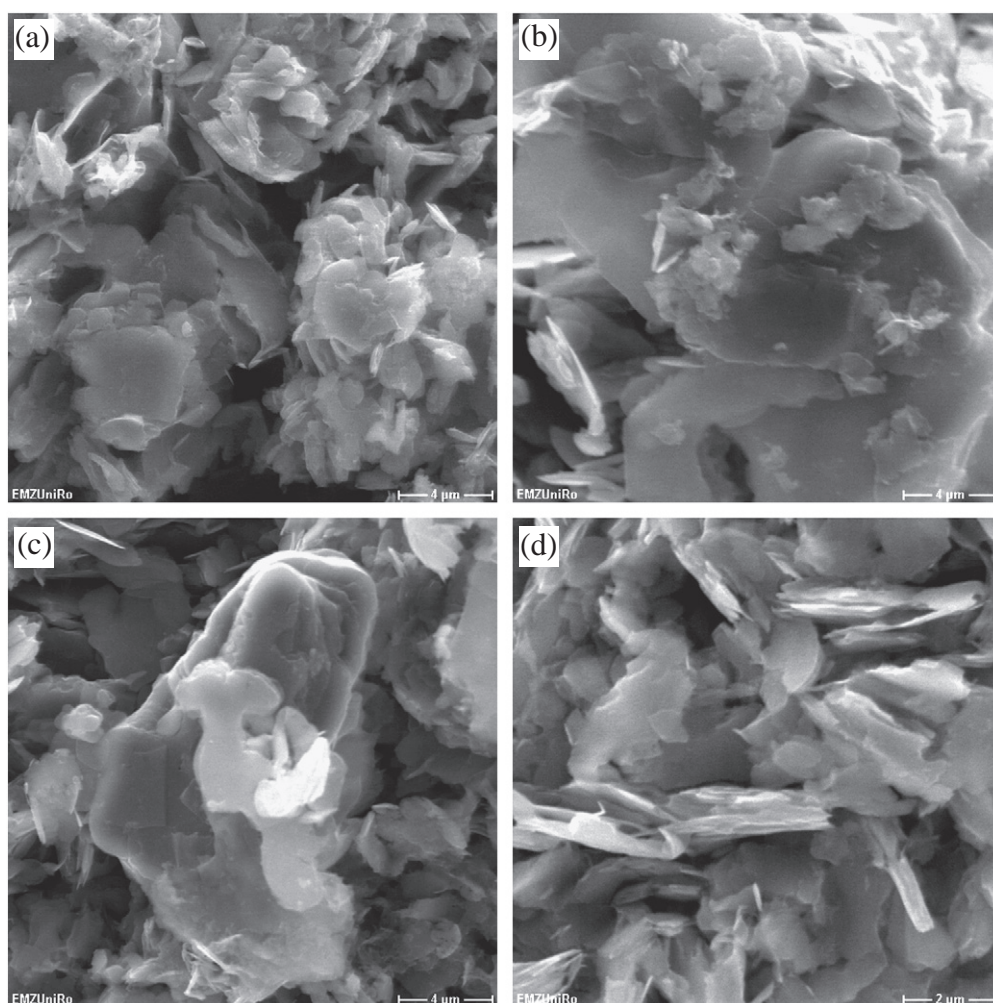


Fig. 5. SEM micrographs of the spark plasma sintered MWCNTs/Fe35Ni at 1300 °C (a), 1400 °C (b), 1500 °C (c, d) after etching, showing the diamond crystals and flakes.

diamond with crystal size about 20 μm also showed clear layer-by-layer textures (Fig. 5c). On the matrix of this diamond crystal, there are many flake-like carbons as shown in Fig. 5(d). Such flake-like carbons were found in all these samples from 1300 to 1500 $^{\circ}\text{C}$. The carbon flakes in these higher temperature sintered samples are similar to those in the 1200 $^{\circ}\text{C}$ sintered one. These flakes also showed layer-by-layer microstructures. The SEM observations agree well with the XRD and Raman results.

Fig. 6 shows the TEM micrographs and selected area diffraction patterns of the spark plasma sintered MWCNTs/Fe35Ni sample at 1200 $^{\circ}\text{C}$ after etching. There are some mono-crystal and poly-crystal diamonds in the samples (Fig. 6a–d). The monocrystalline diamond also shows the layer-by-layer structures (Fig. 6a), which is consistent with the results of the SEM. The selected area diffraction pattern of the crystal in the bottom of the Fig. 5 (a) confirmed that the diamond is mono-crystal along [110] direction (Fig. 6b). The poly-crystal diamond is in size of tens of micrometers (Fig. 6c). The selected area diffraction pattern with diffraction rings were calculated and confirmed that the diamonds are cubic poly-crystals (Fig. 6d). The XRD, Raman, SEM, and TEM identification results have confirmed the diamond formation in MWCNTs with Fe35Ni as catalysts at a lower temperature of 1200 $^{\circ}\text{C}$.

4. Discussions

The XRD, Raman, SEM and TEM results in Figs. 2–6 confirmed that monocrystalline and polycrystalline diamonds were synthesized in the

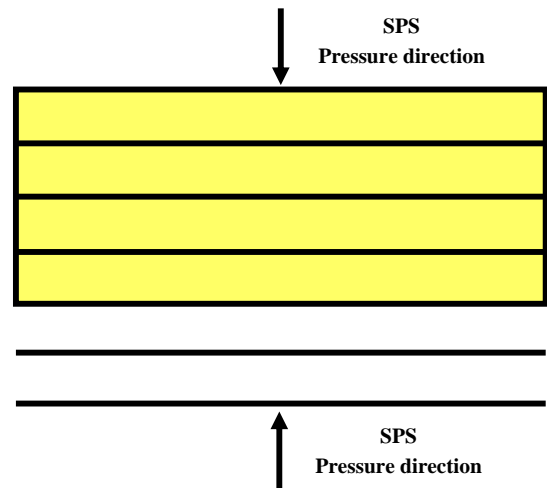


Fig. 7. Schematic illustration of the growth model of diamond crystals from MWCNTs in SPS.

MWCNTs/Fe35Ni sample after SPS at temperatures above 1200 $^{\circ}\text{C}$. The SEM results showed better diamond crystal shapes in the 1200 $^{\circ}\text{C}$ sintered samples. The TEM with selected area diffraction patterns showed the existence of diamond mono-crystals and poly-crystals in

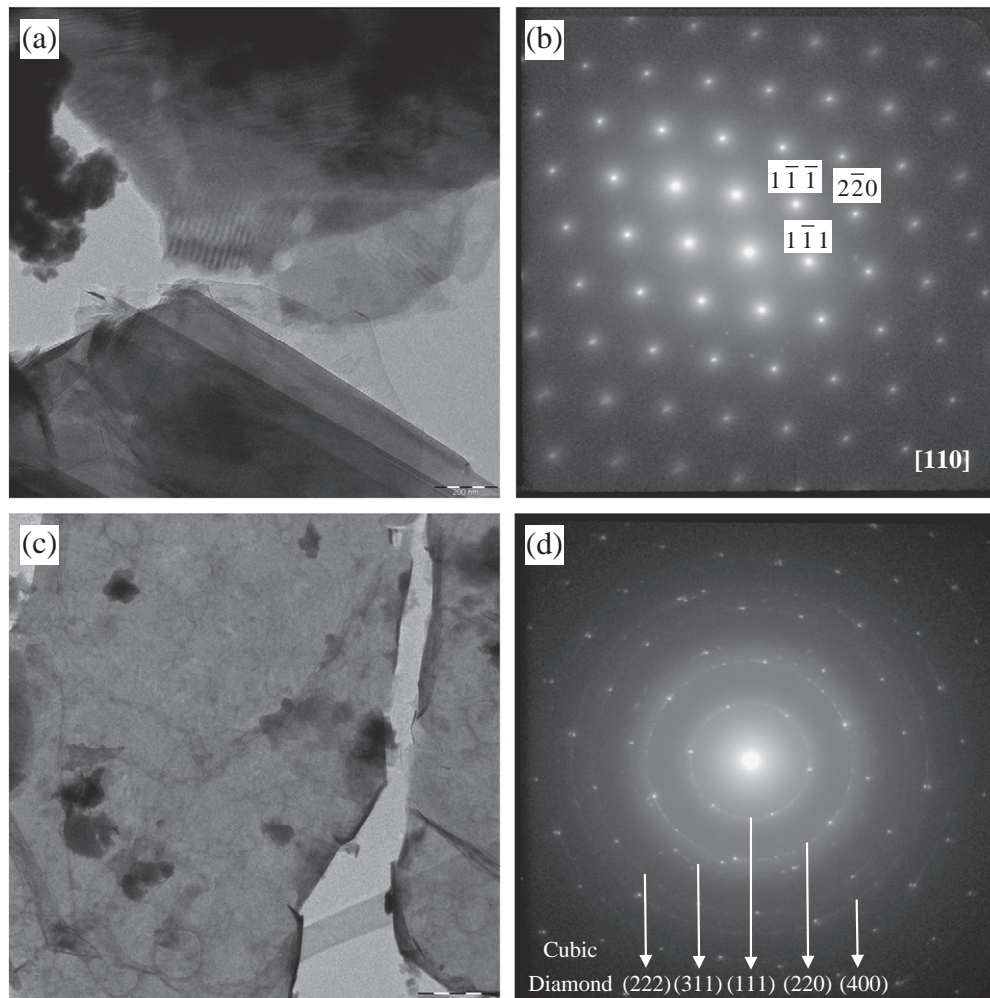


Fig. 6. TEM micrographs with selected area diffraction patterns of the 1200 $^{\circ}\text{C}$ spark plasma sintered MWCNTs/Fe35Ni sample after etching, showing the monocrystalline diamond (a, b) and polycrystalline diamond (c, d).

the 1200 °C sintered samples. Higher temperatures (1300–1500 °C) did not lead to larger diamond crystals as seen in the SEM images. The 1200 °C is the optimal diamond synthesizing temperature for the MWCNTs/Fe35Ni samples. This temperature 1200 °C for the diamond synthesis is much lower than that of the MWCNTs without catalyst (1500 °C) in our previous research [10]. It indicates that the FeNi catalysts are effective to enhance the diamond conversion from MWCNTs in the SPS technique. The melting point of Fe35Ni alloy is about 1460 °C as measured in its phase diagram. During the SPS processing, the melting point of this Fe35Ni powder has been decreased due to the pulsed current induced powder activation, and the applied pressures. There is usually some temperature difference between the mold surface and the actual temperature in the SPS sample. The temperature measurement design in the FCT spark plasma sintering system allowed a very accurate temperature control since the temperature difference between the centre of the sample and the controlling pyrometer was always below 5 °C [16]. The catalysts of Fe35Ni alloy powders were melted at SPS temperature of 1200 °C, which was noticed during the SPS of the MWCNTs/Fe35Ni samples; so that, it reduced the SPS temperature to 1200 °C and the pressure to 70 MPa for the diamond synthesis as well as increased the diamond transitional rate using the MWCNTs as carbon sources. In general, milder conditions were realized for the diamond synthesis by using the Fe35Ni catalysts in this study. In the HPHT method, the carbon–carbon diagram for the diamond synthesis is crucial [17]. In this SPS method, there will be a new carbon–carbon diagram for the diamond synthesis, which can predict the optimal temperature–pressure region.

The layer-by-layer structure of diamond crystals were found in the SEM and TEM micrographs. Our previous research revealed the initial diamond growth mechanism from MWCNTs to diamond in SPS without catalysts, that is from CNTs to intermediate phase carbon onions, and finally to diamond [11]. The diamond crystals in the samples without FeNi catalysts were also shown the similar layer-by-layer structures. Many flake-carbons with layered structures were found in the samples of 1200–1500 °C. This indicates that the diamond crystals were grown up from these carbon flakes. Based upon the above analysis, a model for the growth of diamond crystals during the SPS is proposed in Fig. 7. The direction of pressure during the SPS is along two axial, but not in six directions as in HPHT six-anvil press. Therefore, the diamonds were easier to grow in the directions without pressures. As a result, the MWCNTs were grown to layered diamond flakes perpendicular to the direction of pressure. Finally, several diamond flakes have reacted together and formed a three-dimensional diamond crystal. In a word, the growth mechanism of diamond from MWCNTs is a layer-by-layer model in the SPS method. This growth model is available for the MWCNTs to diamond with and without catalysts. This mechanism will be constructive and helpful for the large diamond crystals synthesis by using the SPS technique.

5. Conclusions

Fe35Ni solvent catalyst has been involved to synthesize diamond from MWCNTs by using the SPS technique. Cubic diamond crystals were synthesized from the MWCNTs/Fe35Ni mixtures at lower SPS temperature of 1200 °C under the pressure of 70 MPa. In the sample, well-crystallized diamond mono-crystals and poly-crystals consisted particle sizes ranged 10–40 μm. The Fe35Ni catalysts achieved an effective reduction of the SPS temperature to 1200 °C and the SPS pressure to 70 MPa for the diamond synthesis, as well as an increment in diamond transitional rate from MWCNTs in the SPS. A model was also proposed to describe the diamond growth and revealed as a layer-by-layer growth mechanism.

Acknowledgements

This research is supported by the DFG-Deutschen Forschungsgemeinschaft (German Research Foundation) with grant No. BU 547/10-1.

Appendix A. Supplementary data

Supplementary data to this article can be found online at doi:10.1016/j.diamond.2011.04.006.

References

- [1] A.A. Giardini, J.E. Tydings, S.B. Levin, *American Mineralogist* 45 (1–2) (1960) 217–221.
- [2] A.L. Vereschagin, G.V. Sakovich, V.F. Komarov, E.A. Petrov, *Diamond and Related Materials* 3 (1–2) (1994) 160–162.
- [3] Y. Hirose, S. Amanuma, K. Komaki, *Journal of Applied Physics* 68 (12) (1990) 6401–6405.
- [4] I. Watanabe, T. Matsushita, K. Sasahara, *Japanese Journal of Applied Physics Part 1- Regular Papers Short Notes & Review Papers* 31 (5A) (1992) 1428–1431.
- [5] K. Kobashi, K. Nishimura, Y. Kawate, T. Horiuchi, *Physical Review B* 38 (6) (1988) 4067–4084.
- [6] S. Naka, K. Horii, Y. Takeda, T. Hanawa, *Nature* 259 (5538) (1976) 38–39.
- [7] Y.Z. Ma, G.T. Zou, H.B. Yang, J.F. Meng, *Applied Physics Letters* 65 (7) (1994) 822–823.
- [8] L. Cao, *Carbon* 39 (2001) 311–314.
- [9] Z. Munir, U. Anselmi-Tamburini, M. Ohyanagi, *Journal of Materials Science* 41 (2006) 763–777.
- [10] F. Zhang, J. Shen, J.F. Sun, Y.Q. Zhu, G. Wang, G. McCartney, *Carbon* 43 (6) (2005) 1254–1258.
- [11] J. Shen, F. Zhang, J.F. Sun, Y.Q. Sun, D.G. McCartney, *Nanotechnology* 17 (9) (2006) 2187–2191.
- [12] F. Zhang, J. Shen, J.F. Sun, D.G. McCartney, *Carbon* 44 (14) (2006) 3136–3138.
- [13] X. Yan, H. Kanda, T. Ohsawa, S. Yamaoka, O. Fukunaga, *Journal of Materials Science* 25 (1990) 1585–1589.
- [14] J. Sung, *Journal of Materials Science* 35 (23) (2000) 6041–6054.
- [15] C.-M. Sun, *Inventor Diamond growth devices and methods*, USA Patent US2008/0313968 A1.
- [16] K. Vanmeensel, A. Laptev, J. Hennicke, J. Vleugels, O. Van der Biest, *Acta Materialia* 53 (2005) 4379–4388.
- [17] N.V. Novikov, *Diamond and Related Materials* 8 (8–9) (1999) 1427–1432.

Provided for non-commercial research and education use.
Not for reproduction, distribution or commercial use.

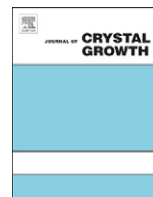


This article appeared in a journal published by Elsevier. The attached copy is furnished to the author for internal non-commercial research and education use, including for instruction at the authors institution and sharing with colleagues.

Other uses, including reproduction and distribution, or selling or licensing copies, or posting to personal, institutional or third party websites are prohibited.

In most cases authors are permitted to post their version of the article (e.g. in Word or Tex form) to their personal website or institutional repository. Authors requiring further information regarding Elsevier's archiving and manuscript policies are encouraged to visit:

<http://www.elsevier.com/copyright>



Growth of diamond from fullerene C60 by spark plasma sintering

Faming Zhang^{a,*}, Furqan Ahmed^{b,c}, Gerd Holzhüter^a, Eberhard Burkel^a

^a Institute of Physics, University of Rostock, August Bebel Strasse 55, Rostock 18055, Germany

^b Department of Materials Science and Engineering, University of Erlangen-Nürnberg, Martens Strasse 5, Erlangen 91058, Germany

^c Department of Metallurgical and Materials Engineering, University of Engineering and Technology, Lahore, Pakistan

ARTICLE INFO

Article history:

Received 28 October 2011

Received in revised form

30 November 2011

Accepted 1 December 2011

Communicated by P. Rudolph

Available online 8 December 2011

Keywords:

A1. X-ray diffraction

A2. Bulk crystal growth

B1. Diamond

B1. Fullerenes

ABSTRACT

The growth of diamond from fullerene C60 was studied by spark plasma sintering (SPS). The phases and microstructures were analyzed by Raman spectroscopy, Synchrotron X-ray, scanning electron microscopy and transmission electron microscopy. Experimental results show that C60 becomes unstable and can be directly transformed into diamond by SPS under a pressure of 50 MPa at temperatures above 1150 °C, without any catalyst being involved. Polycrystalline diamond crystals with sizes up to 250 μm and transition rate about 30 vol% are obtained at SPS temperature of 1300 °C. The mechanism indicates that the high fraction of sp³ hybrids in the fullerene C60 and the generated plasmas in the SPS lead to its transformation into diamond at such low temperatures and pressures. The transformation from C60 to diamond is a direct transition process with a structural reconstruction of carbon atoms without intermediate phases being involved.

© 2011 Elsevier B.V. All rights reserved.

1. Introduction

Due to its unique physical and chemical properties, fullerene C60 is a promising candidate substance for many novel applications in industry. Therefore, it is very important to deeply understand the stability and phase transformation behavior under extreme physical conditions. Duclous et al. [1] reported that the C60 molecules are extremely stable at room temperature, withstanding hydrostatic pressure of up to about 20 GPa. It is transformed irreversibly into a new hard carbon phase above hydrostatic pressure of 27 GPa [2,3]. Under non-hydrostatic high pressures (20 ± 5 GPa), the C60 is unstable to collapse into a diamond phase at room temperature [4]. At high temperatures above 1500 °C, C60 crystals are transformed into diamond in a pressure range of 9–15 GPa [5]. Nanocrystalline cubic diamond with crystallite sizes of 5–12 nm could be synthesized from fullerene C60 at 20 GPa and 2000 °C using a multi-anvil apparatus [6]. Microcrystalline diamonds up to 6 μm were produced from fullerenes C60 to C150 using a shock-wave synthesis under pressures ranged 24–40 GPa [7]. In general, it needs solely super-high pressure or high pressure (in several GPa) and high temperature for the phase transition of C60 to diamond.

The spark plasma sintering (SPS) is a field assisted sintering technique utilizing ON–OFF DC pulses to generate a pulsed electric field, which provides an extreme physical condition. The

SPS has very broad applications for the preparation of conventional and new materials. However, it is a relatively new technique for the synthesis of diamonds. Our researches have shown that carbon nanotubes are unstable and can be converted into diamond without [8–10] or with metallic catalysts [11] under the pulsed electric field of the SPS. Our recent work has shown that C60 can be converted into diamond under the same SPS conditions as carbon nanotubes are converted to diamond (1500 °C, 80 MPa) [12]. Since the C60 has a higher sp³ hybridization fraction than that of carbon nanotubes, it makes the transformation of C60 into diamond easier. Therefore, it is postulated that the C60 may be able to increase the diamond size and transition rate in the SPS diamond synthetic method. In this study, the diamond growth from C60 was studied under the pulsed electric field of the SPS system to increase the size and transition rate of diamond. The spark plasma sintered carbon samples were analyzed using micro-Raman spectroscopy, Synchrotron X-ray, scanning electron microscopy (SEM) and transmission electron microscopy (TEM) techniques. Its phase transformation mechanism is also discussed.

2. Materials and methods

The fullerene C60 was purchased from SES research, Houston, USA. The purity of the pristine C60 was claimed by the producer to be about 99.5%. The pure C60 powders were pressed into a graphite die for SPS treatment to form disc-shaped samples. The SPS experiments were conducted using a Model of HP-D5 FCT

* Corresponding author. Tel.: +49 381 4986864; fax: +49 381 4986862.
E-mail address: faming.zhang@uni-rostock.de (F. Zhang).

spark plasma sintering system (FCT systeme GmbH, Rauenstein, Germany) installed at the Tycho Sinter Lab in the University of Rostock, under an axial pressure of 50–80 MPa at temperatures of 1100–1500 °C in vacuum (< 6 Pa). A heating rate of 100 K/min was used, and the sintering process lasted typically 20 min. The applied direct current for SPS was about 1000 A with a pulse duration of 12 ms and an interval of 2 ms leading to disc-shaped samples with a diameter of 20 mm and a thickness of 5 mm.

The sintered samples were etched in a solution of concentrated H_2SO_4 (90 vol%) and HNO_3 (10 vol%) at room temperature for 12 h. The etched samples were washed using de-ionized water repeatedly, and dried in an oven. The identification was performed with a Renishaw-2000 Laser Raman spectroscopy system with a He–Ne laser excited at 514 nm with a power density of 4.7 mW and a spot diameter of about 5 μm . Further identification was performed with a high-energy X-ray diffraction at beamline BW5 (DESY/HASYLAB Hamburger Synchrotron Laboratory) with a wavelength of 0.123984 Å (100.0 keV). Scanning electron microscope (SEM, Zeiss Supra 25, Germany) and transmission electron microscope (TEM, Zeiss-Libra120, Germany) operating at 120 keV, were employed to characterize the starting materials and the products following the SPS treatment.

3. Results and discussion

Fig. 1(a) shows the TEM micrograph of the fullerene C60 powder with particle sizes from 40 to 100 nm. There are some agglomerates in the particles. The inserted selected area diffraction pattern on a specific C60 particle indicates that the C60 is a single crystal along the $[\bar{1}10]$ direction. Fig. 1(b) shows the SEM micrograph of the C60 powder. The particle agglomerates are from nanometer to 4 μm .

Fig. 2(a) shows the Raman spectra of the raw C60 and the spark plasma sintered (SPSed) C60 samples after etching. The raw C60 shows a sharp peak that appeared at 1460 cm^{-1} and two weak broad peaks centered at 1568 and 1413 cm^{-1} . Previous study [12] demonstrated that SPS processing of C60 with a pressure of 80 MPa and a temperature of 1500 °C is leading to the formation of diamond. Hereby, the SPS pressure was reduced to 50 MPa. As expected, the cubic diamond peaks can also be detected at 1333 cm^{-1} in the Raman spectra taken for the samples SPS processed in the temperature range from 1150 to 1500 °C. However, the diamond band of the samples sintered at 1150 °C is very broad having the lowest height. Its graphite band at 1568 cm^{-1} is at the same value as that of the raw C60. It

indicates that there is only a small fraction of diamond in this 1150 °C SPSed sample. With an increase in temperature to 1200, 1300 and 1500 °C, the diamond band at 1333 cm^{-1} gets sharper and sharper, as well as the graphite band is shifted to a higher value of 1576 cm^{-1} . The result of the 1300 °C SPSed C60 shows a Raman spectrum similar to the 1500 °C SPSed sample. The main

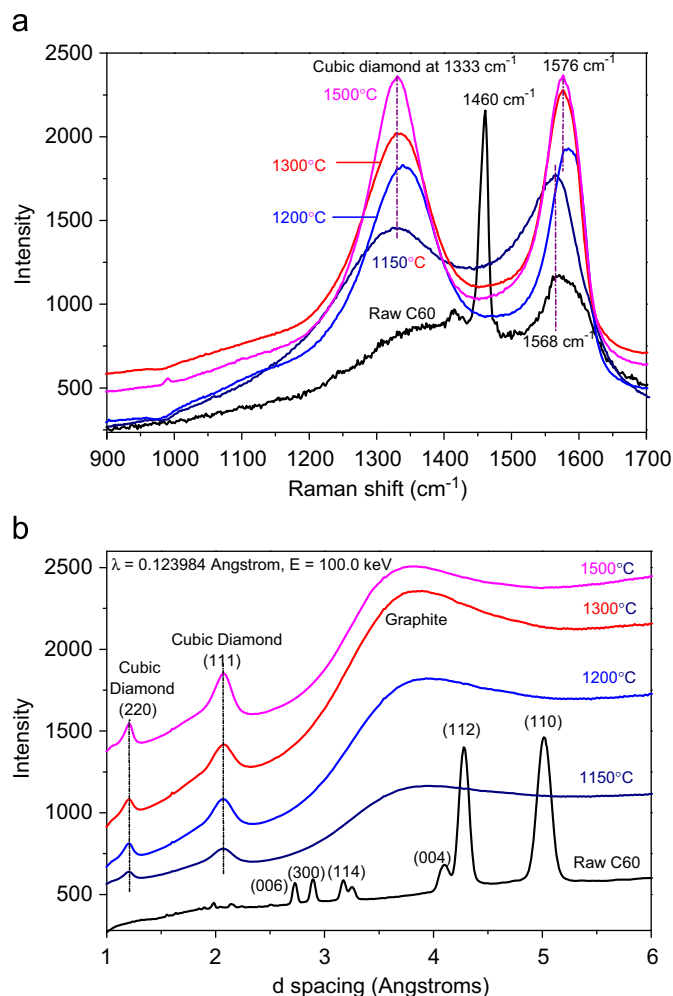


Fig. 2. Raman spectra (a) and synchrotron radiation-high energy X-ray diffraction patterns (b) of the raw C60 and the spark plasma sintered C60 at different temperatures under a pressure of 50 MPa.

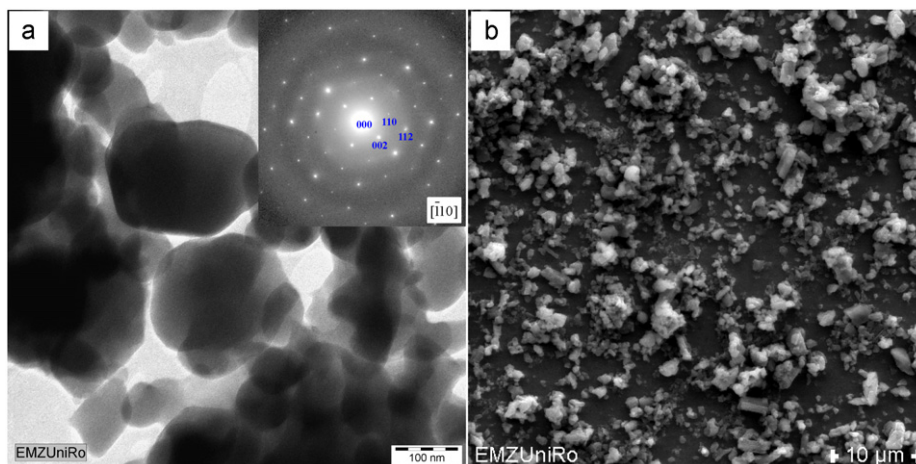


Fig. 1. TEM micrograph with inserted selected area diffraction pattern (a) and SEM micrograph of the raw fullerene C60 powder (b).

peak in the pure C60 spectrum at 1460 cm^{-1} disappears in all the spectra of the samples processed in the temperature range $1150\text{--}1500\text{ }^{\circ}\text{C}$. This indicates that the C60 is completely transformed into diamond and graphite phases after SPS at above temperatures of $1150\text{ }^{\circ}\text{C}$. Fig. 2(b) shows the synchrotron radiation-high energy X-ray diffraction patterns of the raw C60 and the SPSed C60 samples after etching. In the $1150\text{ }^{\circ}\text{C}$ sintered C60 sample, very weak diamond peaks at d spacing of 2.06 and 1.26 \AA are found. The C60 after SPS at temperatures above $1200\text{ }^{\circ}\text{C}$ show more shaped cubic diamond diffraction peaks at d spacing of 2.06 and 1.26 \AA and broad graphite peaks. The synchrotron radiation is generated by the acceleration of ultrarelativistic charged particles and it can penetrate all the SPSed C60 pellets. The peaks of graphite are very broad indicating its amorphous structure. Amorphous graphite is the least graphitic of the graphite types where none of the common crystal faces are visible. The C60 diffraction peaks disappeared indicating the C60 has completely transformed into diamond and amorphous graphite phases after the SPS processing at temperatures from 1150 to $1500\text{ }^{\circ}\text{C}$. The Raman and Synchrotron X-ray results confirmed the diamond formation in the C60 samples. However, the FWHMs of the diamond peaks in the Raman spectra and Synchrotron X-ray diffraction patterns are all broad. Such broad peaks are known to be a sign of fine diamond crystallites or highly defective nature of the crystals. It is calculated from the peak-area ratio in the Raman results that the fractions of the sp^3 hybridized carbon in the final products are about $50\text{ vol}\%$ in the samples of $1200\text{--}1500\text{ }^{\circ}\text{C}$. As calculated from the peak-area ratio in the Synchrotron X-ray results, the fractions of the diamond in the

final products are about $30\text{ vol}\%$ in the samples processed at 1300 and $1500\text{ }^{\circ}\text{C}$. Combining both of them, the transition rate of diamond from C60 is at least $30\text{ vol}\%$ in the SPSed samples at 1300 and $1500\text{ }^{\circ}\text{C}$.

Fig. 3 shows the SEM micrographs of the SPSed C60 samples after etching. In the $1150\text{ }^{\circ}\text{C}$ SPSed sample, it noticed few small diamond particles, as marked by circles (Fig. 3a). Some diamond crystals with hexagonal, tetragonal or triangular shapes are found in Fig. 3(b) of the $1200\text{ }^{\circ}\text{C}$ SPSed sample. The particle sizes of the diamond crystals are from tens of micrometers up to $200\text{ }\mu\text{m}$, as marked by circles. The diamond crystals with perfect hexahedron shapes are clearly observed in the $1300\text{ }^{\circ}\text{C}$ sintered sample (Fig. 3c). The diamond sizes range from 100 to $250\text{ }\mu\text{m}$, and they are larger than those of the sample sintered at $1200\text{ }^{\circ}\text{C}$. Some fine diamond crystals are noticeable on one big diamond crystal. The micrographs of the $1500\text{ }^{\circ}\text{C}$ sintered C60 sample show that the big diamond crystals are almost melted (Fig. 3d). There are many fine diamond crystals below $4\text{ }\mu\text{m}$ on the big crystals (Fig. 3e). It is obvious that the diamond crystal sizes do not increase with the increase in temperature. A processing temperature of $1300\text{ }^{\circ}\text{C}$ is the best for the phase transformation of C60 directly to diamond, according to this study. The particle size of the diamond crystals made from C60 is up to $250\text{ }\mu\text{m}$. It is a very large size for such conversion without any catalyst being involved in the process.

The TEM micrograph of the $1200\text{ }^{\circ}\text{C}$ spark plasma sintered C60 sample is shown in Fig. 4. Fig. 4(a) shows a big diamond crystal with some pure C60 particles. The particle size of the C60 in this SPSed sample lies in the range of $40\text{--}100\text{ nm}$. It is identical to that of the pure C60 (Fig. 1a). The C60 particles are present with

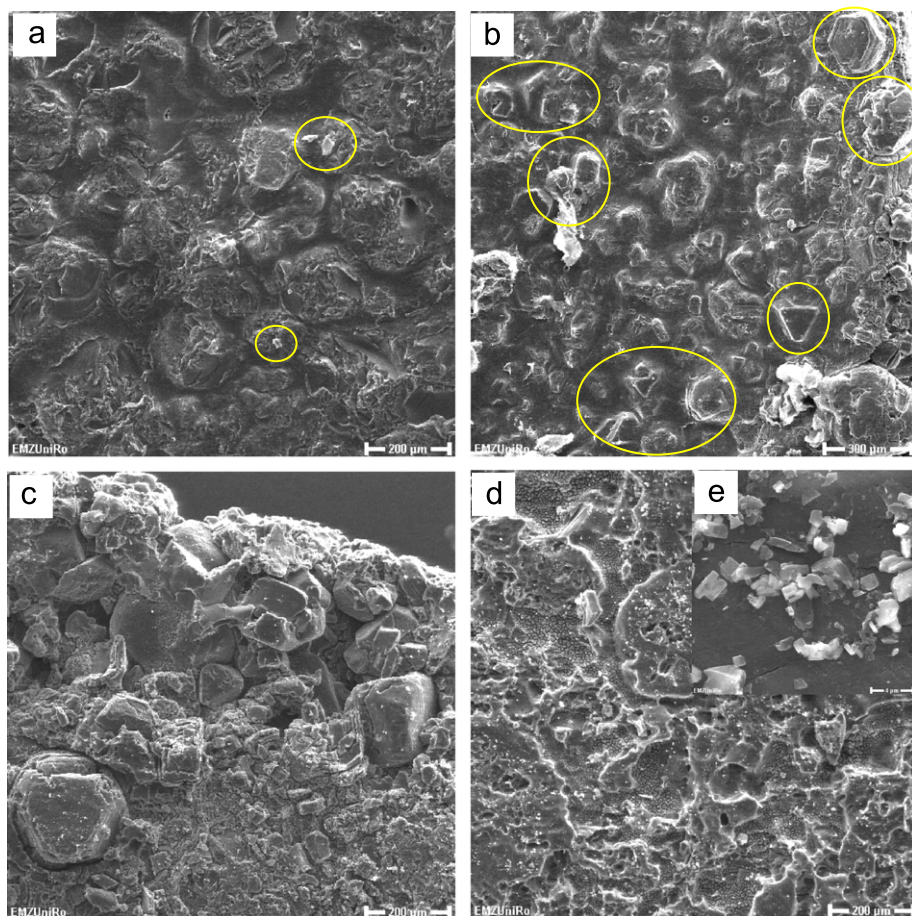


Fig. 3. SEM micrographs of spark plasma sintered C60 samples at $1150\text{ }^{\circ}\text{C}$ (a), $1200\text{ }^{\circ}\text{C}$ (b), $1300\text{ }^{\circ}\text{C}$ (c) and $1500\text{ }^{\circ}\text{C}$ (d, e) after etching, showing the growth of diamond crystals.

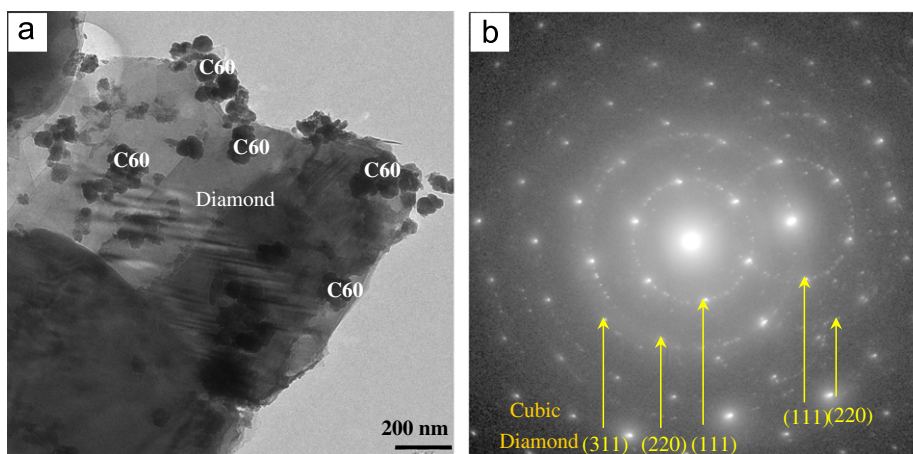


Fig. 4. TEM micrograph of a diamond crystal formed in the 1200 °C spark plasma sintered C60 sample (a) with the selected area diffraction pattern (b), exhibiting the polycrystalline diamonds.

the diamond crystal together. This indicates that the diamond is directly transformed from these C60 particles. The selected area diffraction pattern was diffraction rings were calculated and this confirmed that the diamonds are cubic polycrystals (Fig. 4b). It is noted that there are two sets of diffraction patterns indicating the presence of two cubic polycrystals in the selected area (Fig. 4b). No formation of an intermediate phase was observed for the C60 transformation into diamond in the TEM micrograph. The transformation from C60 to diamond seems to be a direct carbon transformation process with structural reconstruction without the production of any intermediate phase.

The Raman, Synchrotron X-ray, SEM and TEM identifications have confirmed the diamond formation in the C60 by the SPS at milder conditions. The diamond particle size and transition rate both increased using the C60 as carbon source for diamond synthesis. The experimental results validated the hypothesis in the introduction. Due to the high price of the C60, conversion of C60 to diamond by SPS has more theoretical impact than its practical applications for the growth of diamond. For its practical use, this study suggests that the C60 may be able to be used as a doping catalyst to promote the diamond transitions. Vul et al. [13] have studied the effects of fullerene on the high-pressure high temperature synthesis of diamond from graphite and found that the fullerenes increased the percentage of graphite to diamond conversion by a factor of 1.8 and allowed the pressure and temperature of the synthesis to be decreased. Therefore, the application of C60 as one type of catalyst or doping catalyst for diamond synthesis in the SPS or other techniques has some practical prospects. The theoretical impact of the conversion of C60 into diamond by the SPS at such milder condition is very constructive. The carbon atoms in C60 are sp^2 hybridized with a high fraction of sp^3 hybridized structure due to an angular strain. It is a bit difficult to transform the planar sp^2 structure to the diamond sp^3 network. Our previous results confirmed that the graphite with pure sp^2 structure cannot be converted to diamond in the SPS [12]. The C60 can be considered as a folded graphite sheet with the predominant sp^3 hybridization in the pentagons. This makes the transformation of C60 into diamond easier. A dense assembly of C60 spheroids, where 48 out of 60 carbon atoms have quasi-tetrahedral coordination, is sterically fairly close to that of the diamond [1,4]. It implies that a small rearrangement of the atoms of C60 can result in the change of its structure. However, it still needs solely superhigh pressure or high pressure and high temperatures for the phase transition from C60 to diamond [1–6]. In the pulsed electric field of the SPS, the DC currents were passed through the graphite die and the C60

sample. The pulsed electric field in the SPS utilizes high currents up to thousands of ampere and low voltages up to 10 V eventually generating spark plasmas provides most of the energy for the diamond formation under such low temperatures and low pressure. Our previous research has proved the presence of plasmas during SPS of these conductive and high surface area nanocarbon materials [12]. Finally, the C60 gets unstable under such pulsed electric field and can be transformed into diamond at temperatures as low as 1150 °C. In other words, the mechanism for the conversion of C60 to diamond owns to the special structure of the C60 and the unique SPS technique.

4. Conclusions

Fullerene C60 is unstable and can be transformed into crystalline diamond by spark plasma sintering under a pressure of 50 MPa above temperatures of 1150 °C without any catalysts being involved. Well-defined diamonds with particle sizes up to 250 μm and transition rate about 30 vol% are obtained at 1300 °C and no further growth in particle size is seen beyond this temperature. The mechanism analysis indicates that the high sp^3 hybrid fraction in the C60 and the generated plasmas in the pulsed electric field lead to its transformation to diamond. It is a direct transition process from C60 to diamond with a structural reconstruction of carbon atoms without intermediate phases being involved.

Acknowledgment

Financial support from the DFG-Deutschen Forschungsgemeinschaft (German Research Foundation) with Grant no. BU 547/10-1 and DESY Hasyllab Project with Grant No. II-20090264 are acknowledged.

References

- [1] S.J. Duclos, K. Brister, R.C. Haddon, A.R. Kortan, F.A. Thiel, *Nature* 45 (1991) 380–382.
- [2] F. Mosshary, N.H. Chen, L.F. Silvera, C.A. Brown, H.C. Dorn, M.S. de Veies, D.S. Bethune, *Physical Review Letters* 69 (1992) 466–469.
- [3] V. Brazhkin, A. Lyapin, *New Diamond and Frontier Carbon Technology* 14 (5) (2004) 259–278.
- [4] M.N. Regueiro, P. Monceau, J.L. Hodeau, *Nature* 355 (1992) 237–239.
- [5] V.D. Blank, S.G. Buga, N.R. Serebryanaya, G.A. Dubitsky, S.N. Sulyanov, M.Y. Popov, V.N. Denisov, A.N. Ivlev, B. Mavrin, *Physics Letters A* 220 (1996) 149–157.

- [6] N. Dubrovinskaia, L. Dubrovinsky, F. Langenhorst, S. Jacobsen, C. Liebske, *Diamond and Related Materials* 14 (2005) 16–22.
- [7] O.G. Epanchintsev, A.S. Zubchenko, A.E. Korneyev, V.A. Simonov, *Journal of Physics and Chemistry of Solids* 158 (11) (1997) 1785–1788.
- [8] F. Zhang, J. Shen, J. Sun, D.G. McCartney, *Carbon* 43 (6) (2005) 1254–1258.
- [9] J. Shen, F.M. Zhang, J.F. Sun, Y.Q. Zhu, G. McCartney, *Nanotechnology* 17 (2006) 2187–2191.
- [10] F. Zhang, J. Shen, J. Sun, D.G. McCartney, *Carbon* 44 (2006) 3136–3138.
- [11] F. Zhang, M. Adam, E. Otterstein, E. Burkel, *Diamond and Related Materials* 20 (2011) 853–858.
- [12] F. Zhang, C. Mihoc, F. Ahmed, C. Latte, E. Burkel, *Chemical Physics Letters* 510 (2011) 109–114.
- [13] A.Ya. Vul, V.M. Davidenko, S.V. Kidalov, S.S. Ordan'yan, V.A. Yashin, *Technical Physics Letters* 27 (2001) 384–386.

Preparation, microstructures, mechanical properties, and cytocompatibility of TiMn alloys for biomedical applications

Faming Zhang,¹ Arne Weidmann,² J. Barbara Nebe,² Ulrich Beck,³ Eberhard Burkel¹

¹Institute of Physics, Department of Mathematics and Natural Sciences, University of Rostock, 18055 Rostock, Germany

²Center for Biomedical Research, Cell Biology, Department of Medicine, University of Rostock, 18057 Rostock, Germany

³Department of Electrical Engineering and Informatics, University of Rostock, 18059 Rostock, Germany

Received 26 June 2009; revised 11 February 2010; accepted 19 April 2010

Published online 22 June 2010 in Wiley InterScience (www.interscience.wiley.com). DOI: 10.1002/jbm.b.31668

Abstract: The titanium-manganese (TiMn) alloys have been extensively used in aerospace and hydrogen storage. In this study, the TiMn alloys with various manganese contents ranging from 2 to 12 wt % were prepared by using mechanical alloying and spark plasma sintering (SPS) techniques. The microstructures, mechanical properties including hardness, elastic modulus and ductility, cytotoxicity and cell proliferation properties of the TiMn alloys were investigated to explore their biomedical applications. The addition of manganese to the titanium reduced the α to β transformation temperature and was confirmed as a β stabilizer element. The manganese increased the relative density of the alloy and thus high density TiMn alloys with $\alpha+\beta$ structure were prepared by using SPS at 700°C. The hardness increased significantly ranging from 2.4 GPa (Ti2Mn) to 5.28 GPa (Ti12Mn)

and the elastic modulus ranging from 83.3 GPa (Ti2Mn) to 122 GPa (Ti12Mn), the ductility decreased ranging from 21.3% (Ti2Mn) to 11.7% (Ti12Mn) with increasing manganese content in the Ti. Concentrations of Mn below 8 wt % in titanium reveal negligible effects on the metabolic activity and the cell proliferation of human osteoblasts. The Mn could be used in lower concentrations as an alloying element for biomedical titanium. The Ti2Mn, Ti5Mn, and Ti8Mn alloys with superior mechanical properties and acceptable cytocompatibility have a potential for use as bone substitutes and dental implants. © 2010 Wiley Periodicals, Inc. *J Biomed Mater Res Part B: Appl Biomater* 94B: 406–413, 2010.

Key Words: titanium alloys, spark plasma sintering, mechanical properties, cytocompatibility, biomedical applications

INTRODUCTION

Titanium (Ti) and its alloys are widely used as biomaterials especially for orthopedic implants in load bearing sites as dental and orthopedic implants and heart valves, because of their high mechanical properties, corrosion resistance, and biocompatibility.¹ Pure Ti was once used as biomaterial, but the disadvantage for the use of pure Ti as implant materials is its low strength and insufficient hardness.² Therefore, the Ti6Al4V alloy is preferentially in clinical use because of its favorable mechanical properties. However, some studies showed that the vanadium (V) and aluminum (Al) release in the Ti6Al4V alloy could induce Alzheimer's disease, allergic reaction, and neurological disorders.³ Therefore, the exploration of high strength new Ti alloys without Al and V for medical implants has gained great attentions in the past years and is still ongoing.

Vanadium and aluminum free alloys containing nontoxic elements such as iron (Fe),⁴ niobium (Nb),⁵ zirconium (Zr),⁶ tantalum (Ta),⁷ molybdenum (Mo),⁸ nickel (Ni),⁹ gold (Au),¹⁰ silicon (Si),¹¹ and so forth were investigated. We try to explore some new element for the biomedical Ti alloy. Manganese (Mn) is one of the essential trace elements in

human body. The Mn is beneficial to the normal skeletal growth and development¹² and is important for enzymes in the body like the superoxide dismutase therefore involved in the elimination of radicals.¹³ Thus the Mn element should have less toxicity than the Al and V. The Mn was doped in magnesium alloy to improve its corrosion resistance and mechanical properties for biomedical applications.¹⁴ The Mn was incorporated to tricalcium phosphate bioceramics, which resulted in a sufficient cell compatibility.¹⁵ The preliminary results in our group showed that the Mn incorporation into the Ti alloys could enhance the cell adhesion properties.¹⁶

The Ti8Mn alloys have been used in aerospace field and the TiMn₂ Laves phase has been used already for hydrogen storage.^{17,18} Nevertheless, few studies were on the exploration of TiMn alloys for biomedical applications. The TiMn alloys were generally fabricated by traditional casting or powder metallurgy techniques. Because of high melting point, high reactive activity at high temperature, and contamination susceptibility, the Ti alloys are difficult to be produced from the liquid state. The production of Ti alloys via a powder metallurgy (PM) route is attractive because of

Correspondence to: F. Zhang; e-mail: faming.zhang@uni-rostock.de
Contract grant sponsor: DFG (Welisa); contract grant number: GRK1505/1

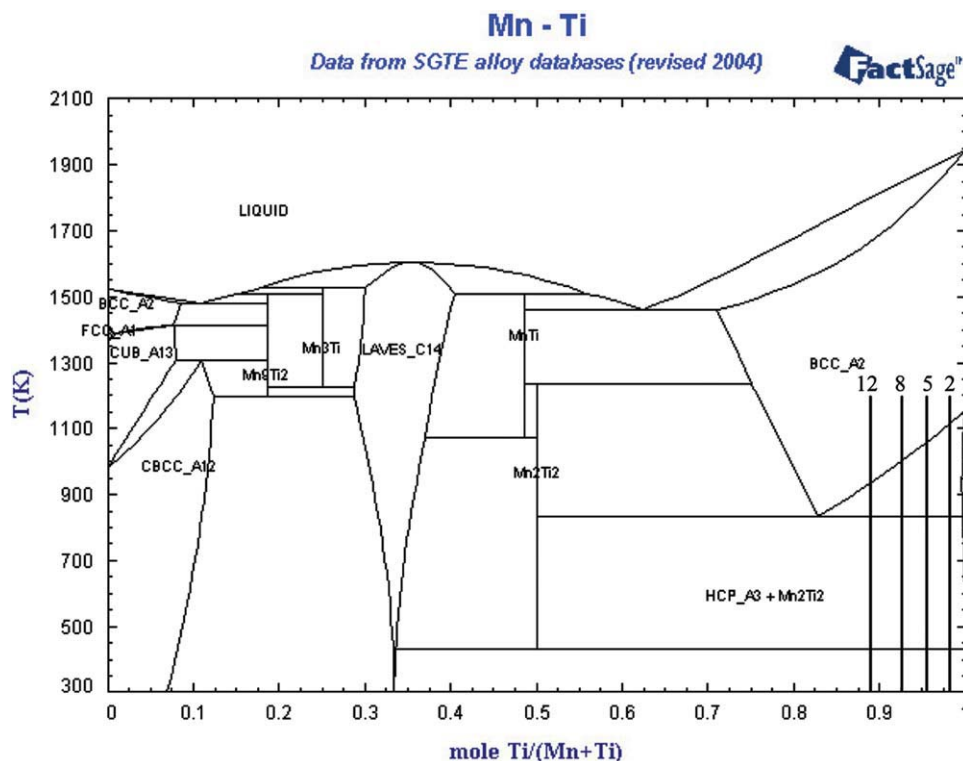


FIGURE 1. Binary phase diagram of TiMn alloy showing the phases of the Ti-2, 5, 8, 12 wt % Mn alloys. [Color figure can be viewed in the online issue, which is available at www.interscience.wiley.com.]

the ability to produce net-shape components. Because of their stable surface oxide film (TiO_2), the Ti alloys are difficult to be sintered by traditional PM sintering techniques.¹⁹ Thus, the spark plasma sintering (SPS)—a pulsed electric current field assisted sintering technique—has been used to prepare the Ti alloys. In our previous study, Ti8Mn and Ti12Mn alloys were prepared by mechanical alloying (MA) and SPS techniques and preliminarily investigated.²⁰ In this study, the Mn element was incorporated into the Ti, and TiMn alloys with 2, 5, 8, 12 wt % Mn amounts were prepared by MA and SPS techniques. The preparation process, microstructures, mechanical properties, cytotoxicity, and cell proliferation properties of the TiMn alloys were investigated for exploration of their biomedical applications. Pure Ti, Mn metals, and Ti6Al4V alloys were also fabricated at the same conditions for a comparison.

MATERIALS AND METHODS

The raw Ti and Mn powders were prepared by gas atomization method with 99.0% purities (Fluka, Germany). TiMn alloys were designed by varying the amount of Mn in the Ti with 2, 5, 8, and 12 (wt %) compositions on the base of the binary phase diagram of TiMn alloys in Figure 1 showing the phases of the Ti-2, 5, 8, 12 wt % Mn alloys. With Mn below 12 wt %, the phase composition of the TiMn alloy is Ti_2Mn_2 phase. After weighting, each component of the designed composition was mechanical alloyed with a high energy planetary ball milling machine (Retsch PM400, Germany). Chromium hardened steel vials and balls were

used as grinding media, with ball to powder ratio of 15:1. Wet-milling in hexane was performed for different hours at 250 rpm. Hexane was used as process control agent to prevent oxidation and excessive contamination from the grinding media.

The sintering was accomplished using a Model HPD-25/1 FCT SPS system (FCT systeme GmbH, Rauenstein, Germany) at a temperature of 500–800°C for various times. The powders were loaded into graphite die to sinter disk-

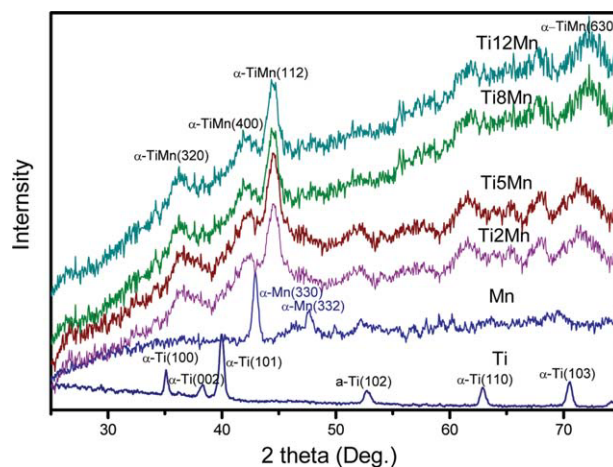


FIGURE 2. XRD patterns of the Ti, Mn powders, and TiMn alloy powders prepared by MA showing the formation of α -TiMn phases. [Color figure can be viewed in the online issue, which is available at www.interscience.wiley.com.]

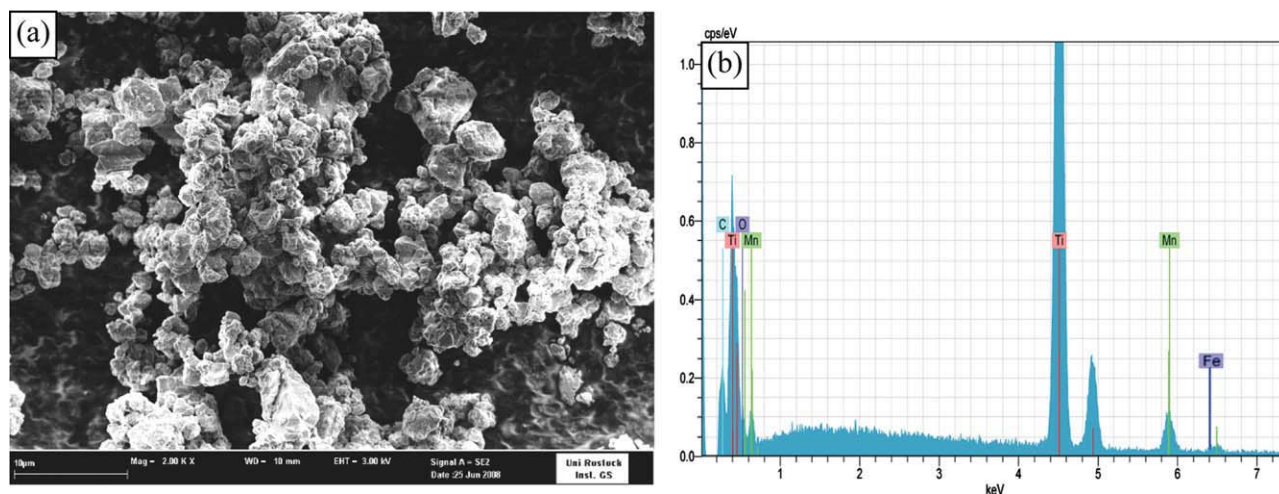


FIGURE 3. SEM micrograph (a) and EDX (b) of the Ti8Mn powder prepared by MA showing the morphology and composition of the powder. [Color figure can be viewed in the online issue, which is available at www.interscience.wiley.com.]

shaped pellets (20 mm diameter, thickness 5–6 mm). The SPS experiments were conducted in vacuum (<6 Pa) under uniaxial pressure 50 MPa. The heating rate was maintained at 100°C/min.

X-ray diffraction (XRD, Bruker D8, Germany) was used to characterize the phase composition of the powders and sintered alloys. The phase transformation of the alloys was performed with a differential scanning calorimetry (DSC, Netzsch Pegasus 404C, Germany). Scanning electron microscopy (SEM, Zeiss Supra 25, Germany) was employed to analyze the microstructures of the powders and sintered alloys. The densities of the sintered alloys were determined by the Archimedes method using water immersion. Hardness and elastic modulus were measured by Universal CETR Nano+Micro tester with a model UNMT-1 multispecimen test system. The measurements were measured with microhead at various forces up to 5N. 15 indents were done on one sample for an average value. The ductility of the TiMn alloys under compressive load was performed on an Instron 5566 testing machine at room temperature with a compression speed of 0.5 mm/min.

Before cell cultivation TiMn alloys were sterilized in 70% ethanol for 15 min. The human osteoblastic cells MG-63 (osteosarcoma cell line, ATCC, LGC Promochem) were cultivated on TiMn alloys in 12-well plates (Greiner Bio-One, Germany) in Dulbecco's modified Eagle medium (DMEM, Invitrogen, USA) with 10% fetal calf serum (FCS, PAA, Austria), 4500 mg/L glucose (high glucose), GlutaMAX, pyruvate, 1% gentamicin (Ratiopharm, Germany), 0.02% plasmocin (Invivogen, USA) at 37°C and in a 5% CO₂ atmosphere. The tissue culture polystyrene (TCPS) was used as an additional control.

The inhibitory influence of the TiMn alloys was studied by measuring osteoblast MG-63 cell's metabolism. The CellTiter 96® Aqueous One Solution Cell Proliferation Assay (Promega) was used. The principle of the test is an enzymatic cleavage of the methyltetrazolium salt (3-(4,5-dimethylthiazol-2-yl)-5-(3-carboxy-methoxyphenyl)) (MTS) by active cells into violet Formosan product. The amount of Formosan product is directly proportional to the number of living cells. 100 μL of the MTS so-

lution were added to each well and incubated for 2 h at 37°C and in a 5% CO₂ atmosphere. The spectrophotometric absorption was analyzed in a 96-well plate by an ELISA reader (Anthos 2010, Anthos Labtec Instruments) at 490 nm.

For flow cytometry, cells were suspended using 0.05% trypsin/0.02% EDTA solution (5 min at 37°C). Then, cells were washed in phosphate buffered saline (PBS), fixed with 70% ethanol over night at -20°C, and intensively washed again. After treatment with 1% RNase (Sigma, Germany) for 20 min at 37°C, the DNA of the cells was labeled with propidium iodide (50 μg/mL, Sigma, Germany) over night at 4°C. Cells were measured in a FACSCalibur™ flow cytometer (BD Biosciences) equipped with a 488 nm argon-ion laser and a Macintosh Power PC (G4). In general, 25,000 events were acquired using CellQuest Pro 4.0.1. Percentage of proliferating cells was then calculated in percent using ModFIT version 3.0 (BD Biosciences).

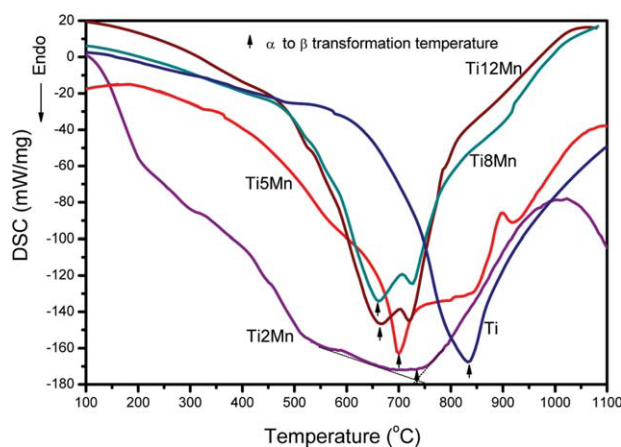


FIGURE 4. Phase transformation behaviors of the TiMn alloys measured by DSC showing the decrease of α to β transformation temperature with increase of Mn amounts in Ti. [Color figure can be viewed in the online issue, which is available at www.interscience.wiley.com.]

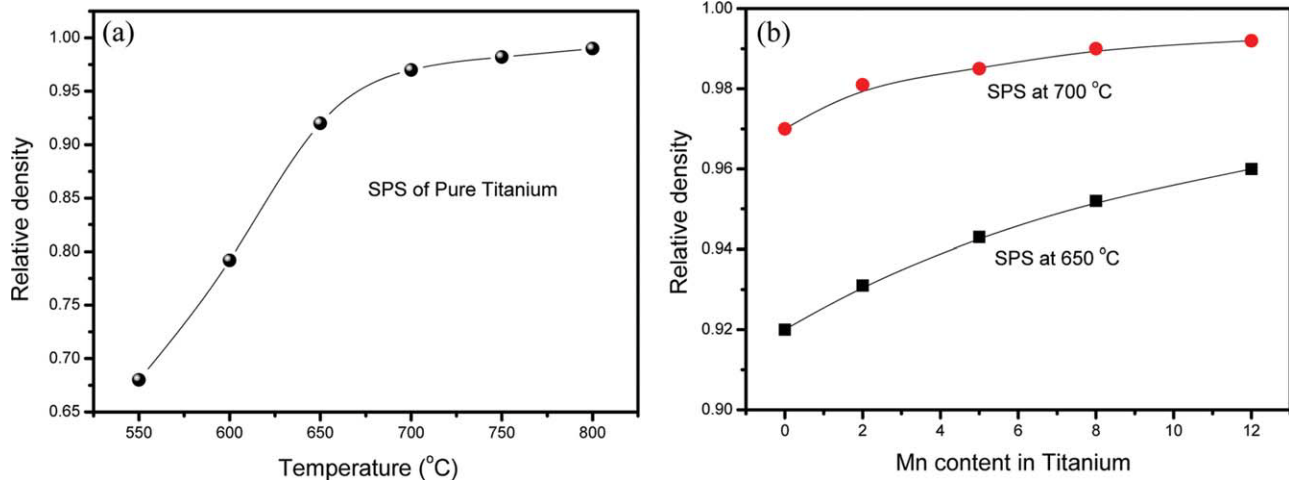


FIGURE 5. Relative density of spark plasma sintered Ti at different temperatures (a) and TiMn alloys with various Mn amounts (b) showing the variation of Ti relative density with the SPS temperature and the enhancement of relative density with increase of Mn amounts in Ti. [Color figure can be viewed in the online issue, which is available at www.interscience.wiley.com.]

Statistical analysis was performed with SPSS 14.0 for Windows (SPSS Inc., Chicago, IL). The differences between the concentrations were evaluated using Students t-test for independent samples because variables present normal distribution (Kolmogorov-Smirnov test). Data were expressed as mean and standard error of the mean. A probability value of $p < 0.05$ was considered as significant.

RESULTS

The TiMn alloy powders with 2, 5, 8, and 12 wt % Mn compositions were mixed and mechanical alloyed for various hours in a high energy ball milling machine. Figure 2 shows the XRD patterns of the pure Ti, Mn powders, and TiMn alloy powders after 60 h MA. Pure Ti and Mn peaks completely disappeared and TiMn phases were formed after 60 h MA. The pure Ti powders are α -Ti phase (PDF# 65-3362) with hexagonal structure and the pure Mn powders are α -Mn phase (PDF# 32-0637) with cubic structure. The synthetic TiMn powders are α -TiMn phase (PDF# 07-0132) with tetragonal structure. There are no obvious changes in the phase compositions with increasing of Mn amount up to 12 wt % in Ti, which corresponds to the binary phase diagram of the TiMn alloy (Figure 1).

Figure 3 shows the SEM micrograph and EDX of the Ti8Mn powders prepared by MA. The powders are agglomerates with mean particle sizes of 4–5 μm in diameter with a narrow size distribution [Figure 3(a)]. The EDX spectra shows that the Ti, Mn peaks belong to the TiMn powder, the C, and the O peaks are from adsorption of air, and the small Fe peak is the contamination from the steel balls and vials during the MA.

The phase transformation behaviors of the TiMn alloy powders were analyzed by using differential scanning calorimetry. Figure 4 shows the transformation temperatures of the TiMn alloys in comparison with the pure Ti. In the case of pure Ti, the transformation temperature from α to β phase occurs at about 840°C. The transformation tempera-

ture in Ti2Mn is 735°C, whereas that of in Ti5Mn alloys is 700°C. The transformation temperatures are 665°C and 660°C in Ti8Mn and Ti12Mn alloys, respectively. As the amount of Mn increased, the transformation temperature decreased to a relative lower temperature. The addition of Mn in Ti has depressed their transformation temperature from α to β phase.

After characterization, the alloy powders were subjected to the SPS furnace. Figure 5 shows the relative density of spark plasma sintered Ti at different temperatures and TiMn alloys with various Mn amounts. With temperature increase from 550–800°C, the relative density of the Ti metal increased from 68% to 99% [Figure 5(a)]. The relative density of TiMn alloys increased as the Mn contents increased at 650 and 700°C, respectively [Figure 5(b)]. The Ti8Mn alloys showed 99% relative density at 700°C for 5 min. The SPS decreased the sintering temperature of Ti and

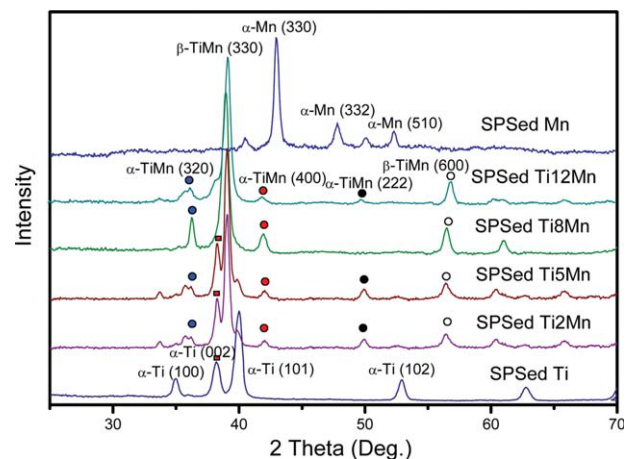


FIGURE 6. XRD patterns of the spark plasma sintered Ti, Mn, and TiMn alloys showing the α + β phase alloy. [Color figure can be viewed in the online issue, which is available at www.interscience.wiley.com.]

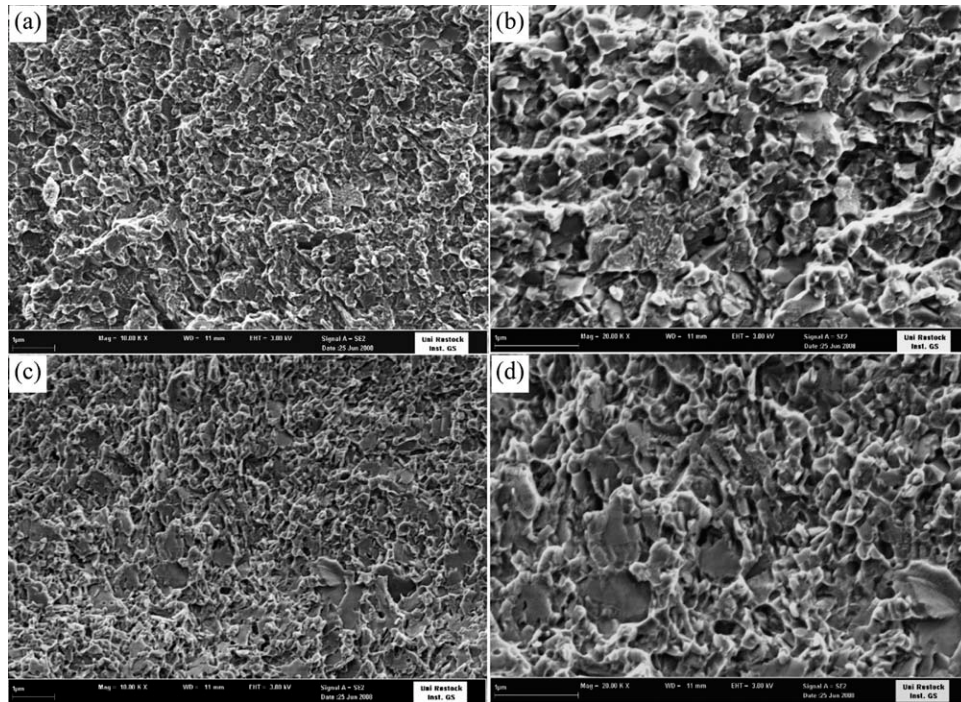


FIGURE 7. SEM micrographs of the fracture surfaces of Ti8Mn (a, b) and Ti12Mn (c, d) alloys prepared by SPS showing the superfine microstructures (Bar 1 μm , magnification 10 kx, 20 kx).

TiMn alloys. The Mn addition increased the relative density of Ti metal during SPS.

Figure 6 shows XRD patterns of the spark plasma sintered Ti, Mn metals, and TiMn alloys. The Ti and Mn still retain α -Ti and α -Mn phases because of the lower sintering temperature in SPS (700°C). However, all the TiMn alloys are mostly β -TiMn phase (PDF# 11-0514) with cubic structure. There is still a small amount of α -TiMn phase in the alloy; therefore, the TiMn alloy is a $\alpha+\beta$ phase alloy. The synthesized alloy has $\alpha+\beta$ microstructures, which is similar to that of Ti6Al4V alloy. In Figure 7 the SEM micrographs of the fracture surfaces of the spark plasma sintered Ti8Mn and Ti12Mn alloys are demonstrated. There are few micropores on the fracture surface of the TiMn alloys. The grain size of the Ti8Mn alloys is about 500 nm in ultrafine microstructure and the fracture mode of the alloy is primary intergranular cracking [Figure 7(a)]. There are some large size grains in the Ti12Mn alloy, which may be because of the sintering of powder agglomerates [Figure 7(b)].

Figure 8 shows the mechanical properties of the TiMn alloys. The 3D image indicates the depth and dimension of the indent by the microindentation technique [Figure 8(a)]. The depth of the indent is 20 μm around; the dimension is about 110 μm in width and length. The hardness results show that the hardness value tended to rise with increasing Mn contents [Figure 8(b)]. The hardness values of all TiMn alloys are significantly higher than that of pure Ti. The pure Ti shows a hardness of 1.60 GPa; Ti2Mn, 2.40 Ti5Mn, 3.65; Ti8Mn, 4.98; Ti12Mn, 5.28 GPa. The hardness of Ti12Mn alloy is comparable with that of the pure Mn (5.44 GPa). From statistical analysis, the hardness values of the TiMn

alloys are significantly higher than that of pure Ti. The elastic modulus results show that, it is also increased as shown in Figure 8(c). The pure Ti is 69.2 GPa, Ti2Mn 83.3 GPa, Ti5Mn 95.0 GPa, Ti8Mn 106 GPa, and Ti12Mn 122 GPa, Mn 68.72 GPa. The increment magnitude of the elastic modulus is lower than that of the hardness. The ductility results of the TiMn alloys are shown in Figure 8(d). The pure Ti exhibits 25.0% ductility, Ti2Mn 21.3%, Ti5Mn 18.2%, Ti8Mn 15.0%, and Ti12Mn 11.7%. The ductility decreased with increase of Mn amounts in Ti. The mechanical properties of the Ti6Al4V alloy were also measured with the same methods. It shows hardness: 4.3 GPa, elastic modulus: 122 GPa, and ductility: 14.0%, which are almost identical to the reported values.²¹ The Ti2Mn, Ti5Mn, and Ti8Mn alloy possess lower elastic modulus and higher ductility than those of the Ti6Al4V alloy.

Figure 9 represent the cytotoxicity and cell proliferation properties of the TiMn alloys. The TCPS was used as a control material. The MG-63 osteoblast cell viability (%) of the pure Ti and TiMn alloys by MTS assay is shown in Figure 9(a). The cytotoxicity increases with increasing amount of the Mn contents in the Ti alloy. Cell's viability on pure Mn and Ti12Mn was about 50% and 72%, respectively ($p < 0.05$). However, cells on the Ti5Mn and Ti8Mn alloys were also influenced concerning viability without statistical difference ($p > 0.05$), but it reached comparative high values (89%, 86%, respectively) comparable with that of pure Ti (93%). The proliferation of MG-63 osteoblasts on the TiMn alloys using flow cytometric cell proliferation analysis is demonstrated in Figure 9(b). The percentage of cells on the pure Ti and TiMn alloys decrease in contrast to the TCPS

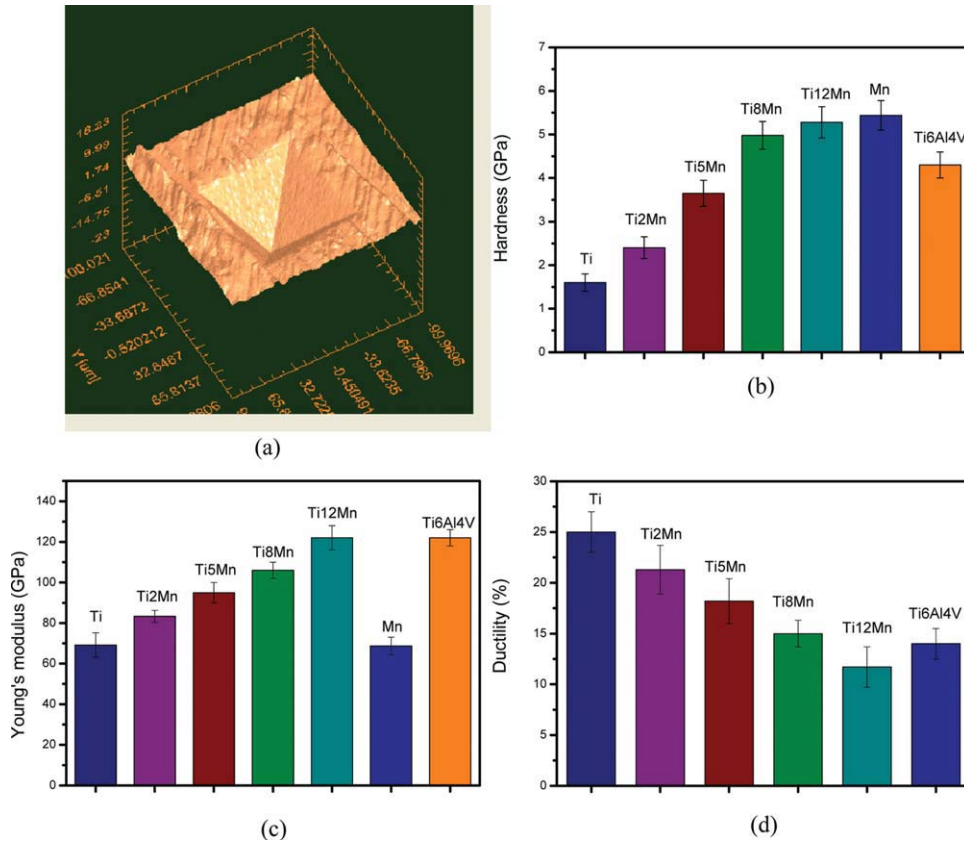


FIGURE 8. 3D (a) image of an indent obtained after microindentation test on the TiMn alloys, hardness (b), and elastic modulus (c) of the Ti, Mn, and TiMn alloys by the microindentation, and ductility (d) of the TiMn alloys showing the increase of hardness and elastic modulus but decrease of ductility with increase of Mn amounts in Ti. [Color figure can be viewed in the online issue, which is available at www.interscience.wiley.com.]

control (53.67%). Proliferating cells on TiMn alloys (Ti2Mn 41.17%, Ti5Mn 40.50%, Ti8Mn 41.57%, and Ti12Mn 39.99%) are decreased compared with that of pure Ti (48.93%), but are not significant with $p > 0.05$ and all ac-

ceptable for biomedical applications. However, the percentage of proliferating cells grown on pure Mn is significantly reduced to 35.87% ($p < 0.05$). The student's t-test that is an established statistical method shows that the

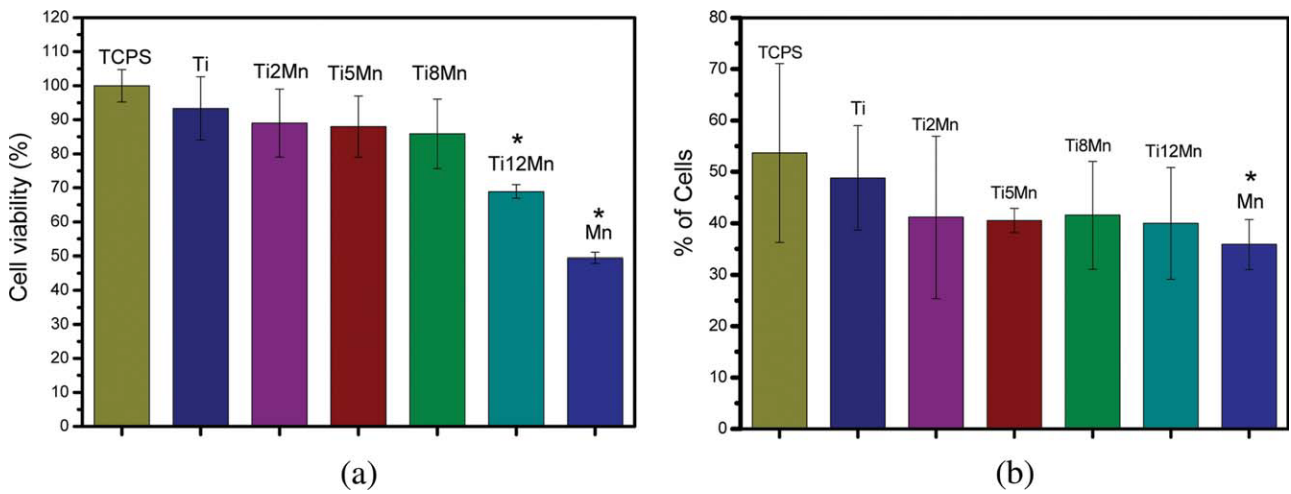


FIGURE 9. Cytotoxicity (a) and cell proliferation (b) of MG-63 osteoblasts on the Ti and TiMn alloys showing the comparable cell viability of Ti2Mn, Ti5Mn, and Ti8Mn alloys with that of pure Ti, and the proliferation of osteoblasts was not inhibited on TiMn alloys but only significantly on pure Mn. Mean \pm SD, $n = 5$, Student's t-test * $p < 0.05$. [Color figure can be viewed in the online issue, which is available at www.interscience.wiley.com.]

proliferation of MG-63 osteoblast cells on TiMn alloys is not remarkably inhibited, and only Mn is significantly decreased ($p < 0.05$). The decrease in pure Mn is about 27% from the Ti value. It is indicated that only very high amount of Mn inhibits cell proliferation. Combining the cytotoxicity and cell proliferation results, it can say that the amount of Mn below 8 wt % has a negligible effect on the cytotoxicity and cell proliferation of all Ti alloys tested.

DISCUSSION

The TiMn alloy powders were prepared by MA for 60 h. The MA is a high energy ball milling process, which involved repeated welding, fracturing, and rewelding operations, leading to microstructure refinement and alloy formation. MA also has the advantage of not involving melting, allowing alloying of elements with significantly different melting points, and it is a process scaleable to commercial sizes.²² Many Ti based alloy powders have been produced by MA method. The melting point of Ti is 1668°C and that of Mn is 1246°C. α -TiMn alloy powders were prepared at a solid state by MA with 422°C difference of melting points. The contamination during MA is a main problem of this technique. In this study, hexane was used as control agent to prevent oxidation and excessive contamination of the TiMn powders from the grinding balls and vial. Therefore, only a small Fe contamination peak is detected in the EDX spectra of the TiMn powder [Figure 3(b)].

High density Ti metal was prepared by using SPS at 750°C for 5 min, and high density TiMn alloys were fabricated at 700°C for 5 min (Figure 5). By using the traditional sintering techniques, high temperatures of 1100–1300°C were required to get a high density Ti and its alloy.²² The SPS has decreased the sintering temperature of Ti and TiMn alloys. The Mn has increased the relative density of Ti alloy, which is because of the lower β transformation temperatures in TiMn alloys. The low sintering temperature is ascribed to the ionization of particles by local sparks during SPS. A pulsed current generated plasmas in SPS that lead to a surface activation of the powder particles, melted the titanium oxide films, and formed neck junctions among powder particles at a lower temperature.^{11,19} A simultaneous pressure impact cause a plastic flow of the powders, which enables the creation of the dense Ti alloys with ultrafine microstructures at high heating rates, lower temperature, and short holding time. Because of the high reactivity of Ti metal above 1000°C, the sintering of Ti avoiding chemical reaction between Ti and die is difficult to be performed. The low sintering temperature used in the SPS allows the use of graphite dies in this study.

The V, Mo, Nb, Fe, Cr, and so forth are all β stabilizers and additions of these elements depress the β transitional temperature. The results in Figure 4 show that, the Mn has decreased the transformation temperature from the α to β phase. The effect of manganese on the α to β transition temperature is significant. With only 2 wt % Mn addition in the Ti, the transition temperature reduced from 840 to 735°C. It decreased ranging from 735 (Ti2Mn) to 660°C (Ti12Mn) with increase of Mn amount in Ti. It is confirmed that the Mn is a β stabilizing addition element for Ti metal. Addition-

ally, the Mn could increase the hardness and elastic modulus of the Ti alloy [Figure 8(b,c)]. The TiMn alloys provide higher hardness and elastic modulus than those of the pure Ti. The Ti5Mn and Ti8Mn alloys possess comparable hardness but lower elastic modulus comparing with Ti6Al4V alloy. The increment of the hardness and elastic modulus of TiMn alloys is ascribed to the formation $\alpha+\beta$ TiMn phases, which are intermetallic phases with excellent mechanical properties. The Ti6Al4V alloy was chosen for orthopedic implant for several reasons. Excellent ductility is one of the most important reasons for its wide use in biomedical industry. The ductility of Ti6Al4V alloy is measured to be 14% at room temperature. The ductility of the TiMn alloy decreased from 21.3% (Ti2Mn) to 11.7% (Ti12Mn) with increase of Mn amount [Figure 8(d)]. However, the Ti2Mn (21.3%), Ti5Mn (18.2%), and Ti8Mn (15.0%) alloys have higher ductility than that of the Ti6Al4V. Compared with the Ti6Al4V, the Ti2Mn alloy presents lower hardness (2.4 GPa), but better elastic modulus (83.3 GPa) and ductility (21.3%), the Ti5Mn alloy exhibits comparable hardness (3.65 GPa) but better elastic modulus (95.0 GPa) and ductility (18.2%), the Ti8Mn alloy shows better hardness (4.98 GPa) and elastic modulus (106 GPa) with a comparable ductility (15.0%). The Ti2Mn, Ti5Mn, and Ti8Mn alloy could be used as biomedical implants in light of their mechanical properties.

Some commercial Ti alloys also contain Mn as an alloying component. The Mn has been doped in magnesium alloy with 1.2 wt % and found the Mn has no toxicity and can improve the corrosion resistance and mechanical properties of Mg.¹⁴ The Mn was doped to tricalcium phosphate bioceramics and showed good cell compatibility.¹⁵ Recently, Fe-35Mn alloy was prepared and showed higher strength and ductility, degradable properties, which make it suitable for biodegradable stent applications.²³ The values concerning cytotoxicity and cell proliferation of the TiMn alloys demonstrate a dependency on the Mn concentration. A lower Mn contents (<8 wt %) in Ti has a low effect on the cytotoxicity and cell proliferation properties ($p > 0.05$). In general, the Ti2Mn, Ti5Mn, and Ti8Mn were comparable in viability and cell proliferation properties with pure Ti. The Ti6Al4V alloy was first used in aerospace industry, and then applied in biomedical field as bone and dental implants. Until now, the Ti8Mn alloy as one of the typical $\alpha+\beta$ Ti alloys has been extensively used in aerospace industry because of its excellent mechanical properties.²⁴ Our research here suggest that the application of the Ti8Mn alloy could be extended to biomedical field. As well as the Ti2Mn and Ti5Mn alloys, they exhibit higher ductility and lower elastic modulus than those of Ti6Al4V. The lower elastic modulus of metals for joint prosthesis could decrease the stress-shielding effect in bone-implant coupling.^{25,26} The Ti2Mn, Ti5Mn, and Ti8Mn alloys all exhibit acceptable cytotoxicity and cell proliferation of the human osteoblasts. Consequently, the Ti2Mn, Ti5Mn, and Ti8Mn alloys all have a potential for the use in the biomedical field as new bone substitutes and dental implants.

CONCLUSIONS

The $\alpha+\beta$ type TiMn alloys with high relative density and ultrafine microstructures were prepared by using MA for 60

h and SPS at 700°C for 5 min. The Mn reduced the α to β transformation temperature of Ti and was confirmed as a β stabilizer element. The hardness increased significantly ranging from 2.4 GPa (Ti2Mn) to 5.28 GPa (Ti12Mn), the elastic modulus as well ranging from 83.3 GPa (Ti2Mn) to 122 GPa (Ti12Mn) and the ductility decreased ranging from 21.3% (Ti2Mn) to 11.7% (Ti12Mn) with increasing manganese content in the Ti. Concentrations of Mn below 8 wt % in titanium reveal negligible effects on the metabolic activity and the cell proliferation of human osteoblasts. Therefore, the Mn could be used in lower concentrations as an alloying element for biomedical titanium. The Ti2Mn, Ti5Mn, and Ti8Mn alloys all have a potential for use as new bone substitutes and dental implants.

ACKNOWLEDGMENTS

The authors acknowledge Mr. Heinz Kessel U. in FCT systeme GmbH for his support in the SPS experiments.

REFERENCES

- Geetha M, Singh AK, Asokamani R, Gogia AK. Ti based biomaterials, the ultimate choice for orthopaedic implants—A review. *Prog Mater Sci* 2009;54:397–425.
- Aparicio C, Gil FJ, Fonseca C, Barbosa M, Planell JA. Corrosion behavior of commercially pure titanium shot blasted with different materials and sizes of shot particles for dental implant applications. *Biomaterials* 2003;24:263–273.
- Mark JJ, Waqar A. Surface engineered surgical tools and medical devices, US: Springer; 2007. p 533–576.
- Kuroda D, Kawasaki H, Hiromoto S, Hanawa T. Development of new Ti-Fe-Ta and Ti-Fe-Ta-Zr system alloys for biomedical applications. *Mater Trans* 2005;46:1532–1539.
- Namura T, Fukui Y, Hosoda H, Wakashima K, Miyazaki S. Mechanical properties of Ti-Nb biomedical shape memory alloys containing Ge or Ga. *Mater Sci Eng C* 2005;25:426–432.
- Ho WF, Chen WK, Wu SC, Hsu HC. Structure, mechanical properties, and grindability of dental Ti-Zr alloys. *J Mater Sci: Mater Med* 2008;19:3179–3186.
- Ying LZ, Niinomi M, Akahori T, Fukui H, Toda H. Corrosion resistance and biocompatibility of Ti-Ta alloys for biomedical applications. *Mater Sci Eng A* 2005;398:28–36.
- Lin DJ, Chuang C, Chern Lin JH, Lee JW, Ju CP, Yin HS. Bone formation at the surface of low modulus Ti-7.5Mo implants in rabbit femur. *Biomaterials* 2007;28:2582–2589.
- Bogdanski D, Köller M, Müller D, Muhr G, Bram M, Buchkremer HP, Stöver D, Choi J, Matthias E. Easy assessment of the biocompatibility of Ni-Ti alloys by in vitro cell culture experiments on a functionally graded Ni-NiTi-Ti material. *Biomaterials* 2002;23:4549–4555.
- Oh KT, Kang DK, Choi GS, Kim KN. Cytocompatibility and electrochemical properties of Ti-Au alloys for biomedical applications. *J Biomed Mater Res* 2007;83:320–326.
- Handtrack D, Despang F, Sauer C, Kieback B, Reinfried N, Grin Y. Fabrication of ultra-fine grained and dispersion-strengthened titanium materials by spark plasma sintering. *Mater Sci Eng A* 2006;437:423–429.
- Blaurock-Busch. Mineral and Trace Element Analysis, Laboratory and Clinical Application. Boulder, CO, TMI/MTM Books, Inc; 1997: 133–139
- Miao L, St Clair DK. Regulation of superoxide dismutase genes: Implications in disease. *Free Radical Biol Med*. 2009;17:344–356.
- Xu LP, Yu G, Zhang E, Pan F, Yang K. In vivo corrosion behavior of Mg-Mn-Zn alloy for bone implant application. *J Biomed Mater Res* 2007;83:703–711.
- Sima F, Socol G, Axente E, Mihailescu IN, Zdrentu L, Petrescu SM, Mayer I. Biocompatible and bioactive coatings of Mn2+-doped β -tricalcium phosphate synthesized by pulsed laser deposition. *Appl Surf Sci* 2007;254:1155–1159.
- Nicula R, Lüthen R, Stir M, Nebe B, Burkel E. Spark plasma sintering synthesis of porous nanocrystalline titanium alloys for biomedical applications. *Biomol Eng* 2007;24:564–567.
- Ivasishin OM. Cost-effective manufacturing of titanium parts with powder metallurgy approach. *Mater Forum* 2005;29:1–8.
- Semboshi S, Masahashi N, Hanada S. Degradation of hydrogen absorbing capacity in cyclically hydrogenated TiMn2. *Acta Mater* 2001;49:927–935.
- Masayuki K, Luciana MH, Kenzo A. Porous Ti-6Al-4V alloy fabricated by spark plasma sintering for biomimetic surface modification. *J Biomed Mater Res* 2004;68:88–93.
- Zhang F, Weidmann A, Nebe BJ, Burkel E. Preparation of TiMn alloy by mechanical alloying and spark plasma sintering for biomedical applications. *J Physics: Conf Ser* 2009;144:012007;1–5.
- Barbieri FC, Otani C, Lepienski CM, Urruchi WI, Maciel HS, Petronia G. Nanoindentation study of Ti6Al4V alloy nitrided by low intensity plasma jet process. *Vacuum* 2007;67:457–461.
- Polkin IS, Borzov AB. New materials produced by mechanical alloying. *Adv Perform Mater* 1995;2:99–109.
- Hermawan H, Dube D, Mantovani D. Development of degradable Fe-35Mn alloy for biomedical applications. *Adv Mater Res* 2007; 15:107–122.
- Ghosh AK, Hamilton CH. Superplastic forming and diffusion bonding of titanium alloys. *Defence Sci J* 1986;36:153–177.
- Arciniegas M, Aparicio C, Manero JM, Gil FJ. Low elastic modulus metals for joint prosthesis: Tantalum and nickel-titanium foams. *J Eur Ceram Soc* 2007;27:3391–3398.
- Santosa DR, Henriquesb VAR, Cairob CAA, Pereiraa MS. Production of a low Young modulus titanium alloy by powder metallurgy. *Mater Res* 2005;8:439–442.



The potential of rapid cooling spark plasma sintering for metallic materials

Faming Zhang^{1,*}, Michael Reich², Olaf Kessler² and Eberhard Burkel¹

¹Chair of Physics of New Materials, Institute of Physics, University of Rostock, 18055 Rostock, Germany

²Chair of Materials Science, Faculty of Mechanical Engineering and Marine Technology, University of Rostock, 18059 Rostock, Germany

Spark plasma sintering (SPS) is a remarkable technique for consolidating a large variety of advanced materials with rapid heating rates. However, adjusting the cooling rates has so far faced limitations. This communication discusses the potentials of SPS integrated with a novel gas quenching system that can allow metallic materials to be sintered and rapidly quenched directly after the sintering step, saving energy and costs. Results on numerical simulations of rapid cooling-SPS and the mechanical properties and microstructures of Ti6Al4V alloy are discussed; exhibiting the feasibility of this *rapid cooling SPS* technique and the major implications for the field of SPS and metallic powder consolidation.

Introduction

Spark plasma sintering (SPS), commonly also defined as field assisted sintering (FAST) or pulsed electric current sintering (PECS) is a novel pressure assisted PECS process utilizing ON-OFF DC pulse energizing. With the repeated application of an ON-OFF DC pulse voltage and current in powdered materials, the spark discharge point and the Joule heating point (local high temperature-state) are transferred and dispersed over the overall specimen [1,2]. The main advantage of SPS over more conventional sintering techniques lies in its ability to rapidly sinter traditionally difficult-to-sinter materials to full density [3]. During SPS treatment, powders contained in a die can be processed for diverse new and traditional bulk material applications, for example, nanostructured materials [4,5], functional graded materials [6], hard alloys [7], titanium alloys [8], bioceramics [9], porous materials [10], diamonds etc. [11]. Some modifications to the SPS technique have been applied in recent years. Anselmi-Tamburini *et al.* [12] modified the SPS die materials and set-up to create high pressures of up to 1 GPa, by which fully stabilized zirconia and ceria ceramics with grain sizes approaching 10 nm could be obtained. Morsi *et al.* [13] modified SPS to a spark plasma extrusion process, whereby aluminum samples with extruded geometries could be prepared. SPS has very high heating rates of up to 1000°C/min, but its cooling rates are very slow with natural cooling or argon gas flooding. To date, the

adjustment of cooling rates during SPS and the effects on the microstructures and properties of materials has been scarcely reported in the literature.

Sinter hardening is a hardening method used for powder metallurgy (PM) in which the parts are sintered and quenched directly after the sintering step, saving energy and costs connected to conventional hardening where the parts have to be reheated to hardening temperature [14–16]. Furthermore, sinter hardening is performed by gas quenching instead of oil quenching, creating benefits in terms of the dimensional stability and cleanliness of the specimen. Because of the poor thermal transfer characteristics (lower cooling rate) of gases under normal conditions, the gases must be optimized by proper adjustment of gas pressure and flow speed. In principle, gas quenching can be performed in two ways [17–20], namely: at low or atmosphere pressure with a high gas velocity; or at high pressure with limited gas velocities. In this short communication, the SPS technique was modified and integrated with a novel gas quenching system. The SPS vacuum was broken and flooded with argon gas and then quenched with high-velocity nitrogen gas. An $\alpha + \beta$ Ti6Al4V alloy was used as a model material. The heat transfer coefficient of the Ti6Al4V alloy during quenching was numerically simulated, and the effects of the cooling rate on the mechanical properties and microstructures of the alloy were investigated. The results prove the feasibility of the rapid cooling-SPS process and open the door for the processing of numerous other metallic powder-based material systems.

*Corresponding author: Zhang, F. (faming.zhang@uni-rostock.de)

Methods and materials

Ti6Al4V powder with particle sizes of about 20 μm was obtained from TLS Technik GmbH & Co., Germany. The SPS experiments were conducted using a Model HP D-125 FCT SPS system (FCT System GmbH, Rauenstein, Germany) installed at the University of Rostock. Fig. 1(a), (b) shows the schematic diagram and image of the gas quenching system in the SPS. The system is rotationally symmetric, with six nozzles in one group and eight groups arranged around the sintered component. The gas is distributed evenly from all nozzles. The gas nozzle field is positioned inside the SPS chamber and quenches the sintered component together with the graphite tool directly after sintering without any movement of the component. The core temperature is measured by a central pyrometer with a focus point at the bottom of the central borehole of the graphite punch (labeled f). The Ti6Al4V powders were first pressed into an $\varnothing 40$ mm graphite die, and sintered at 850°C and 50 MPa under vacuum. A heating rate of 100°C/min was applied, and the sintering process typically lasted 6 min. The applied direct current for the SPS process was 1000 A–2000 A with a pulse duration of 10 ms and an interval of 5 ms. During the cooling, the SPS furnace was flooded with argon gas to 4 kPa at rate of 10 l/min, maintaining the sintering temperature. It was then quenched from 850°C with room temperature nitrogen gas at a very high flow rate of 8000 l/min from the nozzles. Afterwards the nitrogen gas was released from the chamber to an internal gas pressure of 100 Pa–200 Pa. The various cooling rates were achieved by changing the thickness of the graphite dies. The sample dimensions measured 40 mm in diameter and 10 mm–12 mm in height.

The heat transfer coefficients are of interest for the characterization of the nozzle field's cooling effect. These are determined by means of cooling curve measurement and inverse thermal simulation by finite element (FE) software MSC.MARC 2010.1.0, and enable the thermophysical properties of the surrounding graphite die to be considered. In the calculation, the boundary conditions (and the heat transfer coefficients) of the FE-model are varied until the simulated and experimental temperature curves coincide. In

the quenching experiments, the temperatures at four sites of the system are measured via pyrometer and thermocouples. As shown in Fig. 1(a), the center of the sample (A) is measured by the pyrometer; the surface of the sample (B) is measured by thermocouple T_1 , the temperature in the middle of the graphite form (C) is measured by T_2 and the temperature of the lower graphite cone is measured by T_3 . The numerical simulations used a rotationally symmetric finite-element-model considering the axial symmetry. After SPS the density of the sintered alloys was determined by the Archimedes method using water immersion. Then, the samples were machined into small cylinders measuring 8 mm in diameter and 10–12 mm in height. The hardness of the polished samples was measured with a SHIMADAZU Micro Hardness tester HMV at HV1. Their compressive strength and ductility were measured according to standard DIN 50106 on an Instron 8502 testing machine at room temperature with a compression speed of 0.5 mm/min. In the compressive tests, five samples for one group were tested to generate statistic results. The phase analysis of the Ti alloys was performed using diffraction experiments with high energy synchrotron radiation at Beamline P02.2 (DESY/PETRA) with a wavelength of 0.29118 Å (42.58 keV). The fracture surfaces of the compressed samples were analyzed using scanning electron microscopy (SEM, Zeiss Supra25) at 20 keV. The alloys were polished and etched by Weck's reagent for 20 s and subjected to optical microscopy to observe metallographic morphologies.

Results

Various cooling rates can be achieved by changing the thickness of the graphite forms. Fig. 2(a) shows the temperature–time cooling curves of the spark plasma sintered Ti6Al4V alloys with various cooling rates. Below 400°C, the pyrometer cannot measure the temperature of the sample. From the cooling curves, the average cooling rates of 1.6°C/s, 4.8°C/s, 5.6°C/s and 6.9°C/s with an uncertainty of 0.1°C/s were derived by taking the cooling time from 850°C to 400°C into account. The cooling rate of 1.6°C/s was achieved with a 20 mm thick graphite die with

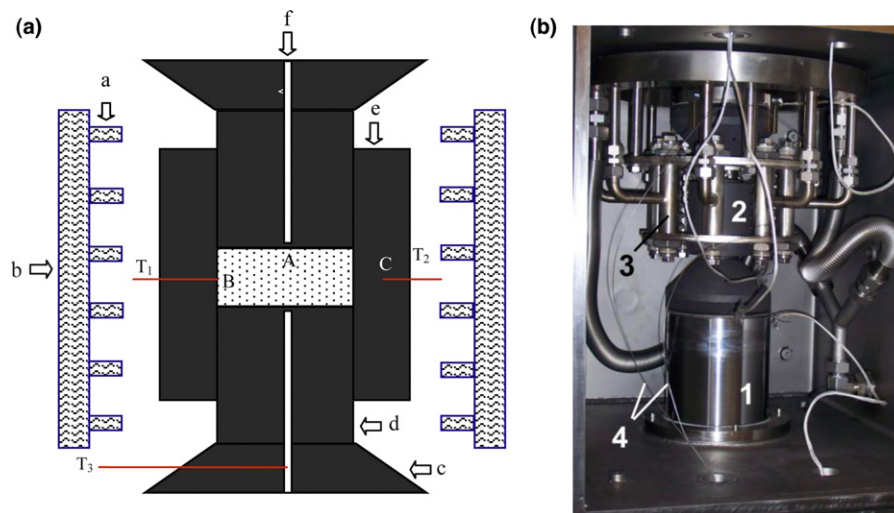


FIGURE 1

Schematic diagram (a) of the apparatus for spark plasma sintering with gas quenching system (a, gas nozzles; b, gas tube; c, graphite cone; d, graphite punch; e, graphite form; f, pyrometer hole for temperature measurement of the sample center A; T_1 , T_2 and T_3 , thermocouples for temperature measurement of the sample surface B, graphite form C, and graphite cone, respectively), and image (b) of SPS vacuum chamber (1, machine stamp, 2, sample block, 3, gas nozzle field, 4, thermocouples).

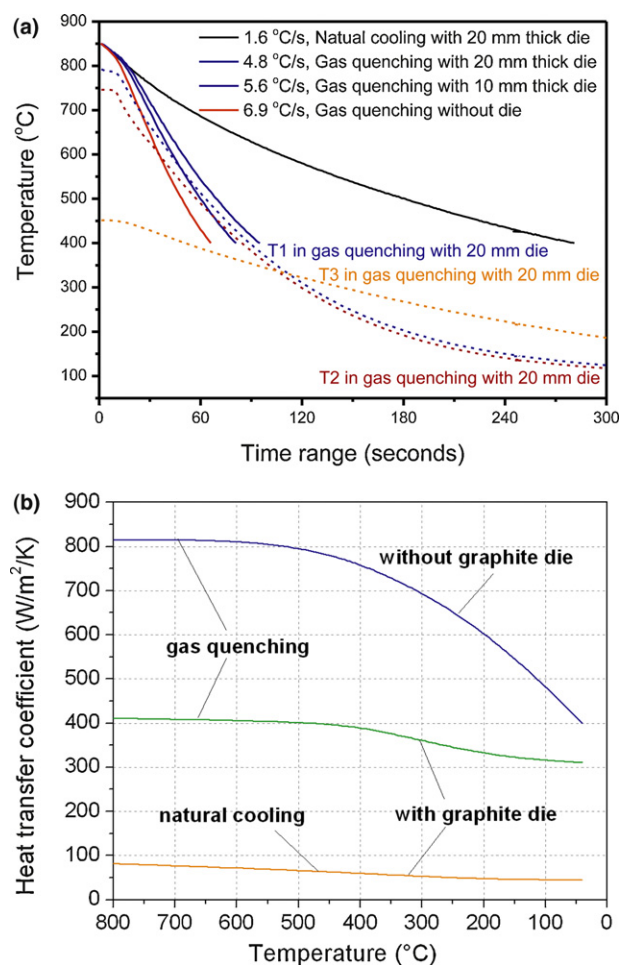


FIGURE 2

The cooling curves of the Ti6Al4V alloy as a function of time (a): (solid lines) pyrometer temperature values with various quenching rates and (dash lines) thermal couple values (T_1 , T_2 , T_3) in gas quenching with 20 mm thick die, and (b) the determined heat transfer coefficients of natural cooling (1.6 °C/s) and gas quenching of the Ti6Al4V alloys with a 20 mm thick die (4.8 °C/s) and without die (6.9 °C/s).

natural cooling, 4.8 °C/s with a 20 mm die with gas quenching, and 5.6 °C/s with a 10 mm die, also with gas quenching. The rate of 6.9 °C/s was achieved in two steps: the powder sample was first sintered at 500 °C for 5 min at 50 MPa in the die to get a 70–80% relative density, and then heated to a sintering temperature of 850 °C to full density it without the die, and the specimen was later directly gas quenched. Various cooling rates may be achieved in this way. The dashed lines show the temperature values from thermocouples during gas quenching with a 20 mm die. At the sintering temperature, the temperature of the graphite form (T_2) is lower than that of the sample surface (T_1) and T_1 is lower than the temperature in the center of the samples, as measured by the pyrometer. The temperature gradient exists during the sintering process as well as during the cooling process. The gas quenching starts from the outer surface of the graphite form: the temperature of the graphite cone (T_3) is reduced from 450 °C to about 200 °C after 300 s of gas quenching, but T_1 and T_2 decrease to below 80 °C in this time. This indicates that gas quenching is only effective in cooling the graphite form and sample in the gas nozzle fields.

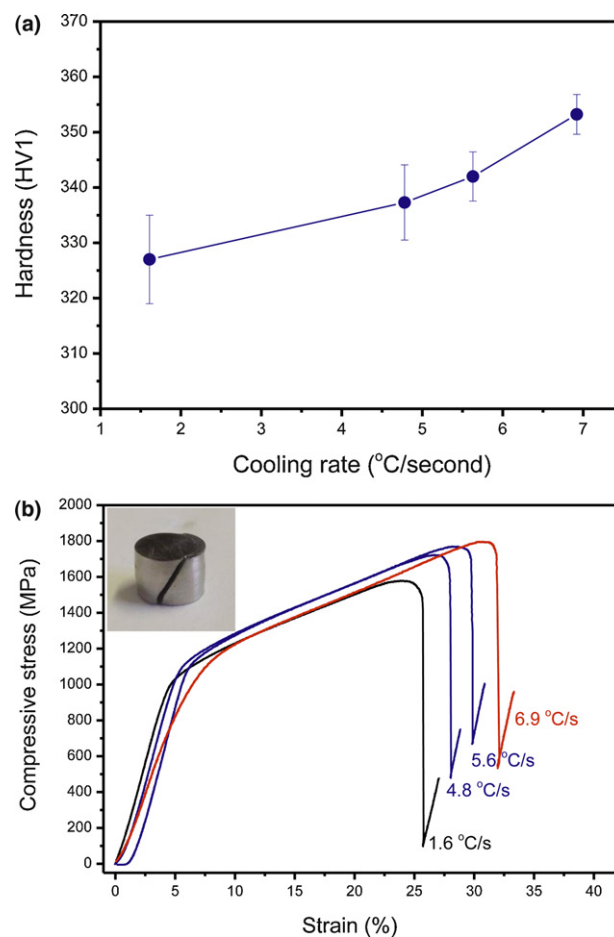


FIGURE 3

Hardness (HV1) (a) and compressive stress–strain curves (b) of the Ti6Al4V alloys at various cooling rates, exhibiting the improved hardness, ultimate compressive stress and ductility. Insert: image of a fractured specimen.

In addition to varying the cooling rate through the wall thickness of the dies, further variation of the cooling rate is possible by adjusting the gas flow rate and gas nozzle field geometry. Fig. 2(b) shows the numerically determined heat transfer coefficients of natural cooling and gas quenching of the Ti6Al4V samples. The heat transfer coefficients are reduced with decreasing temperatures for the samples processed with natural cooling (20 mm thick die) and gas quenching with (20 mm thick die) and without dies. From 800 °C to 400 °C, the coefficient values are higher than those below 400 °C. This indicates that heat transfer and dissipation are faster at higher temperatures, above 400 °C. The natural cooling sample exhibited a heat transfer coefficient of 80 W/(m² K) at 800 °C which is gradually reduced to 50 W/(m² K) at room temperature. The gas quenched sample with a die exhibited a heat transfer coefficient of about 400 W/(m² K) at 800 °C and dropped to about 300 W/(m² K) at room temperature. Quenching without a die results in a heat transfer coefficient of about 810 W/(m² K) at 800 °C and 400 W/(m² K) at room temperature. The quenching intensity without a die is about two times higher than that with a die. However, the gas quenching with a die is also effective to increase the heat transfer coefficients up to five to seven times higher than natural cooling. The heat transfer coefficient is defined as the heat flux divided by the temperature difference.

The value of the heat transfer coefficient is proportional to that of the quenching intensity which can be described by the heat flux density on its surface. With higher heat transfer coefficients it can cool the sample faster, hence, the Ti alloys can be cooled rapidly with gas quenching due to the higher heat transfer coefficients. The sintering and quenching heat-treatment have been completed by one step SPS process without a separate heat treatment operation.

Fig. 3(a) shows the hardness (HV1) of the Ti6Al4V alloy with various cooling rates. All the Ti6Al4V alloys with various cooling rates have similar relative densities of above 99.0%. The naturally cooled samples with a cooling rate of 1.6°C/s have a hardness of 327 ± 8 . The gas quenched samples exhibit a hardness of 337 ± 7 , 342 ± 4 and 353 ± 4 for cooling rates of 4.8, 5.6 and 6.9°C/s, respectively. The hardness increases with a higher cooling rate, thus, sinter hardening of the Ti6Al4V alloys has been realized by SPS with gas quenching. Fig. 3(b) shows the compressive stress-strain curves of the Ti6Al4V alloys with various cooling rates. The stress-strain curves show the elastic deformation, plastic deformation and fracture stages. The insert image shows one of the fractured Ti6Al4V specimens. It is found that the fracture takes

places at an angle of about 45° to the direction of the compressive load. The compressive yield strengths for all the samples are around 1100 MPa, which is higher than the reported values [21,22] (of about 902 MPa). But the ultimate compressive strength has increased with a higher cooling rate, as well as the compressive strains (ductility). Statistically, the samples with natural cooling rate of 1.6°C/s show the ultimate compressive strength of 1578 MPa \pm 80 MPa and ductility of (26 \pm 2)%. At a cooling rate of 4.8°C/s, they reach to (1723 \pm 63) MPa and (28 \pm 2)%, respectively. At a 5.6°C/s cooling rate, the strength is increased to (1775 \pm 70) MPa and (30 \pm 2)%; at 6.9°C/s this is raised to (1832 \pm 43) MPa and (34.0 \pm 3)%. The rapid cooling has increased the ultimate compressive strength and the ductility of the Ti6Al4V alloys.

Fig. 4(a) shows high energy X-ray diffraction patterns of the Ti6Al4V alloys. The raw Ti6Al4V powder shows the α -Ti phase. The naturally cooled sample show both the α and β -Ti phases and weak diffraction peaks from the α -Ti (1 1 2) and (2 0 1) lattice planes. The gas quenched Ti6Al4V alloys exhibit sharper diffraction peaks corresponding to Ti-rich phases with a β -Ti phase, as well as new broad peaks probably from intermetallic phase of Al₂Ti (ICDD No.

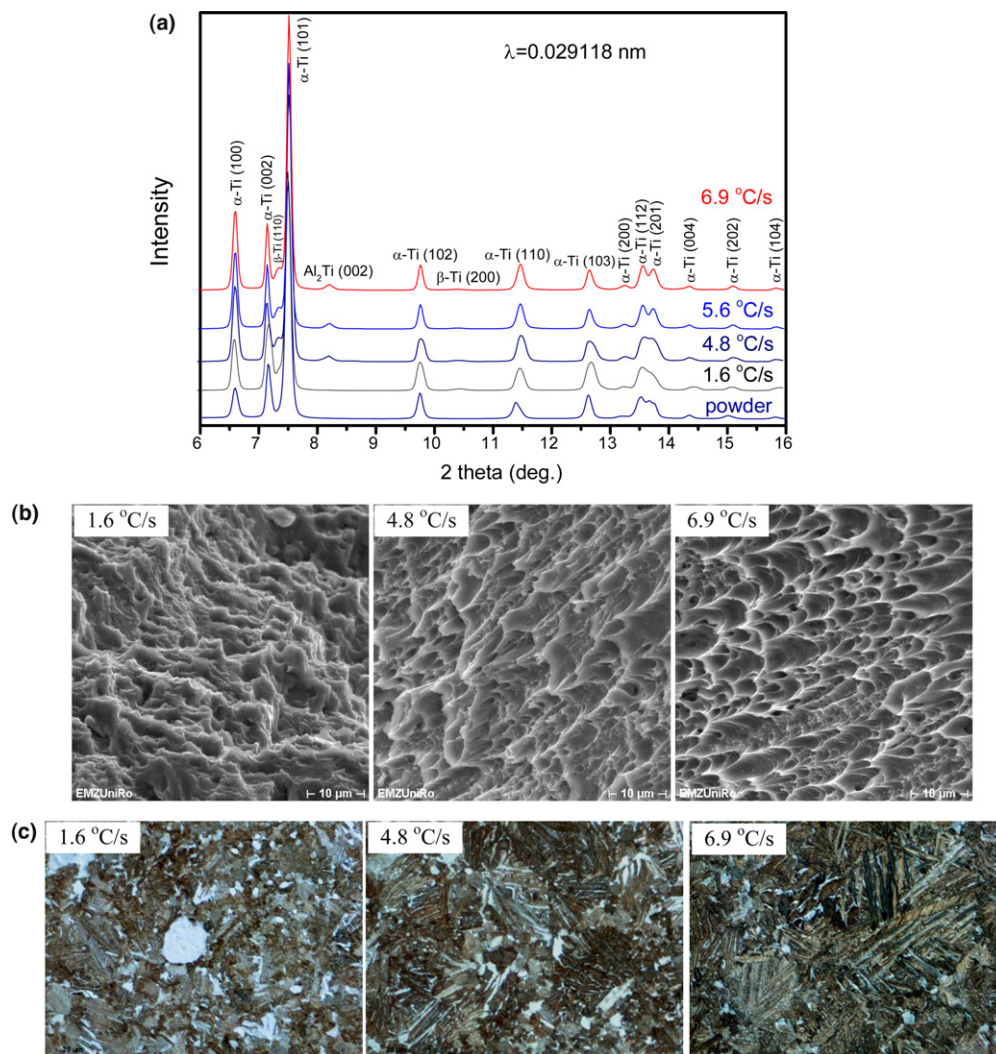


FIGURE 4

Synchrotron radiation high energy X-ray diffraction pattern (a), SEM micrographs of the fracture surfaces (b) and metallographic micrographs of the surfaces (c) of the Ti6Al4V alloys at various cooling rates of 1.6°C/s, 4.8°C/s, 6.9°C/s.

TABLE 1

Mechanical properties and phases of the Ti6Al4V alloys prepared by rapid cooling SPS at various cooling rates.

Cooling rate ($^{\circ}\text{C/s}$)	Hardness (HV 1.0)	Ultimate compressive stress (MPa)	Ductility (%)	Phase compositions
1.6	327 ± 8	1578 ± 80	26 ± 2	α -Ti and β -Ti
4.8	337 ± 7	1723 ± 63	28 ± 2	α -Ti, β -Ti, Al_2Ti
5.6	342 ± 4	1775 ± 70	30 ± 2	α -Ti, β -Ti, Al_2Ti
6.9	353 ± 4	1832 ± 43	34 ± 3	α -Ti, β -Ti, Al_2Ti

42-1136). The gas quenching in the SPS resulted in the formation of nanocrystalline intermetallic phase of Al_2Ti in the alloys. Fig. 4(b) shows SEM micrographs of the fracture surface of the processed Ti6Al4V alloys. The samples all present a ductile fracture mode with a large amount of plastic deformation undergoing transgranular fracture with typical dimples. However, the fracture surfaces present more and more dimples with an increase of the cooling rate, indicating the sample becomes much more ductile after the rapid cooling in the SPS. Fig. 4(c) provides the metallographic morphology of the Ti6Al4V alloys with various cooling rates. In the etched metallographic images, the β -Ti phase (bcc) appears in white and the α -Ti phase (hcp) darker. The samples all show both phases in the microstructures. The naturally cooled sample with 1.6°C/s cooling rate shows a relative homogeneous globular $\alpha + \beta$ microstructure. The rapidly cooled sample shows a different microstructure with a lamellar α phase. As the cooling rate increases, the 6.9°C/s cooled sample has even more lamellar α phase. In general, gas quenching in the SPS results in a morphological change to the lamellar α -Ti phase.

Discussion

The hardness, ultimate compressive strength and ductility of the Ti6Al4V alloys have been increased due to the gas quenching. Sinter hardening is applicable for the Ti6Al4V alloy in which the samples are spark plasma sintered and gas quenched directly after the sintering. It saves energy and costs when compared with conventional hardening, in which the parts must be reheated to the hardening temperature. The microstructure analysis revealed that the rapid cooling led to the precipitation of intermetallic phase (Al_2Ti), more pronounced dimples in fracture surfaces, and a morphological change to lamellar α -Ti phase. Table 1 summarizes the mechanical properties and phases of the Ti6Al4V alloys prepared by rapid cooling SPS at various cooling rates. The hardness, ultimate compressive strength and ductility of the Ti6Al4V alloys were increased corresponding to the phase variations.

SPS is a nonequilibrium sintering process. Because of the higher cooling rates, the soluble Al, V elements in Ti have not enough time to diffuse, and then precipitate as second phases in the Ti6Al4V alloy. The precipitated nanocrystalline Al_2Ti can harden and dispersion reinforce the Ti6Al4V alloys, and therefore, the mechanical properties of the Ti6Al4V alloy are increased. Quenching from the $\alpha + \beta$ phase field can produce a microstructure that consists of a primary α phase, retained β -Ti, new α -Ti formed during quenching and intermetallic precipitates. With increasing cooling rates, the newly formed α -Ti becomes more lamellar. The

lamellar structured α -Ti phase can lead to an increase in ductility of the Ti6Al4V alloy [23].

Using industrial gases for quenching of high value parts offers significant environmental and performance advantages over liquid quenching (water, oil, etc.). Gas quenched parts are clean, thus eliminating the need for post-cleaning operations. Because of the poor thermal transfer characteristics (lower cooling rate) of gases under normal conditions, they have to be optimized by proper adjustment of the gas pressure and flow speed. Gas quenching can be performed at low pressure with a high gas velocity or at high pressure with limited gas velocities [17–20]. In this study, we used the first method in the SPS, at low or atmospheric pressure with a high gas velocity. The flow rate of the nitrogen gas from the nozzles was 8000 l/min, and the pressure of gas was only slightly above normal atmospheric pressure. The thermo-physical properties of the gas are also an important issue. On the basis of availability, and the thermo-physical properties, hydrogen would appear to be good a choice as a quenching agent [24]; however, because of the explosive risks associated with hydrogen it is seldom used as a quench gas in commercial heat treating. Helium is almost as fast as hydrogen, not explosive, but significantly more expensive [25]. Nitrogen is the most popular choice, primarily because it is readily available and inexpensive [26], although argon is used in some special applications, but it does not quench as effectively as nitrogen and is considerably more expensive [27].

Summary

Ti6Al4V alloys have been used in medical applications for several decades, but one of the main problems of this alloy in biomedical applications is its insufficient ductility [28]. This investigation indicates that the traditional Ti6Al4V alloy can be modified by rapid cooling SPS leading to various mechanical changes. The high ductile Ti6Al4V alloy achieved through rapid cooling SPS offers unprecedented opportunities for the easy manufacturing of complex shapes and plates for biomedical and new engineering applications. Rapid cooling SPS combining sintering and gas quenching provides a novel method to tailor the mechanical properties of the Ti6Al4V alloys. It must be pointed out that this rapid cooling SPS is mainly suitable for metallic materials including metals, alloys and metal matrix composites. In general, ceramic materials will probably crack after quenching due to their poor thermal shock resistance. It is a subject of an ongoing investigation.

SPS integrated with gas quenching has been discussed for the first time for the successful modification of Ti6Al4V alloys. Cooling curve measurements and inverse thermal FE simulations reveal that the gas quenching can increase the heat transfer coefficient up to five to seven times. The cooling rates ranging from 1.6°C/s to

6.9°C/s were achieved by changing the thickness of the graphite dies. Sinter-hardening of the Ti6Al4V alloy has been achieved, where the hardness rises from 327 to 353 HV1. The gas quenching has increased the ultimate compressive strength and ductility of the Ti6Al4V alloy from 1578 MPa to 1832 MPa and from 26% to 34%, respectively. The microstructure analysis revealed that the rapid cooling led to the precipitation of nanocrystalline intermetallic phase (Al₂Ti), more pronounced dimples in fracture surfaces and a morphological change to lamellar α -Ti phase.

Rapid cooling SPS can be applied to a wide range of metals, alloys and metal matrix composites, where the parts can be rapidly sintered and rapidly quenched directly after the sintering step, saving energy and cost. Future work will involve adjusting gas flow rate and gas nozzle field geometry, and examine the effects of cooling rates on keeping grain sizes of nanocrystalline metallic materials.

Acknowledgement

This work was gratefully supported by the DFG GRK1505/1 (Welisa). The technical assistance from Mr. Y. Quan is acknowledged. The authors also thank Dr. H.P. Liermann for his supports at the beamline P02.2.

References

- [1] Z.A. Munir, et al. *J. Mater. Sci.* 41 (2006) 763.
- [2] Z.A. Munir, et al. *J. Am. Ceram. Soc.* 94 (2011) 1.
- [3] M. Nygren, Z. Shen, *Key Eng. Mater.* 264–268 (2004) 719.
- [4] M. Nygren, Z. Shen, *Solid State Sci.* 5 (2003) 125.
- [5] R. Sivakumar, et al. *Scripta Mater.* 56 (2007) 265.
- [6] F. Watari, et al. *Compos. Sci. Technol.* 64 (2004) 893.
- [7] F. Zhang, et al. *J. Alloys Compd.* 385 (2004) 96.
- [8] F. Zhang, et al. *J. Biomed. Mater. Res. B* 94B (2010) 406.
- [9] Y.W. Gu, et al. *Biomaterials* 25 (2004) 4127.
- [10] F. Zhang, et al. *Adv. Eng. Mater.* 12 (2010) 863.
- [11] F. Zhang, et al. *Diamond Relat. Mater.* 20 (2011) 853.
- [12] U. Anselmi-Tamburini, et al. *Scripta Mater.* 54 (2006) 823.
- [13] K. Morsi, et al. *Scripta Mater.* 61 (2009) 395.
- [14] M. Dlapka, et al. *J. Heat Treat. Mater.* 67 (2012) 223.
- [15] S.N. Thakur, et al. *Int. J. Powder Metall.* 40 (2004) 45.
- [16] L.A. Dobrzanski, M. Musztyfaga, *J. Achiev. Mater. Manuf. Eng.* 37 (2009) 630.
- [17] N. Lior, *J. Mater. Process. Technol.* 1881 (2004) 155.
- [18] M. Reich, et al. *Key Eng. Mater.* 424 (2010) 57.
- [19] S. Schöne, et al. *Proc. 3rd International Conference on Distortion Engineering 2011, September 14–16, Bremen, Germany, (2011), p. 75.*
- [20] M. Reich, O. Kessler, in: D. Scott MacKenzie (Ed.), *Proc. 6th Int. Quenching and Control of Distortion Conf., 9–13 September 2012, Chicago, IL, USA, ASM International, 2012, p. 563.*
- [21] M. Bram, et al. *Met. Powder Rep.* 61 (2006) 20.
- [22] M.H. Lee, et al. *J. Phys. D: Appl. Phys.* 41 (2008) 105404.
- [23] J.H. Kim, et al. *Acta Mater.* 51 (2003) 5613.
- [24] B. Xiao, et al. *J. ASTM Int.* 8 (2011) 103403.
- [25] J.H. Sung, et al. *Solid State Phenom.* 118 (2006) 221.
- [26] H. Morii, et al. *Nucl. Instrum. Methods Phys. Res. A* 526 (2004) 399.
- [27] C. McGee, et al. *Surface Engineering Coatings and Heat Treatments 2002: Proceedings of the 1st ASM International Surface Engineering and the 13th IFHTSE Congress, ASM International, 2003, p. 457.*
- [28] K.H. Frosch, K.M. Stürmer, *Eur. J. Trauma* 32 (2006) 149.

Company Info

- [At a glance](#)
- [Elsevier locations](#)
- [Mission](#)
- [Senior management](#)
- [Experts](#)
- [Subject information](#)
- [Publishing guidelines](#)
- [Corporate responsibility](#)
- [Open access](#)
- [Universal access](#)
- [Company history](#)
- [Annual reports](#)
- [Press releases](#)
 - [Corporate](#)
 - [Science & technology](#)**
 - [Health sciences](#)
 - [Research & journals](#)
 - [Corporate social responsibility](#)
- [Conferences](#)
- [Exhibitions](#)
- [Content innovation](#)
- [Careers](#)
- [Social Media](#)

Cool It, Quick: Rapid Cooling Leads to Stronger Alloys

Share This:

*Researchers reveal a new technique to produce high strength metallic alloys, at a lower cost using less energy***Oxford, July 10, 2013**

A team of researchers from the University of Rostock in Germany has developed a new way to rapidly produce high strength metallic alloys, at a lower cost using less energy than before. It's expected that this breakthrough will profoundly change how we produce components used in a diverse range of applications; including transport and medical devices.

The research , which appears in the latest issue of the open access journal *Materials Today*, reports on the first Spark Plasma Sintering (SPS) system with an integrated gas quenching mechanism, capable of alternating the phase compositions and retaining the smallest grain features inside a structured metallic alloy.

SPS is a technique used to fuse fine powders into a dense solid material, by placing powder into a mold (or die) and simultaneously applying pulses of electric current and mechanical pressure to it. By varying SPS cooling rates, it is possible to control the phase and grain sizes in a material, and so, to tune its mechanical properties. In their study, the team of researchers led by Dr. Eberhard Burkel, a Professor of Physics of New Materials, demonstrated that rapidly cooling a material directly after SPS fabrication can produce a material with enhanced hardness, strength and ductility.

The new rapid cooling SPS system is based on a commercially available design, modified to include a series of gas inlet nozzles. After sintering, most SPS systems are left to cool naturally, or are flooded with argon gas. The system blasts nitrogen gas into the chamber at high speeds, rapidly cooling the material.

To demonstrate the utility of the system, Grade 5 Titanium (Ti-6Al-4V) – known as the "workhorse" of the titanium industry – was produced at different cooling rates. The most-rapidly cooled alloy was found to be up to 12% harder than the naturally-cooled alloy, and with an improved ductility up to 34±3%. Ti-6Al-4V is the most common titanium alloy in use worldwide, with applications in the aerospace, biomedical and marine industries.

In their article the researchers explain, "This high-ductile alloy offers unprecedented opportunities for the easy manufacturing of complex shapes for biomedical and new engineering applications."

First author of the study, Dr. Faming Zhang, said "The system will play a major role in the production of novel materials, from metals, alloys, metal matrix composites to micro- and nanostructured semiconductors."

#

Notes for Editors

This article is "The potential of rapid cooling spark plasma sintering for metallic materials" by Faming Zhang, Michael Reich, Olaf Kessler and Eberhard Burkel. It appears in *Materials Today*, Volume 16, Issue 5, Page 192-197 (2013) published by Elsevier. [Full text of the article is freely available from here](#) . Journalists wishing to interview the authors may contact Dr. Stewart Bland at +44 1865 84 3124 or s.bland@elsevier.com

About *Materials Today*

Materials Today is the Gateway to Materials Science and home of the Open Access Journal of the same name. The journal publishes peer-refereed review and research articles that assess the latest findings and examine the future challenges, as well as comment and opinion pieces from leading scientists discussing issues at the forefront of materials science. Visit <http://www.materialstoday.com> for access. *Materials Today* also publishes news, interviews, educational webinars, jobs and events; and provides free access to a range of specially selected articles from Elsevier's materials science journals. For more information on all aspects of *Materials Today*, including the editorial calendar and advertising options, contact the editor, Dr. Stewart Bland at s.bland@elsevier.com. Follow [@MaterialsToday](#) on Twitter; and on Facebook: <http://www.facebook.com/elsevier.materials> .

About Open Access Publishing at Elsevier

Elsevier has been providing open access publishing options since 2005. Today, researchers can choose to publish in over 1,500 hybrid journals as well as 39 full open access journals and these numbers will continue to grow rapidly. All of Elsevier's open access publications have been peer reviewed, ensuring that the broader community not only reads the latest research but that it is factual, original and of the highest quality and ethical standards. For more information about Elsevier's open access program, visit www.elsevier.com/openaccess

About Elsevier

Elsevier is a world-leading provider of scientific, technical and medical information products and services. The company works in partnership with the global science and health communities to publish more than 2,000 journals, including *The Lancet* and *Cell* , and close to 20,000 book titles, including major reference works from Mosby and Saunders. Elsevier's online solutions include *ScienceDirect* , *Scopus* , *Reaxys*, *ClinicalKey* and *Mosby's Suite* , which enhance the productivity of science and health professionals, and the *SciVal suite* and *MEDai's Pinpoint Review* , which help research and health care institutions deliver better outcomes more cost-effectively.

A global business headquartered in Amsterdam, *Elsevier* employs 7,000 people worldwide. The company is part of *Reed Elsevier Group plc*, a world leading provider of professional information solutions. The group employs more than 30,000 people, including more than 15,000 in North America. Reed Elsevier Group plc is owned equally by two parent companies, Reed Elsevier PLC and Reed Elsevier NV. Their shares are traded on the London, Amsterdam and New York Stock Exchanges using the following ticker symbols: London: REL; Amsterdam: REN; New York: RUK and ENL.

Media contact

Stewart Bland
Elsevier
+44 1865 84 3124
s.bland@elsevier.com

You are here: [Home](#) / [News](#) / [Cool it, quick](#)

News

Cool it, quick

10 July 2013

Rapid cooling leads to stronger alloys

Read the full research article [here](#).

A team of researchers from the University of Rostock in Germany has developed a new way to rapidly produce high strength metallic alloys, at a lower cost using less energy than before. It's expected that this breakthrough will profoundly change how we produce components used in a diverse range of applications; including transport and medical devices.

[The research](#), which appears in the latest issue of *Materials Today*, reports on the first Spark Plasma Sintering (SPS) system with an integrated gas quenching mechanism, capable of alternating the phase compositions and retaining the smallest grain features inside a structured metallic alloy.

SPS is a technique used to fuse fine powders into a dense solid material, by placing powder into a mold (or die) and simultaneously applying pulses of electric current and mechanical pressure to it. By varying SPS cooling rates, it is possible to control the phase and grain sizes in a material, and so, to tune its mechanical properties. In their study, the team of researchers led by Dr. Eberhard Burkel, a Professor of Physics of New Materials, demonstrated that rapidly cooling a material directly after SPS fabrication can produce a material with enhanced hardness, strength and ductility.

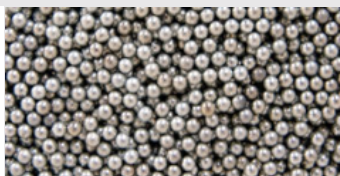
The new rapid cooling SPS system is based on a commercially available design, modified to include a series of gas inlet nozzles. After sintering, most SPS systems are left to cool naturally, or are flooded with argon gas. The system blasts nitrogen gas into the chamber at high speeds, rapidly cooling the material.

To demonstrate the utility of the system, Grade 5 Titanium (Ti-6Al-4V) – known as the "workhorse" of the titanium industry – was produced at different cooling rates. The most-rapidly cooled alloy was found to be up to 12% harder than the naturally-cooled alloy, and with an improved ductility up to 34±3%. Ti-6Al-4V is the most common titanium alloy in use worldwide, with applications in the aerospace, biomedical and marine industries.

In their article the researchers explain, "This high-ductile alloy offers unprecedented opportunities for the easy manufacturing of complex shapes for biomedical and new engineering applications."

First author of the study, Dr. Faming Zhang, said "The system will play a major role in the production of novel materials, from metals, alloys, metal matrix composites to micro- and nanostructured semiconductors."

Read the full research article [here](#).



Related Links

[The potential of rapid cooling spark plasma sintering for metallic materials - Current research article](#)

Elsevier Ltd is not responsible for the content of external websites.

Related Stories

[A hydrogen reservoir made of ... mostly hydrogen](#)

Crystal storage

[Capturing carbon with trapdoors](#)

Novel method of capturing carbon dioxide

[Iron-platinum alloys could improve data storage](#)

New material could aid next generation hard drives

[Model motor nerve system](#)

Researchers from the University of Central Florida (UCF) [Rumsey et al., doi:10.1016/j.biomaterials.2009.03.023] report on the first lab-grown motor nerves that are insulated and organized just like they are in the human body.

[The secrets of antibody armour revealed](#)

A team led by University College London (UCL) has used a combination of X-rays and neutron scattering to determine the structure of secretory immunoglobulin A (SIgA), the most prevalent antibody in the immune system.

Share this article

[More services](#)

This article is featured in:

Metals and alloys • Tools and Techniques

DOI: 10.1002/adem.201000106

Spark Plasma Sintering, Microstructures, and Mechanical Properties of Macroporous Titanium Foams**

By Faming Zhang*, Eileen Otterstein and Eberhard Burkel

Macroporous pure titanium (Ti) foams with porosity of 30–70% and pore size of 125–800 μm were fabricated by using spark plasma sintering (SPS) and NaCl dissolution methods. A mixture of Ti and sodium chloride (NaCl) powders were spark plasma sintered in a temperature range from 550 to 800 °C and the NaCl phase was then dissolved in water. High purity Ti foams were obtained at the SPS temperature of 700 °C for holding time of 8 min under pressure of 50 MPa. The resulting Ti foams consist of pure α -Ti phase with interconnected macropores in square cross sections. The plateau stress and Young's modulus agree with the Gibson–Ashby models, and coarsely follow of linear decline with the increase of the pore sizes, and exponential decay with the increase of the porosity. The macroporous Ti foams with plateau stress 27.2–94.2 MPa and Young's modulus 6.2–36.1 GPa may have a potential to be used as bone implants.

Porous materials with interconnected porosity have widespread applications in many fields of engineering.^[1] Bulk porous metallic materials (honeycomb, foam, and hollow spheres) are known for their interesting combinations of the advantages of a metal (strong, hard, tough, electrically, and thermally conductive, etc.) with the functional properties of porous structures (lightweight with adjustable properties by selecting the density).^[2] Because of this, porous metals are interesting for a number of engineering applications such as structural panels, energy absorption devices, acoustic damping panels, compact heat exchangers, and biomedical implants etc.^[3] Porous titanium (Ti) and its alloy were widely used in the biomedical field due to their outstanding mechanical properties, low density, chemical resistance, and biocompatibility. As a kind of long-term load-bearing implant, the porous structures of Ti and its alloy could lead to a reliable anchoring of host tissue into the porous structure, and allow mechanical interlocking between bone and implant.^[4] The ingrowths of bone into the porous structure could ensure a good transfer of mechanical forces. Therefore, a

porous structure is preferable for the Ti and its alloys using as bone scaffolds.

However, porous Ti and its alloys are difficult to be produced from the liquid state, due to the high melting point, the high reactivity at high temperature above 1000 °C and the contamination susceptibility. Thus, fabrication processes for porous Ti has to date focused on the powder metallurgy (PM) route and avoided the liquid route.^[5] Many techniques have been applied to produce porous Ti and its alloy implants in recent years.^[6–10] Nevertheless, there are still problems to be solved in the field of porous Ti for biomedical applications^[11]: the difficulty to create controlled porosity and pore sizes, the insufficient knowledge of porous structure–property relationships, the requirements of new sintering techniques with rapid energy transfer, and less energy consumption and so on.

Spark plasma sintering (SPS) as one of the field assisted sintering techniques, is a relative new sintering technique for PM and ceramics. SPS is a high efficient and energy saving powder consolidation and sintering technology capable of processing conductive and non-conductive materials.^[12] However, most of SPS researches were performed on dense materials; fewer studies were on porous materials.^[13] The SPS studies on porous Ti alloys were mainly using low temperature and low pressure to decrease the relative density of samples.^[14–19] The samples exhibited pore sizes of some tens of micrometers and a porosity in the range of 20–45%. As bone foams, high porosity (>50%) and macropore size (>200 μm) are essential requirements for the bone growth and the osteoconduction.^[20,21] Macroporous nanostructured tricalcium phosphate scaffolds have been successfully

[*] Dr. F. Zhang, E. Otterstein, Prof. Dr. E. Burkel
Institute of Physics, University of Rostock, August Bebel Str. 55,
D-18055 Rostock, Germany
E-mail: faming.zhang@uni-rostock.de

[**] This research was supported by the DFG-Deutschen Forschungsgemeinschaft (German Research Foundation) with grant no. GRK1505/1 (Welisa). The authors acknowledge the FCT Systeme GmbH for the support in SPS experiments, and Prof. R. Balder in the Department of orthopedic of University Rostock for his support in mechanical testing.

prepared by using SPS with a special die design.^[21] Nevertheless, macroporous Ti foams by SPS were scarcely reported.

The spacer method was developed to fabricate porous metals and ceramics since 1960s. The method can control the pore characteristics by adjusting of the mixing ratio and the particle size of spacer.^[22] The sodium chloride (NaCl) has been used as spacer material for aluminum^[23] and Ti alloys^[24,25] due to its relative high melting point (801 °C), its low cost, and the easy dissolution in water, the less corrosive attack of metals and the low toxicity. The combination of the SPS technique with the NaCl dissolution were tried in aluminum metals at SPS temperature of 570 °C,^[26,27] and the processed porous aluminum demonstrated high sound absorption property.^[28] In fact, Ti has a much higher melting point (1660.0 °C) than aluminum (660.3 °C). Therefore, it is a great challenge to fabricate Ti foams by using the SPS and NaCl dissolution methods.

The objective of this study is to develop macroporous Ti foams with controlled architectures using the SPS in combination with the NaCl dissolution methods. The major parameters involved in the preparation process were studied. The microstructures of the prepared foams were analyzed by using 3D X-ray microcomputed tomography (micro-CT) and scanning electron microscopy (SEM) techniques. The relationship between the mechanical properties and the porous architectures were analyzed and discussed.

Experimental

Raw materials

The precursor Ti powders were prepared by hydride-dehydride method with 99.5% purities in 325 meshes (Alfa Aesar, Germany). The space holder material consisted NaCl crystalline powders with 99.0% purity (Alfa Aesar) sieved in the range of 100–1000 μm.

Pore forming method

The Ti powders and NaCl powders were homogeneously mixed in different weight ratios in a blender with paraffin wax as a binder. The mixtures were loaded into graphite die with graphite paper between the punches and die to sinter disc-shaped pellets (20 mm diameter, thickness 6–7 mm). The SPS experiments were performed using a Model HPD-25/1 FCT SPS system (FCT systeme GmbH, Rauenstein, Germany) at temperatures of 550–800 °C lasting for various time. During the experiments, the temperature is measured by a central pyrometer with a focus point at the bottom of the central borehole of the graphite set-up, 2.88 mm from the bottom of the upper punch and 5.125 mm from the center of a 4.25 mm thick sample inside the die^[29]. The temperature of the die is measured by a second two-color pyrometer, focused on the outer die wall surface at the same height as the center of the compact. The applied direct current for SPS was about 1000–2000 A (voltage < 5 V) with a pulse duration of 12 ms and an interval of 2 ms. The SPS experiments were conducted in vacuum (<6 Pa) under an uniaxial pressure of 30–50 MPa. The

heating rate was maintained at 100 °C min⁻¹. The SPSed samples were then suspended in circulating hot water (80 °C) to dissolve the NaCl space holder for 12 h. The leached Ti forms were cleaned in an ultrasonic water bath for 15 min, rinsed with ethanol and furnace dried at 120 °C for 10 h.

Microstructures analysis

X-ray diffraction (XRD, Bruker D8, Germany) was used to characterize the phase composition of the powders and sintered foams with Cu K α radiation (0.154178 nm). The pore structure of the Ti foam was examined by using X-ray micro-CT (GE, USA). The specimens were mounted on a rotary stage and scanned in their entirety, being rotated by 360° in 1400 equiangular steps (4 pics per 1°). The detector size is 2284 pixel in *x* and *y* and 2304 pixel in *z* direction. The voxel size of the images is 10.2 μm in all three axes. The macroporous structures and the microstructures of the obtained Ti foams were analyzed by using a SEM (Zeiss Supra 25, Germany) equipped with EDX. The contents of oxygen and carbon in the Ti foams were evaluated by inert gas fusion techniques using a LECO TCH-600 analyzer.

Properties measurements

The porosities and densities of the sintered porous Ti samples were determined by the Archimedes principal method, i.e. the porosity was calculated from the dry weight of the specimen in ambient air, the wet weight of the specimen in ambient air after boiling water impregnation, and the wet weight of the specimen under water after boiling water impregnation. The mechanical behavior of the porous Ti foams was investigated by uniaxial compression experiments at room temperature. The plateau stress measurements were carried out on a universal testing machine Zwick Roell Z050, equipped with a 50 kN load cell at 0.5 mm min⁻¹. The strain was measured with a strain gauge. The Young's modulus was calculated by dividing the plateau stress by the plateau strain.

Results and Discussions

Pore Forming Process

Figure 1 shows the SEM micrographs of the starting Ti and NaCl powders. The Ti powders have irregular morphologies and size distribution of 10–30 μm (Fig. 1a). These NaCl powders have cuboid shapes with round angles and size distribution of 150–300 μm, which is according to the sieved size of 100–50 mesh [Fig. 1(b)].

Figure 2 shows the schematic illustration of the pore forming process by using the SPS and NaCl dissolution methods. The Ti and NaCl powders were sieved to the required particle size, firstly [Fig. 2(a)]. Then, the Ti and NaCl powders with different weight ratios were mixed thoroughly [Fig. 2(b)]. Additionally, the Ti/NaCl mixtures were subjected to SPS at various parameters [Fig. 2(c)]. The spark plasma sintered samples were suspended in circulating hot water (80 °C) for as long as 12 h [Fig. 2(d)].

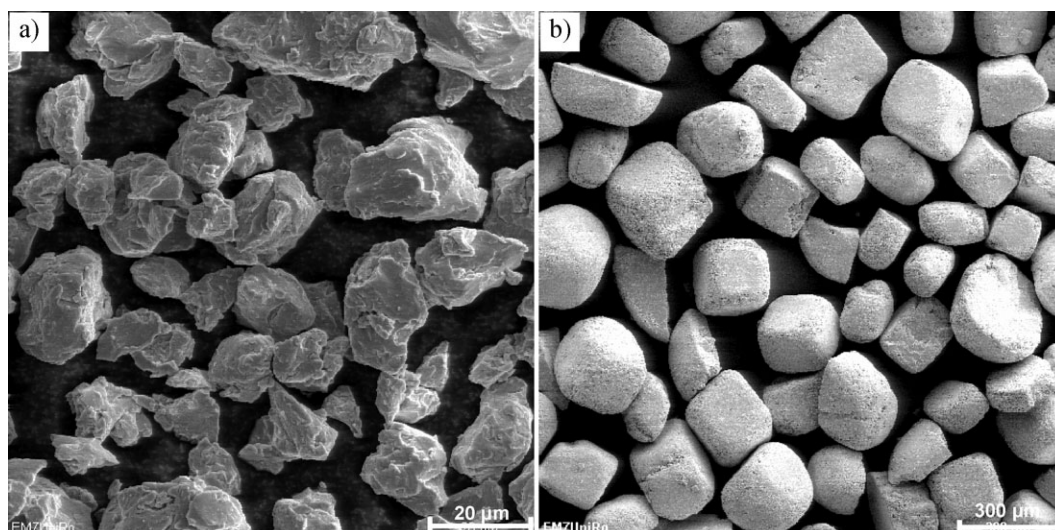


Fig. 1. SEM micrographs of the starting Ti (a) and NaCl (b) powders.

After cleaning and drying, the porous Ti foams were obtained finally [Fig. 2(e)].

The influence of the weight ratio and particle size of NaCl on the porosity and pore size of Ti foams with corresponding SPS parameters is shown in Table 1. The pore sizes of the sintered foams were measured from the SEM images. It shows mean pore sizes about 125 μm in the foams with a NaCl spacing material in the range of 88–149 μm, mean pore size about 250 μm with NaCl of 224–297 μm, 400 μm with NaCl of 388–500 μm sizes, 800 μm with NaCl of 784–1000 μm sizes. After porosity characterization by the Archimedes method, it is noticed that more NaCl particles were needed to obtain the same porosity in the large pore sized foams. To achieve a porosity of 55% in the 125 μm foams, the weight ratio of Ti/NaCl is about 1:1.28. However, the weight ratio of Ti/NaCl is about 1:1.75 in the 800 μm foams for the same porosity. It might be due to the decreased specific surface area in the large sized NaCl particles as spacer materials.

The Ti/NaCl mixtures (Ti/NaCl = 1:1.32) were spark plasma sintered at temperatures of 550–800 °C under a pressure of 30–50 MPa. The exact SPS parameters are shown

in Table 1. The SPSed samples at 750 and 800 °C were failed because of the melting of NaCl particulates resulting in an explanation of the mixture and breakage of the graphite die. The parameters were adjusted, and the Ti foams were prepared by the SPS at conditions of 730 °C for 8 min under 30 MPa. However, the XRD result in Figure 3 shows that there are some rutile TiO₂ phases (PDF#21-1276) and few TiCl₂ phase (PDF#10-0315) in the 730 °C sintered foams. The presences of TiO₂ and TiCl₂ are due to the reaction of the Ti with oxygen and dissociated Cl⁻ in NaCl. It is likely that the temperature at the necks of the Ti particles exceeds 730 °C due to the high local contact resistance. Hence NaCl is able to melt causing contamination of the sample. High purity Ti foams were prepared at 700 °C for 8 min under 50 MPa. The starting Ti powders are in the α-Ti phase with hexagonal structure. The Ti foams remain in the α-Ti phase structure without any impurities when the SPS process temperatures are below 700 °C. There is usually some temperature difference between the mold surface and the actual temperature in the SPS sample. The temperature measurement design in the FCT SPS system allowed a very accurate temperature control since the temperature difference between the center of the sample and the controlling pyrometer was always below 5 °C.^[30] The radial temperature gradient in the electrical conductive samples is about 79 °C around.^[29] The Ti powders are electrical conductive materials. The sintering temperature of 700 °C plus the temperature difference 5 °C and temperature gradient 79 °C was still lower than the melting point of NaCl (801 °C). Thus, high purity Ti foams can be prepared at the SPS temperature of 700 °C.

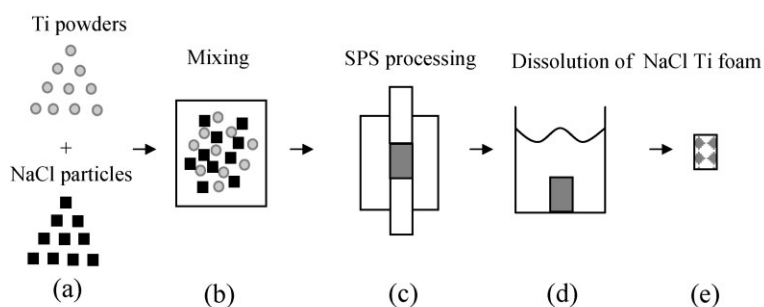


Fig. 2. Schematic illustration of the pore forming process by using the SPS and NaCl dissolution: sieving of the Ti and NaCl powders (a), mixing of the Ti and NaCl powders (b), processing by the SPS (c), dissolution of the NaCl in water (d), obtaining of the Ti foams (e).

Microstructures

The 3D reconstruction by topographical methods is the most realistic way to get space information

Table 1. The influence of the weight ratio and particle size of NaCl on the porosity and pore size of the Ti foams with corresponding SPS parameters.

Ti powder	NaCl powder	Weight ratio (Ti: NaCl)	Porosity	Pore size	SPS parameters (Temperature, dwell time)
10–30 μm	88–149 μm (170–100 mesh)	1:1.28	~55%	~125 μm	700 °C, 8 min
10–30 μm	149–297 μm (100–50 mesh)	1:0.72	~30%	~250 μm	700 °C, 8 min
		1:0.93	~45%	~250 μm	700 °C, 8 min
		1:1.32	~55%	~250 μm	550 °C, 8 min
					600 °C, 8 min
					650 °C, 8 min
					700 °C, 8 min
					730 °C, 8 min
					750 °C, 5 min
					800 °C, 3 min
		1:1.64	~70%	~250 μm	700 °C, 8 min
10–30 μm	354–500 μm (45–35 mesh)	1:1.46	~55%	~400 μm	700 °C, 8 min
10–30 μm	707–1000 μm (25–18 mesh)	1:1.75	~55%	~800 μm	700 °C, 8 min

about the internal structure of the foams in a non-destructive way. The micro-CT 3D reconstructions of the spark plasma sintered Ti foams with 55% porosity and 250 μm pore size are shown in Figure 4. The 3D cropped isometric view of cross sections in the Ti foam shows the uniform pore distribution and interconnected 3D porous structures with a high porosity [Fig. 4(a)]. The micro-CT 2D top view and side views show that the macropore shapes are in square cross sections, uniform distribution of pore sizes and high interconnectivity [Fig. 4(b–d)]. The 3D surface, cell wall thickness, connectivity were examined by the micro-CT in a non-destructive way. The 3D cropped internal surface exhibits highly porous structures and interconnectivity with pore size of $243 \pm 50 \mu\text{m}$ and cell wall average thickness $20.4 \mu\text{m}$.

The SEM micrographs of the Ti foams with the same porosity of 55% but different pore sizes of 125, 250, 400, and 800 μm is shown Figure 5. All the foams from 125 to 800 μm exhibit highly interconnected porous structures

and uniform pore distribution. It is found that the pores have irregular quadrate cross sections. They are similar to those of the initial NaCl particles of cuboid shapes in Figure 1(b).

Figure 6 shows the SEM micrographs of the porous Ti foams with the same pore size of 250 μm but different porosity of 30, 45, 55 and 70%. The thickness of the pore walls in the 30% porosity foams is about 100 μm, decreasing to 50 μm in 45% porosity foams, and to 20 μm in 55%, finally ending at 10 μm in 70% porosity foams. The interconnectivity was also enhanced with the increase in porosity. The 30 and 45% porosity foams show poor interconnectivity because of the lower porosity [Fig. 6(a and b)]. But the 55 and 70% higher porosity samples showed good interconnectivity [Fig. 6(c and d)]. The macropores are in square cross sections in all the Ti foams with different porosities.

Figure 7 shows the SEM microstructures of the polished cross-section, pore edge, and pore wall of the Ti foams, and EDX analysis on the pore matrix. Few micropores ranged 1–2 μm were detected in the SEM micrograph of the polished cross-section of the Ti foam [Fig. 7(a)]. It is indicated that the Ti foams have been densified after SPS at 700 °C for 8 min under 50 MPa. When polishing porous metals, the pores have to be filled with resin. This prevents release of particles, which cause the rough finish seen in the Figure 7(a). Furthermore it prevents the smaller pores from being filled with debris. The typical pore edge and wall of the Ti foams are shown in Figure 7(b and c). The grain sizes of the Ti foams still range about 10–30 μm without rapid grain growth due to the rapid sintering of SPS. There are some micropores smaller than 10 μm on the pore walls. The micropores could allow body fluid circulation whereas the macropores may provide a scaffold for bone–cell colonization. The surfaces of the pore walls of the macropores of the porous Ti are relatively rough. The EDX analysis shows that the matrix of the pore wall contains only Ti elements

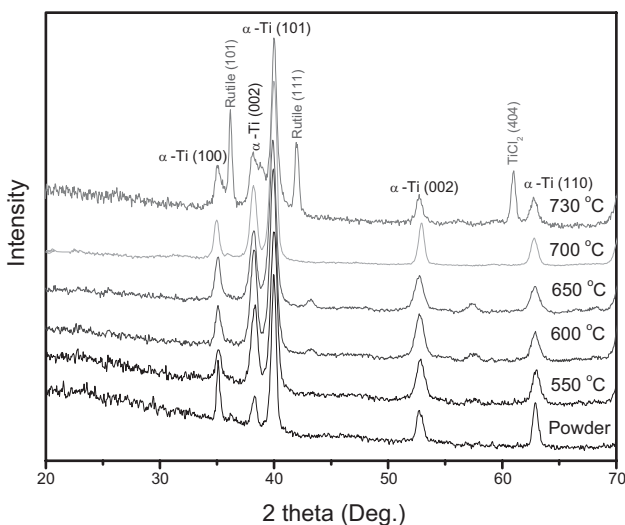


Fig. 3. XRD patterns of the raw Ti powder and Ti foams processed by SPS at 550, 600, 650, 700, and 730 °C.

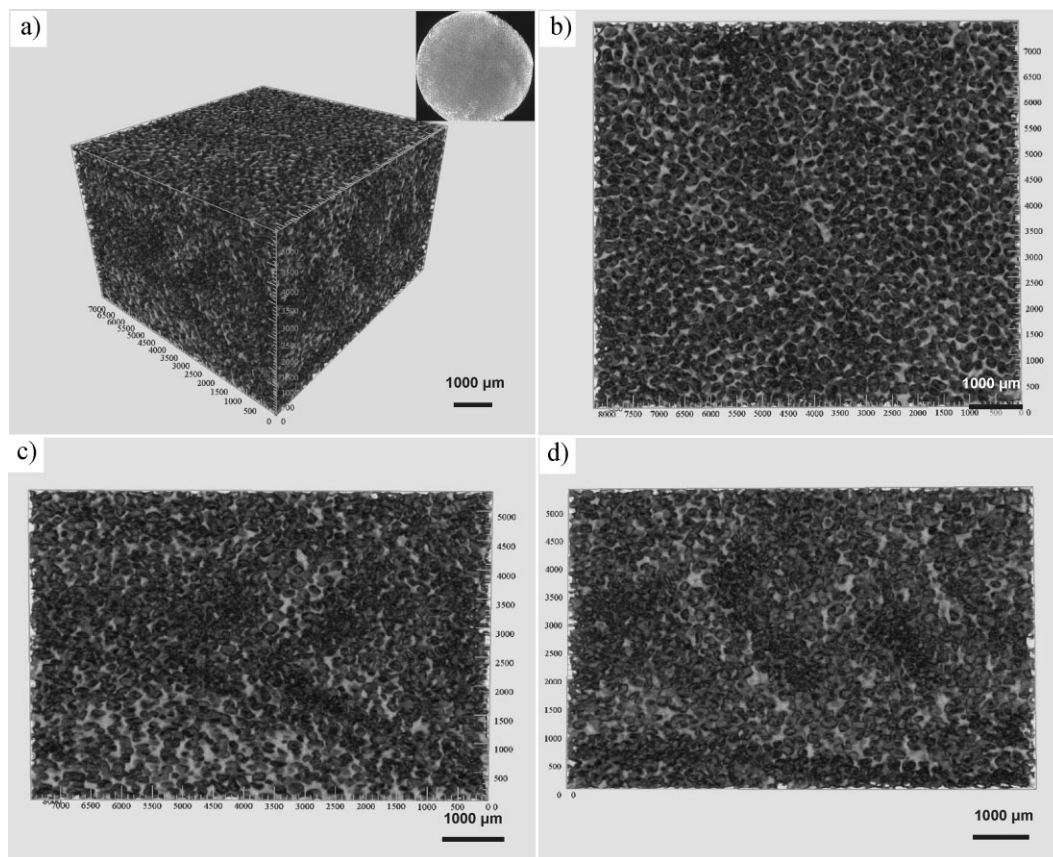


Fig. 4. Micro-CT 3D reconstructions of the Ti foam (250 μm of pore size, 55% of porosity) exhibiting the isometric view of cross sections with a sample navigation (top-right corner) (a), 2D top view (b), left side view (c), and right side view (d).

without O element [Fig. 7(d)]. The chemical analysis by inert gas fusion technique shows that the final C contents in these SPSed Ti foams are 0.08 ± 0.02 wt%, and O contents are 0.29 ± 0.04 wt%. It is between the Grade 2 (C: 0.10 wt%, O: 0.25 wt%) and Grade 3 (C: 0.10 wt%, O: 0.35 wt%) Ti. They are accordingly to the XRD results in Figure 3 that high purity Ti foams were prepared by SPS at 700 °C.

Mechanical Properties

Figure 8 shows the effect of pore size and porosity on the plateau stress and Young's modulus of the porous Ti foams. The measured plateau stress and Young's modulus of the Ti foams were compared with the theoretical values that calculated from Gibson–Ashby model. According to the Gibson–Ashby model, the relationship between the relative plateau stress and relative density is given by^[31]:

$$\frac{\sigma}{\sigma_0} = C \left(\frac{\rho}{\rho_0} \right)^{3/2} \quad (1)$$

where σ is the plateau stress of the foams, σ_0 the yield stress of the dense material; C the constant 0.3 from the data of cellular metals and polymers, ρ is the density of the foams, ρ_0 is the density of the dense material. The density of the pure Ti

is 4.5 g cm^{-3} with yield stress of 692 MPa.^[31,32] The density of the Ti foam with 55% porosity and 250 μm pore size is 1.69 g cm^{-3} . Substituting these values in Equation (1), the theoretical value was calculated to be 47.78 MPa, which is comparable to the measured plateau stress 45.1 ± 3.0 MPa. According to the Gibson–Ashby model, the relationship between the relative Young's modulus and relative density is given by^[31]:

$$\frac{E}{E_0} = A \left(\frac{\rho}{\rho_0} \right)^2 \quad (2)$$

where E is the Young's modulus of the foams, E_0 the Young's modulus of the dense materials, A the constant of one including data of metals, rigid polymers, elastomers, and glasses. The Young's modulus of the pure Ti is 105 GPa according to the Equation (2).^[31,32] The measured Young's modulus of the above Ti foams with 55% porosity is 13.46 ± 1.4 GPa. Substituting the values into Equation (2), it is calculated that the theoretical value is 14.81 GPa which is also comparable to the measured one. All the Ti foams prepared by the SPS were measured and calculated. As seen from the Figure 8, it can be deduced that all the experimental data agrees with the Gibson–Ashby model (1) and (2) in the present study. The relationship between the pore sizes and the mechanical properties of the

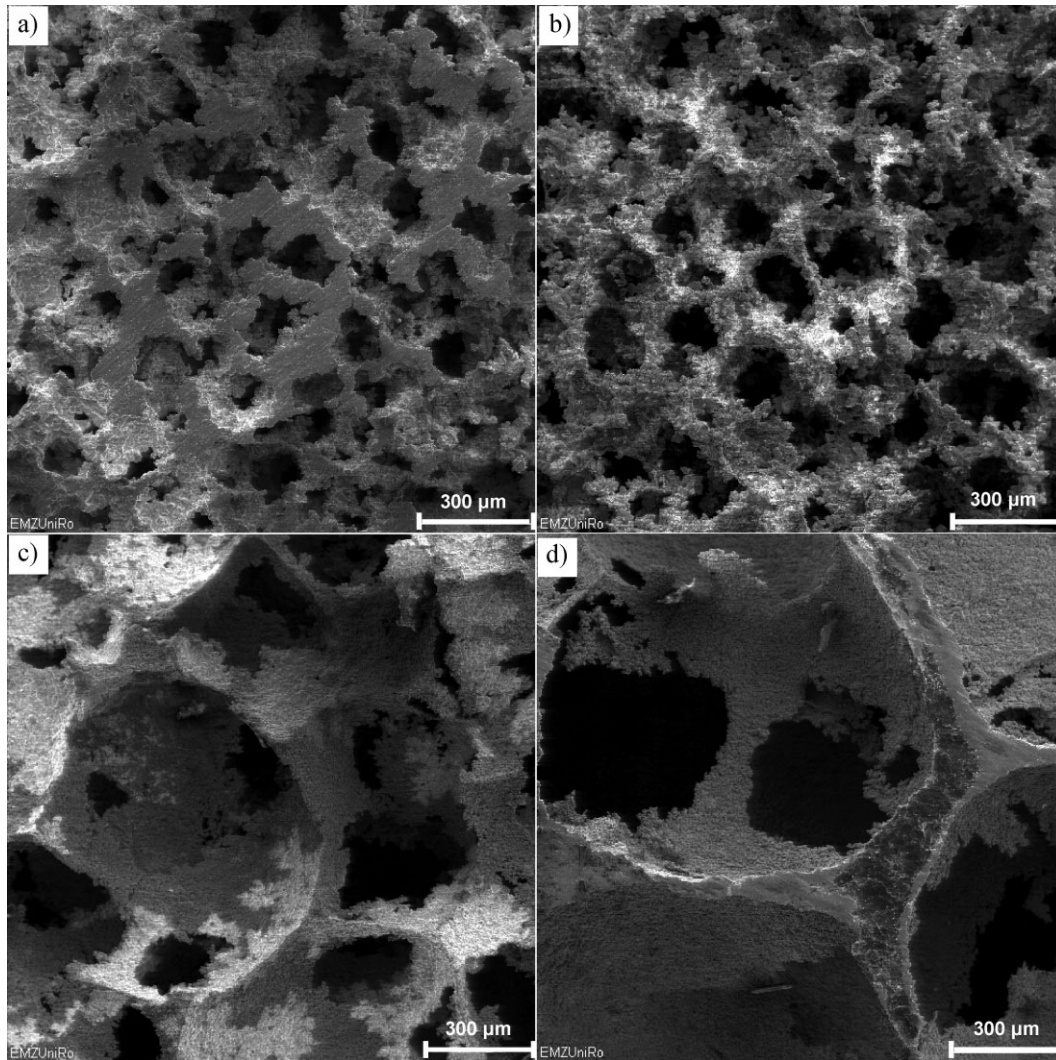


Fig. 5. SEM micrographs of the Ti foam surfaces with the same porosity of 55% but different pore sizes of 125 (a), 250 (b), 400 (c), and 800 μm (d).

Ti foams is shown in Figure 8(a and b). The plateau stress decreased from 49.7 ± 3.8 to 27.2 ± 3.0 MPa with the pore size increase [Fig. 8(a)]. The Young's modulus reduced from 18.3 ± 2.0 to 8.9 ± 1.5 GPa with the pore size increase [Fig. 8(b)]. It coarsely obeys a linear decay with the pore size increase. The effect of the porosity on the mechanical properties of the Ti foams is shown in Figure 8(c and d). The plateau stress decreased from 94.2 ± 5.9 to 28.8 ± 3.3 MPa, and the Young's modulus decreased from 36.1 ± 3.5 to 6.2 ± 1.8 GPa with porosity increase. It generally obeys the rule of exponential decline with the porosity increase.

The plateau stress and Young's modulus coarsely obey linear declines with the pore size increase and exponential decline with the porosity increase. Liu^[33] found that the plateau stress of the porous hydroxylapatite ceramics decreases linearly with increasing macropore size for a given total porosity. In this study, we found the plateau stress and Young's modulus coarsely obey linear declines

with the pore size increase [Fig. 8(a and b)]. Rice RW^[34] has proposed a function on the relationship of porosity with strength of porous solids,

$$\sigma = \sigma_0 \exp(-cp) \quad (3)$$

where σ_0 is zero-porosity strength, σ the strength at pore volume fraction p , and the constant c is related directly to the pore characteristics such as pore shape and size. In this study, we used the same Ti powder and NaCl spacer material; therefore, σ_0 and c can be considered as constant. According to the above function, the strength (σ) should decrease exponentially as the pore volume fraction (p) increases. Our results in Figure 8(c and d) are well in accordance with the above function.

It is reported that powder sintered pure Ti foams with porosity of 55–75% showed plateau stress and Young's modulus are in the range of 10–35 MPa and 3–6.4 GPa.^[35] Plateau stresses of 30–65 MPa and Young's modulus of 1.2–2.8 GPa were reported for commercial Ti foams

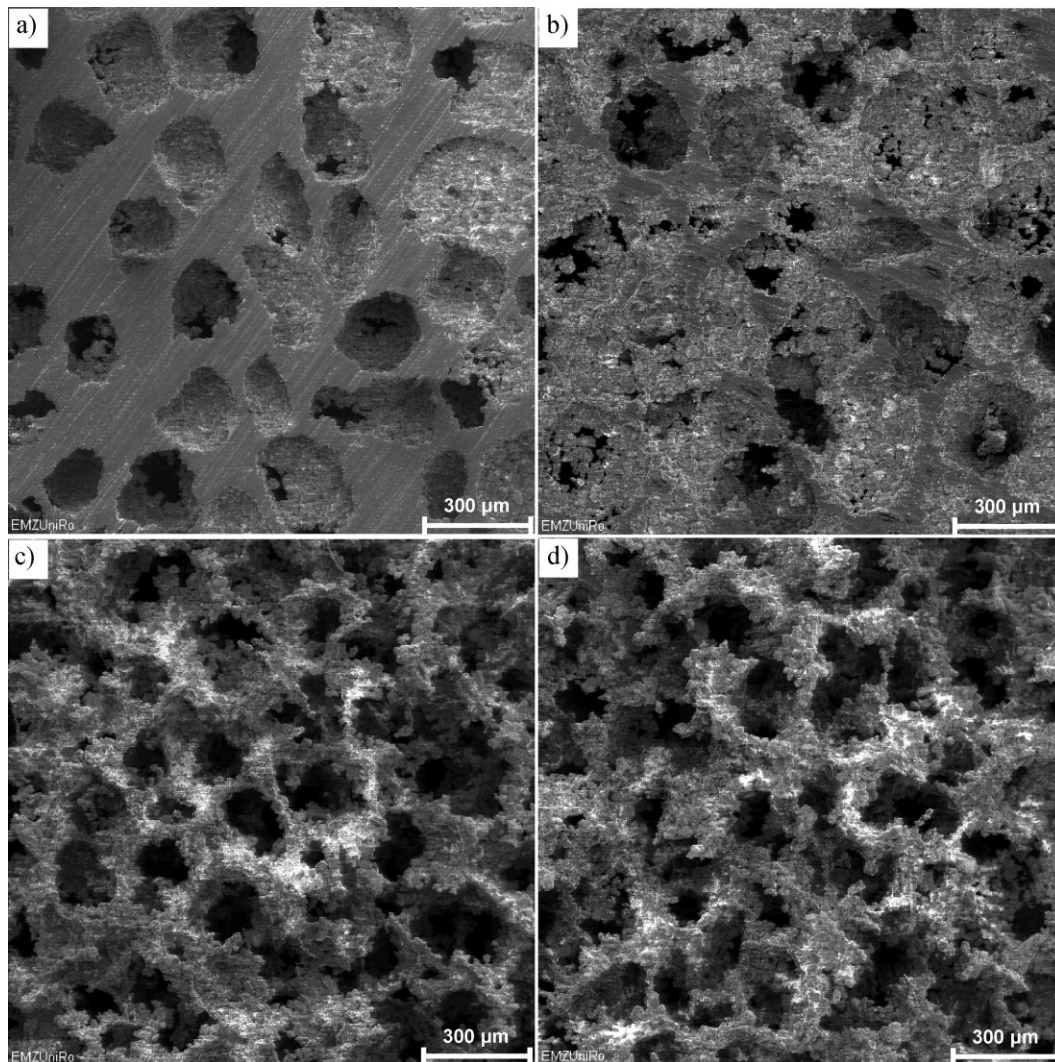


Fig. 6. SEM micrographs of the Ti foam surfaces with the same pore size of 250 μm but different porosities of 30% (a), 45% (b), 55% (c), and 70% (d).

with 70–80% porosity produced by a solid sacrificial template.^[36] Ti foams prepared by slip casting of particle stabilized emulsions showed yielding strengths of 141 ± 5.7 and 121 ± 5.4 MPa for samples with a porosity of 56.1 and 65.2%.^[37] In this study, the 250 μm pore sized Ti foams with 55% porosity shows plateau stress of 45.1 ± 3.0 MPa and Young's modulus of 13.46 ± 1.4 GPa. The same pore sized Ti foams with 70% porosity exhibit plateau strength of 28.8 ± 3.3 MPa and Young's modulus of 6.15 ± 1.5 GPa. The results are comparable to the reported values of the samples that prepared by powder sintered and solid sacrificial template foams, but lower than those of the slip casting of particle stabilized emulsions. The Ti powders used in this study are coarse particles in the range of 10–30 μm . The sintering activity and density could be enhanced by ball milling of the raw Ti powders. It is believed that pure Ti foams with higher mechanical properties can be prepared by using the ball milling, SPS, and NaCl dissolution methods. Additionally, the phase

structure in these Ti foams is the low temperature α -Ti phase but not the high temperature β -Ti phase because of the lower SPS temperature of 700 $^{\circ}\text{C}$. The β -Ti phase has a cubic body centered crystalline structure, while the α -Ti phase has a hexagonal crystalline structure which provides β -alloys with an improved notched fatigue resistance and a superior resistance to wear and abrasion.^[38] The doping of β phase stabilized elements in Ti, for example Fe, V, Ta, Nb, Mn, Mo, Ni, Cr, Cu, etc. could decrease the phase transformation temperature from α to β phase to below 700 $^{\circ}\text{C}$.^[39] It can be predicted that β -Ti alloy foams with much higher mechanical properties could be produced by using the SPS and NaCl dissolution methods.

Implants sometimes were used to substitute bone defects in tumor or spine surgery. Porous Ti foam with its osteoconductive properties is an ideal alternative bone graft. The porous structure with pore sizes of 200–500 μm of the Ti foams may be able to permit bone cell penetration and tissue integration. The plateau stress of the human vertebral bone

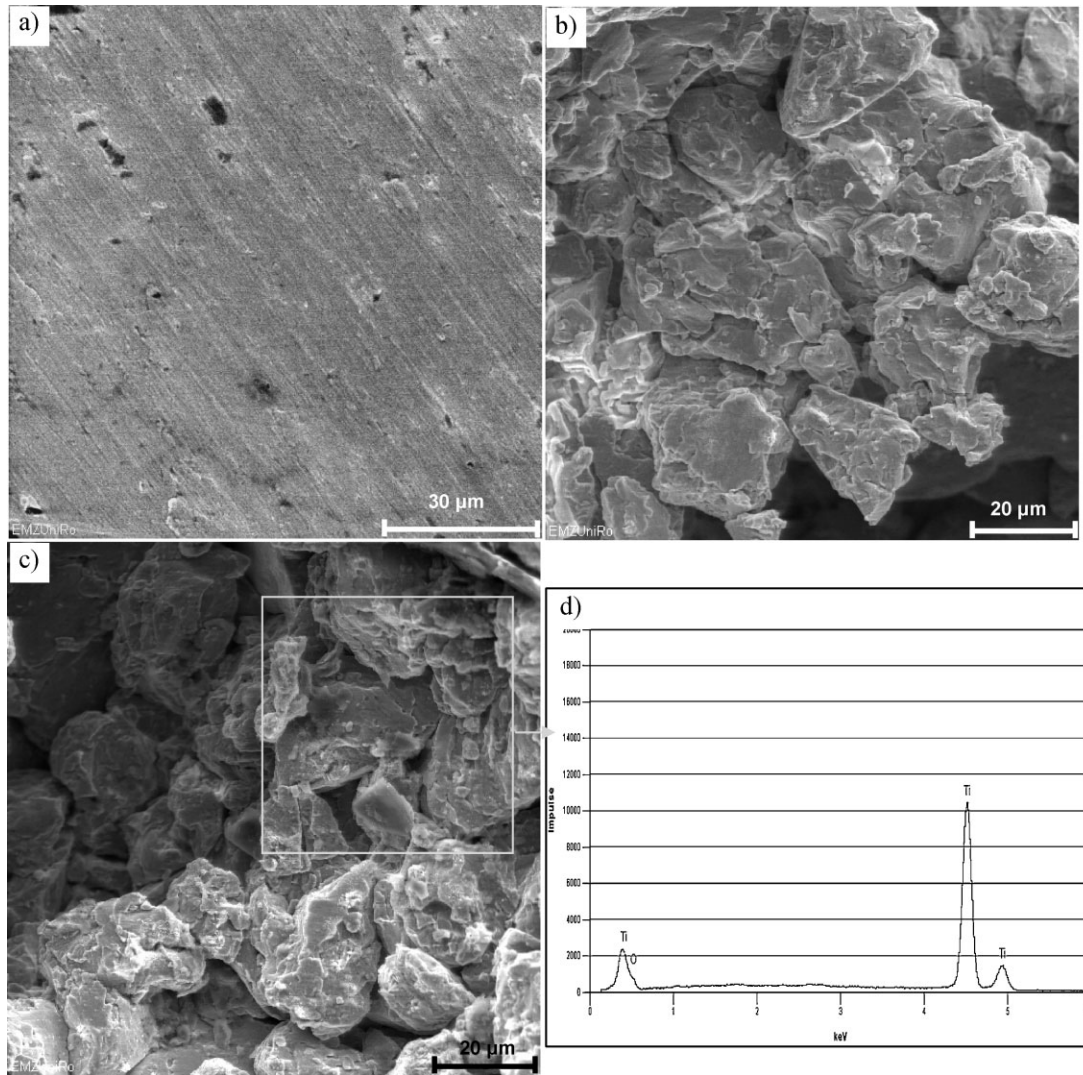


Fig. 7. SEM micrographs of the microstructure of the polished cross-section (a), pore edge (b), and pore wall (c) of the Ti foams, and EDX analysis on the pore matrix (d).

(load-bearing site) ranges from 24 to 43 MPa, and femoral cancellous bone (load-bearing site) is in the range of 48–80 MPa.^[40] The average Young's modulus of compact bone of human ranges 7–30 GPa.^[40] The plateau stress of the presented Ti foams in the range of 27.2–94.2 MPa is comparable to that of the cancellous bone which is enough for biomedical applications. For biomedical applications, the main problem of Ti and Ti alloys in clinical view is their high Young's modulus. Stress shielding is known to lead to bone resumption and eventual loosening of the implant.^[41] The dense Ti generally showed much higher Young's modulus (70–120 GPa) than that of human bone. Thus, the porous structures were incorporated in the Ti and Ti alloys. In this study, the porous Ti foams show lower Young's modulus values (6.2–36.1 GPa) than that of dense ones which are comparable to those of natural compact bone (7–30 GPa). The macroporous Ti foams with plateau stress 27.2–94.2 MPa and Young's modulus 6.2–36.1 GPa have a potential to be used as bone implants. The low Young's modulus of Ti foams is

desirable to reduce the amount of stress shielding of the bone into which the foam is implanted. Combining the good biocompatibility of the pure Ti and the high interconnected porous structure, the Ti foams achieved by the SPS and NaCl dissolution methods with mechanical properties comparable to those of human bone makes these materials to be ideal bone implant foams.

In summary, macroporous pure Ti foams with porosities of 30–70% and pore sizes of 125–800 μm were prepared by using SPS and NaCl dissolution methods for bone implant applications. The Ti foams prepared by SPS at 700 °C for 8 min under 50 MPa showed pure α-Ti phase structure. The Ti foams consist of interconnected macropores with square cross sections. The plateau stress and Young's modulus agree with the Gibson–Ashby models, and coarsely obey linear declines with the pore size increase and exponential decays with the increase of porosity. The Ti foams processed by SPS and NaCl dissolution methods showed mechanical properties within those of human bone range.

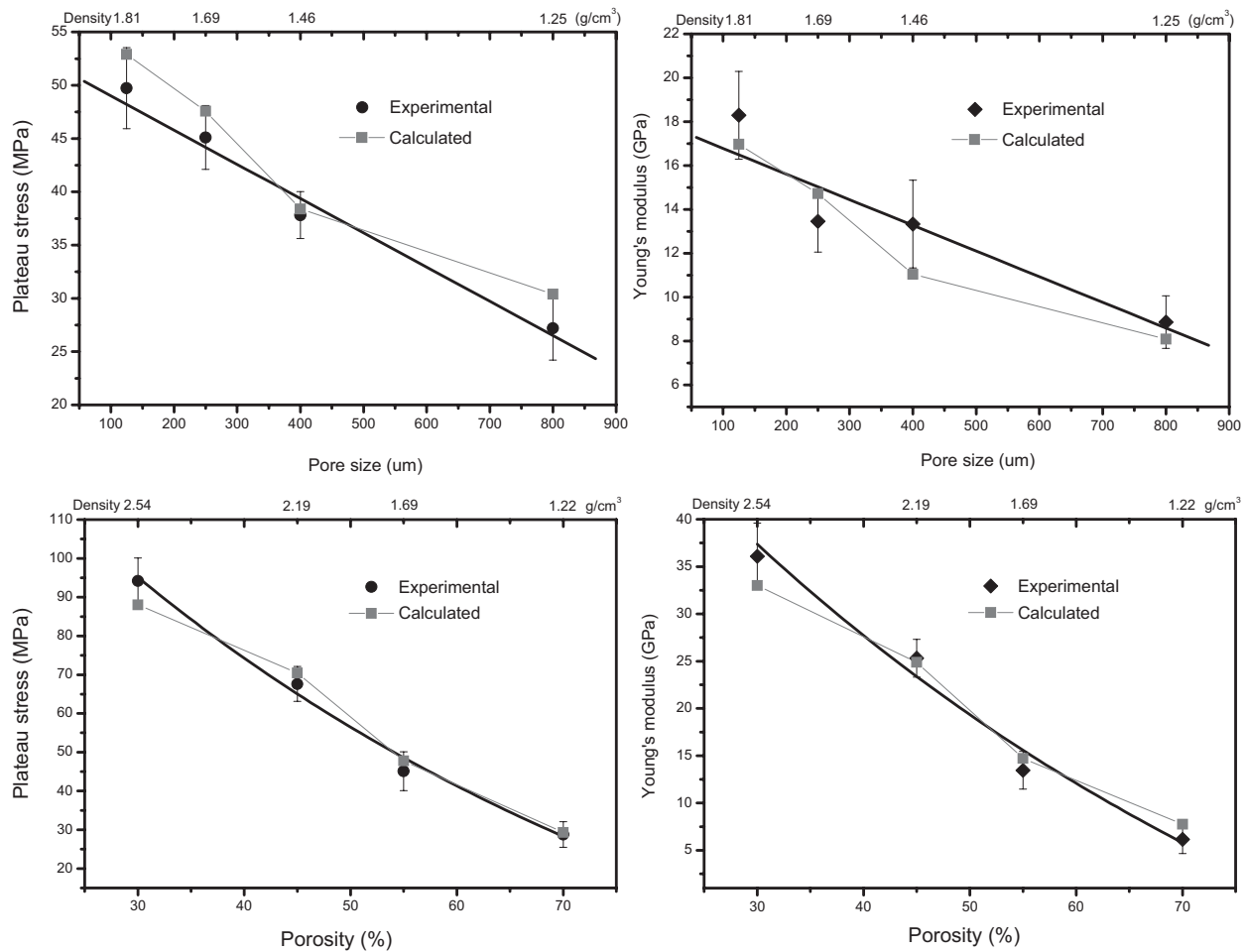


Fig. 8. The effects of pore sizes (a, b) and porosities (c, d) on the plateau stress and Young's modulus of the Ti foams.

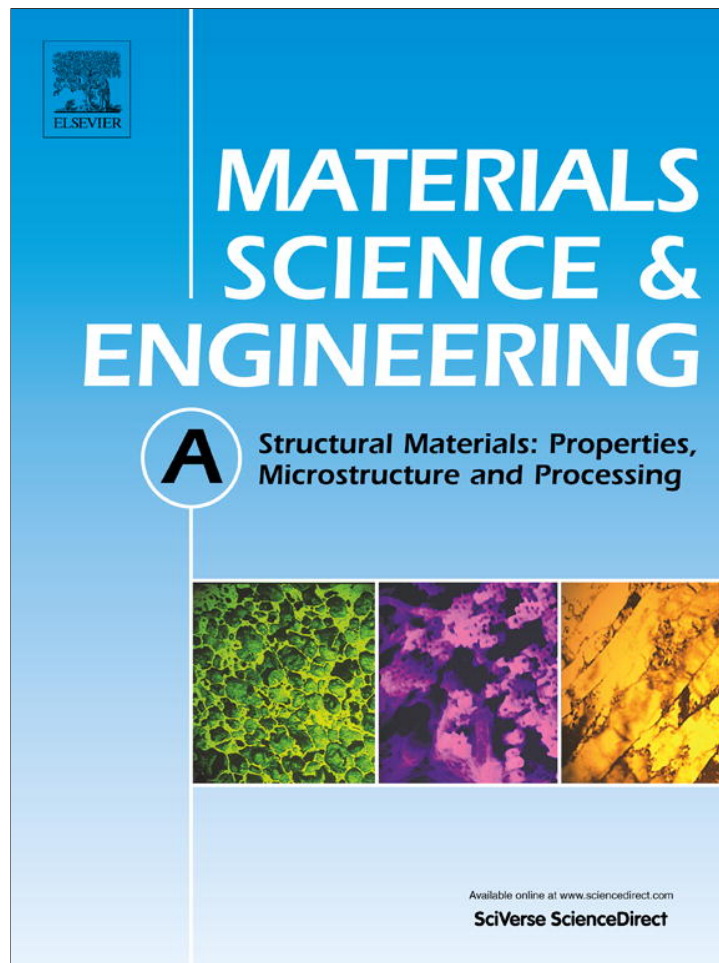
Received: March 4, 2010
Final Version: May 19, 2010

[1] A. G. Evans, J. W. Hutchinson, M. F. Ashby, *Prog. Mater. Sci.* **1999**, 3, 171.
 [2] E. Solórzano, M. A. Rodríguez-Perez, J. A. de Saja, *Adv. Eng. Mater.* **2008**, 6, 596.
 [3] J. Banhart, *Prog. Mater. Sci.* **2001**, 46, 559.
 [4] J. P. Li, S. H. Li, C. A. Van Blitterswijk, K. de Groot, *J. Biomed. Mater. Res. A* **2005**, 73, 223.
 [5] D. C. Dunand, *Adv. Eng. Mater.* **2004**, 6, 369.
 [6] E. R. Garrett, S. P. Abhay, P. A. Dimitrios, *Biomaterials* **2008**, 27, 3625.
 [7] Y. Chino, D. C. Dunand, *Acta Mater.* **2008**, 1, 105.
 [8] Y. He, Y. Jiang, N. Xu, J. Zou, B. Huang, C. T. Liu, P. K. Liaw, *Adv. Mater.* **2007**, 19, 2102.
 [9] B. Neirinck, T. Mattheys, A. Braern, J. Fransae, O. V. der Biest, J. Vleugels, *Adv. Eng. Mater.* **2009**, 8, 633.
 [10] Y. B. An, N. H. Oh, Y. W. Chun, Y. H. Kim, J. S. Park, K. O. Choi, T. G. Eom, *Scr. Mater.* **2005**, 53, 905.

[11] R. Brindle, J. Eisenhauer, J. Rash, *PM² Industry vision and Technology Roadmap*. U.S. Department of Energy, Office of Industrial Technologies. **2001**, 9, 29.
 [12] Z. A. Munir, U. Anselmi-Tamburini, *J. Mater. Sci.* **2006**, 41, 763.
 [13] S. Grasso, Y. Sakka, G. Maizza, *Sci. Technol. Adv. Mater.* **2009**, 10, 053001.
 [14] M. Kon, L. M. Hirakata, K. Asaoka, *J. Biomed. Mater. Res. B* **2004**, 68, 88.
 [15] Y. Sakamoto, K. Asaoka, M. Kon, T. Matsubara, K. Yoshida, *Bio-Med. Mater. Eng.* **2006**, 2, 83.
 [16] R. Nicula, R. Lüthen, M. Stir, B. Nebe, E. Burkel, *Biomolec. Eng.* **2007**, 24, 564.
 [17] I. H. Oh, H. T. Son, C. S. Kang, J. S. Lee, J. I. Cho, J. C. Bae, B. T. Lee, H. Y. Song, *Mater. Forum* **2007**, 539–543, 635.
 [18] T. Chandra, J. M. Torralba, T. Sakai, *Mater. Forum* **2003**, 426–424, 3079.
 [19] M. Zadra, F. Casari, L. Girardini, A. Molinari, *Powder Metall.* **2008**, 51, 59.
 [20] F. Zhang, J. Chang, K. Lin, J. Lu, *J. Mater. Sci. : Mater. Med.* **2008**, 19, 167.
 [21] F. Zhang, K. Lin, J. Chang, J. Lu, C. Ning, *J. Euro. Ceram. Soc.* **2008**, 3, 539.

- [22] C. E. Wen, Y. Yamada, K. Shimojima, Y. Chino, H. Hosokawa, M. Mabuchi, *J. Mater. Res.* **2002**, *17*, 2633.
- [23] Y. Conde, J. F. Despois, R. Goodall, A. Marmottant, L. Salvo, C. S. Marchi, A. Mortensen, *Adv. Eng. Mater.* **2006**, *9*, 795.
- [24] A. Bansiddhi, D. C. Dunand, *Acta Biomater.* **2008**, *4*, 1996.
- [25] X. Zhao, H. Sun, L. Lan, J. Huang, H. Zhang, Y. Wang, *Mater. Lett.* **2009**, *28*, 2402.
- [26] C. E. Wen, M. Mabuchi, Y. Yamada, K. Shimojima, Y. Chino, H. Hosokawa, T. Asahina, *J. Mater. Sci. Lett.* **2003**, *20*, 1407.
- [27] M. Hakamada, Y. Yamada, T. Nomura, Y. Chen, H. Kusuda, M. Mabuchi, *Mater. Trans.* **2005**, *12*, 2624.
- [28] M. Hakamada, Y. Yamada, T. Nomura, Y. Chen, H. Kusuda, M. Mabuchi, *Appl. Phys. Lett.* **2006**, *88*, 254106.
- [29] K. Vanmeensel, A. Laptev, O. Van der Biest, J. Vleugels, *J. Euro. Ceram. Soc.* **2007**, *55*, 979.
- [30] K. Vanmeensel, A. Laptev, J. Hennicke, J. Vleugels, O. Van der Biest, *Acta Mater.* **2005**, *53*, 4379.
- [31] C. E. Wen, Y. Yamada, K. Shimojima, Y. Chino, T. Asahina, M. Mabuchi, *J. Mater. Sci.: Mater. Med.* **2002**, *13*, 397.
- [32] M. Long, H. J. Rack, *Biomaterials* **1998**, *19*, 1621.
- [33] D. M. Liu, *Ceram. Inter.* **1997**, *23*, 135.
- [34] R. W. Rice, *J. Mater. Sci.* **1993**, *8*, 2187.
- [35] W. Niu, C. Bai, G. Qiu, Q. Wang, *Mater. Sci. Eng. A* **2009**, *506*, 148.
- [36] A. Schuh, J. L. R. Vidael, W. Hoenle, T. Schmichal, *Materialwiss. Werkst.* **2007**, *12*, 1015.
- [37] B. Neirinck, T. Mattheys, A. Braem, J. Fransaer, O. Van der Biest, J. Vleugels, *Adv. Eng. Mater.* **2009**, *11*, 63.
- [38] E. Eisenbarth, D. Velten, M. Mueller, R. Thull, J. Breme, *Biomaterials* **2004**, *25*, 5705.
- [39] F. Zhang, A. Weidmann, J. B. Nebe, U. Beck, E. Burkel, *J. Biomed. Mater. Res.* **2010**, *94B*, 406.
- [40] F. Zhang, J. Chang, J. Lu, K. Lin, C. Ning, *Acta Biomaterialia* **2007**, *6*, 896.
- [41] M. Geetha, A. K. Singh, R. Asokamani, A. K. Gogia, *Prog. Mater. Sci.* **2009**, *3*, 397.

Provided for non-commercial research and education use.
Not for reproduction, distribution or commercial use.



(This is a sample cover image for this issue. The actual cover is not yet available at this time.)

This article appeared in a journal published by Elsevier. The attached copy is furnished to the author for internal non-commercial research and education use, including for instruction at the authors institution and sharing with colleagues.

Other uses, including reproduction and distribution, or selling or licensing copies, or posting to personal, institutional or third party websites are prohibited.

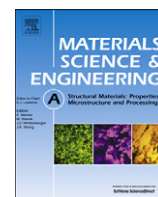
In most cases authors are permitted to post their version of the article (e.g. in Word or Tex form) to their personal website or institutional repository. Authors requiring further information regarding Elsevier's archiving and manuscript policies are encouraged to visit:

<http://www.elsevier.com/copyright>



Contents lists available at SciVerse ScienceDirect

Materials Science & Engineering A

journal homepage: www.elsevier.com/locate/mseaTi₆Al₄V foams fabricated by spark plasma sintering with post-heat treatmentYujie Quan^a, Faming Zhang^{a,*}, Henrike Rebl^b, Barbara Nebe^b, Olaf Keßler^c, Eberhard Burkel^a^a Institute of Physics, University of Rostock, Rostock 18055, Germany^b Department of Cell Biology, Biomedical Research Centre, University of Rostock, Rostock 18057, Germany^c Chair of Materials Science, Faculty of Mechanical Engineering and Marine Technology, University of Rostock, Rostock 18051, Germany

ARTICLE INFO

Article history:

Received 16 August 2012

Received in revised form

19 November 2012

Accepted 10 December 2012

Available online 20 December 2012

Keywords:

Metallic foams

Titanium alloys

Sodium chloride

Spark plasma sintering

Heat treatment

ABSTRACT

Ti₆Al₄V foams were fabricated by the spark plasma sintering (SPS) with post-heat treatment using a blend of Ti₆Al₄V and sodium chloride powders. The microstructure and properties of the foams were investigated by scanning electron microscopy, X-ray micro-CT, Synchrotron X-ray, compression test and cell experiments. Results showed that the Ti₆Al₄V foams fabricated at 700 °C and 50 MPa in the SPS cannot get high relative densities. These sintered foams were post-heat treated in a pressureless mode of the SPS at 1100 °C for 5 min. This heat treatment is very effective to reduce the microporosity and to densify the foam walls. Young's modulus of the foams was in the range of 33.0–9.5 GPa and yield strength ranged from 110.2 MPa to 43.0 MPa with porosity values from 44.7% to 70.0% obeying the Gibson–Ashby models. The human osteoblast cell line MG-63 validated the cellular acceptance of the foam surfaces. The pressureless SPS provides a new method for the heat treatment of metallic foams.

© 2012 Elsevier B.V. All rights reserved.

1. Introduction

The Ti₆Al₄V alloys were introduced in 1954 by adding 4% vanadium to titanium to stabilize its α phase and 6% aluminum to stabilize its β phase. Ti₆Al₄V alloys have interesting mechanical properties, as well as inherent biocompatibility and corrosion resistance due to its native oxide layer [1,2]. However, the mismatches of Young's moduli of the human bones and the implants lead to stress shielding effects responsible for bone resorption and eventual loosening of implants. Porous structures are expected to provide a better interaction with the bones. This is partly due to increased bone growth through the porous surface into the implant material and increased body fluid transport through three-dimensional interconnected array of pores, leading to improved implant fixation [3]. In addition, a lower Young's moduli of porous metals than those of dense metals are expected to reduce the extent of stress shielding and, hence, to prolong implant's life-time [3,4].

However, the fabrication of porous Ti alloy with standard techniques is difficult due to the high melting point and the extreme chemical affinity to atmospheric gases like oxygen, hydrogen, and nitrogen, especially at elevated temperatures. Currently, the fabrication of porous Ti alloy is mainly focused on powder metallurgy approaches [5–11]. The use of space holder materials allows a simple and accurate control of pore fraction, shape and connectivity in titanium alloys. Sodium chloride (NaCl) is a suitable space holder material because of its high solubility in

water (359 g/L at room temperature), its complete inertness to titanium alloy, and its low toxicity [12]. This method provides foam structures close to homogenous pore structures and high levels of porosities (60–80%). Open-celled pure titanium foams were fabricated by vacuum hot pressing of a blend of Ti and NaCl powders followed by NaCl removal in water [13]. However, the Ti₆Al₄V/NaCl mixture is difficult to be densified by the hot pressing due to higher creep resistance of this alloy at 790 °C [13]. Promising approach to produce Ti alloys is the spark plasma sintering (SPS) process [14–16]. The SPS can easily sinter Ti and Ti alloy powders applying pressure and high pulsed DC currents. Thus the local surfaces of the particles melt, allowing junctions to be formed between particles in contact. Recently a combination of the SPS technique with a NaCl space holder was used in porous pure Ti to fabricate macroporous Ti foams with controlled architectures [15]. This indicated that the SPS may be able to fabricate Ti₆Al₄V foams from Ti₆Al₄V/NaCl powder mixture. The present work focuses on the preparation of Ti₆Al₄V foams by the SPS with post-heat treatment using NaCl space holder. The microstructures of the fabricated foams are investigated by scanning electron microscopy, X-ray micro-CT, X-ray diffraction. Their Young's moduli and yield strengths are examined by compression tests. The human osteoblast cell line MG-63 was used to evaluate the cellular acceptance of the foam surfaces.

2. Experimental procedures

As a basis of the powder mixtures, Ti₆Al₄V powder with particle sizes of 5–35 μm and chemical purity of 99.0% (TLS

* Corresponding author. Tel.: +49 381 4986864; fax: +49 381 4986862.
E-mail address: faming.zhang@uni-rostock.de (F. Zhang).

Technik GmbH & Co, Germany) was blended with 99.0% pure NaCl powders of grain sizes between 125 μm and 250 μm with poly (vinyl alcohol) as a binder.

The SPS experiments were performed using the SPS system (FCT system GmbH, Rauenstein, Germany) installed at the Tycho Sinter Lab in the University of Rostock. All blends were SPS treated under vacuum in cylindrical graphite dies. After heating the samples with a rate of 100 $^{\circ}\text{C}/\text{min}$ up to 700 $^{\circ}\text{C}$, a pressure of 50 MPa was applied for 8 min to get disc-shaped pellets (20 mm diameter, thickness 5–7 mm). Porous $\text{Ti}_6\text{Al}_4\text{V}$ foams were obtained through dissolution of the NaCl phase in renewed deionized water for 72 h at room temperature. The alloy foams

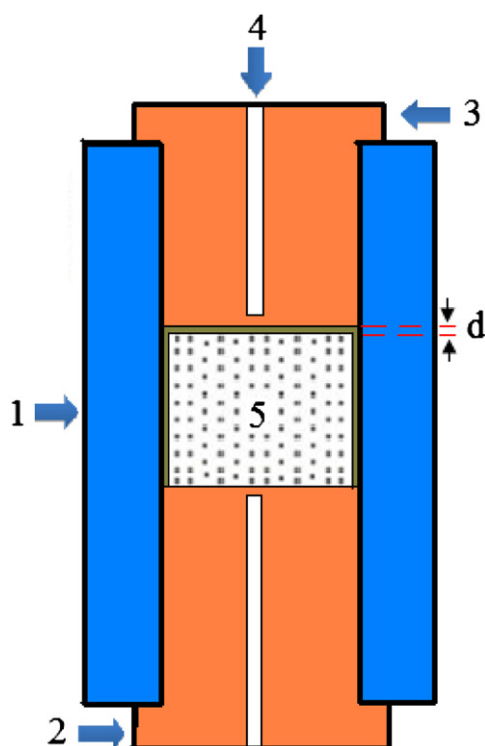


Fig. 1. Schematic diagram of the graphite die set-up for the pressureless mode of the SPS (1. graphite form, 2. graphite bottom punch, 3. graphite top punch, 4. Pyrometer measurement hole, 5. sample, d , gap ≥ 0 mm).

were cleaned in an ultrasonic water bath for 30 min and furnace dried at 120 $^{\circ}\text{C}$ for 12 h. By changing the weight ratio of NaCl, a series of samples with different porosities were obtained. In addition, a SPS post-heat treatment was used to increase the density and strength of the foams. It was carried out by a pressureless mode of the SPS [17,18]. The setup of the pressureless SPS is shown in Fig. 1. A small gap d greater than or equal to 0 mm was designed to avoid damage to the porous materials. After removing NaCl the foams were spark plasma sintered at 1100 $^{\circ}\text{C}$ for 5 min in this pressureless mode.

The density of the samples was measured by the Archimedes method in water. The mass of the samples was measured on a balance. The sample was attached to a thread and fully immersed in a small beaker with water, without touching the bottom of the beaker. The weight of the sample in water was measured, whereby the loss of weight of the sample when suspended in water is equal to the mass of fluid displaced, from which its volume and hence density can be calculated. The microstructures of the porous $\text{Ti}_6\text{Al}_4\text{V}$ were analyzed by using a scanning electron microscope (Zeiss Supra 25, Germany). The pore structure of the sample was analyzed with an X-ray micro-CT (GE, USA). The specimens were mounted on a rotary stage and scanned over the whole volume, being rotated by 360 $^{\circ}$ in 1400 equiangular steps (4 pics per 1 $^{\circ}$). The detector size is 2284 pixel in x and y and 2304 pixel in the z direction. The voxel size of the images is 10.2 μm in all three axes. The phase composition was analyzed using high energy synchrotron radiation (42.58 keV) at Beamline P02.2 (Petra III/Desy). Mechanical tests were conducted by uniaxial compression experiments at room temperature. The standard specimens were 20 mm in diameter and height. The stress measurements were carried out on a universal testing machine Instron 8520, equipped with a 250 kN load cell at 0.5 mm/min. The strain was measured with the travel distance of the testing machine. The compressive yield strength was determined from the stress–strain curve according to the 0.2% offset method [19].

The human osteoblast-like cell line MG-63 (ATCC, CRL-1427, LGC Promochem, Wesel, Germany) was used for the evaluation of the cellular acceptance of the surfaces [20]. In general, the cells were cultured in Dulbecco's modified Eagle's medium (DMEM) with 10% fetal calf serum (FCS, PAA), and 1% gentamicin (Ratiopharm GmbH, Ulm, Germany) at 37 $^{\circ}\text{C}$ in a humidified atmosphere with 5% CO_2 . For cell analyses, 1×10^5 cells were grown on the porous $\text{Ti}_6\text{Al}_4\text{V}$ plates for 24 h, fixed with 4% glutaraldehyde (1 h), dehydrated through a graded series of acetone, dried in a critical point dryer (K 850, EMITECH, Taunusstein, Germany) and sputtered with a

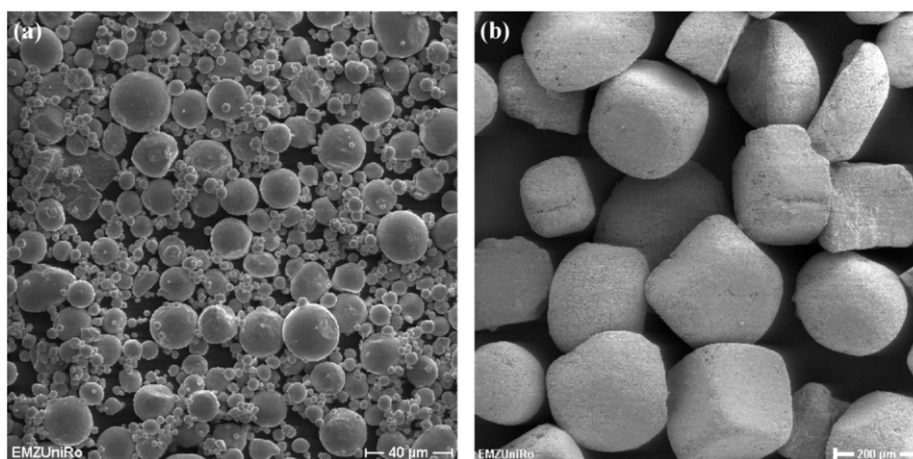


Fig. 2. SEM images of the raw $\text{Ti}_6\text{Al}_4\text{V}$ (a) and NaCl powders (b).

coater (SCD 004, BAL-TEC, Balzers, Lichtenstein). The samples were investigated with a SEM DSM 960A (Zeiss, Germany).

3. Results

The $\text{Ti}_6\text{Al}_4\text{V}$ and NaCl powders are shown in Fig. 2. The $\text{Ti}_6\text{Al}_4\text{V}$ powders have spherical morphologies and size distributions of 5–35 μm . The cuboidal sodium chloride powders have round angles and size distribution of 125–250 μm . In the preparation process, the size of the metal powder should be smaller than the average powder size of the space holder. By choosing the size,

shape and quantity of the space holder material, the mechanical properties of the metal foams can be adjusted.

Table 1 shows a summary of the $\text{Ti}_6\text{Al}_4\text{V}$ foam parameters after spark plasma sintering. Different weight ratios of NaCl powders were mixed with the $\text{Ti}_6\text{Al}_4\text{V}$ powders to get various porosities. After the foams were SPSed at 700 °C, they show porosities of 47.6%, 57.6%, 63.9% and 72.5% ($\pm 1.0\%$), respectively. When they were post-heat treated at 1100 °C, they display porosities of 44.7%, 54.4%, 60.7% and 70.0% ($\pm 1.0\%$). The densities of the foams have been increased 5.5%, 7.5%, 8.9% and 9.1% at above specific porosities after the heat treatments. Detailed microstructural views of the $\text{Ti}_6\text{Al}_4\text{V}$ foam with 70.0% porosity are shown in Fig. 3. Fig. 3a and b displays the foams

Table 1
Summary of parameters of $\text{Ti}_6\text{Al}_4\text{V}$ foams after spark plasma sintering.

Parameters	3 g $\text{Ti}_6\text{Al}_4\text{V}$ /1.02 g NaCl	3 g $\text{Ti}_6\text{Al}_4\text{V}$ /1.6 g NaCl	3 g $\text{Ti}_6\text{Al}_4\text{V}$ /2.2 g NaCl	3 g $\text{Ti}_6\text{Al}_4\text{V}$ /3.4 g NaCl
Density after SPS at 700 °C (g/cm^3)	2.32	1.887	1.607	1.22
Density after heat treatment at 1100 °C (g/cm^3)	2.45	2.02	1.74	1.33
Porosity after SPS at 700 °C (%)	47.6	57.6	63.9	72.5
Porosity after SPS at 1100 °C (%)	44.7	54.4	60.7	70.0
Relative density after SPS at 700 °C (%)	52.4	42.4	36.1	27.5
Relative density after heat treatment at 1100 °C (%)	55.3	45.6	39.3	30.0
Increments in density (%)	5.5	7.5	8.9	9.1

Density of dense $\text{Ti}_6\text{Al}_4\text{V}$ 4.43 g/cm^3 .

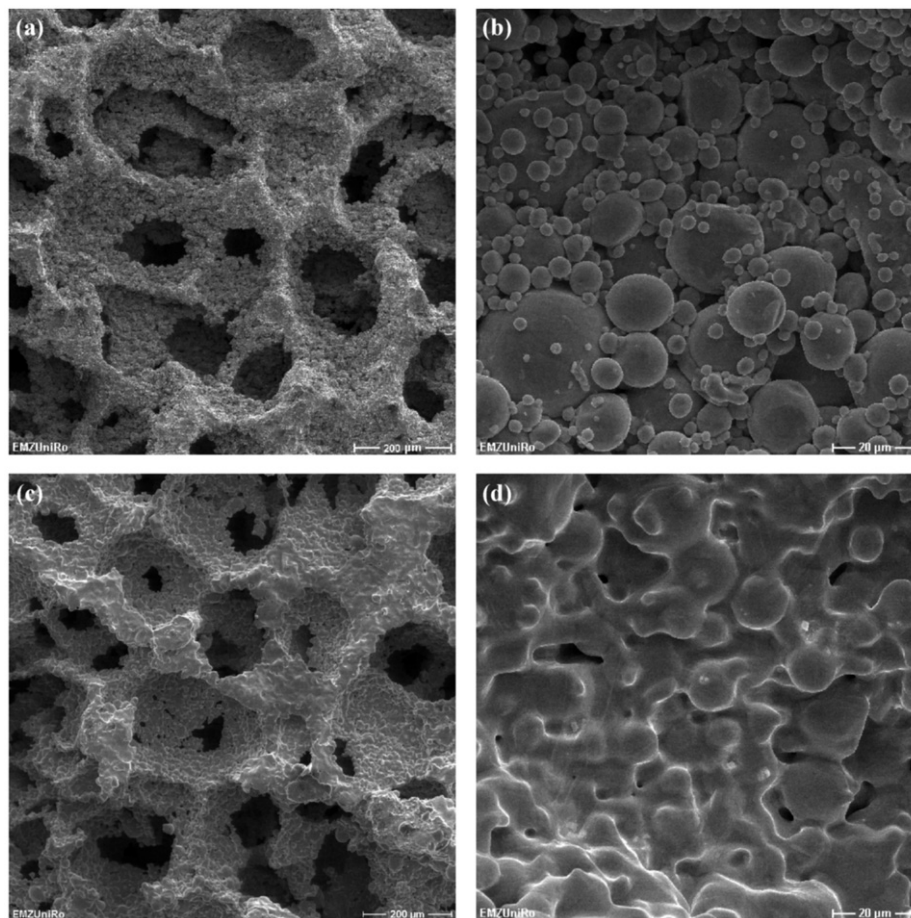


Fig. 3. SEM images of the porous structures and pore walls of the $\text{Ti}_6\text{Al}_4\text{V}$ foams with 70% porosity of the spark plasma sintered at 700 °C, 50 MPa (a,b), and SPS post-heat treatment at 1100 °C (c,d).

fabricated at 700 °C and 50 MPa. They show the porous structure and pore walls, revealing relatively uniformly shaped macropores having rough surfaces, with many micropores ($< 10 \mu\text{m}$) and the shapes and sizes of the original alloy powders being visible. This indicates that the $\text{Ti}_6\text{Al}_4\text{V}/\text{NaCl}$ mixture is difficult to be densified and, as expected, the diffusion at 700 °C was not sufficient to smooth the micropores due to very high melting point of $\text{Ti}_6\text{Al}_4\text{V}$. Fig. 3c and d displays $\text{Ti}_6\text{Al}_4\text{V}$ foams post-heat treatment at 1100 °C at a pressureless mode. After the heat treatment, the junctions between $\text{Ti}_6\text{Al}_4\text{V}$ powder grains are formed with only few micropores left. As seen in Fig. 3d, most of the micropores disappeared due to the heat treatment. This indicates that the pressureless heat treatment contributes to reduce the microporosity of the foams, since no pressure was applied and only diffusion dominated the SPS process. Thus, $\text{Ti}_6\text{Al}_4\text{V}$ foams with higher density of the walls have been fabricated by the SPS at 700 °C and the post-heat treatment at 1100 °C.

The outer shape of the $\text{Ti}_6\text{Al}_4\text{V}$ foam with 54.4% porosity fabricated by the SPS with post-heat treatment is shown in Fig. 4a. Fig. 4b–d displays the micro-CT 3D reconstructions of the foam. The 3D cropped isometric view of cross sections in $\text{Ti}_6\text{Al}_4\text{V}$ foam shows the relative uniform pore distribution and interconnected 3D porous structures. The Micro-CT 2D top view and side view show that the macropore shapes are in square cross sections with a relative uniform distribution of pore sizes of $210 \pm 40 \mu\text{m}$ and with an average cell wall thickness of $22.1 \pm 5 \mu\text{m}$.

Fig. 5 shows the SEM micrographs of the porous $\text{Ti}_6\text{Al}_4\text{V}$ foams with different porosities of 44.7%, 54.4%, 60.7% and 70.0% ($\pm 1.0\%$) fabricated by the SPS with post-heat treatment. The macrostructure of the foam is composed of homogeneously dispersed porous

cavities and continuously connected $\text{Ti}_6\text{Al}_4\text{V}$ struts. It shows mean pores with a size of 150–250 μm achieved with a NaCl spacing material in the range of 125–260 μm . The thickness of the pore walls decreases with increasing porosity. The higher porosity samples show good interconnectivity. The primary pores replicate the size and shape of the angular NaCl particles with rounded corners. Thus, pore shapes can be controlled by using NaCl powders with various shapes. Finally, interconnected pores are visible either as black pores or as necks between adjacent pores in cross sections. These interconnected pores are usually in the range of 20–150 μm in size, indicating that osteoblasts may be able to penetrate into the porous structure.

Fig. 6 demonstrates the synchrotron radiation high energy X-ray diffraction of $\text{Ti}_6\text{Al}_4\text{V}$ foams produced by the SPS. The diffraction pattern confirms the α -Ti phase in the $\text{Ti}_6\text{Al}_4\text{V}$ powder. The α -Ti phase is still present in $\text{Ti}_6\text{Al}_4\text{V}$ foams after the SPS process at 700 °C. In addition to the crystalline diffraction peaks of the α -Ti phase, peaks of intermetallic phase $\text{Al}_3\text{Ti}_{0.8}\text{V}_{0.2}$ (ICDD no. 43-1154) are visible. After the post-heat treatment by the SPS at 1100 °C, it shows that the intensity of the α -Ti (002) peaks is weaker and the peak of $\text{Al}_3\text{Ti}_{0.8}\text{V}_{0.2}$ phase is stronger than those in the 700 °C sintered sample. Additionally, β -Ti (211) plane was detected in the 1100 °C sintered sample. However, there are no impurity peaks visible in the XRD patterns. The X-ray diffraction obtained from the porous $\text{Ti}_6\text{Al}_4\text{V}$ in Fig. 6 proved that the space holder NaCl phase was removed completely. The post-heat treatment has increased the ratio of the β -Ti phase and intermetallic phase $\text{Al}_3\text{Ti}_{0.8}\text{V}_{0.2}$ in the microstructures.

For the evaluation of the mechanical properties of the porous samples, compression tests were performed. Fig. 7a

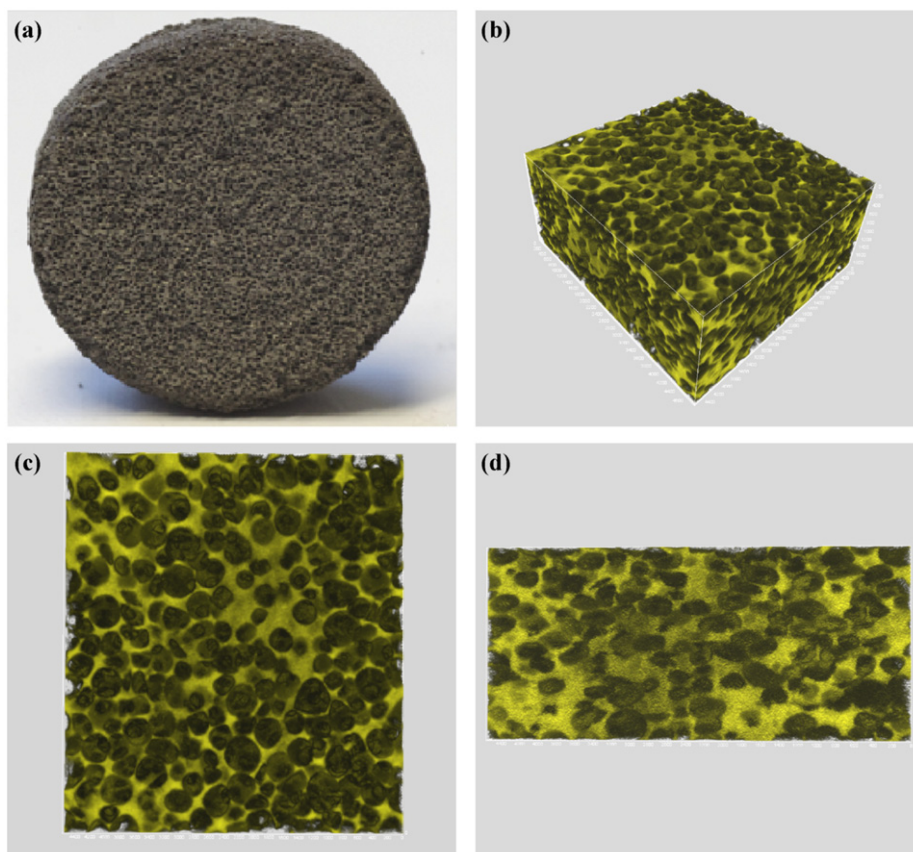


Fig. 4. Micro-CT three-dimensional 3D reconstructions of the $\text{Ti}_6\text{Al}_4\text{V}$ foam (54.4% of porosity) with outer shape of the alloy foam (a), an isometric view (b), 2D top view (c), and left side view (d) (scale bar 200 μm).

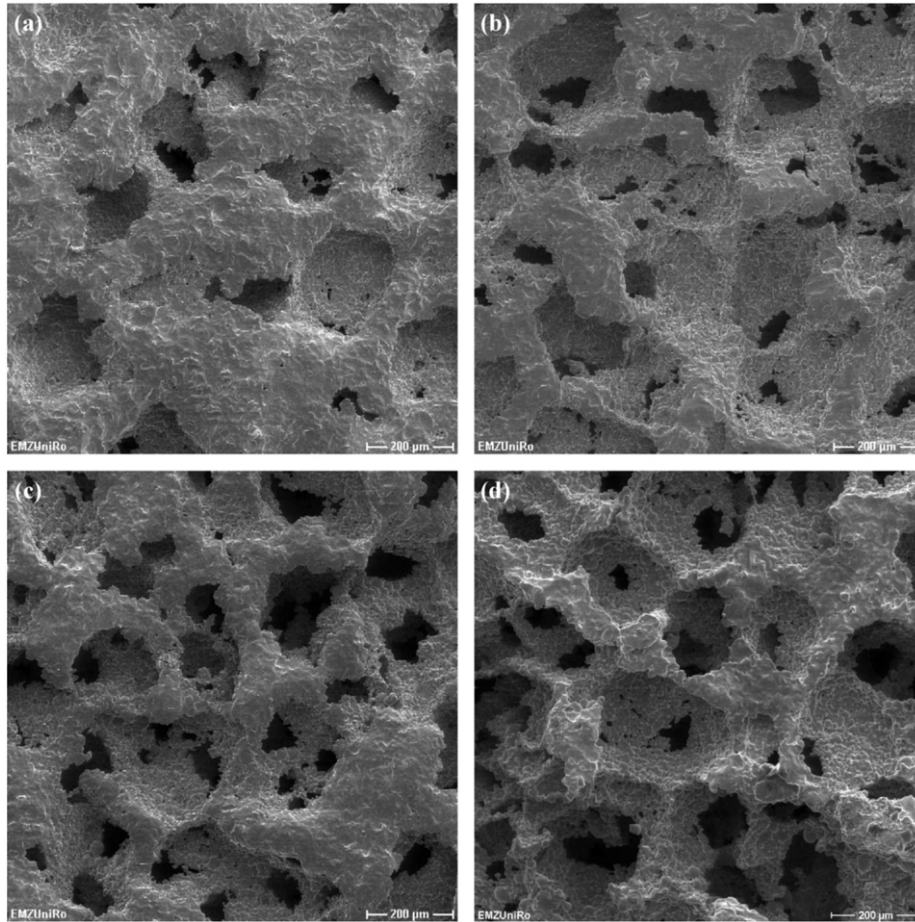


Fig. 5. SEM images of the Ti₆Al₄V foams prepared by SPS with post-heat treatment with different porosities of (a) 44.7%, (b) 54.4%, (c) 60.7%, and (d) 70.0% (± 1.0%).

shows Young's modulus and compressive yield strength as a function of relative density for Ti₆Al₄V foams and the predicted theoretical values. Young's modulus of the porous metals is compared with a prediction according to the Gibson and Ashby model [21]:

$$\frac{E}{E_0} = C \left(\frac{\rho}{\rho_0} \right)^2 \quad (1)$$

where E and E_0 are Young's modulus of foam and bulk materials with densities ρ and ρ_0 , respectively, using $E_0 = 117$ GPa and $\rho_0 = 4.43$ g/cm³ for Ti₆Al₄V [22]. The proportionality constant C has to be considered as 1 for titanium alloys [21]. The estimated Young's moduli ranging from 34.11 GPa to 9.84 GPa obey exponential decays with the increase of porosity, and the actual measured Young's moduli of the foams that are comparable with the calculated Young's modulus based on the density of the Ti₆Al₄V foam. Besides Young's modulus, the strength is an important property of orthopedic implants, particularly in load bearing applications. According to the Gibson–Ashby model, the relationship between the yield strength and relative density is given by [21]

$$\frac{\sigma}{\sigma_0} = C \left(\frac{\rho}{\rho_0} \right)^n \quad (2)$$

where σ_0 and ρ_0 are the yield strength and the density of the solid material σ and ρ of the foam, respectively. The experimental data indicate that C is around 0.3 and the strength of the foam is proportional to the strength of the solid ($n = 3/2$) [23]. The density of dense solid Ti₆Al₄V is 4.43 g/cm³ with yield

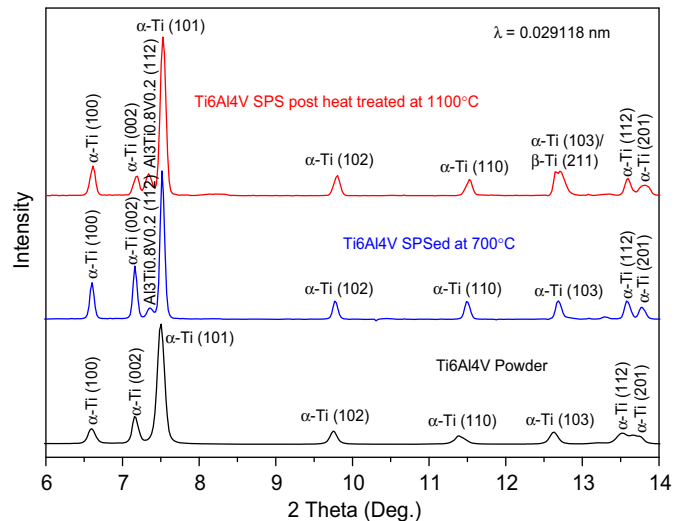


Fig. 6. Synchrotron radiation high energy X-ray diffraction patterns of the Ti₆Al₄V powder and spark plasma sintered Ti₆Al₄V foams.

strength 902 MPa [24,25]. The yield strength of Ti₆Al₄V foams and predicted theoretical values for open porous material are given in Fig. 6b. It can be seen that the measured values for porous Ti₆Al₄V are slightly higher than the analytical predictions by Gibson–Ashby model for open structures, and also much higher than the compressive strength of cancellous bone (10–50 MPa).

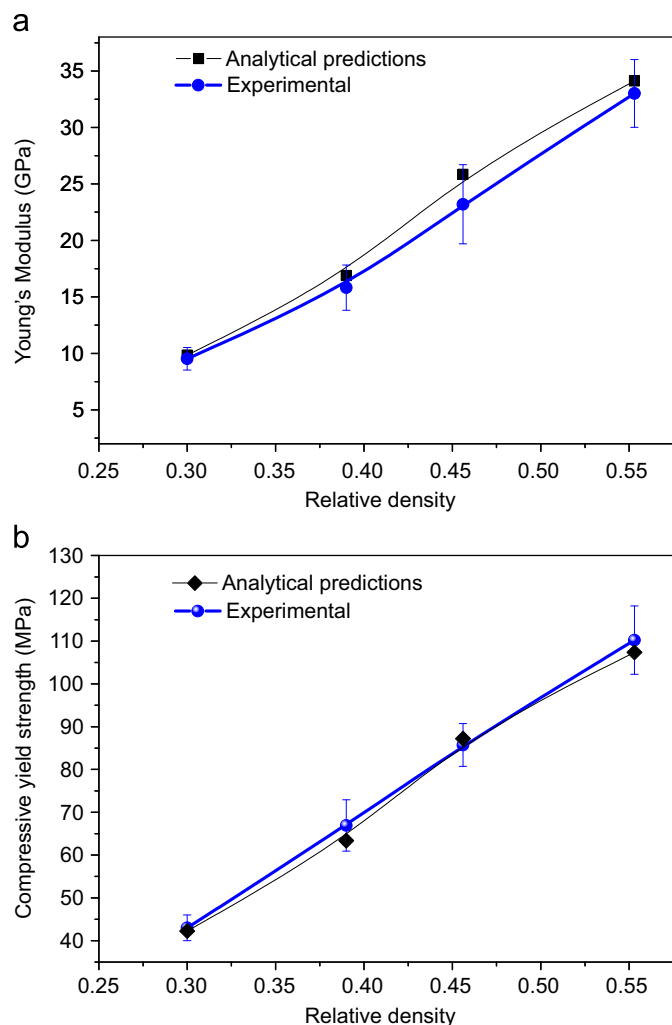


Fig. 7. Young's modulus (a) and yield strength (b) of the $\text{Ti}_6\text{Al}_4\text{V}$ foams and theoretically predicted values.

The experimental values are all comparable with the calculated data obeying the Gibson and Ashby model.

Human osteoblast like cells (MG-63) were cultured on the porous $\text{Ti}_6\text{Al}_4\text{V}$ samples. Fig. 8 shows the SEM images of human bone-like MG-63 cells on porous $\text{Ti}_6\text{Al}_4\text{V}$ foams with 44.7%, 54.4%, 60.7%, and 70.0% ($\pm 1.0\%$). After 24 h they exhibit a well spread morphology and excellent bonding to the surface. The cells form filopodia reach the adjacent grains of the $\text{Ti}_6\text{Al}_4\text{V}$ structure. The cells grow inside the pores to a large extent implying a good integration when implanted into the bone. For a better interconnectivity, higher porosity $\text{Ti}_6\text{Al}_4\text{V}$ foams (above 60%) are recommended for the biomedical applications. This cell tests display that the pore sizes and porous surface of the $\text{Ti}_6\text{Al}_4\text{V}$ foams fabricated by the SPS are suitable for the osteoblasts in-growth.

4. Discussion

In this study, the $\text{Ti}_6\text{Al}_4\text{V}$ foams were fabricated by using SPS at 700 °C with controlled porosity followed by dissolution of NaCl phase and post-heat treatment at 1100 °C. The NaCl has a melting point of 801 °C. In the actual experiments, the temperatures of 650 °C, 700 °C, 720 °C, and 750 °C have been tested in the first step of SPS. At 720 °C, a little NaCl melted and reacted with Ti

resulted in some impurities formation. At 750 °C, most of the NaCl spacer melted and the expansion of the sample destroyed the graphite die. The sintering temperature was determined as 700 °C finally. A relatively high pressure of 50 MPa allows the use of pressure to enhance the densification of the $\text{Ti}_6\text{Al}_4\text{V}/\text{NaCl}$ mixture. The higher pressures from 60 to 80 MPa have been tested. At these pressures, the graphite dies were easy to break due to the thermal expansion of $\text{Ti}_6\text{Al}_4\text{V}/\text{NaCl}$ mixture during sintering. In the end, the parameters of 700 °C and 50 MPa were selected. Previous investigations showed that high-density pure Ti foams can be fabricated with NaCl as space holder by the SPS at 700 °C and 50 MPa [15]. However, the $\text{Ti}_6\text{Al}_4\text{V}/\text{NaCl}$ mixture cannot be densified at the same condition. It indicates that this $\text{Ti}_6\text{Al}_4\text{V}/\text{NaCl}$ mixture is difficult to be consolidated either in the hot pressing [13] or in the SPS. The $\text{Ti}_6\text{Al}_4\text{V}$ foams were post-heat treated by the pressureless SPS method at 1100 °C for 5 min. The alpha-beta transus temperature of the $\text{Ti}_6\text{Al}_4\text{V}$ alloy is about 1000 °C. In the second run, several temperatures (1050 °C, 1100 °C, 1150 °C and 1200 °C) over the transus temperature were tested. The results indicated that at 1050 °C it cannot densify the foam walls well. At 1150 °C and 1200 °C, the samples were overheated with melting of grain boundaries. Hence, 1100 °C was confirmed as the optimal heat treatment temperature. The densities of the foams have been increased as shown in Table 1. The relative density values can give the information of macroporosity and microporosity in the foams. The macroporosity was determined by the fraction of NaCl spacer after the SPS at 700 °C and dissolution in water. The post-heat treatment by pressureless SPS at 1100 °C will contribute in reducing the microporosity of the foams. As the schematic diagram of the graphite die setup for the pressureless SPS in Fig. 1 indicated, the gap d is greater than or equal to 0 mm between the top punch and the sample. When the gap is zero, the current can pass through the sample at the beginning of sintering. After densification and shrinkage of the sample, it became into a break circuit again. When the gap is greater than zero, it is a break circuit. The current can only pass through the graphite punch and outer form, but not the sample. The sample was heated by the temperature field of the graphite die. There was no pressure being applied, therefore the surface diffusion, volume diffusion and grain boundary diffusion dominated the densification process in the pressureless SPS. These diffusions mainly play roles of reducing the microporosities in the foams. This pressureless SPS is similar to a conventional pressureless sintering. The only difference between them is the efficiency where the pressureless SPS is much faster with a faster heating rate and a shorter holding time. This post-heat treatment by the pressureless SPS is similar to the technique of hot isostatic pressing (HIP) used to reduce the microporosity of metals and to increase the density of many ceramic materials, thereby improving the material's mechanical properties. The post-heat treatment by the pressureless SPS can be done in vacuum and argon gas up to 40 hPa. The results in this study indicate that this pressureless SPS method can be used for post-heat treatment of $\text{Ti}_6\text{Al}_4\text{V}$ foams, and possibly for all the metallic foams, dense metals and ceramics.

Because of the passive oxide film that was formed at room temperature, Ti alloys has very good corrosion resistance. The oxide films on the powder surfaces would probably have some effects on the sintering temperatures; however, it is not noticeable during the SPS process. In another side, the biological properties of a Ti implant depend on its surface oxide film [26]. TiO_2 has good cell biocompatibility and it is already used as a coating on many Ti alloys [27]. In this study, there are no bad effects observed for the oxide films interaction with the MG-63 cells. Consequently, this method using SPS by dissolution of NaCl spacer and post heat treatment provides a foamed structure with a close homogenous pore structure, high levels of porosity and improved mechanical properties. The mechanical properties of

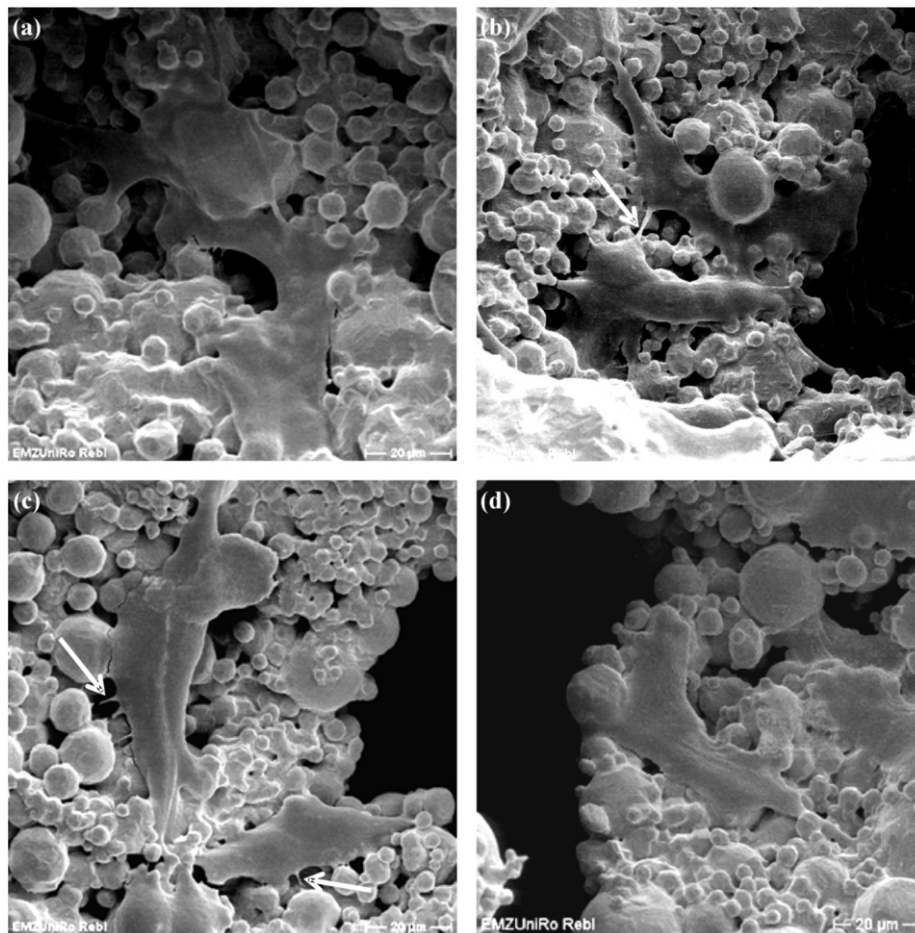


Fig. 8. SEM of human bone-like MG-63 cells on porous $\text{Ti}_6\text{Al}_4\text{V}$ foams (a) 44.7%, (b) 54.4%, (c) 60.7%, and (d) 70.0% (± 1.0). The cells display a well spread morphology and moreover the cells extend various filopodia to the adjacent grains (arrow).

the metal foam can be adjusted by choosing the size, shape and quantity of the space holder material used. The highly porous nature of the alloys combining improved mechanical properties with osteoconductivity makes these materials ideal for bone scaffolds. The future highlights will be net-shape processing of foams with complex forms by the SPS method. Prospectively, this kind of $\text{Ti}_6\text{Al}_4\text{V}$ foams has potential to alleviate the problem of mechanical mismatch between the bones and the Ti alloy implants and may provide a new candidate as a long-term bone substitute for biomedical applications.

5. Conclusions

$\text{Ti}_6\text{Al}_4\text{V}$ foams were fabricated by the SPS with post-heat treatment using a blend of $\text{Ti}_6\text{Al}_4\text{V}$ and sodium chloride powders. $\text{Ti}_6\text{Al}_4\text{V}$ foams fabricated at 700 °C and 50 MPa in SPS cannot achieve high relative densities. The sintered foams were post heat treated in a pressureless mode of the SPS at 1100 °C for 5 min. This heat treatment is very effective in reducing microporosity and to densify the foam walls. Young's moduli of the foams were in the range from 33.0 ± 3.2 GPa to 9.5 ± 1.0 GPa and the yield strengths ranged from 110.2 ± 8.0 MPa to 43.0 ± 2.8 MPa with porosity values from 44.7% to 70.0% (± 1.0)% obeying the Gibson–Ashby models. The human osteoblast cell line MG-63 validated the cellular acceptance of the foam surfaces. This pressureless SPS method can be used for post-heat treatment

of $\text{Ti}_6\text{Al}_4\text{V}$ foams, and possibly for all the metallic foams and dense solids.

Acknowledgments

This research was supported by the DFG (German Research Foundation) with Grant no. GRK1505/1 (Welisa). Mr. Quan acknowledges the support from China Scholarship Council (CSC) with File no. 2010603007. Fruitful discussion with Prof. D.C. Dunand in Northwestern University, USA is acknowledged. We would like to thank Dr. H.P. Liermann for his assistance in using Beamline P02.2 (Petra III/Desy).

References

- [1] M. Long, H.J. Rack, *Biomaterials* 19 (1998) 1621.
- [2] M.J. Donachie, *Titanium: A Technical Guide*. (1988) 5–11.
- [3] L.D. Zardiackas, L.D. Dillon, D.W. Mitchell, L.A. Nunnery, R. Poggie, *J. Biomed. Mater. Res.* 58 (2001) 180–187.
- [4] J.T. Clemow, A.M. Weinstein, J.J. Klawitter, J. Koeneman, J. Anderson, *J. Biomed. Mater. Res.* 15 (1981) 73.
- [5] J. Banhart, *Prog. Mater. Sci.* 46 (2001) 559–632.
- [6] D.C. Dunand, *Adv. Eng. Mater.* 6 (2004) 369–376.
- [7] N.G.D. Murray, D.C. Dunand, *Compos. Sci. Technol.* 63 (2003) 2311–2316.
- [8] N.G.D. Murray, D.C. Dunand, *Acta Mater.* 52 (2004) 2269–2278.
- [9] I.M. Robertson, G.B. Schaffer, *Powder Met.* 53 (2010) 27–33.
- [10] Y. Sakamoto, K. Asaoka, M. Kon, T. Matsubara, K. Yoshida, *Bio-Med. Mater. Eng.* 16 (2006) 83–91.
- [11] P.A. Noel, D.C. Dunand, A. Mortensen, *Composites* 25 (1994) 953–956.
- [12] A. Bansiddhi, D.C. Dunand, *Acta Biomater.* 4 (2008) 1996.

- [13] B. Ye, D.C. Dunand, *Mater. Sci. Eng. A* 528 (2010) 691–697.
- [14] F. Zhang, A. Weidmann, J.B. Nebe, U. Beck, E. Burkel, *J. Biomed. Mater. Res. B* 94B (2010) 406–413.
- [15] F. Zhang, E. Otterstein, E. Burkel, *Adv. Eng. Mater.* 12 (2010) 863–872.
- [16] F. Zhang, E. Burkel, in: Anthony N. Laskovski (Ed.), *Biomedical Engineering, Trends, Researches and Technologies*, InTech 978-953-7619.
- [17] F. Zhang, K. Lin, J. Chang, J. Lu, C. Ning, *J. Eur. Ceram. Soc.* 28 (2008) 539–545.
- [18] A. Ibrahim, F. Zhang, E. Otterstein, E. Burkel, *Mater. Des.* 32 (2011) 146–153.
- [19] *Testing Metallic Materials, Compression Test, DIN 50106, Issue: 1978-12.*
- [20] H. Rebl, B. Finke, R. Lange, K.-D. Weltmann, J.B. Nebe, *Acta Biomater.* 8 (10) (2012) 3840–3851.
- [21] L.J. Gibson, M.F. Ashby, *Cellular Solids: Structure and Properties*, 2nd edition Cambridge University Press, 1997, pp. 175–281.
- [22] H. Choe, S.M. Abkowitz, S. Abkowitz, D.C. Dunand, *Mater. Sci. Eng. A* 396 (2005) 99.
- [23] J. Biener, A.M. Hoodge, A.V. Hamza, L.M. Hsiung, J.H. Satcher, *J. Appl. Phys.* 97 (2005) 024301.
- [24] M. Bram, H. Schiefer, D. Bogdanski, M. Koller, H.P. Buchkremer, D. Stover, *Met. Powder Rep.* 61 (2006) 20–23.
- [25] M.H. Lee, K.B. Kim, J.H. Han, J. Eckert, D.J. Sordelet, *J. Phys. D: Appl. Phys.* 41 (2008) 105404.
- [26] B. Feng, J.Y. Chen, S.K. Qi, L. He, J.Z. Zhao, X.D. Zhang, *J. Mater. Sci. Mater. Med.* 13 (5) (2002) 457–464.
- [27] D.Y. Kim, M. Kim, H.E. Kim, Y.H. Koh, H.W. Kim, J.H. Jang, *Acta Biomater.* 5 (6) (2009) 2196–2205.